

High Resolution Scattering of He Atoms and D₂ Molecules from the LiF(001) Crystal Surface

Dissertation

zur Erlangung des Doktorgrades
der Mathematisch-Naturwissenschaftlichen Fakultäten
der Georg-August-Universität zu Göttingen

vorgelegt von
Yasin Ekinici
aus Denizli, Türkei

Göttingen 2003

D7

Referent: Prof. Dr. F. Huisken

Korreferent: Prof. Dr. W. Lauterborn

Tag der mündlichen Prüfung: 15.12.2003

.....

Nichts hindert mehr, hier ist Magie zur Hand.

.....

Faust, 2. Teil, J. W. von Goethe

Dedicated to
my wife Dilek
and
my son Ilyas Fatin Erge.

Abstract

In the present dissertation a flexible, high-resolution molecular beam apparatus is described which allows surface scattering experiments over a wide range of final angles for fixed incident angles of 0 to 90 degrees. These features have been utilized in this work for investigation of the free-jet expansion of D_2 beams and the scattering of He and D_2 beams from LiF(001) and Si(111):H(1 \times 1) surfaces.

The n- D_2 beam is first characterized by mass spectrometer analysis of the cluster fragments and measurements of velocity distributions at stagnation temperatures of 108-300 K and at pressures between 10-120 bar. The mass spectra are measured in the range 1-40 a.u. Under conditions of massive condensation, maxima in the intensities of the ion fragments attributed to the neutral clusters $(D_2)_5$ and $(D_2)_8$ are observed. Terminal mole fractions of the dimers are investigated in the light of available theories [1] and in comparison with the published H_2 data [2]. It is observed that the D_2 dimer mole fractions at high source temperatures are found to be less than the dimer mole fractions of H_2 for the same scaling parameter [1], which takes the thermodynamics and kinematic of the expansion into account. This is ascribed to the more probable rotational relaxation of the D_2 molecules. Temperature and velocity lags between the monomers and the clusters are observed which are in accordance with a two-step dimerization model [3].

Preparatory experiments for the focusing of neutral and thermal He beams with a bent-thin Si(111):H(1 \times 1) crystal mirror are presented next. *Ex-situ* prepared, hydrogenated Si(111) crystals are characterized with He atom scattering (HAS) in order to test the reliability of the transportation and storage of the crystals for further applications. The crystal surface showed diffractive scattering and selective adsorption resonances, indicating that the crystal has an ordered surface. The specular reflectivity of the crystal surface is found to be about 10^{-4} . It is observed that Si(111):H(1 \times 1) surface is highly sensitive to hydrocarbon contamination. Both the poor reflectivity and extreme sensitivity to contaminations of the Si(111):H(1 \times 1) crystal surface will limit its further applications.

The surface lattice constant of the LiF(001) surface is measured by HAS at surface temperatures of 110-720 K. The thermal expansion coefficient of the surface is found to be the same as the thermal expansion coefficient of the LiF bulk within the precision of the experiments, which is contrary to previous results [4, 5]. The LiF(001) surface remains in the ideal (1 \times 1) structure without any significant lateral contraction or

expansion in the surface plane.

Scattering experiments of D_2 molecular beams from the LiF(001) surface are also presented. Elastic diffraction and rotationally inelastic diffraction (RID) peak intensities for incident angles $\theta_i=0$ to 90 degrees, for incident beam energies $E_i=20$ -120 meV and for surface temperatures between 130-600 K along the $\langle 110 \rangle$ and $\langle 100 \rangle$ symmetry axes are measured and analyzed. The relative and absolute intensities in the RID and Bragg peaks are used to extract rotational transition probabilities of the D_2 molecule. High probabilities of the translational energy transfer to molecular rotations are observed. At certain incident angles and energies maxima in the diffraction and rotational transitions, so called rotational and diffractive rainbows, are observed. A strong coupling between rotational transitions and diffractive scattering is observed. The surface temperature attenuation of the diffraction and RID peaks showed that the rotational transitions and the surface phonon de/excitations are decoupled. Selective adsorption resonances (SAR) determined from drift-TOF spectra of the specular peak showed that the attractive potential well depth is 35.3 meV, which is somewhat less than the previous experimental results ($D=37.7$ meV) [6], but larger than the well depth of the theoretical Kroes-potential ($D=31$ meV) [7]. The diffraction and RID transition probabilities are compared with the theoretical CCWP calculations [8] carried out for the Kroes-potential [7]. It is found that the theory is highly successful in predicting the probabilities of the diffractive and the rotational transitions. However, when rotational and diffractive rainbow effects are observed, the theoretical agreement is found to be less satisfactory. This is attributed to the high sensitivity of rainbow effects on the surface corrugation and the anisotropic part of the potential. Hence, the theoretical interaction potential requires further improvements.

Contents

1. Introduction	5
2. Theoretical Concepts in Particle Scattering from Surfaces	11
2.1 Scattering from Surfaces	11
2.2 Interaction Potentials	14
2.2.1 Model Potentials	15
2.2.2 Potentials for Molecule-Surface Interaction	16
2.3 Calculation Methods	22
2.3.1 Close-Coupling Calculation	22
2.3.2 Time-Dependent and Close-Coupling Wave Packet Method	23
2.4 Thermal Attenuation and the Effect of the Potential Well	24
2.5 Resonant Scattering	26
3. The Apparatus and Experimental Details	27
3.1 The Apparatus	30
3.1.1 The Beam Source	36
3.1.2 The Chopper and the TOF Module	38
3.1.3 Target Chamber	38
3.1.4 Target Manipulator	39
3.1.5 Variable Detector Angle	46
3.1.6 Crystal Holder	46
3.1.7 The Detector	47
3.1.8 Differential Pumping System	50
3.1.9 D ₂ Recycling Unit	52
3.2 Data Analysis and Experimental Resolution	54
3.2.1 Calibration of Elastic TOF Experiments	54
3.2.2 Inelastic TOF Experiments	60

3.2.3	Angular Scan Experiments	66
3.3	Conclusions	68
4.	Characterization of the Molecular Beams	71
4.1	General Properties of Supersonic Free-Jet Beams	71
4.2	Characteristics of He Beams	76
4.3	Internal Relaxation and the Overall Characteristics of n-D ₂ Beam	84
4.4	Cluster Formation in n-D ₂ Beams	93
4.4.1	Experiment	95
4.5	Conclusions	105
5.	Preparatory Experiments for He-Microscopy	111
5.1	Experiment	113
5.2	Conclusions	124
6.	Thermal Expansion of the LiF(001) Surface	127
6.1	LiF(001) Surface	129
6.2	Experiment	133
6.2.1	Surface Preparation	133
6.2.2	Precision Considerations	137
6.2.3	Debye-Waller Factor	143
6.2.4	Thermal Expansion Coefficient	145
6.3	Conclusions	149
7.	The Scattering of D₂ from LiF(001)	151
7.1	Experiment	153
7.1.1	Calculation of Probabilities	157
7.2	Selective Adsorption Resonances	160
7.3	Debye-Waller Factor Analysis	166
7.4	Scattering with Different Incident Beam Energies	171
7.5	Constant Incident Angle Measurements	179
7.6	Scattering of D ₂ Dimers from the LiF(001) Surface	197
7.7	Conclusions	199
8.	Summary and Outlook	203
A.	Complete Data for D₂-LiF(001)	209

1. Introduction

"It is all a matter of intensity."

N. F. Ramsey

The atomic and molecular beam method was introduced at the beginning of the last century in order to study the kinetic theory [9]. With the effusive beam sources, it was possible to carry out a number of pioneering experiments which contributed to establishing the fundamentals of modern physics [10]. The basic idea is to isolate the particles and introduce the intended perturbation to them in a fully controlled manner. In the second half of the century, supersonic beam sources, which provide high intensities, were proposed by Kantrowitz and Grey [11] and successfully demonstrated by Becker and Bier [12]. Through this development, the molecular beam method has become a powerful and wide-spread method in various research fields such as laser spectroscopy, collisions and reaction dynamics of molecules and clusters, magnetic and electric resonance spectroscopy, and surface science [13–15].

The extensive cooling reached in supersonic free-jet expansion allows the production and investigation of weak van der Waals complexes. Clustering and condensation have been and are still objects of research activity [13, 15]. Intense research effort is involved with quite different motivations, such as, to avoid the clustering, to study the formation kinetics, to investigate van der Waals complexes, to understand the evolution from molecular to bulk properties, and for applications in semiconductor surface manipulation and fusion research [16, 17]. The expansion characteristics and clustering properties of D_2 are investigated in Chapter 4. The understanding of clustering kinetics of hydrogen and its isotopes can contribute to the *hydrogen research* which is becoming one of the main research fields and challenges of the future [18, 19].

As surface probes, atomic and molecular beams have the advantage that only the properties of the upper-most surface layer are investigated without contributions of bulk atoms. The method is also a non-destructive probe and extremely sensitive to adsorbates. Especially helium atom beams provides high intensity and monochromaticity

which has made HAS a standard tool to study dispersion curves of surface phonons [20–22]; structural properties of clean surfaces, adsorbates, and defects [23–25]; surface growth, phase transition, surface diffusion and adsorption [26, 27]. With the progress of theoretical and experimental methods in past 30 years, considerable advances have been made in atomic and molecular scattering from surfaces, which has been the subject of several reviews [28–36] and books [20, 23, 37–40].

The wide application of molecular beams, particularly, of the He atom scattering (HAS) technique as a tool in surface science is surely indebted to the developments and improvements in beam generation and detection techniques and UHV technology. The evolution of the beam machines designed for surface analysis can be found in ref. [35, 41]. A typical HAS apparatus incorporates three essential units; source, sample, detector. The sample is placed in the center of the apparatus, preferably in a separate chamber enabling the installation of other surface analysis tools and instruments for surface preparation, and to achieve the required ultrahigh vacuum conditions. Since the beam source requires large pumps, the source chamber and incident beam direction are mostly fixed in the laboratory. In elastic diffraction scattering experiments a setup is adopted by several authors where the detector can rotate in the scattering plane. In the inelastic experiments, however, a long target-to-detector length is necessary for energy resolution and several differential pumping stages preceding the detector are required to reduce the background signal, therefore making it difficult to rotate the detector [42]. There are three setups are proposed for the solution of this problem. The most common one employs a geometry in which the angle between the incident and scattered beams is fixed [43]. This setup is cheap, highly convenient and adequate for inelastic scattering. On the other hand, it implicates the restriction for elastic diffraction scattering experiments that the total scattering angle is fixed and the observed diffraction peaks have different incident angles which means further complication for the theoretical comparison. In a second solution the source is rotated and the detector is fixed [44]. This set up provides both to combine the detector with several pumping stages and the flexible geometry for elastic scattering experiments. The construction of a rotatable source, however, requires a large target chamber and has the technical difficulties of the linkage of large source chamber with the first differential pumping stage. A third solution to the problem is presented in Chapter 3 involves not only rotating the detector, but also all the pumping stages preceding the detector chamber around the target while keeping the target and source chambers fixed.

The surface imaging techniques, such as STM, SEM and AFM, have undergone a rapid development and have found many applications. These techniques have, how-

ever, the disadvantage of being inappropriate for nonconducting surfaces and of being potentially destructive. An HAS-scanning microscope with increased intensity and spatial resolution will overcome these problems and offers a tool of surface analysis extended to the studies of adsorbates, polycrystalline surfaces, phase transitions, as well as delicate systems such as cell membranes and thin films of organic molecules. However, the difficulty of manipulation of neutral atoms is the main hurdle for the realization and the development of a HAS-scanning microscope. The manipulation of neutral atoms, so called, *atom optics*, has become a field of intensive research. Manipulation and focusing of neutral atoms have been realized by using electric, magnetic and optical fields [45]. These methods utilize the Stark, Zeeman and AC Stark effects of cold atoms and they are not suitable for neutral ^4He atoms of thermal energies, which have no spin¹ and a low dipole polarizability. There have been two approaches proposed and realized for the focusing of He atoms: Fresnel zone plates and bent-crystal mirrors [47, 48]. In Chapter 5 these two methods are compared in detail and preparatory experiments for the utilization of Si(111):H(1×1) thin crystals as bent-crystal mirrors for the focusing of neutral He beams are presented.

He and H₂ scattering from the LiF(001) surface is a classical and historical example of the particle scattering from crystal surfaces. Stern and his colleagues [49–51] and Johnson [52, 53] observed the diffraction of helium atoms and hydrogen molecules from LiF(001), demonstrating the wave nature of the atoms and molecules. 70 years after the first observation of the scattering of He from the LiF(001) surface [49, 50], the particle-surface interactions on LiF(001) are still a matter of experimental and theoretical interest [54–56].

The scattering of He from the surface is a direct method of measuring the lattice constant. The diffraction of the atoms is defined by Bragg’s law and provides direct information on the structure of the surface reciprocal lattice. Earlier structural and dynamical investigations of the LiF(001) surface assumed an ideally terminated (1×1) surface structure resulting from the cleavage of the bulk, which has the rock salt structure like most of the alkali halides. However, it has been reported that the thermal expansion coefficient of the LiF(001) surface is significantly larger than the bulk values [4, 5, 57]. In this case, presuming that the lattice constants of the surface and the bulk are the same at 0 K, a difference in the coefficient of the thermal expansion by a factor of two, leads to a discrepancy of a few percent between the bulk and the surface lattice

¹This is not true for ^3He , which can be focused with a hexapole magnet system [46]. Since it is an expansive isotope, it is not appropriate for wide-spread applications.

constants at room temperature. Although this discrepancy is of little consequence for most surface scattering experiments, some physical properties which are surface lattice constant dependent, such as surface phonon dispersions [58] and the bound state energies [59], should be corrected according to the "real" surface lattice constant. Moreover, an understanding of the relaxation parallel to the surface plane is important for a better insight into surface-related phenomena, such as atom (molecule)-surface potentials, surface diffusion, thermal conductivity and surface phonons, adsorption and also surface rumpling relaxation which is still under investigation [60,61]. In Chapter 6, the thermal expansion and the lattice constant of the LiF(001) surface are readdressed. With the apparatus of high angular resolution described in this work, it is possible to measure the lattice constant of crystal surfaces with a precision of 0.2% . To our knowledge there is no other work reporting the temperature dependence of lattice constant $a(T)$ with a precision reached in this work.

Whereas the scattering of atoms and particularly He at surfaces has been extensively studied [31,33], much less theoretical and experimental work has been done for the scattering of molecules. The molecular scattering technique is a direct method to probe the molecule-surface interaction potential, which is a basic prerequisite for the understanding of physisorption and chemisorption and particularly the role of internal degrees of freedom. During a collision, the molecule may exchange energy not only with surface phonons but also between its own translation and internal vibrational and rotational degrees of freedom. After extensive theoretical works based on available results on H₂ molecule scattering from LiF(001) it appeared to be a well understood system and a closed chapter [62–68]. In these investigations the effects of quadrupole-electrostatic interactions, magnetic quantum number changes and the azimuthal orientation of the molecule were mostly overlooked [62,69]. However, a recent theoretical study [7,70] pointed out that the scattering process must strongly depend on these effects. The confirmation of this prediction was recently observed in comparing the diffraction experiments with n-H₂ and p-H₂ [54]. These earlier experiments motivated the investigation of the D₂ scattering from LiF(001) presented in Chapter 7. In D₂ scattering from LiF(001) the rotational transitions are more pronounced since D₂ has lower rotational transition energies than H₂. Therefore, it allows the investigation of the coupling of the diffractive and rotational transition processes. The rotational transitions are also expected to be more sensitive to the interaction potential, particularly the anisotropic parts. The diffraction and RID peaks are more clear, compared to H₂, because of the lower detector background signal at mass 4 amu. Moreover, a comparison of H₂ and D₂ scattering should provide deeper insight into

the molecular scattering from alkali halide surfaces. Furthermore, molecular scattering from the LiF(001) surface provides a benchmark system for understanding more complicated systems such as reactive scattering from metal surfaces [71].

This report is organized in the following way:

- In Chapter 2, basic theoretical concepts of the atom and molecule scattering from surfaces are presented. It provides the necessary tools for the interpretation of the experimental results.
- In Chapter 3, a new molecular beam apparatus, Magie-2, is presented. After describing basic units of the apparatus and highlighting its superior features, experimental set-up and details used in latter chapters are described. The calibration of the time-of-flight (TOF) method is discussed. Angular and energy resolution in elastic and inelastic experiments is described.
- In Chapter 4, utilizing the opportunity of experimenting with direct-beam (source-to-detector angle is 180°) of the apparatus, overall characteristics of the supersonic expansions of the He and D₂ beams are investigated and the clustering properties of the D₂ beam are studied.
- In Chapter 5, the transportation and characterization of the Si(111):H(1×1) crystal surfaces with HAS experiments are presented, which serve as preparatory experiments for the focusing of the neutral, thermal He beams with the bent-crystal surface. The feasibility of the transportation of the crystals into the vacuum and its inertness in vacuum for further application as a focusing tool are tested and discussed.
- In Chapter 6, by using HAS, the thermal expansion properties of the LiF(001) surface are investigated.
- In Chapter 7, elastic and RID inelastic scattering of D₂ molecules from LiF(001) surface are studied with changing the total angle of the scattering geometry and the incident beam energy. Drift-TOF spectra of the specular peak are presented, providing incident energy-resolved scattering of the D₂ molecules. Also the coupling of the surface phonons and the rotational transitions is readdressed.
- Finally, in Chapter 8, the attained results and conclusions are summarized and the future work under the fiat of obtained knowledge from this work is pointed.

2. Theoretical Concepts in Particle Scattering from Surfaces

In this Chapter the basic concepts which are necessary for understanding the experimental results presented in the next chapters are discussed briefly. In Section 2.1 the kinematics of atom and molecule scattering from two dimensional ordered surfaces are discussed. The kinematical equations which are indispensable tools to understand the observed diffraction pattern are provided. They supply information of the surface symmetry from the diffraction angles of the observed peaks. In addition to this, from the time-of-flight (TOF) measurements simple kinematical equations directly provide information about the surface phonons. Nevertheless, the full understanding of scattering experiments requires an insight into the atom (or molecule)-surface interaction. The interaction potentials and computational methods are presented in Sections 2.2 and 2.3. In these sections some commonly used model potentials and also more realistic potentials used specifically for H₂ (or D₂) scattering from LiF surface are reviewed. In the comparison of the theory and the experiments the inelastic effects due to the thermal vibrations of the surface atoms must be taken into account. This point is discussed in Section 2.4. The temporary resonant trapping of the scattering particle in the potential well, so called selective adsorption, provides important information on the interaction potential and is introduced in Section 2.5.

2.1 Scattering from Surfaces

The scattering of particles from a two dimensional surface can be described by simple energy and momentum conservation equations. The lattice points of a perfect two dimensional periodic surface are defined from an arbitrary origin by the translational lattice vectors [72],

$$\mathbf{R} = m \cdot \mathbf{a} + n \cdot \mathbf{b} \quad , \quad (2.1)$$

where m and n are integers and \mathbf{a} and \mathbf{b} are *primitive lattice vectors*¹. The parallelogram defined by these vector form the boundaries of the *unit cell*. The observed diffraction patterns have a direct correspondence with the reciprocal lattice of the surface. The relation between the real and reciprocal lattice vectors is defined through:

$$\mathbf{a}^* = 2\pi \frac{(\mathbf{b} \times \hat{\mathbf{z}})}{\mathbf{a} \cdot (\mathbf{b} \times \hat{\mathbf{z}})} \quad , \quad (2.2)$$

$$\mathbf{b}^* = 2\pi \frac{(\hat{\mathbf{z}} \times \mathbf{a})}{\mathbf{b} \cdot (\hat{\mathbf{z}} \times \mathbf{a})} \quad , \quad (2.3)$$

where $\hat{\mathbf{z}}$ is the unit vector normal to the surface plane. Any reciprocal lattice vector is thus given by

$$\mathbf{G}_{mn} = m \cdot \mathbf{a}^* + n \cdot \mathbf{b}^* \quad . \quad (2.4)$$

The LiF has the rock salt structure and on the (001) surface is the \mathbf{G}_{mn} is defined as

$$\mathbf{G}_{mn} = \left(\frac{2\pi}{a}m, \frac{2\pi}{a}n \right) \quad , \quad (2.5)$$

where a is the lattice constant.

Elastic Scattering When a beam of atoms² with a definite wave vector is incident on surface at a polar angle of θ_i measured with respect to the surface normal, the scattering can be observed at certain final angles which are defined by energy and momentum conservation. If the incident and outgoing wave vectors of the atoms are, respectively, $\mathbf{k}_i = (\mathbf{K}_i, k_{iz})$ and $\mathbf{k}_f = (\mathbf{K}_f, k_{fz})$, as shown in Figure 2.1, the conservation equations for elastic scattering are:

$$\mathbf{K}_f - \mathbf{K}_i = \Delta\mathbf{K} = \mathbf{G}_{mn} \quad , \quad (2.6)$$

$$\Delta E = E_f - E_i = \frac{\hbar^2}{2m}k_f^2 - \frac{\hbar^2}{2m}k_i^2 = 0 \quad , \quad (2.7)$$

where $K_{i(f)} = k_{i(f)} \cdot \sin\theta_{i(f)}$. The allowed diffraction channels \mathbf{G}_{mn} are called *open channels*. The angular positions of the diffraction peaks provide information about the symmetry and size of the surface unit cell.

¹It is common to use the convention that small letters stand for 3D vectors and the capital letters for 2D vectors on the surface plane.

²It may lead to confusion using the terms *atom*, *molecule* and *particle*, alternatingly throughout the manuscript. Actually, it is a matter of taste unless it is a specific case. For instance, here we say atom and mean a *simple* particle, but the arguments here would be valid also for elastically scattered molecules.

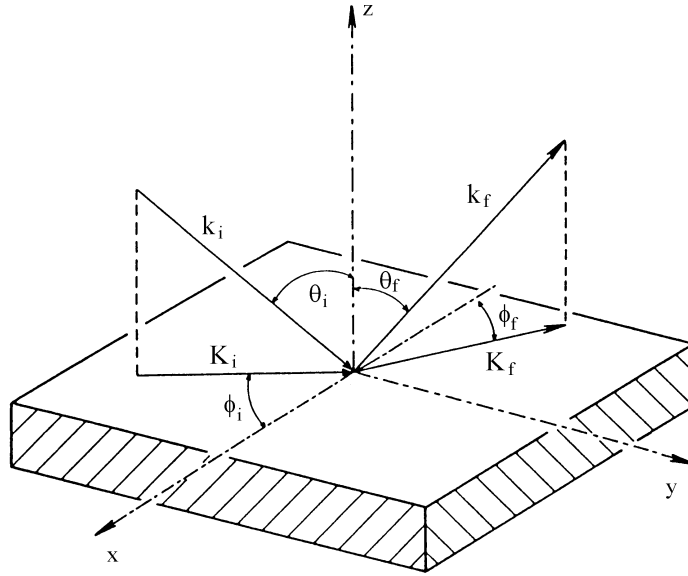


Figure 2.1: Schematic representation of the scattering geometry. The initial and final wave vectors \mathbf{k}_i and \mathbf{k}_f have components \mathbf{K}_i and \mathbf{K}_f parallel to the surface. The initial and final polar angles are denoted by θ_i and θ_f the azimuthal angles by ϕ_i and ϕ_f . In the case of in-plane scattering; $\phi_i = \phi_f$.

Rotationally Inelastic Diffraction The rotational and vibrational states of molecules can be changed in the scattering process, called *rotationally inelastic diffraction* (RID). In RID the translational energy of the molecule, E_i is transformed into rotational energy of the molecule, or vice versa. In this process there is no exchange of energy with the surface phonons and the conservation equations are given by

$$\Delta\mathbf{K} = \mathbf{G}_{mn} \quad , \quad (2.8)$$

$$\Delta E = E_f - E_i = \Delta E_{rot} = E_{j_i} - E_{j_f} \quad , \quad (2.9)$$

where E_{j_i} and E_{j_f} are, respectively, the energies of the initial and final rotational quantum levels of the transition: $(j_i \rightarrow j_f)$. These arguments are also valid for vibrational excitation of molecules.

Phonon Inelastic Diffraction The scattering particle may also create or annihilate a surface phonon, thus changing its energy and momentum. The conservation relations

are, then³:

$$\Delta\mathbf{K} = \mathbf{G}_{\mathbf{mn}} + \mathbf{Q} \quad , \quad (2.10)$$

$$\Delta E = \pm\hbar\omega \quad , \quad (2.11)$$

where \mathbf{Q} is the wave vector of a phonon of frequency ω . Phonon energies of $+\hbar\omega$ and $-\hbar\omega$ denote annihilation and creation of phonons, respectively. The combination of Equations 2.10 and 2.11 yields:

$$\frac{\hbar\omega}{E_i} = \frac{\sin^2(\theta_i)}{\sin^2(\theta_f)} \left(\frac{\Delta K}{K_i} + 1 \right)^2 - 1 \quad . \quad (2.12)$$

Equation 2.12 gives in the $(E, \Delta\mathbf{K})$ plane a curve which depends on E_i , \mathbf{K}_i , θ_i and θ_f , which is called the *scan curve*. The intersection points of the scan curve with the surface phonon dispersion curves, $\pm\omega(\mathbf{Q})$ give the observable phonons.

2.2 Interaction Potentials

Even the simple kinematic analysis of the diffractive scattering discussed above implicitly assumes that the scattered atoms are repelled from the top atom layer providing the surface structure. The scattering experiments give also essential information on the particle-surface interaction potential. The interaction potential causing a surface corrugation seen by the particle, thus defines the diffraction peak intensities and, in case of molecular scattering, leading an additional molecular anisotropy, the rotational transition of the molecule. In this section the interactions of He atoms and D_2/H_2 molecules with alkali-halide surfaces are discussed. In the ionic crystals the crystal ions have closed electronic shells and there is no free electron gas as in a metal, thus the interaction between the particle and the crystal surface is defined by the summation over binary interactions between the gas atom and individual lattice ions [39,40]. The interaction potential of a He atom with ionic crystals consists of a short-range repulsion, a long range attractive, and an induced dipole interaction part due to the electric field of the lattice ions [73].

Repulsive Interaction The repulsion potential results mainly from the overlap of the electron clouds of the gas atom with the top layer atoms of the surface. The customary expression for the repulsive interaction of two interacting atoms due to the

³In this discussion the possibility of multiphonon interaction has been excluded.

Pauli exclusion principle is the Born-Mayer form [40]

$$V_0 = D \exp(-\alpha(z - z_0)) \quad , \quad (2.13)$$

where z is the distance from the surface, D is the potential well depth and α is the softness of the potential or reciprocal range parameter.

Attractive Interaction The attraction part is predominantly from van der Waals dispersion forces. At large distances from the surface the long-range interaction gas atom and the surface can be approximated by [30, 74]

$$V_0 = -\frac{C_3}{z^3} \quad , \quad (2.14)$$

where C_3 is a constant, which depends on the optical properties of gas atom and the solid. Lifshitz have derived the following expression for C_3 [75]:

$$C_3 = \frac{\hbar}{4\pi} \int_0^\infty \alpha(i\omega) \frac{\varepsilon(i\omega) - 1}{\varepsilon(i\omega) + 1} d\omega \quad , \quad (2.15)$$

where $\alpha(i\omega)$ is the electric dipole polarizability of the gas atom and $\varepsilon(i\omega)$ is the dielectric function of the solid.

Induced Dipole Interaction This describes the effect of the electric field intensity, $E(\mathbf{r})$ of the surface ions on the gas atom by [73]

$$V_i(r) = \frac{1}{2} \alpha |E(r)|^2 \quad , \quad (2.16)$$

where α is the polarizability of the gas atom.

2.2.1 Model Potentials

Conventionally, the interaction model potential is expanded in a two-dimensional Fourier series, reflecting the surface periodicity [76, 77],

$$V(\mathbf{r}) = \sum_{\mathbf{G}} V_{\mathbf{G}}(z) \exp(i\mathbf{G} \cdot \mathbf{R}) \quad . \quad (2.17)$$

The zeroth order of this function; $V_0(z)$ is the laterally averaged gas-surface potential and can be defined with simple models.

Hard Corrugated Wall Model In the HW model it is assumed that the attractive part of the potential is negligible and the repulsive part is infinitely steep. The position of the surface wall is represented by the locus of the classical turning points, $z = \zeta(\mathbf{R})$ which is the corrugation function. The potential is defined by:

$$V(\mathbf{r}) = \mathbf{V}(\mathbf{R}, \zeta[\mathbf{R}]) = \begin{cases} \infty & z \leq \zeta(\mathbf{R}) \\ 0 & z > \zeta(\mathbf{R}) \end{cases} . \quad (2.18)$$

For the corrugation function, mostly, the first term in the Fourier series in Equation 2.17 is sufficient. In the case of LiF(001) it is usually approximated as [78]

$$\zeta(\mathbf{R}) = \frac{1}{2}\zeta_0 \cdot [\cos(2\pi x/a) + \cos(2\pi y/a)] , \quad (2.19)$$

where $2\zeta_0$ is the peak-to-valley height of the surface corrugation. For the He-LiF(001) system with $k_i=11 \text{ \AA}^{-1}$, the best-fit corrugation parameter is found as $\zeta_0=0.3 \text{ \AA}$ [78, 79]. A further improvement of this simple model is hard corrugated surface with an attractive well [80].

Morse Potential The Morse potential [81] defines both attractive and the repulsive parts of the interaction as

$$V_0(z) = D (\exp[-2\alpha(z - z_0)] - 2 \exp[-\alpha(z - z_0)]) . \quad (2.20)$$

It has the advantage of simplicity with having only two parameters (z_0 can be arbitrary) and the Schrödinger equation can be solved analytically to provide the exact energy eigenvalues of the bound states for the motion perpendicular to the surface:

$$\epsilon_\nu = -D \left[1 - \frac{\alpha \hbar}{\sqrt{2mD}} \cdot (\nu + 0.5) \right]^2 , \quad (2.21)$$

where ν is a positive integer and m is the mass of the gas atom. The parameters of the Morse potential and also for other model potentials used for the He-LiF(001) system are listed in Table 2.1.

2.2.2 Potentials for Molecule-Surface Interaction

The interaction potential of H_2 and D_2 with ionic crystal surfaces is more complicated since the dependence on the molecular orientation and bond distance must be included. The interaction of H_2 is much stronger than the He case since the average polarizability is 3.9 times larger [30].

Table 2.1: Model potentials and experimental parameters reported in the literature for the He-LiF(001) interaction.

Potential	Formula	Parameters
Morse	$V_0(z) = D (\exp[-2\alpha(z - z_0)] - 2 \exp[-\alpha(z - z_0)])$	$\alpha=1.1 \text{ \AA}^{-1}$, $D=8.03 \text{ meV}$ [82]
<i>9-3</i>	$V_0(z) = (3^{3/2}D/2) \left[\left(\frac{\sigma}{z+z_0} \right)^9 - \left(\frac{\sigma}{z+z_0} \right)^3 \right]$	$\sigma=1.85 \text{ \AA}$, $D=9.20 \text{ meV}$ [59]
Σ Yukawa-6	$u_N(r) = \frac{\epsilon(1+\alpha r_0)}{\alpha r_0 - 5} \left[\frac{6r_0}{(1+\alpha r_0)r} \exp[\alpha(r_0 - r)] - (r_0/r)^6 \right]$	$z_0=2.63 \text{ \AA}$, $D=9.2 \text{ meV}$ [83]
<i>12-3</i>	$V_0(z) = \frac{D}{3} [(z_0/z)^{12} - (z_0/z)^3]$	$z_0=2.8 \text{ \AA}$, $D=8.7 \text{ meV}$ [84]
<i>Zeta</i>	$V_0(z) = A_+\zeta(10, z/a) - 2B_+\zeta(4, z/a)$	$A_+=82.3 \text{ meV}$, $B_+=18.9 \text{ meV}$ [84]
<i>Exp-3</i>	$V_0(z) = \frac{\alpha z_0 D}{\alpha z_0 - 3} \left[\frac{3}{\alpha z_0} \exp[-\alpha(z - z_0)] - (z_0/z)^3 \right]$	$\alpha=4.78 \text{ \AA}^{-1}$, $z_0=2.3 \text{ \AA}$, $D=8.8 \text{ meV}$ [85]
Shifted Morse - Hybrid	$V_0(z) = \frac{D}{1+\Delta} (\exp[-2\alpha(z - z_0)] - 2 \exp[-\alpha(z - z_0)] - \Delta)$ and for $z > z_p$; $V_0(z) = -C_3/z^3$	$z_0=1.63 \text{ \AA}$, $\alpha=1.29 \text{ \AA}^{-1}$, $D=7.74 \text{ meV}$, $\Delta=0.075$, $z_p=3.48 \text{ \AA}$, $C_3=81.7 \text{ meV \AA}^3$ [86]

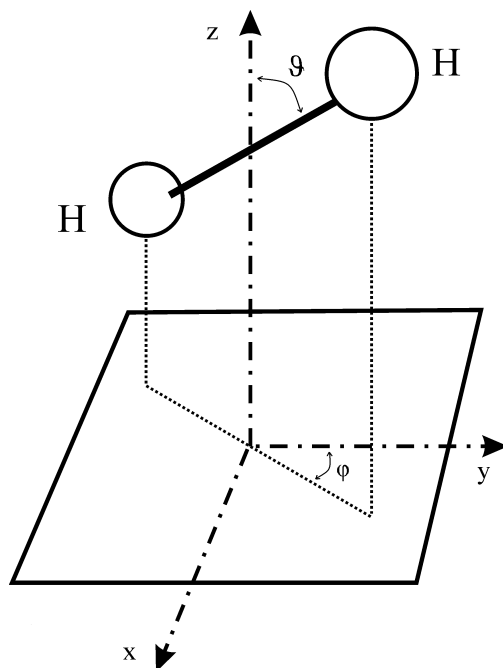


Figure 2.2: The coordinate system of the H_2 or D_2 molecule at a surface.

Hard Wall Model The interaction of a diatomic molecule with the surface is described by a hard corrugated surface with a shape function, such that the previously discussed corrugation function $\zeta(x, y)$ is replaced by

$$\zeta = \zeta(x, y, \vartheta, \varphi) \quad . \quad (2.22)$$

This model assumes a hard, prolate ellipsoidal molecule. ϑ , φ are, respectively, polar and azimuthal angle of the molecule with respect to the surface normal as shown in Figure 2.2. This model was used by Garibaldi *et al.* to estimate the rotational transitions in H_2 and HD scattering from LiF [64]. The best fit corrugation amplitude is found as $\zeta_0 = 0.17 \text{ \AA}$ for H_2 -LiF interaction from the comparison of experimental data by Boato *et al.* [87].

The accuracy of this model is poor and the validity range of the approximations can only be tested by comparison with the exact quantum calculations; it weakly allows for $\Delta m_j \neq 0$ transitions and the quadrupole-electrostatic interaction cannot be represented in the interaction potential. On the other hand, it may provide some direct insight into the dynamics of the scattering process and can be used as a mathematical tool to investigate the role of the corrugation and the molecular anisotropy in scattering processes. This model is more reliable for systems where the interaction and the corrugation are small and electrostatic interactions are not present as on metal

surfaces [88].

Wolken Potential An empirical potential used in many calculations [68, 89, 90] and used first by Wolken [62, 63], has a simple form given as

$$V(\mathbf{r}, \vartheta) = [V_0(z) + \beta V_1(z)Q(\mathbf{R})] \cdot [1 + \lambda_2 P_2(\cos \vartheta)] \quad . \quad (2.23)$$

The first part of the potential describes the interaction potential averaged over the orientation of the molecule. It has an uncorrugated, z-dependent potential, which is given by Equation 2.20 and a corrugated part with an amplitude parameter given by β and with a corrugation function $Q(\mathbf{R})$, which is similar to Equation 2.19. The potential function $V_1(z)$ is a repulsion potential given by

$$V_1(z) = D \exp[-2\alpha(z - z_0)] \quad . \quad (2.24)$$

The second part of the Equation 2.23 accounts for the orientational dependent potential where ϑ is the polar angle of the molecule axis with respect to surface normal. λ_2 is the anisotropy parameter defined by the ratio of the static dipole polarizabilities for parallel and perpendicular configuration of the molecule on the surface. The parameters used in earlier studies for this potential are $D=38$ meV, $\alpha=1.18$ \AA^{-1} , $\lambda_2=0.24$, and the fitting parameter was derived as $\beta=0.055$ [63].

Note that the model potential described here is independent of the azimuthal angle of the molecular axis (φ), thus the magnetic quantum number m_j cannot be changed during the collision. The assumption is absolutely valid only for a flat surface. It is argued in many works [63, 64] that collisions of H_2 with the surface would be dominantly m_j conserving. Nevertheless, recent theoretical and experimental results showed that m_j transitions may play an important role in scattering, particularly due to the quadrupole-ionic lattice interaction [7, 54, 91, 92].

Kroes Potential A more realistic potential proposed by Kroes and coworkers is an interaction potential with 6 main contributions [7, 56, 70, 93]:

$$V(\mathbf{r}, \vartheta, \varphi) = V_{rep} + V_6 + V_8 + V_{els} + V_{ind} + V_3 \quad . \quad (2.25)$$

V_{rep} is the short-range repulsion energy between two closed-shell species given by

$$V_{rep}(R, \gamma) = a(\gamma) \exp[-b(\gamma)R] \quad , \quad (2.26)$$

where R is the distance between the molecule center and a Li^+ or a F^- ion on the surface. γ is the angle between the vector from an individual surface ion and the

H₂ bond vector⁴. The parameters a and b are obtained from fitting this potential expression to self-consistent field (SCF) calculations [7, 94].

V_6 is the energy contribution from the attractive induced dipole-induced dipole interactions between the molecule and one of the surface ions, written as

$$V_6(R, \gamma) = -C_6(\gamma)R^{-6}f_{d6}(R) \quad , \quad (2.27)$$

where C_6 is the anisotropic coefficients obtained from the static polarizabilities of the ions and the H₂ molecules using Slater-Kirkwood rule [95, 96]. $f_{d6}(R)$ is a Tang-Toennies damping function expressed as [97]

$$f_{dn}(R) = 1 - \left[\sum_{k=0}^n \frac{(bR)^k}{k!} \right] \exp[-bR] \quad . \quad (2.28)$$

V_8 is the induced dipole-induced quadrupole interaction given by

$$V_8(R, \gamma) = -C_8(\gamma)R^{-8}f_{d8}(R) \quad . \quad (2.29)$$

V_{els} is the interaction of the permanent quadrupole of the H₂ with the electrostatic field of the ionic lattice, given by [65]

$$\begin{aligned} V_{els} = & -\Theta \sqrt{\frac{\pi}{30}} \sum'_{nm} \left(A_{nm} \exp[iG(nx + my)] \exp(-\gamma_{nm}z) \right. \\ & \times \left[\exp(i2\xi)Y_{22}(\vartheta, \varphi) + \exp(-i2\xi)Y_{2-2}(\vartheta, \varphi) - 2i \exp(i\xi)Y_{21}(\vartheta, \varphi) \right. \\ & \left. \left. + 2i \exp(-i\xi)Y_{2-1}(\vartheta, \varphi) - \sqrt{6}Y_{20}(\vartheta, \varphi) \right] \right) \quad , \quad (2.30) \end{aligned}$$

where

$$\begin{aligned} \gamma_{nm} &= G\sqrt{n^2 + m^2} \\ A_{nm} &= \frac{|e|G^2}{2\pi} \frac{1 - \exp(-\gamma_{nm}a_l/\sqrt{2})}{1 - \exp(-\gamma_{nm}\sqrt{2}a_l)} \gamma_{nm} [1 - (-1)^{n+m}] \\ \exp(i\xi) &= \frac{(n - im)}{\sqrt{n^2 + m^2}} \quad , \quad (2.31) \end{aligned}$$

and Θ is the quadrupole moment of H₂ e is the electronic charge and a_l is the lattice constant. The prime on the summation sign indicates that the integers $n = m = 0$ are excluded.

⁴The angle γ should not be confused with ϑ .

V_{ind} is the interaction of the induced dipole moment of H_2 with the electrostatic field and can be written as [98]

$$V_{ind}(x, y, z, \vartheta, \varphi) = V_{ind}^0 + V_{ind}^2 \quad , \quad (2.32)$$

where V_{ind}^0 is the isotropic part given by

$$V_{ind}^0 = -\frac{64\pi^2\alpha^{(0)}e^2}{a_l^4} \exp(-2Gz) [1 + \exp(-\sqrt{2})\pi]^{-2} [1 + \cos(Gx) \cos(Gy)] \quad , \quad (2.33)$$

and V_{ind}^2 is the anisotropic part of the potential given by

$$\begin{aligned} V_{ind}^2 = & \alpha^{(2)}G^2 \sum_{nm}' \sum_{n'm'}' \Phi_{nm} \Phi_{n'm'} \left[\left(\frac{nn'}{2} - \frac{mm'}{2} + \frac{nm'}{i} \right) Y_{22}(\vartheta, \varphi) \right. \\ & + \left(\frac{nn'}{2} - \frac{mm'}{2} - \frac{nm'}{i} \right) Y_{2-2}(\vartheta, \varphi) - (in + m)\sqrt{n'^2 + m'^2} Y_{21}(\vartheta, \varphi) \\ & + (in - m)\sqrt{n'^2 + m'^2} Y_{2-1}(\vartheta, \varphi) \\ & \left. - 0.5\sqrt{2/3} \left(nn' + mm' + 2\sqrt{(n'^2 + m'^2) + (n^2 + m^2)} \right) Y_{20}(\vartheta, \varphi) \right] \quad (2.34) \end{aligned}$$

$\alpha^{(0)}$ and $\alpha^{(2)}$ are the isotropic and anisotropic polarizabilities of H_2 . The components Φ_{nm} are the electrostatic potentials of the substrate ions.

V_3 is the long-range molecule- surface interaction potential due to the induced dipole-induced dipole interaction of the H_2 with the ions below the surface layer and given by [99]

$$V_3(z, \vartheta) = -C_3(\vartheta)z'^{-3} \quad , \quad (2.35)$$

where z' is taken as

$$z' = z + \frac{3}{4}\sqrt{2}a_l \quad , \quad (2.36)$$

because of the assumption that the layer below the surface layer is like a continuous solid. The parameter $C_3(\vartheta)$ is determined from the calculated values of $C_3(\vartheta = 0)$ and $C_3(\vartheta = \pi)$ [94].

The azimuthal angle dependence of the interaction potential allows m_j transitions. Especially the interaction between the quadrupole moment of the molecule and the electrostatic field of the surface ions is responsible for the large $\Delta m_j \neq 0$ transitions [70].

2.3 Calculation Methods

Many theoretical models of the molecule-surface scattering process have been applied for comparison with the experimental results [33]. The calculation models consist of choosing an interaction potential model and solving either the time-independent or the time-dependent Schrödinger equation. Even with the treatment of the surface as a rigid, phononless lattice the large number of diffractive and rotational states involved does not allow an exact calculation. Thus, in most cases, approximations with different accuracies have to be used [33, 100]. In this section the close-coupling (CC) [62, 63, 101], time-dependent wave packet (TDWP) [102, 103] and close-coupling wave packet (CCWP) methods are discussed. Some other approaches applied to molecule-surface scattering are the Eikonal approximation [64], the quasiclassical trajectory (QCT) method [104–107], the sudden approximation [66, 67, 90, 108, 109], the impulsive collision approximation [110], and the semiclassical perturbation (SCP) method [89].

2.3.1 Close-Coupling Calculation

This method, adapted from gas phase collisions [13, 111], is regarded as a nearly exact method of calculation [101]. CC calculations treating both diffraction and rotational transitions in H₂-LiF system were first carried out by Wolken [62, 63] and later extensively by Drolshagen *et. al* [68]. For a given scattering geometry and interaction potential the elastic inelastic scattering intensities are calculated by solving the time-independent Schrödinger equation for a diatomic molecule from a rigid lattice;

$$\hat{H}\Psi(\mathbf{r}, \vartheta, \varphi) = E \Psi(\mathbf{r}, \vartheta, \varphi) \quad , \quad (2.37)$$

where E is the collision energy. \hat{H} is the Hamiltonian describing the motion of a rigid, diatomic molecule interacting with a model potential and is given by

$$\hat{H} = -\frac{\hbar^2}{2m}\nabla^2 + \frac{\hbar^2}{2I}\hat{J}^2 + V(\mathbf{r}, \vartheta, \varphi) \quad . \quad (2.38)$$

Here m and I are, respectively, the mass and the moment of inertia of the molecule. The term $-\frac{\hbar^2}{2m}\nabla^2$ accounts for the translational energy and \hat{J}^2 is the rotational energy operator of the rigid rotor. The total wave function of the molecule can be expanded in a basis set of diffractive and rotational states as

$$\Psi(\mathbf{r}, \vartheta, \varphi) = \sum_{\mathbf{G}} \sum_{jm_j} \psi_{\mathbf{G}jm_j}(z) Y_{jm_j}(\vartheta, \varphi) \exp[i(\mathbf{K} + \mathbf{G}) \cdot \mathbf{R}] \quad . \quad (2.39)$$

With the Ansatz Equation 2.39, Equation 2.37 can be converted into a set of coupled equations which have to be solved for the unknown functions $\psi(z)$:

$$\left[\frac{d^2}{dz^2} + d_{\mathbf{G}j}^2 \right] \psi_{\mathbf{G}jm_j}(z) = \frac{2m}{\hbar^2} \sum_{\mathbf{G}'j'm'_j} U_{\mathbf{G}jm_j}^{\mathbf{G}'j'm'_j}(z) \psi_{\mathbf{G}'j'm'_j}(z) \quad , \quad (2.40)$$

where

$$d_{\mathbf{G}j}^2 = \frac{2m}{\hbar^2} \left[E - \frac{j(j+1)\hbar^2}{2I} \right] - (\mathbf{K} + \mathbf{G})^2 \quad , \quad (2.41)$$

$$U_{\mathbf{G}jm_j}^{\mathbf{G}'j'm'_j}(z) = \frac{1}{A} \int_{UC} d\mathbf{R} \int Y_{jm_j}^*(\vartheta, \varphi) \exp(-i\mathbf{G} \cdot \mathbf{R}) \\ \times V(\mathbf{r}, \vartheta, \varphi) \exp(i\mathbf{G}' \cdot \mathbf{R}) Y_{j'm'_j}(\vartheta, \varphi) d\omega \quad . \quad (2.42)$$

The \mathbf{R} integration in Equation 2.42 is over the unit cell with area A . The set of coupled equations is solved for the following scattering boundary conditions on the channel wave function:

$$\begin{aligned} \psi_{\mathbf{G}jm_j}(z) &= 0 && ; \text{ for } z = -\infty \quad , \\ \psi_{\mathbf{G}jm_j}(z) &= 0 && ; \text{ for } z = \infty \quad \text{and} \quad d_{\mathbf{G}j}^2 < 0 \quad , \\ \psi_{\mathbf{G}jm_j}(z) &= \\ & \frac{1}{(d_{\mathbf{G}'j'}^2)^{1/2}} \left[\exp(-id_{\mathbf{G}'j'}^2 z) \delta_{\mathbf{G}\mathbf{G}'} \delta_{jj'} - S(\mathbf{G}jm_j \rightarrow \mathbf{G}'j'm'_j) \exp(id_{\mathbf{G}'j'}^2 z) \right] \\ & && ; \text{ for } z = \infty \quad \text{and} \quad d_{\mathbf{G}j}^2 \geq 0 \quad . \end{aligned} \quad (2.43)$$

Note that when $d_{\mathbf{G}j}^2 < 0$ the channels are closed and only the incident specular channel (i.e. $G_{mn} = 0$) has physical meaning.

2.3.2 Time-Dependent and Close-Coupling Wave Packet Method

In the time-dependent wave packet (TDWP) method [102,103], the scattering process is treated by solving the time-dependent Schrödinger equation

$$\hat{H}\Psi = i\frac{\partial\Psi}{\partial t} \quad . \quad (2.44)$$

The Hamiltonian is time-independent and also given by Equation 2.38. Thus, Equation 2.44 can be written as

$$\Psi(t + \Delta t) = \exp[-i\hat{H}\Delta t]\Psi(t) \quad . \quad (2.45)$$

The term $\exp[-i\hat{H}\Delta t]$ is called the propagator. If $\Psi(t = t_0)$ is known, then $\Psi(t)$ can be obtained by the finite difference method. The TDWP calculation proceeds as follows [93]: First, a suitably chosen initial wave packet is positioned far from the surface where the molecule-surface interaction is negligibly small. Then, the initial wave packet is propagated towards the surface as in Equation 2.45. The wave function is continually analyzed at regular time intervals. The propagation is stopped when the interaction of the scattered part of the wave packet with the surface is negligible. Finally, the scattering probabilities are extracted from the final wave function. With the FFT (fast Fourier transformation) and Chebichev numerical techniques, the TDWP method is computationally effective and provides numerically exact solutions [56, 93]. The major advantage of the method is that it provides detailed physical insight into the dynamics of all the processes occurring during the scattering event.

The close-coupling wave packet (CCWP) method is a hybrid of the CC and TDWP methods, in which the translational parts are treated by the TDWP approach and the rotational degrees of freedom are treated like in the CC method [8, 112, 113]. This method reduces the computing times significantly. For instance, the TDWP method needs very long propagation times for the calculations on H₂-LiF(001) at low incident energies (~ 20 -100 meV) due to the trapping of the molecule in the rather deep interaction potential well [7, 93]. On the other hand, the CCWP method is highly efficient in handling a large number of channels with a strong interaction.

2.4 Thermal Attenuation and the Effect of the Potential Well

The theoretical methods presented above assume that the atoms of the crystal lattice are at rest. However, the zero-point motions and thermal vibrations of the surface atoms lead to inelastic scattering and the attenuation hence the intensities of the elastic peaks. In order to compare the theoretical and experimental results, it is necessary to correct for this attenuation. A standard method to predict the thermal attenuation is based on the Debye-Waller factor, which is widely used for x-ray and neutron diffraction techniques. In the Debye-Waller model the intensity of a peak at a crystal temperature T_s is given by [114]

$$I(T_s) = I^0 \cdot \exp[-2W_{\mathbf{k}}(T_s)] \quad , \quad (2.46)$$

where I^0 is the intensity for a rigid lattice and $W(T_s)$ is the Debye-Waller exponent⁵ defined by

$$W_{\mathbf{k}}(T_s) = \frac{1}{2} \langle (\mathbf{u} \cdot \Delta \mathbf{k}_i)^2 \rangle \quad . \quad (2.47)$$

Here \mathbf{u} is the thermal vibrational amplitude of the surface atom and the outer brackets refer to a thermal average and $\Delta \mathbf{k}_i$ is the momentum change of the gas particle in the scattering event. This model is based on the assumption that the interaction time is short and that the scattering cross section is small and highly localized. Both approximations are not generally valid in the case of scattering of atoms and molecules. Nevertheless, its simple factorizable form makes it useful for describing the thermal attenuation in particle scattering.

The following simple expression for the DW factor is obtained by assuming that the thermal attenuation is sensitive only to the vibrations perpendicular to the surface [115]:

$$W(T_s) = \frac{3\hbar^2(k_{iz} + k_{fz})^2 T_s}{2Mk_b\Theta_D^2} \quad , \text{ for } T_s/\Theta_D \geq 0.7. \quad (2.48)$$

Here Θ_D is the surface Debye temperature, M is the average mass of the surface atom and k_{iz} and k_{fz} are the surface normal components of the initial and final wave vectors, respectively. The wave vectors $k_{i(f)z}$ must be corrected due to the potential well depth of the surface interaction, so called Beeby correction [116]:

$$k'_{i(f)z} = [k_{i(f)z}^2 + \frac{2mD}{\hbar^2}]^{1/2} \quad , \quad (2.49)$$

where m is the mass of the gas particle. Combining Equations 2.48 and 2.49 $W(T_s)$ can be easily expressed as a function of incident energy, E_i and angle θ_i :

$$W(T_s) = \frac{12m(E_i \cos^2 \theta_i + D)T_s}{Mk_b\Theta_D^2} \quad . \quad (2.50)$$

This equation indicates that the elastic intensities increases for higher incident angles and for low incident energies in agreement with the experiments. However, this expression is a very restrictive form and in general does not agree well with experiment. A full treatment of the thermal attenuation for realistic cases requires a detailed investigation of multiple phonon exchange and considerable theoretical effort has been devoted to deriving a more accurate theory for particle surface-scattering [114, 117, 118].

⁵The superscript is used to prevent the confusion with the incident intensity.

2.5 Resonant Scattering

In addition to diffractive processes, mentioned in the previous sections, there are a variety of resonant events which can occur in the scattering of particles from the surface. The existence of the potential well of the interaction of gas atom with the surface leads to an important phenomenon called selective adsorption resonance (SAR). In the first successful experiments [51] Stern and his coworkers already observed sharp minima or maxima in the intensities of diffraction peaks as a function of incident azimuthal angle at a constant angle of incidence. These features were correctly interpreted by Lennard-Jones and Devonshire [119] as resonant transitions of the incident particles into the bound states of the particle-surface potential well. This interesting phenomenon in surface scattering experiments allows for a precise determination of bound states energies, ϵ_ν of the interaction potential and thus provides a unique tool for investigating the particle-surface interaction [34].

In the resonant scattering process the particles impinging on the crystal surface can be captured under certain kinematic conditions. After surfing on the surface for several picoseconds, the trapped particles can be scattered back into the continuum and interfere with the directly scattered particles thereby leading to a significant modulation of the scattered beam intensity [37, 38]. The kinematic condition for SAR scattering of a molecule can be written as,

$$\frac{\hbar^2}{2m} [(\mathbf{K}_i + \mathbf{G}_{\parallel})^2 + \mathbf{G}_{\perp}^2] = E_i + |\epsilon_\nu| + \Delta E_{rot} \quad , \quad (2.51)$$

where \mathbf{G}_{\parallel} and \mathbf{G}_{\perp} are the components of the \mathbf{G} -vector parallel and perpendicular to the scattering plane, respectively. If the rotational transition energy $\Delta E_{rot}=0$ Equation 2.51 describes a purely elastic SAR. Since the elastic resonances involve only elastic scattering processes with a \mathbf{G} -vector, they correspond to a diffraction process and therefore are predominantly dependent on the corrugation of the potential. Hence, this type of resonant event is sometimes called corrugation- or diffraction mediated selective adsorption (DMSAR) [120]. The process with $\Delta E_{rot} \neq 0$ is called rotationally mediated selective adsorption (RMSAR) [121]. In addition to these, an impinging particle can enter into a bound state with the involvement of surface phonons, namely creation or annihilation of one or more phonons. This process is usually called phonon-assisted selective adsorption (PASAR) [122, 123]. Similarly, a captured particle can be reemitted into the vacuum with the help of phonons, which is called phonon-assisted selective desorption (PASDR). These and other resonance processes have been reviewed by Miret-Artes [120].

3. The Apparatus and Experimental Details

In this chapter a recently built, high-resolution molecular scattering apparatus, originally designed for focusing neutral He atom beams and other atom optics experiments, is described. The instrument is not only a prototype of an apparatus for investigating atom optics with thermal beams but also a next generation general-purpose molecular beam-surface scattering machine. In the apparatus the target chamber is mounted on a rotatable central base, the source arm is placed on a linear track and the flexible detector track-arm is mounted on a circular track. With this setup the source-detector angle can be varied easily from 40 to 190 degrees. This feature, combined with its high angular resolution and signal-to-background ratio, allows a wide range of new experiments in molecular and atomic beam scattering.

There are world wide different setups for the molecular beam machines. The mostly used system is the fixed-angle (or Göttingen) setup where the source-to-detector angle (θ_{SD}) is constant and the crystal polar and azimuthal angles are varied [43, 124–126]. This setup is cheap, highly stable and has high resolution. Here high resolution indicates three essential features of the apparatus: a high incident beam monochromaticity, as well as a high TOF energy resolution and a very high angular resolution. Moreover, it means a high signal-to-background ratio allowing the detection of the low coherent inelastic signal from surface phonons out of the background. There are several advantages of a fixed-angle setup. Firstly, the source chamber is big, because the high-speed ratio He sources need big pumps with large pumping speeds. Secondly, several differential pumping stages preceding the detector can be installed in order to reach high signal-to-background ratios. Thirdly, for high energy resolution of the inelastic scattering a long chopper-to-detector distance is necessary. Hence, beam machines tend to be huge, making it difficult to have movable source or detector. The fixed-angle setup is particularly adequate for measuring surface phonon dispersion curves,

however theoretical comparison of diffraction intensity profiles is time consuming. Because theoretical analysis needs fixed-incident conditions while with Göttingen setup the angular distributions are measured by changing the incident angle. The rotatable-detector setup is favorable for comparison with the theory. It allows measuring the diffraction peaks for a fixed angle of incidence [44, 127, 128]. This setup makes the comparison of the calculations and experiments easier and makes possible the direct measurement of the incident beam intensity, allowing the determination of absolute diffraction probabilities. However, since the detector is close to the sample making the differential pumping almost impossible, the resolution (in all three senses) of this setup is rather low.

The setup presented here combines both the advantages of the fixed-angle and rotatable-detector setups in which the detector arm with several differential pumping stages can be rotated. The high resolution, flexible detector setup has several advantages:

- In addition to surface scattering experiments, other interesting molecular beam experiments with a $\theta_{SD}=180^\circ$ configuration, thus a direct molecular beam are possible. So that the apparatus is not only for the investigation of particle-surface scattering experiments, but it is a multi-purpose molecular beam machine which can be used, for instance, for investigation of free-jet expansion of molecular beams and a variety of interesting experiments such as reviewed in refs. [13, 15]. The experiments presented in Chapter 4 are carried out at the $\theta_{SD}=180^\circ$ configuration.
- Atom optics experiments can be carried out. Beam focusing with Fresnel zone plates is possible and it can be combined with a sample surface for the realization of spatially resolved surface scan with neutral atomic beams [47]. For the beam focusing with reflective mirror the optimum focusing and reflection geometry can be chosen [48, 129]. One of the construction purposes of the apparatus is to focus neutral helium atoms with a Si(111):H(1×1) concave mirror bent by an electrostatic force arrangement [129]. The demagnification of the mirror is determined by the ratio of the source-to-target and target-to-detector distances. With this apparatus a demagnification ratio of 5:1 can be reached when differential pumping stages are removed and a chamber with piezoelectrically controlled pinhole aperture is inserted in front of the detector. The aperture can be moved in 2D to scan the focused beam and is sealed in the chamber and provides two pumping stages offering high signal-to-background ratio with the spatial resolution of the

focussed spot of the order of nm.

- The intensity of the incident beam can be measured by rotating the detector on the incident beam axis and the absolute reflectivity of the surface can be determined. This is useful for testing the quality of crystal surfaces as well as for the theoretical comparison.
- Fixed incident angle or fixed final angle scattering experiments are possible. The determination of diffraction intensities for a constant incident angle makes theoretical comparison much easier. In the case of constant total angle experiments where the incident angles for each observed elastic peaks are different, a large number of theoretical calculations is necessary for a comparison with the experimental data. Although the computational techniques such as the Eikonal approximation or the closed-coupling (CC) calculations are not very time consuming ones for today's computers, the more realistic approaches such as the time-dependent wave packet (TDWP) method for the molecular scattering where dozens of open channels must be taken into account are still expensive [70]. It may also be interesting to do constant final angle experiments which is also possible for the present apparatus by synchronizing the incident and total angles. Most importantly, scattering intensities for all initial and final angles can be measured providing full information about the scattering process.
- Although from the kinematical viewpoint, a fixed-angle setup is adequate for the determination of surface phonon dispersion curves, probing the different total angles can be advantageous. The inelastic scattering cross-section of a certain phonon of interest can be increased by optimizing the detector angle or, if the phonon of interest overlaps with a selective adsorption resonance, it may be possible to observe the equivalent phonon of interest at a different angle of incidence.
- Constant- \mathbf{Q} scans are possible making the measurement of phonon dispersion curves straightforward. As discussed in Section 2.1, for a fixed-angle apparatus, the TOF spectrum corresponds to a parabolic scan-curve through $(\Delta E, \Delta K)$ space where ΔE and ΔK are coupled via Equation 2.12 and ΔK is not known until ΔE is measured. If the final angle is zero, then $\Delta K = k_i \sin \theta_i$ and the TOF spectrum records a scan curve of a vertical line on the $(\Delta E, \Delta K)$ plane providing the phonons at this specific ΔK . By rotating the detector and crystal, so that the final angle is maintained at $\theta_f=0^\circ$, it is possible to scan over the entire Brillouin zone with straight, vertical scan lines.

- Grazing angle experiments are possible, which have interesting applications for quantum reflection experiments and for the scattering from the steps and defects [130–132].

This chapter is organized as follows: First, the construction of the apparatus is presented. The functional units are described, later on, in more detail. Then, the functionality of the apparatus is illustrated and the angular and TOF resolving power are discussed by presenting standard experiments such as the elastic and inelastic scattering of He atoms from the LiF(001) surface.

3.1 The Apparatus

In this section, a general description of the apparatus is given and its new features are introduced which make it superior and a multi-purpose beam machine, allowing very different types of experiments which is an important advantage since the beam machines are highly costly in construction. The apparatus is constructed high flexible and in a modular construction. The intensity can be increased at the expense of the angular and TOF resolution (to be discussed later in detail) by changing the source-to-target and target-to-detector distances. Additional differential pumping stages can be inserted between the crystal chamber and the detector to increase the signal-to-background ratio. Its modular structure also makes it possible to insert new functional units and to pump down or vent the vacuum chambers separately.

The general scheme of the apparatus is shown in the 3D view in Figure 3.1. The scaled schematic top and the side views of the apparatus are shown in Figures 3.2 and 3.3. The whole apparatus -except the source chamber turbo pump- is based on the main support. The main support is mechanically stable and supported with damping feet to reduce the vibrations from the laboratory floor. The relatively large source chamber turbo pump has an extra support and is connected to the source chamber with a damper to depress its vibration. The source chamber, the first differential pumping stage chamber (DPS-1), the chopper chamber and the iris chamber are mounted on two parallel rails. It is possible to change the source-to-target distance by introducing bellows or removing one of the chambers between the source and target chambers. In this work, however, always fixed source-to-target distance is used. The DPS-2, DPS-3, PT-1, PT-2, and the detector chambers are mounted on two parallel rails of the detector arm, enabling to change the target-to-detector distance. The detector arm is mounted on a circular rail, which allows rotating the detector angle about a vertical

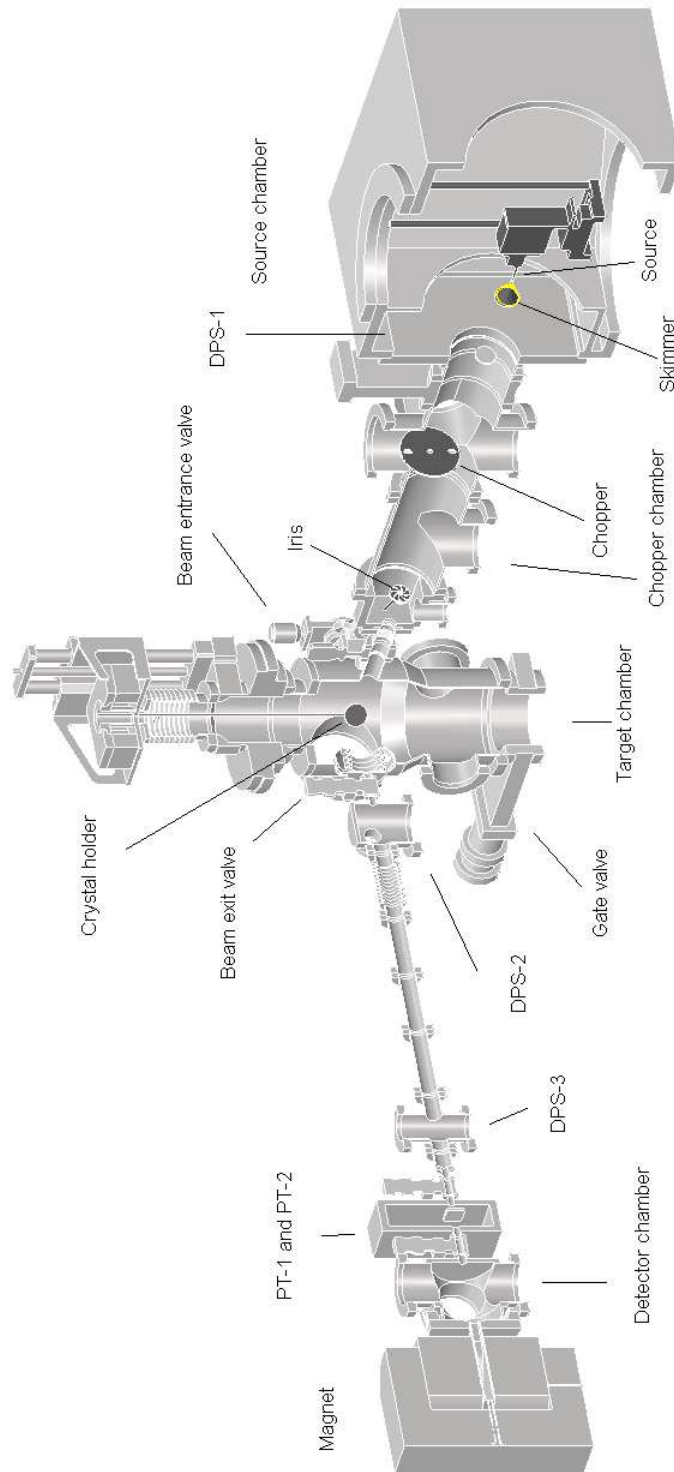


Figure 3.1: A three-dimensional, scale schematic diagram of the apparatus. The vacuum pumps are not shown. In this work piezo-table chamber is replaced by two additional differential pumping stages.

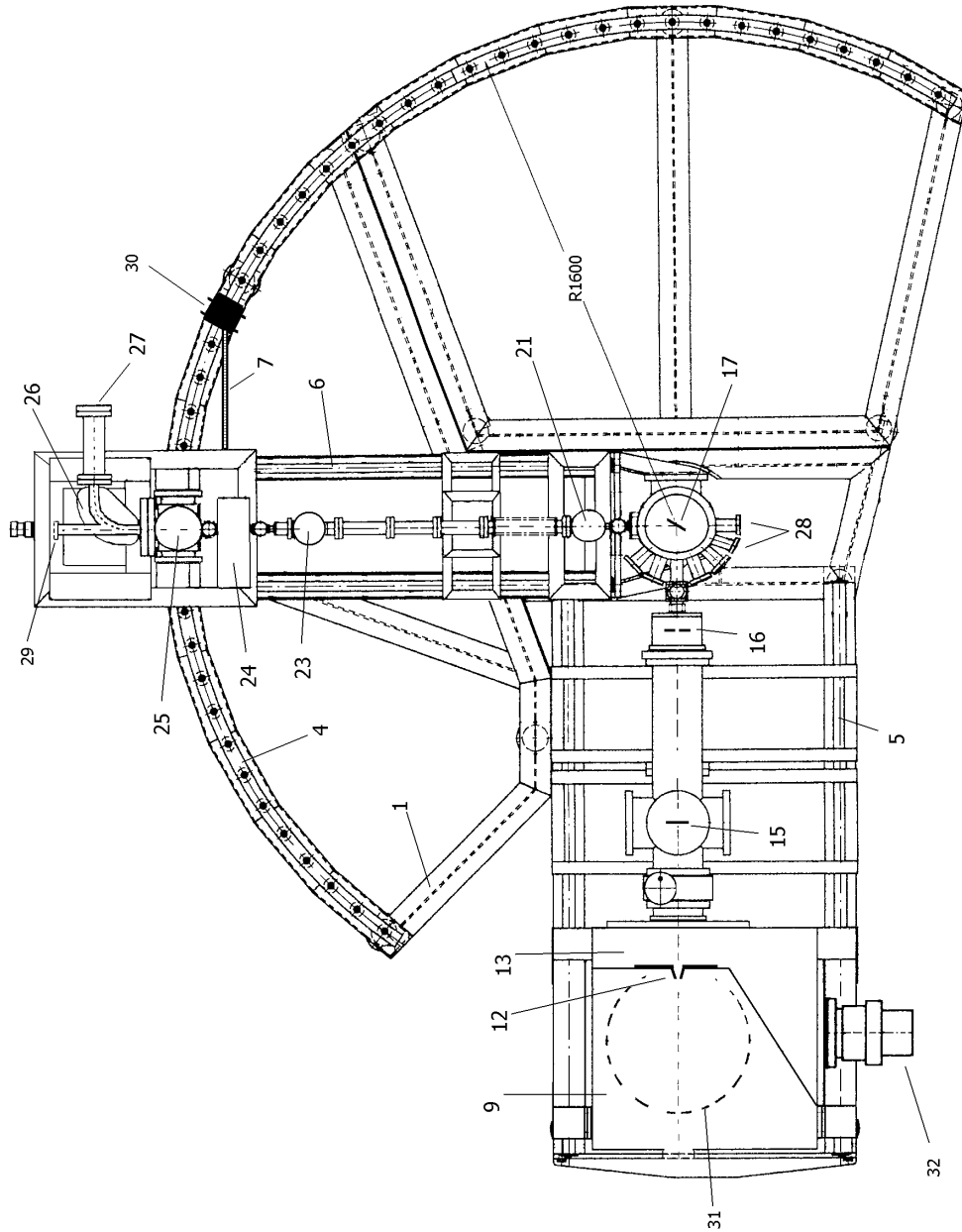


Figure 3.2: A scaled schematic top view-diagram of the Magie-2, in the case of source-detector angle, $\theta_{SD}=90^\circ$. The radius of the circular track is 1.6 m. (1) The main support of the apparatus. (2) Support feet(x14). (3) Detector arm. (4) Detector arm circular track. (5) Source arm track. (6) Detector linear track. (7) Detector linear track. (8) Detector linear track. (9) Detector linear track. (10) Detector linear track. (11) Detector linear track. (12) Detector linear track. (13) Detector linear track. (14) Detector linear track. (15) Detector linear track. (16) Detector linear track. (17) Detector linear track. (18) Detector linear track. (19) Detector linear track. (20) Detector linear track. (21) Detector linear track. (22) Detector linear track. (23) Detector linear track. (24) Detector linear track. (25) Detector linear track. (26) Detector linear track. (27) Detector linear track. (28) Detector linear track. (29) Detector linear track. (30) Detector linear track. (31) Detector linear track. (32) Detector linear track.

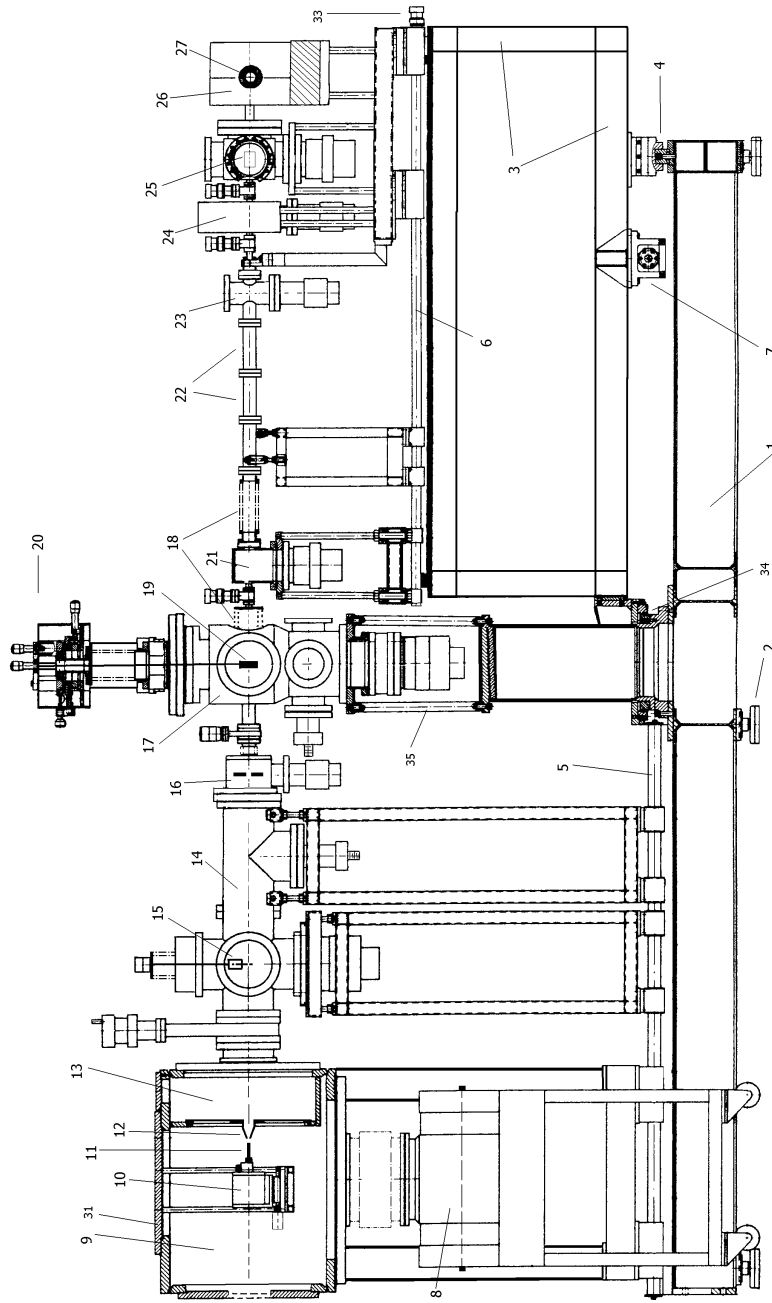


Figure 3.3: Scaled side view of the apparatus, in the case of source-detector angle, $\theta_{SD}=180^\circ$. (7) The rod for the detector arm's rotation. (8) Source chamber turbo pump. (9) Source chamber. (10) Source manipulator. (11) Nozzle. (12) Skimmer. (13) DPS-1. (14) Chopper chamber. (15) Chopper. (16) Iris chamber and iris. (17) Target chamber. (18) Bellows. (19) Target holder. (20) Target manipulator. (21) DPS-2. (22) Room for additional pumping stages. (23) DPS-3. (24) PT-1 and PT-2. (25) Detector chamber. (26) Electromagnet. (27) The channeltron. (28) Beam ports. (29) Glass window. (30) Stepping motor. (31) Top flange for the source holder. (32) DPS-1 turbo pump. (33) Turning knob for linear translation of detector arm. (34) Angular decoder of the detector's rotation. (35) Supporting rods(x3).

axis at the center of the target chamber with respect to source arm from 40° to 190° . The target chamber is mounted on the three supporting rods and can be rotated around its axis, enabling to change the beam entrance ports.

In this work PT-1 and PT-2 are simple vacuum chamber similar to DPS-2. For atom optics experiments, they are replaced by one vacuum chamber with two-stage pumping separated with piezo-table, which provides movable μ -apertures for the scanning of the beam profile and determining the size of the focused beam spot.

In the source chamber, the source is mounted on a manipulator allowing 5 degrees of freedom which is mounted on the top flange of the source chamber. The target manipulator enabling 6 degrees of freedom is mounted on the top of the main target chamber. The iris chambers entails a circular aperture with the adjustable diameter of 0.8 to 5.0 mm. The detector chamber consists of a mass spectrometer.

The details of the beam collimation and dimensions of the apparatus are shown in Figure 3.4. A glass window at the backside of the detector serves for the beam path alignment. The alignment of the collimation apertures is done by a telescope and with a He/Ne laser and is justified with the He beam intensity. Note that in Figure 3.4 the target-to-detector distance is given as L_{TD}^0 . This is the distance for the detector position $L_D=0$ mm. For detector position $L_D > 0$, the target-to-detector distance is given by $L_{TD} = L_{TD}^0 - L_D$.

The description of the pumping system is provided in Table 3.1. To avoid the oil contamination in vacuum only turbo-molecular pumps are used. The differential pumping stages are only used for the purpose to reduce He the background pressure in the detector chamber.

Briefly, the beam is generated in the source chamber by skimming the core of a supersonic free jet expansion. The skimmed beam travels through the differential pumping stage-1 (DPS-1), the chopper chamber, the iris chamber and is scattered from a surface in the target chamber. The scattered beam reaches the detector preceded by several differential pumping stages.

The stepper motors, TOF module, temperature controllers and the signal output are connected to a computer via a CAMAC¹ unit. All control and measurement programs are written with LabVIEW², automating the angular scan and TOF measurements.

¹The CAMAC (Computer Automated Measurement And Control) is a modular interface for data handling.

²LabVIEW is a graphical programming language developed by National Instruments, Austin, TX, USA

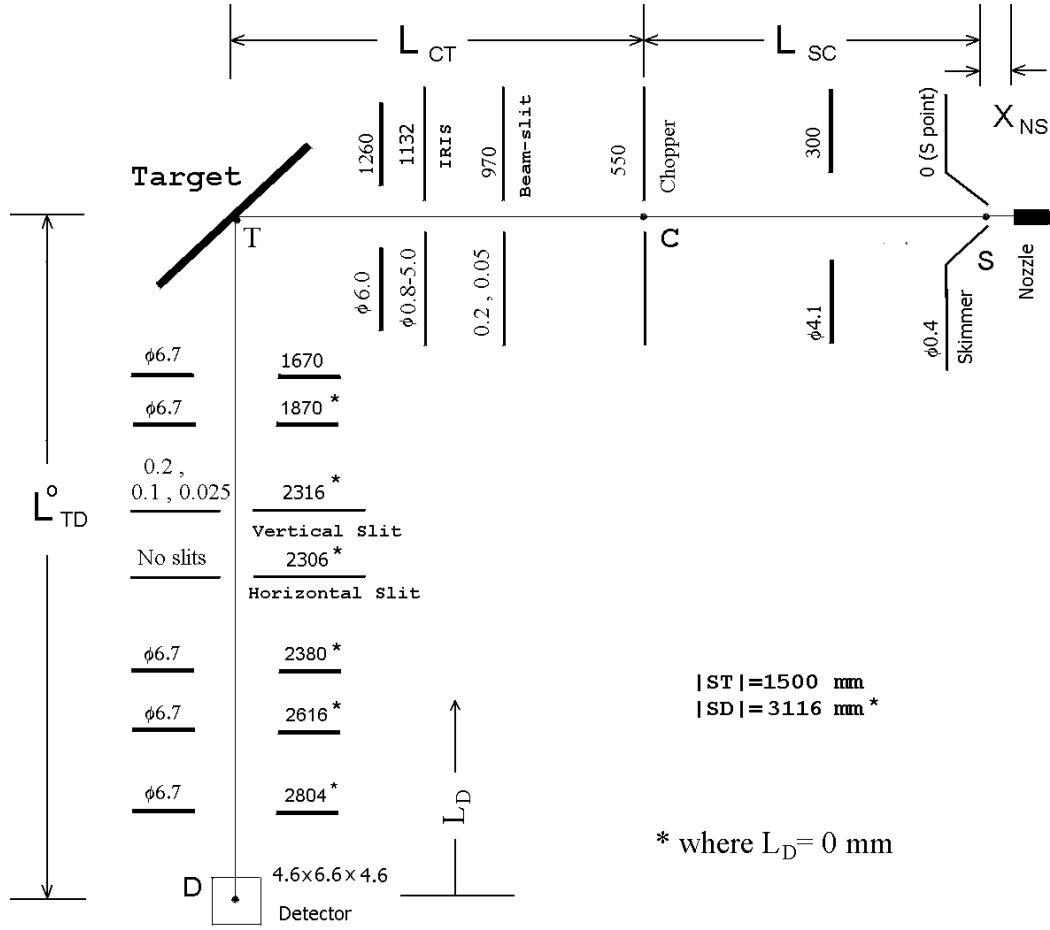


Figure 3.4: The beam path and the dimensions of the collimating apertures of the apparatus given for the case where $\theta_{SD} = \widehat{STD} = 90^\circ$. All dimensions are given in mm. The skimmer tip is taken as the origin. The nozzle-skimmer distance is mostly set to 10 mm. The effective ionization region has a width, height and length of 4.6, 6.6, and 4.6 mm, respectively (see Section 3.1.7). (*) indicates that the dimensions of the movable parts on detector arm are given for detector position, $L_D = 0 \text{ mm}$ where $0 < L_D < 1200 \text{ mm}$. For instance, $L_{TD} = L_{TD}^0 - L_D$. Generally $L_D = 217$ or 300 mm is used.

Table 3.1: Pumping system of the apparatus.(★): In this work PT-1 and PT-2 are simple vacuum chamber similar to DPS-2.

Chamber	Aperture	UHV pump [Pumping speed(He)(ls ⁻¹)]	Forevacuum pump [Throughput(m ³ h ⁻¹)]
Source	Skimmer (400 μ)	Balzers TPH 2200 S [3200]	Leybold WS501 [505] Leybold WS251[251] Leybold Trivac D65B [65]
DPS-1	4.1 mm	Leybold Turbovac 361 [380]	Leybold Trivac D16B [16.5]
Chopper	20 mm	Leybold Turbovac 361 [380]	Leybold Trivac D16B [16.5]
Iris	6.0 mm	Leybold Turbovac 50D [32]	Leybold Trivac D4B [4.2]
Target	6.7 mm	Leybold Turbovac 361 [380]	Leybold Trivac D16B [16.5]
DPS-2	6.7 mm	Leybold Hy.Cone 200 [180]	Leybold Trivac D8B [8.5]
DPS-3	6.7 mm	Pfeiffer TPU 062 [56]	
PT-1	6.7 mm (★)	Pfeiffer TMU 065 [56]	Leybold Trivac D4B [4.2]
PT-2	6.7 mm	Pfeiffer TMU 065 [32]	Leybold Trivac D4B [4.2]
Detector		Pfeiffer TMU 260 [220]	Leybold Trivac D8B [8.5]

3.1.1 The Beam Source

The nozzle is mounted on a goniometer which is placed on a linear translation table so that the nozzle can be moved translational in 3D and tilted in vertical and horizontal directions. The movements are controlled manually by turning knobs and read by dial counters. The coordinate conventions and their definitions and features are given in Table 3.2. The y- and z-movements need to be adjusted each time after the source holder remounted. They also serve to determine the nominal skimmer diameter and to test the quality of skimmer or beam alignment (see Section 4.2). The x-movement provides the advantage of optimizing the intensity at different stagnation conditions with changing the skimmer-nozzle distance (X_{NS}). The tilting movements need to be optimized as the nozzle may not be along the collimation line. This is particularly important for home-made glass nozzles. The experiments with the source movements will be demonstrated in Chapter 4. In the experiments presented in this work the skimmers of orifice diameters of 48 μ and 400 μ are used³. They are 1-inch long cones

³In the most of the experiments a 400 μ skimmer was used.

Table 3.2: The coordinate convention of the source manipulator. The positive increments along the coordinate axes is defined with increasing dial number. The backlash of the movements is about two dials, except for y-movement which has a backlash of 30 dials.

Coordinate	Definition	Movement	Limits
x-axis	In the direction of beam	$25\mu/\text{dial}$	60 mm
y-axis	To the left with respect to beam	$12\mu/\text{dial}$	± 12 mm
z-axis	Upwards	$13\mu/\text{dial}$	± 12 mm
β -angle	Vertical tilt (around \hat{y})	12.5 mdeg/dial	$\pm 17^\circ$
γ -angle	Horizontal tilt (around \hat{z})	12.5 mdeg/dial	$\pm 17^\circ$

made of nickel⁴. The total included internal and external angles at its orifice are 25° and 30° , respectively, and the base angle is 70° . This unique geometry and very sharp orifice edge feature give minimal disturbance of the gas passing through the orifice. The nozzle-skimmer distance is mostly kept at 10 mm which is an optimized value (see Section 4.2).

A source orifice of 10μ nominal diameter was used. The source is heated by a resistance wire wrapped around the orifice tube. The source is cooled by the circulating liquid nitrogen. The temperature is measured by a Pt-100 resistor and is controlled by a temperature controller⁵. The stagnation temperature can be set with a fluctuation of $\Delta T_0 < \pm 0.1$ within the range of 100-400 K. The source and the gas supply line are designed to work at pressures up to 1000 bar. To avoid clogging of the nozzle, high purity helium (^4He of grade 6.0) is used and a 10μ pore filter kept in liquid nitrogen temperature is mounted in the gas supply line. Turbo-molecular pump is used instead of a diffusion pump, which allows the usage of micro-skimmers [133] without clogging. In the beam focusing experiments, the size of the focussed beam spot is also determined by the source size, which is defined by the skimmer diameter, given that skimmer diameter is much smaller than the sudden-freeze diameter.

The base pressure of the source chamber is 1×10^{-7} mbar and when helium gas is supplied it is in 10^{-3} mbar range. Supplying high pressure He gas into the vacuum through the micro-nozzle results in a supersonic expansion of the He gas. The characteristics of the expansion and the skimmed beam will be discussed in Chapter 4.

⁴Beam Dynamics Inc., Minneapolis, Minnesota, USA

⁵Eurotherm-2404: Eurotherm Regler GmbH, Limburg an der Lahn, Germany

3.1.2 The Chopper and the TOF Module

The time-of-flight (TOF) method is used to analyze the translational energy of the beam, which is the most commonly used method in molecular beam experiments [134, 135]. The idea of the method is simple. The incident beam is pulsed with a mechanical chopper of 0.1 mm thick metal disc with two identical equilateral trapezoid slits of height of 15 mm and of sides of 1mm and 5 mm. The vertical chopper position is changed manually allowing to use different slit widths, or doing beam experiments without chopper. The total flight time of the beam pulse from the chopper to the detector is measured with time-amplitude converter electronics. The bearing-supported chopper can run in the range of 75-500 Hz in both rotational directions.

A computer controlled program is triggered with a LED and photo detector and starts accumulating the counts of detected particles after a delay time. The pulse counts are accumulated in the multichannel scaler (MCS) in the certain time bins corresponding to arrival time to the detector. Measurement time, width and the number of time bins and delay time are set prior to the experiment depending on the required resolution, velocity of atoms and the range of the energy loss spectra. Narrower time bin means better energy resolution, but less signal-to-background ratio of the TOF spectrum. Larger slit width increases the beam intensity, so that the measurement time, but reduces the resolution of the TOF spectrum. The similar trade off is valid in case of the variation of the target-detector length. It is sometimes worth optimizing the slit width and target-detector length for a particular experiment. In TOF measurements the intensity of beam should not exceed about 100 kcps. It is observed that when the intensity is high an artificial shoulder is created in the TOF peak due to the saturation of the channeltron. In Section 3.2 the characterization and calibration experiments of the TOF apparatus are presented.

3.1.3 Target Chamber

The schematic side and top views of the target chamber are provided in Figures 3.5 and 3.6. The functional purpose of the target chamber is providing high and clean vacuum conditions that the sample surface has a negligible interaction with the residual ambient gases over the course of a measurement run. The total pressure of the target chamber reaches ultra high vacuum conditions in the 10^{-8} mbar range within several hours after the pumping down and without baking out. These conditions guarantee clean LiF(001) and Si(111):H(1×1) surfaces used in this work. The chamber can be

baked up to 150° C resulting in total pressures in the 10^{-10} mbar range. For a bake out at higher temperatures, the parts with teflon sealing must be removed. The requisite vacuum conditions depends not only on total pressure but also on both the species present in the residual gas and their reactivity with the sample. The Si(111):H(1×1) surface is particularly reactive with hydrocarbon compounds. For this reason all the high vacuum pumps are turbomolecular pumps and for the target and its neighboring chambers oil filters preceding the rotary pumps are installed. Although turbo pumps have a relatively poor compression ratio for helium, they provide good vacuum conditions free of pump oil vapors. But still some oil vapor can get into the vacuum chamber through backstreaming during pumping down. To avoid this a gate valve⁶ is mounted between the target chamber and the turbo pump so that the chamber can be vented without turning the turbo pump off. The "clean pumping down" is realized with, first, pumping down the chamber with a membrane pump⁷. When a pressure of few mbar is reached the gate valve (see also Figure 3.1) is opened slowly so that the turbo pump continues running at full speed. This procedure guarantees pumping down the chamber within half an hour without backstreaming of oil vapor and a simple alternative to the load lock systems. A mass spectrometer⁸ is installed to check the cleanliness of the vacuum in the target chamber.

As shown in Figures 3.5 and 3.6 the chamber has several ports for mounting necessary devices for vacuum and surface characterization such as a cold finger and the electrical feedthroughs and as well as for variable detector angle several beam ports and a flexible bellow. A large glass window with Viton-sealing allows inserting and removing samples and parts into and from the vacuum quickly.

3.1.4 Target Manipulator

The schematic diagrams of the target manipulator are shown in Figures 3.7, 3.8 and 3.9. The target (or crystal, sample) manipulator provides 6 degrees of freedom. The convention and features of the coordinates of the target and the detector manipulators are provided in Table 3.3. The manipulator is mounted on the top of the target chamber and the samples can be mounted with a holder on the manipulator. The polar angle rotation (θ) is realized by using differentially pumped seals (see Figure 3.7). Three spring-loaded Teflon seals are used and the space between them is differen-

⁶MDC Vacuum Products Co., Hayward, CA, USA

⁷Sasika Hochvakuum und Labortechnik GmbH, Ilmenau, Germany. Model: MPC 601 T

⁸Balzers Model:QMG 551, FL-9496 Balzers, Liechtenstein

3. The Apparatus and Experimental Details

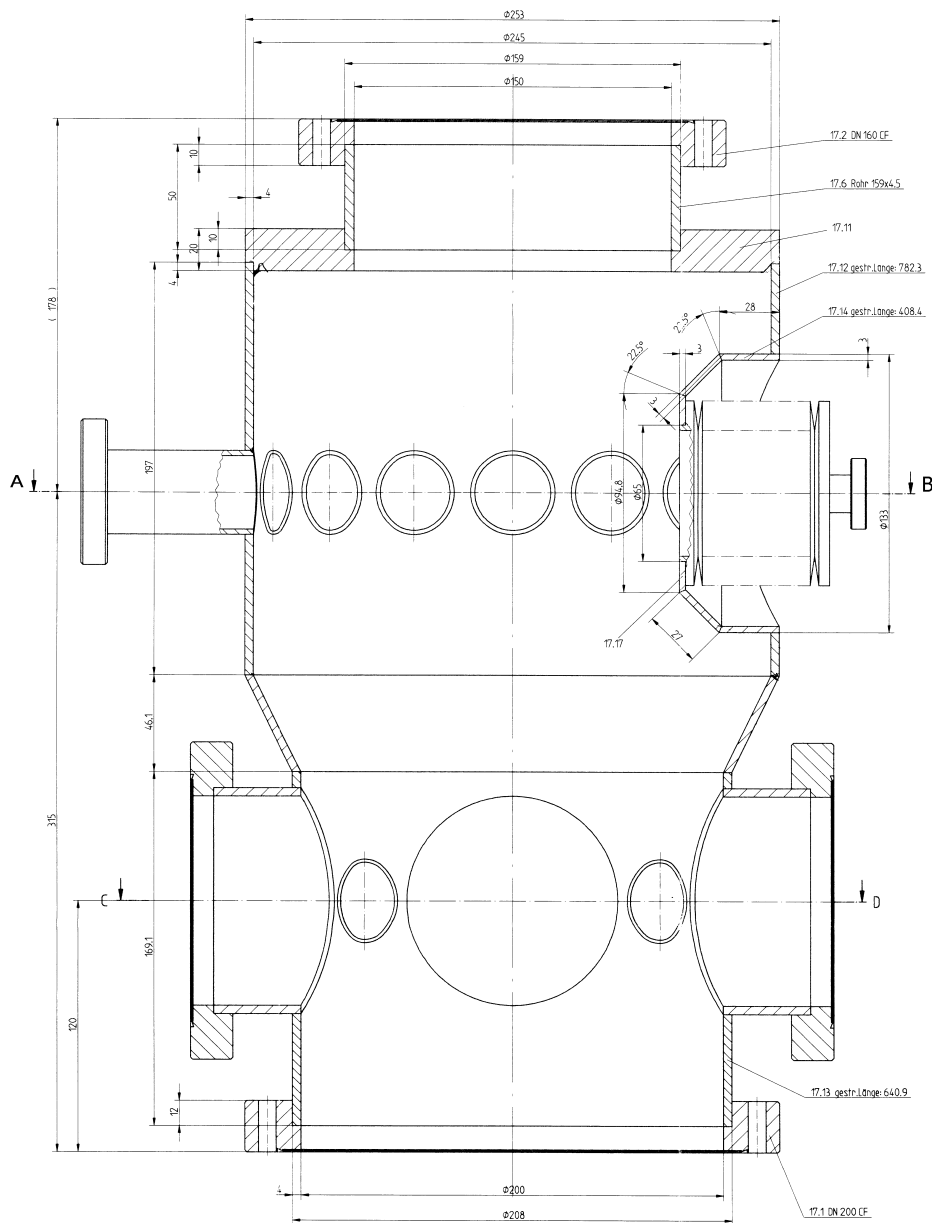


Figure 3.5: The target chamber in side view. The target manipulator is mounted on the top and the turbo pump is mounted at the bottom of the chamber. Between the turbo pump and the chamber there is a gate valve allowing the clean pumping down.

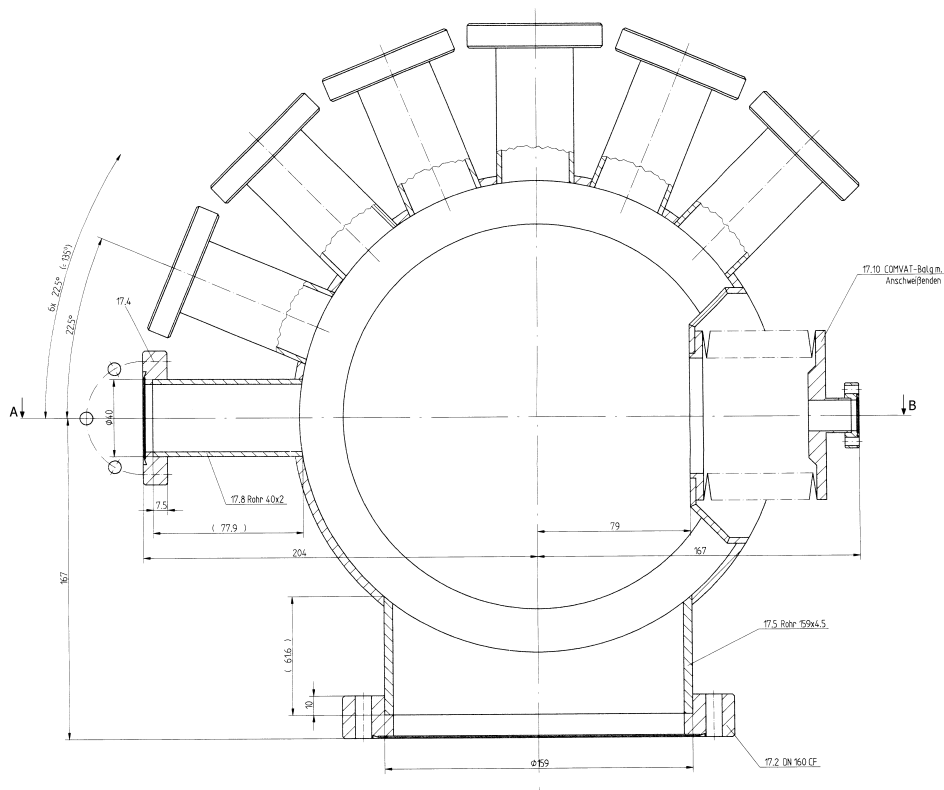


Figure 3.6: The target chamber in top view on the beam path plane. The seven beam entrance ports enable setting the detector angle with 22.5° intervals. The reentrant bellow allows the rotational freedom of the detector within 12° .

Table 3.3: The coordinate convention of the target and the detector manipulator. The corresponding steps to the 1 mm translation and 1° rotational movements are given. All movements except the azimuthal rotation, ϕ are controlled by stepping motors. (*) denotes the corresponding rotation angle of the turning knob to 1° rotation of the sample.

Coordinate	Definition	Movement	Limits
x-axis	Parallel to surface	400 steps/mm	± 12.5 mm
y-axis	Upwards	3650 steps/mm	± 50 mm
z-axis	Perpendicular to surface	400 steps/mm	± 12.5 mm
β -angle	Around the x-axis	1834.9 steps/deg	$\pm 1.3^\circ$
ϕ -angle	Around the z-axis	8.29°/deg *	360°
θ -angle	Around the y-axis	657.22 steps/deg	360°
θ_{SD} -angle	Around the y-axis	151020.02 steps/deg	40-190°

tially pumped with the rotary pump of the target chamber. This setup is particularly suitable to move heavy instruments in vacuum with a large diameter and allows a rotational freedom of 360°. The estimated gas leakage under static conditions is about 10^{-13} mbar L/s and the pressure rise upon rotation is less than 10^{-10} mbar [136–138].

A stepping motor and an independent angle decoder control the polar rotation. The backlash is about 1° and the angles should be measured in one direction. x, y, z, and tilting (β) movement are enabled with a large bellows. A linear screw motion controlled by the stepping motors is converted into two parallel linear motion of plates which allow x- and z-movements. The tilting is realized in a similar way but the sliding plate moving on a rounded surface (see Figure 3.8) . The center of the curvature of the convex part corresponds to the center of the sample holder. The tilt movement is used for adjustment purposes and has a narrow range. The y-movement moves the base plate up and down through a spindle. The x, y, z, and tilting positions and angle are controlled by the stepping motors. A conventional rotary feedthrough mounted on the top of the tilting motion plate translates the rotational motion around the y axis into the azimuthal rotation (see Figure 3.9). The azimuthal rotation is controlled manually with a freedom of 360°.

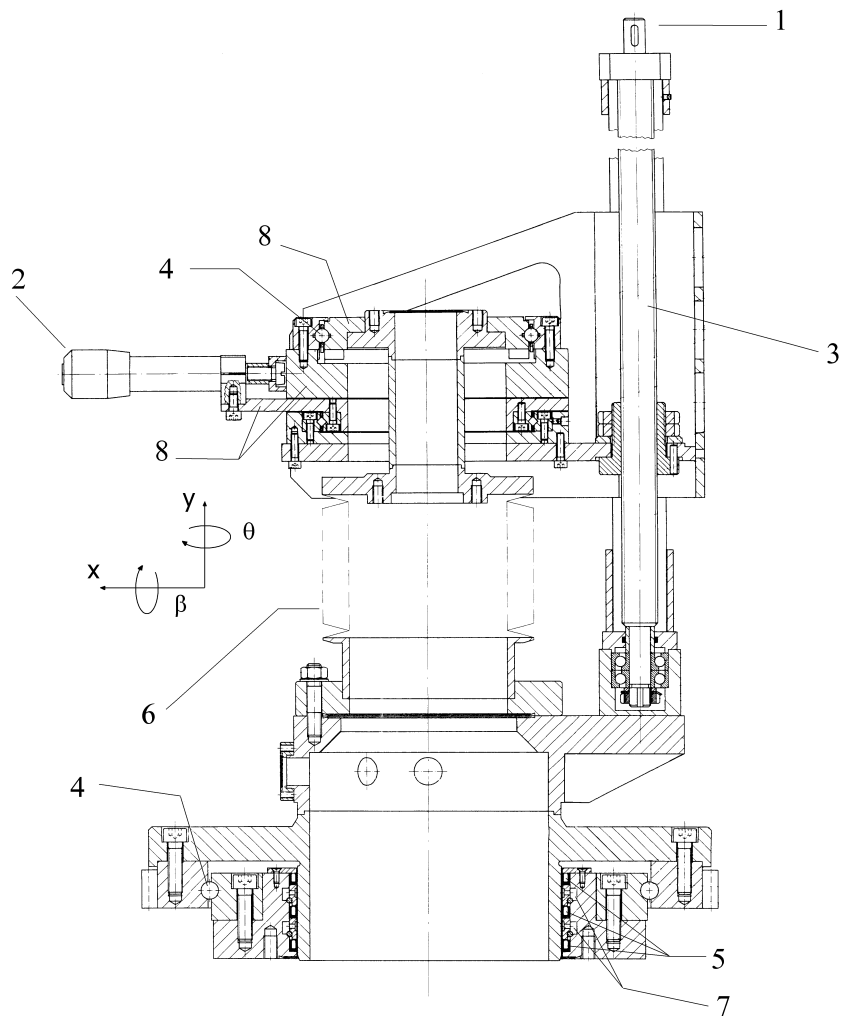


Figure 3.7: The scheme of the manipulator with x, y and polar angle movements shown in detail. (1) y-movement. (2) x-movement. (3) Spindle. (4) Ball bearings. (5) Spring-loaded teflon seal. (6) Bellows. (7) Differentially pumped case. (8) Sliding plates.

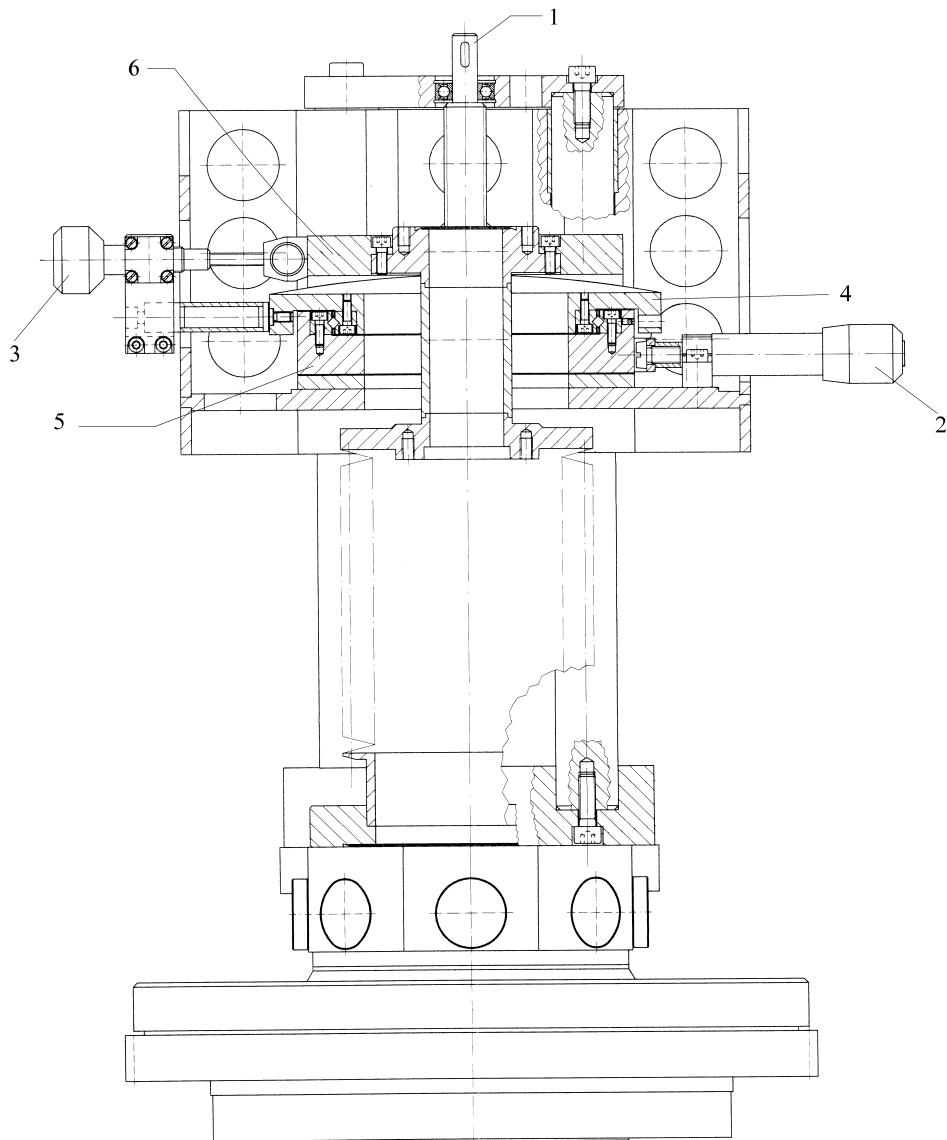


Figure 3.8: The scheme of the manipulator with z and tilt angle movements shown in detail. (1) y-movement. (2) z-movement. (3) Tilt movement. (4) Sliding plate for x-movement. (5) Sliding plate for z-movement. (6) Sliding plate on a convex surface resulting the tilting angle in. The center of the convex curvature is the center of the target holder.

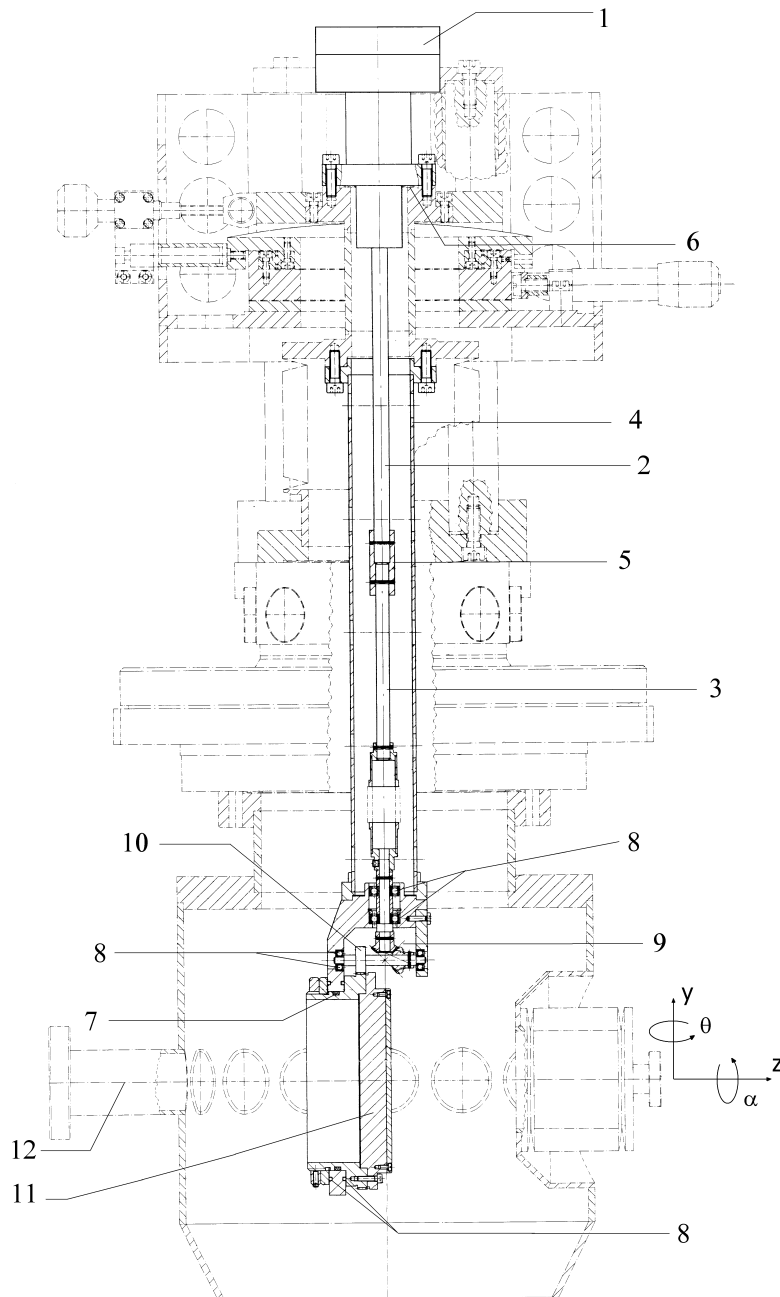


Figure 3.9: The scheme of the manipulator with azimuthal movement showed in detail. (1) Manual turning knob for azimuthal rotation. (2) Rotary feedthrough. (3) Shaft. (4) Connection tube. (5) U-joint. (6) CF-sealing. (7) O-ring. (8) Ball bearings. (9) Bevel gears. (10) Pinion gear. (11) Target holder. (12) Beam line.

3.1.5 Variable Detector Angle

Several beam entrance ports enable setting the source-to-detector angle (θ_{SD}) with intervals of 22.5° (see Figure 3.6). The flexible bellows connection allow varying the detector angle by $\pm 12^\circ$. Thus, the set up give access any total angle from 40° to 190° . Similar setups were used by two other groups [139, 140]. The angle encoder of the θ_{SD} is mounted on the rotation center of the detector arm and requires no reset for the whole angular range. A stepping motor fixed on the circular track pushes and pulls the detector arm through a spindle. Changing the beam entrance ports needs venting the chopper and the iris chambers (these chambers are not separated with a valve, although it is in principle possible). To connect an new beam port the bolts of the target chamber connecting with its base and the bolts of the stepping motor base are loosened and target chamber and detector arm are moved to a new position together. Finally the vented chambers are pumped down. The whole procedure can be done by one person and takes half an hour. The requirement of the vacuum conditions in vented chambers depends on the crystal to be investigated. As LiF(001) crystals are rather inert and can be investigated even under poor vacuum conditions, a total pressure of 10^{-7} mbar in the iris chamber can be reached in one hour and new series of experiments can be carried out.

3.1.6 Crystal Holder

The crystal holder used in the LiF(001) experiments is shown in Figure 3.10. The diameter of the holder is 32 mm. The holder is mounted by the back rod with three screws onto a disk fixed on the manipulator. It is connected to liquid nitrogen trap via a copper braid which prevents none of the degrees of freedom of the manipulator. Three sapphire plates provide good thermal conduction at low temperatures and good thermal isolation at high temperatures. The crystal is mounted on the molybdenum plate with two clamps fastened with screws. A hole of 0.7 mm diameter and 3-5 mm depth is drilled on the side of the crystal before the cleavage. A K-type thermocouple (Ni-Cr/Ni-Al) with wires of 0.1 mm diameter is used. A thin ceramic stick was inserted between the wires in order to prevent the shortcut and to make a good thermal contact of the crystal and the thermocouple. The thermocouple was so tightly fixed within the crystal that it was impossible to take it out without breaking the crystal. The temperature of the crystal is controlled with a temperature controller similar to the source temperature controller. This compact and thermally good isolated construction

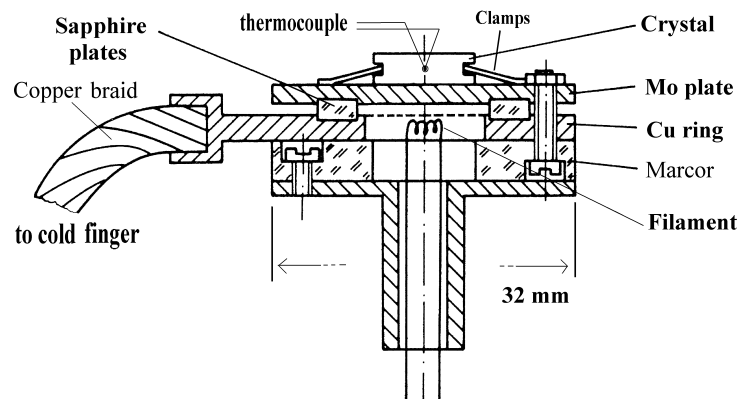


Figure 3.10: The scheme of the crystal holder.

enables cooling the crystal to 110 K with liquid nitrogen and heating up to 900 K by radiation from a filament at 100 Watt. After the cleavage in air the crystal is mounted on the crystal holder, the connections of the thermocouple are fixed and the chamber is pumped down. The whole procedure takes only 5 minutes.

3.1.7 The Detector

The home made detector incorporates the electron bombardment ionizer, extractor and focusing optics, the 90° magnetic mass spectrometer, and the channeltron ion detection. The detector was developed by Samelin and the detailed description of the detector can be found in his master thesis [141]. The construction of the ionizer and the ion extraction unit is given in Figure 3.11. The neutral atoms arriving at the ionization region are ionized by the impacting electrons, which are emitted from a hot cathode. The cathode is a $10 \times 6 \times 5$ mm tungsten block coated with barium oxide⁹. The effective ionization width, height and length are given as 4.6 mm, 6.6 mm, 4.6 mm, respectively and these values will change slightly at different settings of the detector [141]. The emitted electrons are accelerated by the repeller voltage into the inner grid. After ionization the ions are extracted and focused into the magnetic deflection unit. Through the magnetic field, the particles are selected according to

⁹Spectra-MAT Inc., Watsonville, CA, USA

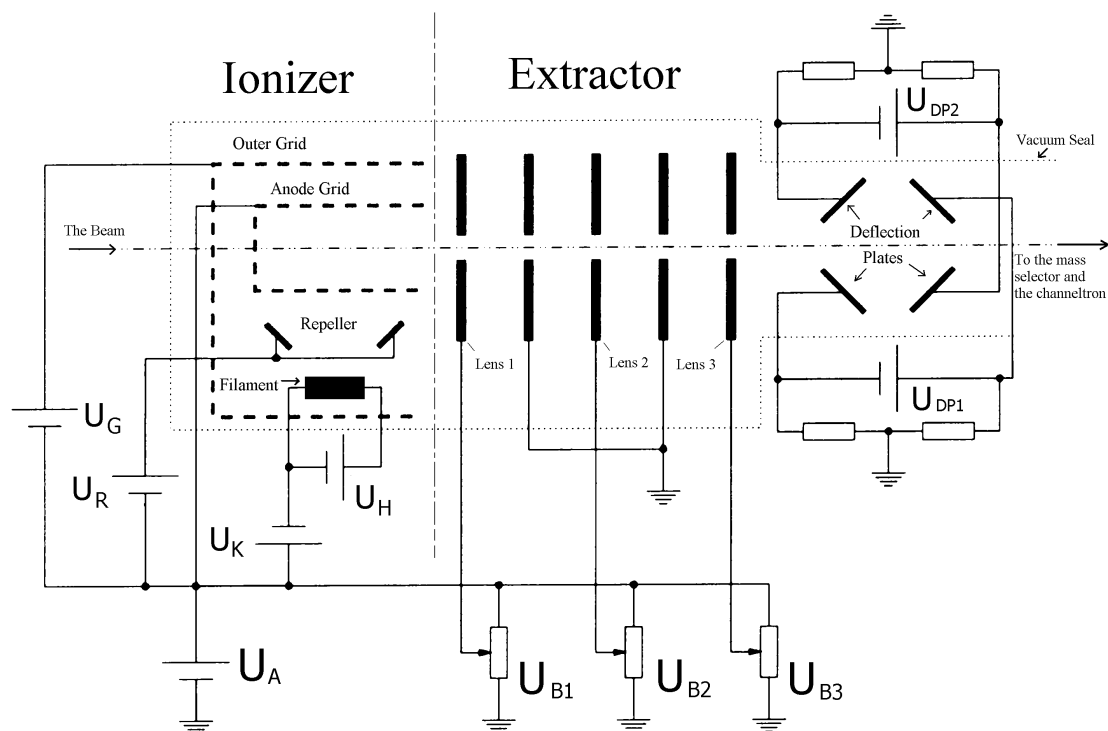


Figure 3.11: The scheme of the detector. The electrons are emitted from the hot cathode and repelled into the anode. The ionized molecules are extracted and focused into the mass spectrometer.

their mass/charge ratio and detected by a channeltron¹⁰. The signal increases with the increasing channeltron voltage and the best working range is where the signal starts to saturate with increasing voltage (see Figure 3.12). The channeltron voltage was set to 2.3 kV.

The settings of the detector are given in Table 3.4. These settings, however, used for scattering experiments. To avoid the saturation of the channeltron in the case of direct beam ($\theta_{SD}=180^\circ$) the detector efficiency is reduced by reducing the emission current, I_E and increasing U_{B3} .

The signal measured by the detector has three parts: The true signal, I_{Beam} is caused by the molecular beam crossing the ionization region. Diffused helium background, I_{Diff} is caused by diffusion of He from preceding chambers into the detector chamber. The background signal, I_{BG} caused by detection of background gas in the detector chamber. I_{BG} has two contributions; the tail of the H_2 peak and partial pressure of

¹⁰Model: DeTech-418, Detector Technology, Inc. Palmer, MA, USA

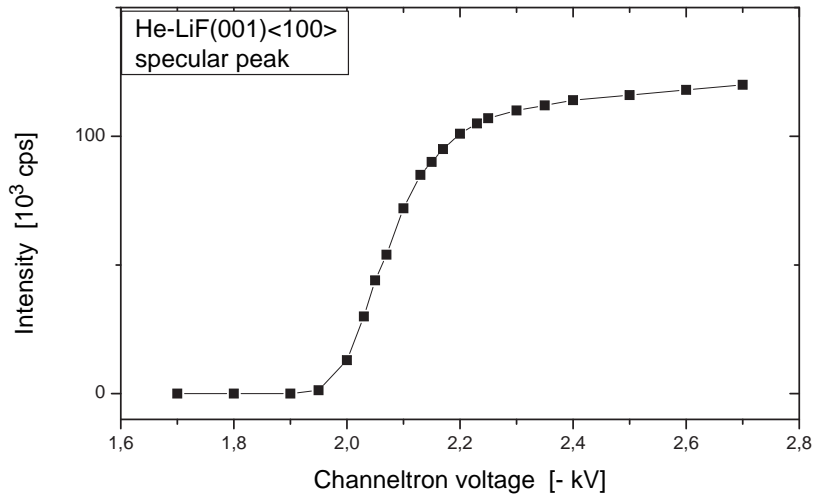


Figure 3.12: The channeltron voltage dependence of the measured signal. The best working region is where the signal tends to saturate.

Table 3.4: The settings of the detector.

U_A	U_G	U_K	U_R	U_{B1}	U_{B2}	U_{B3}	U_{DP1}	U_{DP2}	U_H	I_E
1.0 kV	97.4 V	160 V	4 V	960 V	814 V	0 V	0 V	0 V	8 V	4 mA

the helium when the valves are closed. The background mass spectrum of the detector chamber is given in Figure 3.13. The background pressure is $P_{DC} = 2.5 \times 10^{-10}$ mbar. As seen in the figure I_{BG} is 100 cps and the main contribution is the partial pressure of helium. This indicates a leak in the chamber. The leak was in the turbo pump and could not be sealed easily, so that the background signal remained at about 100 cps throughout this work. The helium background partial pressure can be estimated from the detector's background sensitivity and for a emission current of 4 mA the count rate is given as [141];

$$I_{BG} \approx 0.66 \times 10^{16} P \quad . \quad (3.1)$$

Here the I_{BG} is in cps and P is the partial pressure of the helium in mbar. Hence, the estimated partial pressure of the helium is then $P \approx 1.5 \times 10^{-14}$ mbar. A background of 100 cps is low enough to do even most of the inelastic scattering experiments. However there is also contribution of diffused background which is reduced by differential

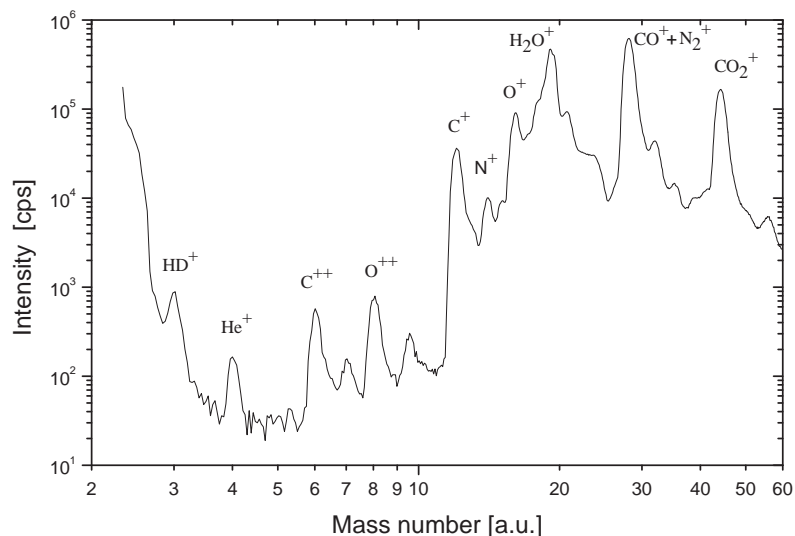


Figure 3.13: The mass spectrum of the detector background gas. The detector valve is closed. The total pressure is $P_{DC} = 2.5 \times 10^{-10}$ mbar. Cathode voltage is 160 V and emission current is 4 mA. The major peaks are labelled. He peak is due to a leak. HD peak is due to the natural abundance of deuterium (1.4×10^{-4}) in hydrogen.

pumping. This will be discussed below. The sensitivity of the detector for diffused background is also expressed with Equation 3.1. The probability of the detection of a He atom in the beam depends on the emission current [141] and the ionization probability¹¹ is measured at 4 mA as $W = 2.1 \times 10^{-6}$. The ionization probability of the D_2 molecule is about 2.3 times higher than of the helium atom.

3.1.8 Differential Pumping System

It is a typical characteristic of molecular beam machines to use numerous differential pumping stages along the beam path to reduce the diffusion of the beam gas into the detector chamber. The He pressure in the source chamber is about 10^{-3} mbar and by using several pumping stages with small apertures the diffused He background in the detector chamber should be reduced to less than 10^{-14} mbar. The list of the chambers and description of the pumps and the apertures are given in Table 3.1.

¹¹In fact, the given probability is for room temperature beam and the ionization probability for electron impact ionization detectors is inversely proportional to beam speed, v_{He} .

Since there are three pumping stages before the target chamber, the main contribution of diffused background in the detector comes from the beam load stopped in the target chamber. The flux of the beam entering the source chamber is defined by the iris aperture area σ from Section 4.2 and is

$$\dot{N} = 0.16 \frac{P_0}{kT_0} \sqrt{\frac{5kT_0}{m_{He}}} \left(\frac{d}{x}\right)^2 \cdot \sigma \quad , \quad (3.2)$$

where P_0 and T_0 are stagnation pressure and temperature, x is the position of the iris and d is the nozzle diameter. The partial pressure of helium in the target chamber is then

$$P_{TC} = \frac{Q}{S_{TC}} = \frac{\dot{N}kT}{S_{TC}} \quad , \quad (3.3)$$

where S_{TC} is the pumping speed of the pump given in the Table 3.1. The helium pressure at the target chamber effusively reaches through the apertures and chambers to the detector chamber. The pressures in the down stream chambers can be calculated with aperture conductance and pumping speed relations under the fiat of free molecular flow. The conductance of a thin aperture plate of surface area A is [142] given by

$$C_A = \frac{1}{4} \bar{v} A \quad , \quad (3.4)$$

where \bar{v} is the mean speed of the molecules in room temperature. The apertures of differential pumping stages between the target and detector chambers are copper gasket tubes of 6.7 mm diameter and 15 mm length. The conductance of a tube of length L and diameter D is given in terms of the aperture plate conductance as

$$C = \frac{C_A}{1 + \frac{3L}{4D}} \quad . \quad (3.5)$$

The gas flux from a chamber of pressure P to the next chamber through an aperture of conductance C is given by

$$Q = C \cdot P \quad . \quad (3.6)$$

Using the equations above the general expression of diffuse background in the detector chamber can be derived as

$$P_{DC} = P_{TC} \cdot C_{TC} \cdot \prod_n \left[\frac{C_n}{S_n} \right] \cdot \frac{1}{S_{DC}} \quad , \quad (3.7)$$

where C_n and S_n are the conductance of the apertures and pumping speed of the pumps between the target and detector chamber, and S_{DC} is the pumping speed

of the detector chamber's pump. For an iris diameter of 3 mm and source stagnation conditions of 100 bar and 300 K the He partial pressure in target chamber is calculated from Equations 3.2 and 3.3 as $P_{TC} = 4.1 \times 10^{-8}$ mbar. The measured pressure was 4.0×10^{-8} mbar (corrected by the factor 6.9 for ionization probability of He). In the earlier experiments of this work the pumping stages PT-1 and PT-2 were not installed and in that case the calculated and measured diffused background intensity at the detector were 8.4 kcps (from Equations 3.1 and 3.7) and 2.0 kcps, respectively. The discrepancy is reasonable since the detector sensitivity can be slightly different than the given value and the exact calculations of the conductance of apertures and the effective pumping speed of the pumps depending on the geometry of chambers are difficult. The diffused background was too high to carry out inelastic scattering experiments so that we installed two chambers more (PT-1 and -2) were installed making the diffused background insignificant.

3.1.9 D₂ Recycling Unit

For use of the expensive D₂ gas a recycling system was built in. The schematic description of the D₂ recycling and the gas supply system for the high pressure nozzle source is shown in Figure 3.14. A system of by-pass valves is designed to swap the operation quickly with He and D₂ without mixing of the two gases. In operation with He gas, the valve V14 (see Figure 3.14) is opened. To start the recycling of D₂ the V14 is closed and V13 is opened. Secondly, the gas line between P4 and V11 and also common used gas line between the nozzle and the by-pass valves are pumped out. The recycling unit consists of a series of filters following the source chamber forevacuum pump and separate the recycled D₂ gas from oil and gaseous contaminants. The most essential part of the purification process is represented by two Al₂O₃ filters cooled with liquid nitrogen. After the purification stage the gas pressure is raised up to 130 bar by a two-stage compressor¹². A final filtering stage for both He and D₂ is installed before the nozzle with a cold trap with a 10 μ filter.

When the recycling system had a leak, the signal became lower, the speed and the speed ratio of the molecular beam got smaller due to the contamination. After fixing of the malfunction there is no contamination of the gas is noted within an operation of more than a week. As the gas lines of the recycling unit are very long (about 50 m), during the operation with the D₂ gas it can run more than a week without a refill.

¹²SERA-5142: Seybert&Rahier GmbH + Co., Immenhausen, Germany

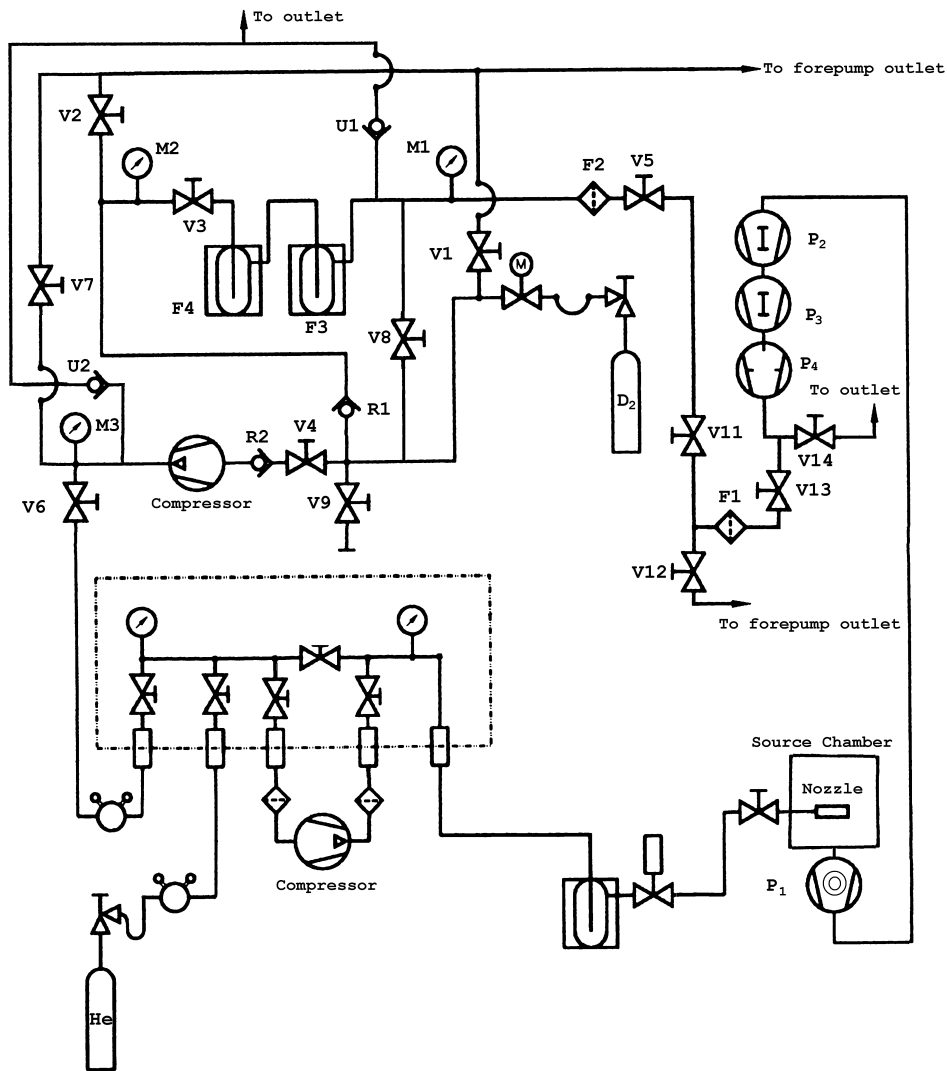


Figure 3.14: The scheme of the gas recycling and supply system of the Magie-2. The symbols are in DIN 28401 Norm. The pumps of the source chamber P_1 , P_2 , P_3 , and P_4 are described in Table 3.1. F1 is an oil filter. F2 is an active carbon filter. F3 and F4 are liquid nitrogen cooled Al_2O_3 filters.

3.2 Data Analysis and Experimental Resolution

In this section the calibration and the resolution of elastic and inelastic scattering experiments are discussed. The peak-centering accuracy of TOF experiments reached by most of HAS experiments have not been particularly great and few percent of precision in the incident energy is regarded as sufficient. The flexible flight length (L_{CD}) of the present apparatus allows *in-situ* calibration of flight path and time origin of the TOF technique rather than a rudimentary estimation from construction schematics which can change due to misalignment problems and time origin can shift due to the trigger and detection electronics. The angular and energy resolution of the apparatus is demonstrated by He scattering from the LiF(001) surface. LiF(001) is a well studied (both experimentally and theoretically) surface and easy to work with. Therefore, LiF had been chosen in test experiments of Magie-2.

3.2.1 Calibration of Elastic TOF Experiments

High energy resolution atomic helium scattering experiments are used to probe bound state and phonon energies of surface as a precise method where an energy spread of less than 1% has become achievable from supersonic free jet expansion. Since all measurements scale with the incident beam energy, the uncertainty in the incident energy of the elastic beam is a substantial issue limiting the precision. We present here an in situ calibration method with a variable chopper frequency and flight path for fixed experimental conditions which can be altered while mounting a new crystal or aligning the crystal. Therefore in situ calibration is a substantial feature and improvement of high resolution apparatus over conventional calibration procedures where the flight distance is calibrated with a known crystal lattice or theoretically predicted value of the beam speed [135].

The rotating disk chopper pulses the beam and triggers the detector electronic with a timing pulse. Generally, the timing pulse is generated with a time offset, t_c due to the widths of the triggering LED and slit and triggering level and it depends also on the chopper frequency. The trigger pulse starts a delay generator and sequentially initiating after a delay time, t_d the multichannel scaler which accumulates the counts in time intervals. The TOF spectrum of the direct He beam is shown in Figure 3.15. The total counts collected in each channel of time is plotted as scattered data. A typical TOF spectrum of the beam is a symmetric peak which is plausible to fit to

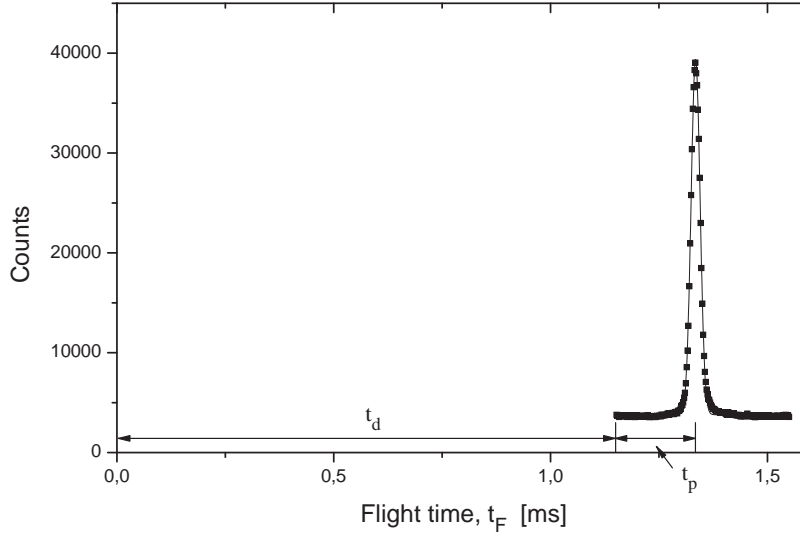


Figure 3.15: Time of flight spectrum of direct He beam. $P_0=150$ bar, $T_0=297$ K. Channel width is $2 \mu\text{s}$, the number of channels is 200, the delay time is 1.15 ms, the chopper frequency is 300 Hz, and the measurement time is 30 s. The detector position, $L_D=21.7$ cm. The best-fit Gaussian curve is also shown. The peak position fitted curve is 0.184 ms.

Gaussian type of curve¹³. The mean flight time of atoms given as

$$t_F = t_d + t_p + t_c \quad , \quad (3.8)$$

$$t_F = 1.150 + 0.184 - 0.018 = 1.316 \text{ ms.}$$

t_d is the set delay time and t_p is taken as the peak position of the fit curve giving mean flight time of the beam. t_c is found in the following procedure. One can assume that if the chopper frequency is infinite there is no delay. Thus the true t_F is when $1/f = 0$. In Figure 3.16 it is shown that how the measured flight time with the chopper frequency changes. The delay is found to be proportional to the inverse frequency; $t_c = a/f$ where $a = 5.26 \pm 0.09$ and for $f = 300$ Hz t_c is $t_c = -0.018$ ms.

A second source of the time offset t_c occurs when the chopper is not perfectly aligned with the beam. The simplest way of testing it is to rotate the chopper in the opposite direction and see if there is a shift in the flight time. As the chopper can be rotated in both directions, rotating the chopper in opposite direction at 300 Hz and measuring

¹³In fact, the beam spread incorporates a tail which can be represented by a broad Gaussian curve [143]

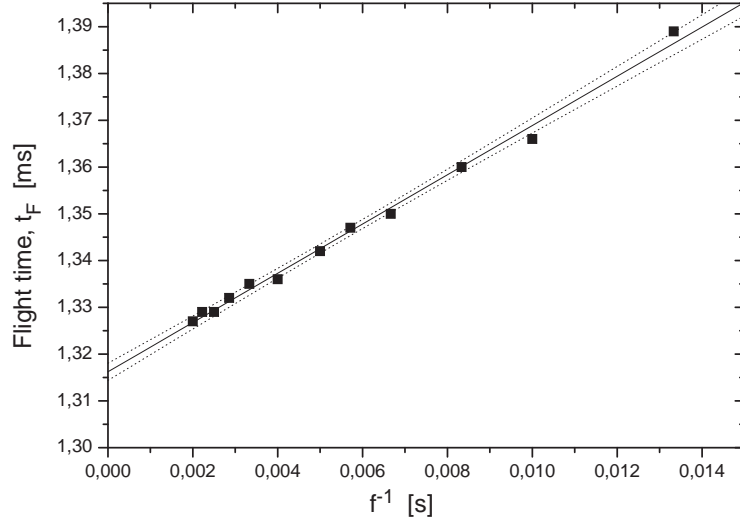


Figure 3.16: Total flight-time versus inverse chopper frequency for the same conditions as in Figure 3.15. For $f^{-1}=0$, the chopper delay time is zero.

TOF spectra at the same conditions resulted in flight time difference of, $\Delta t_F = 0.006$ ms. The actual offset is half of this value and changes when the beam path is changed. The correction time and the delay time are taken into account in the measurement program in all experiments in this work.

After determination of the time origin of the TOF flight path origin L_{CD}^0 can be determined by varying the flight distance L_{CD} where

$$L_{CD} = L_{CD}^0 - L_D \quad , \quad (3.9)$$

in which $7 \text{ cm} \leq L_D \leq 34 \text{ cm}$ (in the current configuration). Flight-time, t_F versus detector position, L_D is a linear relation and extrapolation of this line intersects with position axis indicating exact flight distance. It is also worthwhile to repeat this measurement at a different (low) temperature and see whether extrapolated lines of different temperatures intersect at the zero-flight-time axis. As seen in Figure 3.17, extrapolation of t_F versus L_D intersects each other at zero axis within the confidence bands of 95%.

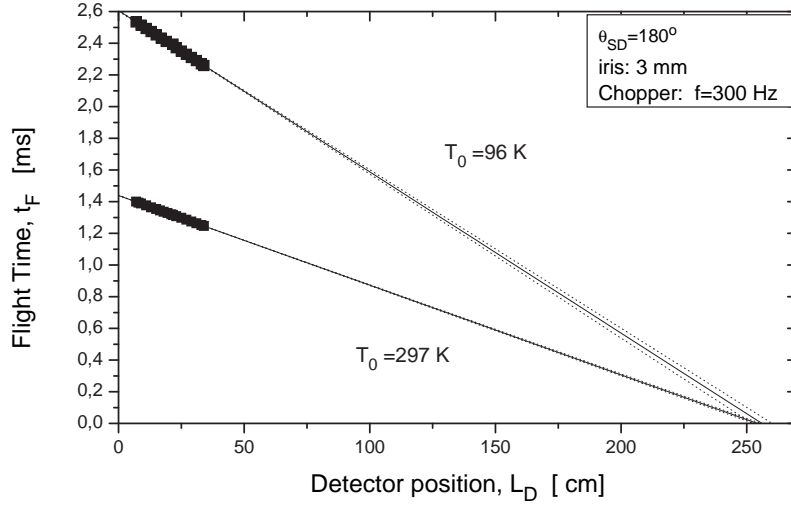


Figure 3.17: Flight time versus detector position of the beam at two stagnation temperatures of 297 K and 96 K. Confidence bands of 95% are also shown. The intersections of the extrapolated lines with the x-axis correspond to the L_{CD}^0 distance.

The results of these measurements are highly reasonable;

$$\begin{aligned} L_{CD}^0 &= 2577 \pm 40 \text{ mm (measured by 96 K beam),} \\ L_{CD}^0 &= 2569 \pm 2 \text{ mm (measured by 297 K beam),} \\ L_{CD}^0 &= 2566 \text{ mm (estimated from the construction drawings).} \end{aligned}$$

The relative larger error of the cooled beam is due to the larger temperature fluctuation at the given temperature. For the room temperature beam the error is smaller and this value will be used in this work. Principally the accuracy can be improved by removing the pumping stages and measuring the plot in Figure 3.17 for a broader range of L_D .

Although the peak-centering accuracy is mostly more stringent for the precision of the lattice constant and energy spectra experiments, the actual energy resolution of the apparatus is highly of interest and even crucial for inelastic scattering experiments in order to compare with theory and to understand some phenomena such as kinematic focussing [125, 144–150]. The TOF spectrum of direct beam in Figure 3.15 is fitted to a Gaussian peak. The FWHM of the peak is, $\Delta = 20.7 \pm 0.3 \mu\text{s}$. The width of the peak is not only due to the velocity distribution of beam, but also due to the smearing

effect of the finite chopper gate function and detector length¹⁴. The resulting time spread of the TOF peak is a convolution of three separate broadening contributions and approximately can be convoluted by adding the square of their widths (FWHM):

$$\Delta^2 = \Delta_B^2 + \Delta_D^2 + \Delta_C^2 \quad , \quad (3.10)$$

where Δ is the measured width of the TOF spectrum and Δ_B , Δ_D , and Δ_C are time widths due to isolated smearing effects of velocity distribution, detector and chopper gate function, respectively. To determine the exact velocity spread of the beam it is necessary to know the values of Δ_C and Δ_D . They can be estimated by

$$\Delta_B = L_{CD}\Delta u/u^2 \quad , \quad (3.11)$$

$$\Delta_C = w/f2\pi r \quad , \quad (3.12)$$

$$\Delta_D = X_D/u \quad , \quad (3.13)$$

where L_{CD} is the chopper-detector distance, u is the beam velocity, Δu is the FWHM of the beam velocity distribution, w is effective slit width¹⁵, r is the radius of the chopper at the beam center, f is the chopper frequency, X_D is the effective length of the ionization region of the detector. To extract Δu from a measured TOF spectrum in Figure 3.15 the parameters given above are sufficient, where $L_{CD} = 2349$ mm (for the detector position $L_D = 217$ mm, see Equation 3.9), $w = 2$ mm, $f = 300$ Hz, $r = 65.3$ mm $X_D = 4.6$ mm¹⁶ and $u = 1761$ m/s, resulting $\Delta_C = 16.3\mu s$ and $\Delta_D = 2.6\mu s$. Hence the total instrumental TOF width is

$$\Delta_M = \sqrt{\Delta_D^2 + \Delta_C^2} = 16.5 \mu s. \quad (3.14)$$

As mentioned the chopper contribution normally requires a more precise treatment to be estimated. Rather than a rudimentary estimation, we have the opportunity of

¹⁴The specific collimation geometry contributes also to the time spread. For instance, it causes a broadening by leading a flight path distribution. Since, here, the collimation is narrow, this effect is excluded. A narrow collimation geometry can have also dramatic effects. For instance, a narrow collimation at the detector side monochromatize the diffracted beam.

¹⁵In general case, $w=(w_{slit},w_{beam})$; indicating the larger of the quantities of slit width or beam cross-section width. A more accurate expression would be convolution of slit function and beam cross-section.

¹⁶The total length of the filament is 10 mm, so that effective detector length can be assumed approximately half of this value. The given value is from ref. [141].

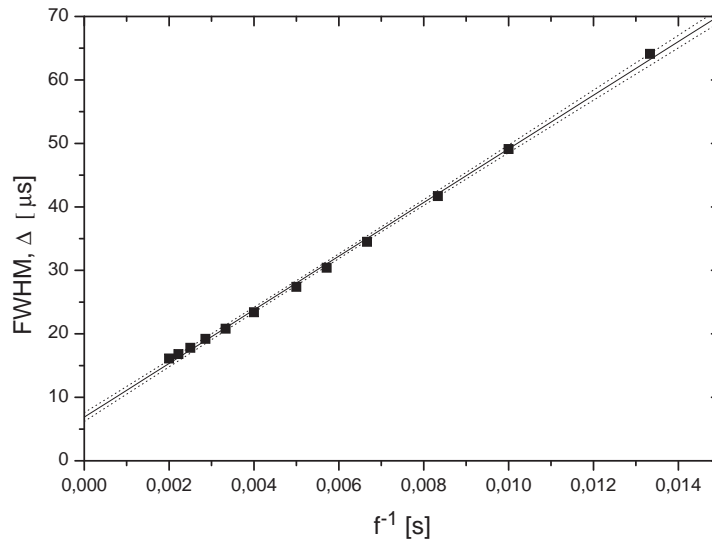


Figure 3.18: Measured width of the TOF spectra (FWHM) as a function of inverse chopper frequency. For $f^{-1}=0$, the contribution of the chopper slit function is zero.

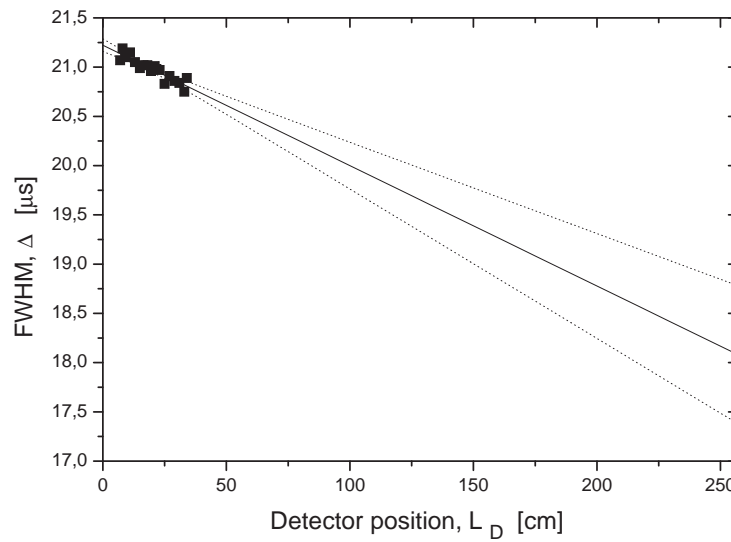


Figure 3.19: The dependence of the TOF spectrum on the detector position for the same conditions as in Figure 3.15. The intersection of the extrapolated line with the y-axis on the right hand side (which is the L_{CD}^0) corresponds to the total instrumental width of the TOF spectrum.

finding the chopper contribution experimentally and more accurately. f can be varied in the range of 75-500 Hz, where Δ_C is proportional to $1/f$, as given in Equation 3.12. If the chopper were rotating with an infinite frequency there would have been no contribution of chopper gate function to the broadening; thus, zero Δ_C . The intersection of the extrapolation of line to zero can in Δ versus $1/f$ plot gives without Δ_C . As shown in Figure 3.18 zero gate opening time corresponds to $\Delta = 6.9 \pm 0.7 \mu\text{s}$ which is equal to $\sqrt{\Delta_B^2 + \Delta_D^2}$. Hence, at $f = 300$ Hz the chopper contribution is $\Delta_C = 19.5 \pm 1.0 \mu\text{s}$. There is no way of straight measurement of Δ_D and also it has very small effect. Using the approximately predicted value of Δ_D in Equation 3.13, the total instrumental contribution is equal to

$$\Delta_M = 19.7 \pm 1.0 \mu\text{s}. \quad (3.15)$$

The variable flight path gives the opportunity to determine instrumental broadening without any assumption. It allows in situ characterization of the instrumental broadening and can be carried out easily for various instrumental and beam conditions. In the Δ versus flight distance graph, zero flight distance value of Δ is equal to Δ_M . From Figure 3.19, Δ_M is equal to

$$\Delta_M = 18.1 \pm 0.7 \mu\text{s}. \quad (3.16)$$

This result is more reliable than the results of previous methods. After in situ calibration and characterization of TOF spectra, the velocity and velocity distribution of the beam can be determined accurately. From the measured t_F and Δ the speed ratio is calculated as

$$S = 1.65 \frac{u}{\Delta u} = 1.65 \frac{t_F}{\Delta_B} = 1.65 \frac{t_F}{\sqrt{\Delta^2 - \Delta_M^2}}. \quad (3.17)$$

Thus, the determined speed ratio from the TOF spectrum in Figure 3.15 is $S=216 \pm 23$.

3.2.2 Inelastic TOF Experiments

One of the main purposes of building molecular beam scattering machines is to determine the dispersion curves of surface phonons via inelastic scattering of He atoms. Briefly, the energy loss/gain of the pulsed He beam is determined by measuring the TOF spectrum of the scattered beam at a constant angle. The kinematics of the inelastic scattering is discussed in the previous chapter. The energy resolution in the case of inelastic scattering requires further consideration where the resolution not only depends on the parameters of the scattering but also on the specific scattering geometry and on the dispersion of surface phonons.

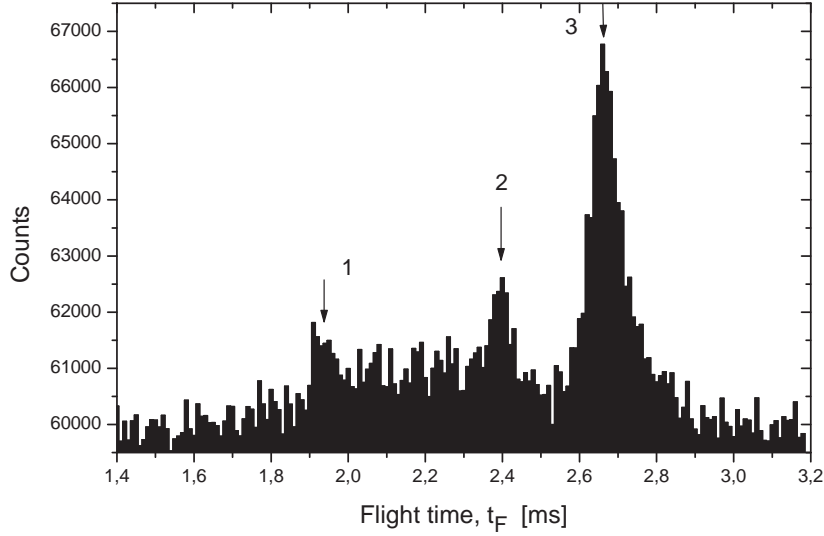


Figure 3.20: TOF spectrum at $\theta_i = 61.48^\circ$ for He of 120 bar and 98 K from LiF(001) in the $\langle 100 \rangle$ direction. The channel width is $10 \mu\text{s}$ the time delay is 1.40 ms, The second peak is the elastic peak, the first one is the energy-gain peak and the third one is the energy-loss peak. $\theta_{SD} = 90^\circ$.

In Figure 3.20 a TOF spectrum is given showing elastic and inelastic scattering from the crystal surface at an incident angle of $\theta_i = 68.48^\circ$. The flight time of elastic scattering is measured from the specular peak TOF spectrum as $t_F = t_{CD}^e = 2.40$ ms, corresponding to $k_i = 6.21 \text{ \AA}^{-1}$ and $E_i = 20.14$ meV. It is a common practice transforming time-of-flight spectra to energy-shift spectra. The TOF abscissa in Figure 3.20 can be transformed to the energy-loss abscissa as shown in Figure 3.21 with a transformation formula given as

$$\Delta E = E_i \left[\left(\frac{u_f}{u_i} \right)^2 - 1 \right] = E_i \left[\left(\frac{t_{TD}^e}{t_{TD}} \right)^2 - 1 \right] , \quad (3.18)$$

where u_i and u_f are the initial and final velocities of the He atoms, respectively, and t_{TD}^e and t_{TD} are the flight times of elastically and inelastically scattered atoms from the target to the detector, respectively. In TOF experiments only the total flight time from the chopper to the detector, t_F is measured, which is equal to

$$t_{CD} = t_{CT} + t_{TD} . \quad (3.19)$$

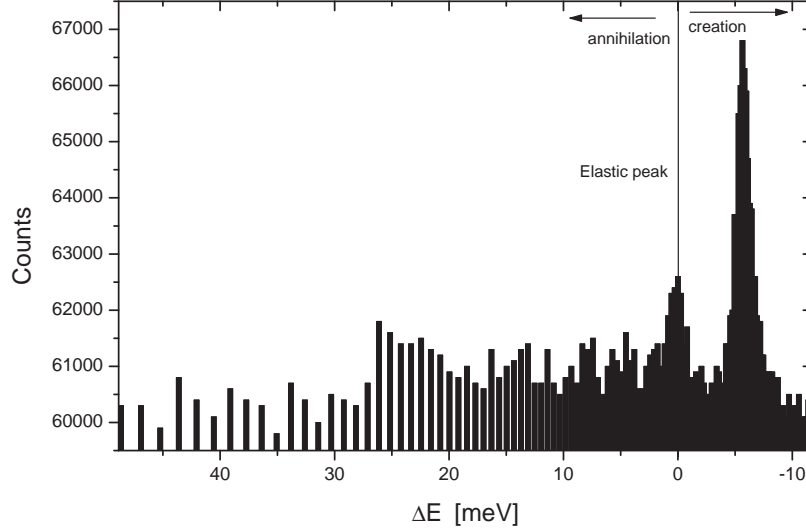


Figure 3.21: TOF spectrum in Figure 3.20 transformed into energy spectrum. The observable peaks are diffuse elastic scattering and phonon creation and annihilation. The incident beam energy is $E_i = 20.14$ meV. Note that intensity is not corrected.

Defining all quantities in terms of measured quantities, ΔE can be written as

$$\Delta E = E_i \left[\left(\frac{L_{TD} t_{CD}^e}{L_{CD} t_{CD}^e} \right)^2 - 1 \right] , \quad (3.20)$$

where L_{CD} , L_{CT} , and L_{TD} are the chopper-detector, chopper-target, and target-detector distances, respectively.

In transformation of the abscissa from t_{CD} to ΔE , the area under the given peak stays constant. Thus, the relative amplitudes of the peaks should be rescaled when the inelastic scattering probabilities are of interest. This scaling is simply given by the Jacobian of the transformation. Defining $f_t(t_{TD})$ to be the TOF spectra distribution of intensity and $f_E(\Delta E)$ to be the distribution as a function of energy shift,

$$f_E(\Delta E) = f_t[t_{TD}(\Delta E)] \frac{dt_{TD}(\Delta E)}{d(\Delta E)} , \quad (3.21)$$

and from Equation 3.18 the Jacobian is calculated to be

$$\frac{dt_{TD}(\Delta E)}{d(\Delta E)} = -\frac{t_{TD}^3}{L_{TD}^2} . \quad (3.22)$$

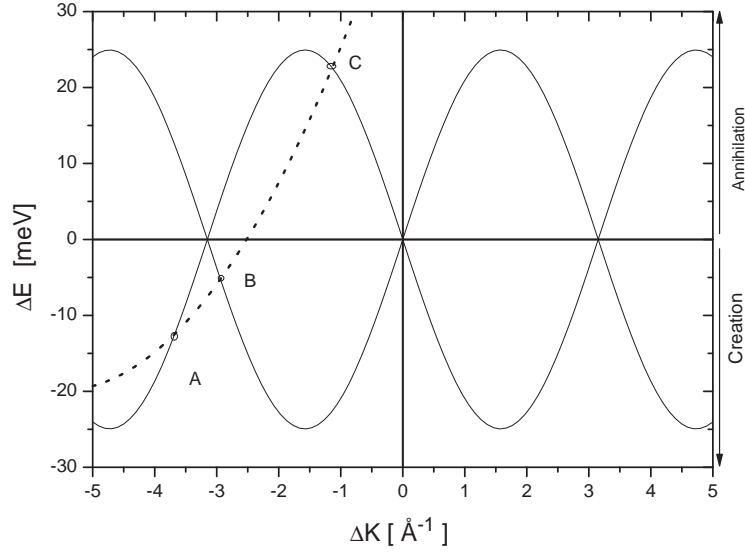


Figure 3.22: Dispersion relation of the Rayleigh mode and its intersection with the scan curve of the beam with an angle of $\theta_i = 61.48^\circ$ and energy of $E_i = 20.14$ meV. $L_{CD} = 2352$ mm and the chopper frequency is 300 Hz. There are three potentially observable peaks for this scan curve. Different scan curves reveal different points of the dispersion curve. In this way it is possible to probe the dispersion curve in the whole Brillouin zone. In most studies the incident angle is changed in small steps to get the entire picture of the dispersion curve.

Similarly, in order to get the momentum gain/loss of the scattered atoms ΔK given as

$$\Delta K = k_i \left[\frac{t_{TD}^e \sin \theta_f}{t_{TD}} - \sin \theta_i \right] . \quad (3.23)$$

In Figure 3.21, although, it is convention to transform the intensity by the appropriate Jacobian, the intensity was not corrected because the Jacobian function given in Equation 3.22 leads to a significant increase of the creation peak, which is already the dominating peak, and a suppressing of the elastic and annihilation peaks. The peaks in Figure 3.21 correspond to the energies of $\Delta E = -5.72$ meV and $\Delta E = 22.76$ meV, which mean that a phonon of energy ΔE is created and annihilated, respectively, by the scattering event. In Figure 3.22 the scan curve and sinusoidal approximation of dispersion curves of Rayleigh mode are sketched. The intersection points of the scan curve $S(\Delta \mathbf{K})$ and Rayleigh mode dispersion curve $D(\Delta \mathbf{K})$ determine the energies at which peaks are expected to appear in the energy spectrum measured for the given incident energies and angles. In this way, by repetitive measurements with different

angles of scattering or beam energies, namely different scan curves it is possible to plot the phonon dispersion curve in Brillouin zone. The intersection points of $S(\Delta\mathbf{K})$ and $D(\Delta\mathbf{K})$ in Figure 3.22 are

$$\begin{aligned} A(E,K) &= (-12.69 \text{ meV}, -3.69 \text{ \AA}^{-1}), \\ B(E,K) &= (-5.28 \text{ meV}, -2.94 \text{ \AA}^{-1}) \quad \text{and} \\ C(E,K) &= (22.70 \text{ meV}, -1.15 \text{ \AA}^{-1}) \end{aligned}$$

These values are in good agreement with the measured phonon energy value from energy-loss spectrum in Figure 3.22; $\Delta E = -5.72$ meV at point B, and $\Delta E = 22.76$ meV at point C, which is fairly observable with a broad and small peak. Point A is not observed in the energy-loss spectrum.

Resolution of the TOF Spectra: As seen in Figure 3.21 the resolution of the peaks deteriorates as the energy increases in the annihilation region. The resolution of the energy-loss spectrum is an important issue in the measurements of surface phonon dispersion curves and the optimization of the design of the He atom spectrometer and extensively discussed elsewhere [140, 150]. The total resolution is determined by both the time spread of the scattered beam pulse at the detector and finite angular resolution of the apparatus. The angular resolution and TOF resolution of the apparatus is coupled because of dispersive characteristics of phonon modes. Quite accurate analytical expressions for the energy and wave-vector resolution for the single phonon scattering case are derived including of both instrumental and kinematic smearing effects [150].

Since the primary concern here is the effectiveness of the apparatus as an inelastic phonon spectrometer, we will assume a nondispersive scattering mode. In this case the energy and angular resolutions decouple, so that we can draw some general conclusions concerning the energy resolution of phonon scattering. It is also necessary to note that this approximation may have dramatic errors in case of kinematic focusing which appears when the condition

$$\frac{\partial S}{\partial K} = \frac{\partial D}{\partial K} \quad , \quad (3.24)$$

is satisfied. In this case the resolution is greatly reduced by kinematic smearing effects [144].

The TOF width of the pulse that has undergone elastic scattering from the target has been discussed above. The contributions of chopper, detector and the beam spread also exist in the case of the inelastic scattering. The contribution from the chopper

shutter function is unchanged in this case

$$\Delta_C = \Delta_C^e \quad , \quad (3.25)$$

where the superscript e denotes elastic scattering. However there will be changes in Δ_D and Δ_B associated with phonon creation and annihilation, which are formulated as

$$\Delta_B = \Delta_B^e \left[\frac{L_{CT}}{L_{CD}} + \frac{L_{TD}}{L_{CD}} \left(1 + \frac{\Delta E}{E_i} \right)^{-3/2} \right] \quad , \quad (3.26)$$

$$\Delta_D = \Delta_D^e \left[1 + \frac{\Delta E}{E_i} \right]^{-1/2} \quad . \quad (3.27)$$

The effective energy resolution is then

$$\delta(\Delta E) = \frac{\partial(\Delta E)}{\partial t_{CD}} \Delta \quad , \quad (3.28)$$

leading to

$$\frac{\delta(\Delta E)}{E_i} = -2 \left(1 + \frac{\Delta E}{E_i} \right) \frac{\Delta}{t_{TD}^e} \quad . \quad (3.29)$$

Under these conditions the main contributions are Δ_C and Δ_B , and Δ_D is insignificant. Thus we can assume that instrumental contribution is constant which is given above as $\Delta_m = 18.1 \mu\text{s}$. So that the resolution of the peaks in Figure 3.21 are calculated as $\delta(\Delta E) = 0.58 \text{ meV}$ at $\Delta E = -5.72 \text{ meV}$ and $\delta(\Delta E) = 1.47 \text{ meV}$ at $\Delta E = 22.76 \text{ meV}$. The resolution is optimum in the creation side and it gets worse asymptotically in the annihilation side with the increasing phonon energy. Namely, the slower the atoms after the scattering event, the better resolution in energy-loss spectra. Note that the actual widths of the peaks will be larger than the values calculated above which indicate instrument-limited resolution. Finite angular resolution and dispersion of phonon modes reduce the ultimate resolution.

The resolution is not only the limiting factor in an inelastic scattering experiment. For instance, the time width of an inelastic scattering peak in the creation side increases dramatically with the energy of the created phonon that the peak becomes so broad as to not able to observed above background. In this case the TOF can be optimized by reducing the chopper frequency and increasing the chopper slit width, however at the expense of resolution in the annihilation side. There is always the trade-off between the resolution and the intensity with clever adjustment of the TOF parameters. The discussions above give some general considerations to be taken into account in inelastic experiments and some general conclusions concerning the energy resolution of single phonon scattering on LiF(001). More detailed discussion requires

a complicated analysis of momentum and energy resolution in case of the dispersive modes where TOF and angular resolution are coupled in which Monte Carlo simulation techniques may be simpler than analytic techniques [150].

Constant- \mathbf{Q} measurements, on the other hand, offers much simpler TOF data to understand and to compare with theoretical measurements. As discussed in Section 3.1 constant- \mathbf{Q} TOF measurements enable measuring phonons at a specific ΔK where energy and momentum are decoupled. In contrast to the parabolic scan curves where ΔK is unknown until ΔE is determined, the constant- \mathbf{Q} measurements have well defined ΔK values and observed peaks are well separated. The resolution in ΔK axis of the scan line can be expressed as

$$[\delta(\Delta K)]^2 = [\delta(k_i) \sin \theta_i]^2 + [k_i \cos \theta_i \Delta \theta]^2 \quad , \quad (3.30)$$

where $\delta(k_i)$ is the momentum spread of the incident beam and $\Delta \theta$ is the angular resolution of the apparatus. Similarly a simple energy resolution can be given as

$$[\delta(\Delta E)]^2 = [\delta(\Delta E_{TOF})]^2 + \left[\frac{\partial D}{\partial K} \delta(\Delta K) \right]^2 \quad , \quad (3.31)$$

where $\delta(\Delta E_{TOF})$ is the nondispersive TOF resolution as given in Equation 3.29.

3.2.3 Angular Scan Experiments

The dependence of the diffraction peak widths on the angle of incidence is determined by a variety of factors. The instrumental factors are non-zero incident beam divergence and detector aperture. In addition to these, the imperfections of the surface under investigation, such as finite domain size, random terrace distributions, and finite energy spread of the beam contribute to the broadening. The understanding of peak shapes is substantial to deconvolute the nonideal instrumental effects in both diffraction and inelastic experiments [125, 149, 151]. Additionally, from the measurement of peak broadening due to the finite domain size of the real surfaces actual domain size can be extracted when the instrumental broadening is known and if the *transfer length* (or coherence length) of the apparatus is in the same order with domain size of the surface of interest. The transfer length is defined as the pure instrumental broadening corresponding to the broadening from the same length of surface domains [151]. With a precise treatment of peak shapes average domain size, terrace width or even distribution of terrace widths can be determined [152–154]. An analytical description of the

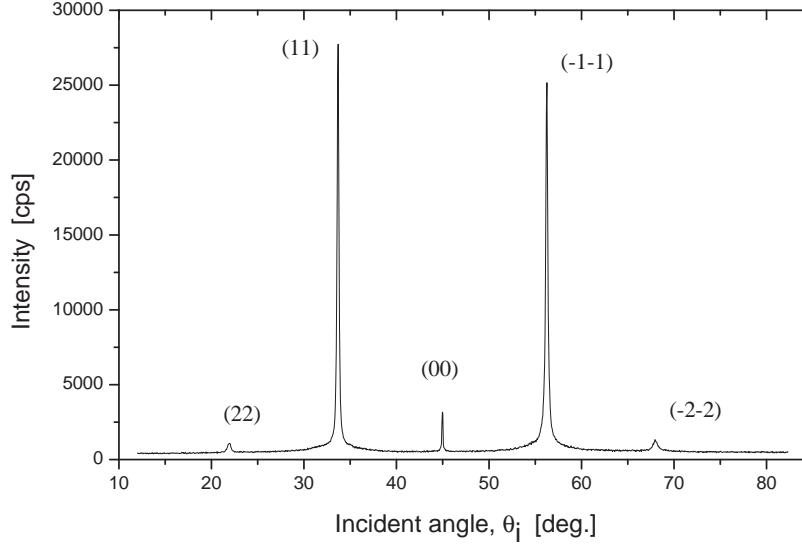


Figure 3.23: Typical angular distribution of diffraction peaks from LiF(001) in the $\langle 100 \rangle$ direction with He beam of 300 K and 100 bar. The slight discrepancy of the intensities of the symmetric diffraction peaks is due to the misalignment of the azimuthal angle. $\theta_{SD} = 90^\circ$.

widths of the diffraction peaks for the case where $\theta_i + \theta_f = 90^\circ$, is given as [125]

$$\Delta\theta = \left[(\delta_B \cot \theta_i)^2 + \left(\delta_B \frac{L_{ST}}{L_{TB}} \tan \theta_i \right)^2 + \delta_D^2 + \left(\frac{\Delta\lambda}{\lambda} \right)^2 (1 - \cot \theta_i)^2 + \left(\frac{\lambda}{d \sin \theta_i} \right)^2 \right]^{1/2} (1 + \cot \theta_i)^{-1}, \quad (3.32)$$

where δ_B is the incident beam divergence defined by the iris diameter, δ_D is the angle subtended by the detector aperture seen by the crystal, d is the average domain size and λ and $\Delta\lambda$ are, respectively, the mean value and the width of the distribution of the wavelengths of the incident atoms. Note that this formula defines the width of the polar angle for the case of a fixed source-detector angle geometry. Similar expressions can be written for azimuthal angle or moving detector peak widths [125]. In Equation 3.32 the factors contributing to the broadening are given, respectively, as beam divergence, spot size, the detector divergence, the energy spread of the beam, and average size of the terraces on the surface.

In Figure 3.23 an angular distribution of the diffraction intensities from LiF(001) along the $\langle 100 \rangle$ azimuthal direction is shown. The dominating structures are the elastic diffraction peaks. The specular intensity in Figure 3.23 is significantly lower than the first order diffraction peaks which is in accordance with theoretical results [144]. In Table 3.5, the peak positions and the peak widths from a scan with the source

Table 3.5: The measured and expected widths of specular and diffraction peaks with a beam of $k_i=11.23 \text{ \AA}^{-1}$ and $S=94$ ($\Delta\lambda/\lambda=1.76\%$).

Peak (m,n)	θ_i	$\Delta\theta(\text{Exp.})$	$\Delta\theta(\text{Theo.})$
(-2,-2)	21.83°	0.43°	0.44°
(-1,-1)	33.65°	0.22°	0.22°
(0,0)	45.00°	0.12°	0.12°
(1,1)	56.33°	0.27°	0.25°
(2,2)	68.14°	0.52°	0.47°

conditions of 100 bar and 300 K are listed. The iris diameter, R_I is 1 mm and the corresponding beam divergence is 0.050° . In the last column the predicted peak widths from Equation 3.32 are listed, assuming the domain sizes are very large with respect to wavelength of beam. Attention should be paid when defining the detector aperture. Although the diameter of the detector aperture is 6.7 mm the effective ionization width is narrower than the diameter of the detector aperture as mentioned in Section 3.1.7.

Elastic diffraction peaks are very sensitive to the beam energy broadening, especially at higher orders. The specular peak width is limited by the absolute resolution of the apparatus. In the current collimation, the greatest factor contributing to the resolution is the detector aperture, where in case of infinitely narrow beam, the specular peak width would have been 0.108° .

The instrumental resolution of the apparatus can be increased by inserting collimation slits defining the beam divergence and detector angle. For high resolution experiments two slits of 0.2 mm are provided before the target and in the detector arm (see Figure 3.4). The detector slit is installed in DPS-3 in order to prevent diffused He background of the beam stopped by the slit. By inserting the two slits the transfer length of the apparatus is increased to 2000 \AA enabling to measure large terrace widths.

3.3 Conclusions

In this chapter the recently built high resolution beam apparatus is presented. The details of basic functional units are provided. The capabilities of the apparatus for studying elastic and inelastic experiments have been demonstrated. The experiments

have shown that, the current status of the apparatus is good enough to carry out surface characterization experiments. Some of the many advantages of having a rotatable detector angle are shown. The in situ characterization and calibration of the TOF system are demonstrated.

In case of not sufficient resolution for inelastic scattering, chopper frequency can be increased and slit width can be reduced. Target-detector length can be easily increased by 27 cm that also improves the instrumental resolution. Magie-2 is not optimized to carry out inelastic phonon scattering. Although it has rather long source-target and chopper-target length, which reduce the intensity. The source-target can be shortened without many disturbances by removing the iris or shortening the chopper chamber.

The required angular resolution can be changed with iris and for extreme angular resolutions the micro-slits can be used which enhance the transfer length up to 2000 Å. This high angular resolution feature will be utilized in Chapter 6. The movable detector angle feature will be used to investigate the dependence of the diffraction and rotational transitions of the D_2 -LiF(001) on the incident angle in Chapter 7.

4. Characterization of the Molecular Beams

Free-jet expansion sources provide molecular beams of high intensity and well-defined energy, which makes them an important tool for atomic and molecular physics and surface science. The continuum-jet expansion of molecules from a high-pressure gas source into a low-pressure ambient background leads to a nearly complete conversion of the source enthalpy into directed flow energy resulting in beams with extremely low internal temperatures. Consequently, atomic beams have high speed ratios (narrow velocity distributions), and beams of molecules with few occupied rotational or vibrational states are attained. Under special conditions, weakly bound van der Waals complexes and clusters are formed in such beams. In this chapter, firstly, the fundamental concepts and the nature of supersonic-expansion sources are described. Then follows a description of the overall characteristics of the He and D₂ beams, which are used in the surface scattering experiments presented in the following chapters. The ideal free-jet expansion of atoms is introduced first and then the influence of real-gas effects is discussed briefly, leaving the details and deeper discussion to the literature [13, 155] and reviews [143, 156–159]. Expansions of diatomic molecules and the role of the relaxation of the internal degrees of freedom are illustrated for a D₂ beam expansion. The experimental results on clustering and condensation of a normal D₂ (n-D₂) beam are presented and discussed in the light of currently available theories.

4.1 General Properties of Supersonic Free-Jet Beams

The free-jet molecular beam is formed when a gas expands from a high-pressure source at pressure P_0 through a small nozzle of diameter d into a region of low pressure P_B . With $P_0 \gg P_B$, the gas is accelerated from the, so-called, stagnation state (P_0, T_0) , until it reaches the sonic speed (Mach number, $M=1$) at the narrowest point of the

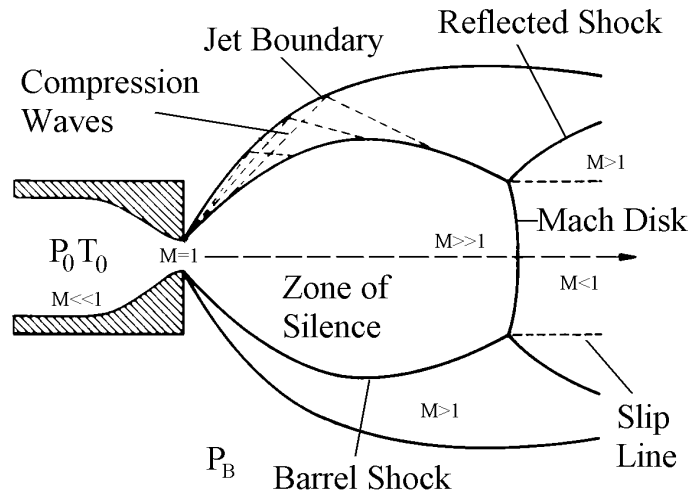


Figure 4.1: Continuum supersonic expansion of free-jet from P_0 into an ambient of low background pressure P_B [143].

nozzle and then expands with increasing velocity and decreasing gas density, at some distance, the flow changes from a continuum to a free-molecular flow without any further intermolecular collisions. In the process the enthalpy of the stagnant gas in the source is converted into translational energy according to the first law of thermodynamics. This results in a beam with a low internal temperature T and narrow velocity spread.

As the flow is in the supersonic regime it cannot sense the downstream external conditions immediately and at some point the gas overexpands and eventually must resolve this inconsistency with P_B via shock waves [160]. These thin areas of high pressure and temperature enclose the zone of silence, with the barrel shock at the sides and the Mach-disc shock normal to the centerline, as shown in Figure 4.1. The position of the Mach disc, x_M , is given by [161]

$$x_M = \frac{2}{3}d \left(\frac{P_0}{P_B} \right)^{1/2} . \quad (4.1)$$

Under the operating conditions of the present experiments, large pumps maintain $\frac{P_0}{P_B} \sim 10^8$, thus the Mach disk is located about a hundred millimeters downstream of the nozzle exit. At these large distances the pressure in the expanding gas is so low that the Mach disk does not exist. To reduce the gas load on the beam line vacuum the beam is extracted by using a conical skimmer. Thus the pressure in the next chambers

is sufficiently low to assure a long mean free path and the beam continues without significant attenuation from the collisions with the background gas. The shape and position of the skimmer is critical to prevent the formation of shock waves and the reflection of scattered beam molecules inside and outside of the skimmer wall into the centerline beam [158, 162–164]. Hence, the main features of the extracted centerline beam can be approximated as an isentropic expansion with negligible viscosity and heat conduction into the perfect vacuum. At some point the collisions cease to be important and the velocities and the ambient temperature said to be frozen in.

For an isentropic ideal-gas expansion it is possible to compute the flow rate at the narrowest point of the source nozzle which is ideally also the sonic point where $M=1$. The flow rate at the exit is $\dot{m} = \rho u A$, where ρ is the gas density, u is the velocity and A is the area of the exit. Using thermodynamical relations of an isentropic expansion, one can express the flow rate (number of molecules per second) as a function of source conditions as [165]:

$$\dot{N} = F(\gamma)n_0\sqrt{\frac{2kT_0}{m}}\left(\frac{\pi d^2}{4}\right) \quad , \quad (4.2)$$

where T_0 is the source temperature, n_0 is the gas density in the source ($\frac{P_0}{kT_0}$) and $F(\gamma)$ is a constant given as 0.513 and 0.484 for monatomic and diatomic gases, respectively. The ideal free-jet centerline intensity per steradian can be expressed in terms of the flow rate and a peaking factor, κ as

$$I_0(\text{molecules /s} \cdot \text{sr}) = \frac{\kappa}{\pi}\dot{N} \quad , \quad (4.3)$$

where κ is 2.0 and 1.47 for monatomic and diatomic gases, respectively, for a sharp-edged orifice [165]. For an ideal effusive source, in which the mean free path in the source is greater than the nozzle dimensions, the peaking factor is 1.0. Another useful quantity is the throughput of the source, which needs to be considered for the selection of the source-chamber pump and the estimation of the background pressure, and using Equation 4.2 is given by

$$\Phi(\text{torr} \cdot \text{l/s}) = C \cdot \left(\frac{T_c}{T_0}\right) \sqrt{\frac{300}{T_0}} P_0 d^2 \quad , \quad (4.4)$$

where T_c is the temperature of the source chamber and C is a constant which is 45 and 42 ($\text{l}\cdot\text{cm}^{-2}\cdot\text{s}^{-1}$) for He and D_2 , respectively [143].

The main advantages of the nozzle molecular-beam technique are that it provides higher intensities and narrower velocity distributions in comparison with the effusive sources. As given in Equation 4.3, the peaking factor of the nozzle beams are at best

Table 4.1: The centerline Mach-number and speed-ratio correlation parameters for different γ s. d is the effective source-orifice diameter. ^afrom ref. [161]; ^bfrom ref. [167]; ^cfrom ref. [165].

γ	x_0/d ^a	A ^a	B ^b	α ^c	β ^c	c_2 ^d	c_3 ^d	ν_2 ^d	ν_3 ^d
5/3	0.075	3.26	3.22	0.527	0.545	0.0465	0.00630	11/9	23/9
7/5	0.4	3.65	3.64	0.783	0.353	0.0655	0.00785	17/15	41/15
9/7	0.85	3.96	3.95	1.022	0.261	0.0150	0.00051	23/21	59/21

two times higher than that of the effusive-beam sources. The high intensity reached by free-jet sources is because it enables one to operate at very high P_0d values. For the high speed-ratio feature of the nozzle beam, a deeper inspection into the details of the expansion process is needed. Just after the nozzle exit as the jet expands molecules move with increasing Mach number along divergent hyperbolic paths. As a result the density of the gas and the collision frequency drops rapidly. The earlier continuum region of the expansion can be treated as an isentropic expansion in thermodynamic equilibrium, and beam density, Mach number, beam temperature and collision rates can be calculated with the following equations [166]:

$$\frac{T}{T_0} = \left(1 + \frac{\gamma - 1}{2} M^2\right)^{-1}, \quad (4.5)$$

$$u = M \sqrt{\frac{\gamma k T_0}{m}} \left(1 + \frac{\gamma - 1}{2} M^2\right)^{-1/2}, \quad (4.6)$$

$$\frac{P}{P_0} = \left(1 + \frac{\gamma - 1}{2} M^2\right)^{-\gamma/(\gamma-1)}, \quad (4.7)$$

$$\frac{n}{n_0} = \left(1 + \frac{\gamma - 1}{2} M^2\right)^{-1/(\gamma-1)}, \quad (4.8)$$

where u is the beam velocity and M is the Mach number defined as

$$M = \frac{u}{\sqrt{\gamma k T / m}}. \quad (4.9)$$

Hence, once M is known, all thermodynamical properties of the beam can be determined. The centerline Mach number in the region between the source and the first shock wave can be calculated by the method of characteristics (MOC) as [161]

$$M = A \zeta^{\gamma-1} - \frac{1}{2A} \frac{\gamma + 1}{\gamma - 1} \zeta^{\gamma-1}, \quad (4.10)$$

where ζ is the reduced distance from the source given by

$$\zeta = \frac{x - x_0}{d} . \quad (4.11)$$

The constants x_0 and A are listed in Table 4.1. This equation is based on the assumption that far out in the expansion, the streamlines of the beam are straight and appear to be originating from a point source at x_0 . Knuth suggested [167] a simpler expression for the Mach-number from either interpolating or extrapolating the MOC results for large M numbers as

$$M = B \cdot \left(\frac{x}{d}\right)^{\gamma-1} , \quad (4.12)$$

where B is listed in Table 4.1. The speed-ratio is related to the Mach-number and internal temperature of the beam, T with

$$S = \sqrt{\frac{\gamma}{2}} M = \sqrt{\frac{mu^2}{2kT}} . \quad (4.13)$$

Experimentally it is frequently possible to determine only the parallel temperature, namely the velocity distribution parallel to the beam direction by TOF and is related to the speed ratio as given in Equation 3.17.

At some point in the expansion, the mean free path becomes large compared to the dimension of the expansion. As a result the kinetic processes which depend on the collision frequency first decrease and finally cease. Since the thermodynamic properties of the beam along the centerline is known from the equations given above, the number of collisions experienced by a gas particle can be estimated. The average number of two-body collisions remaining in the expansion can be written as [168]

$$Z_2(x/d) = 1540 \cdot \sigma(T_0) \left(\frac{P_0 d}{T_0}\right) F_{LJ}^{(2)}(x/d, \gamma) , \quad (4.14)$$

and for three-body collisions given as

$$Z_3(x/d) = 8.39 \times 10^{-3} \cdot \sigma(T_0)^{5/2} \left(\frac{P_0^2 d}{T_0^2}\right) F_{LJ}^{(3)}(x/d, \gamma) . \quad (4.15)$$

Here the cross section σ , pressure P_0 , temperature T_0 and source diameter d are given in \AA^2 , torr, K, and cm, respectively. The collision integrals $F_{LJ}^{(2)}(x/d, \gamma)$ and $F_{LJ}^{(3)}(x/d, \gamma)$ are given for a Lennard-Jones potential as

$$F_{LJ}^{(2)}(x/d, \gamma) = c_2(\gamma)(x/d)^{-\nu_2} , \quad (4.16)$$

and

$$F_{LJ}^{(3)}(x/d, \gamma) = c_3(\gamma)(x/d)^{-\nu_3} , \quad (4.17)$$

where c_2 , ν_2 , c_3 and ν_3 are constants and given in Table 4.1.

An exact analysis of the transition from the continuum region to the collision-free molecular-flow region where the translational relaxation continues until the beam temperature and density decrease sufficiently, is not straightforward and requires the solution of the Boltzmann equation for a quantitative analysis [169]. The thermodynamic relations above hold for continuum flow in thermal equilibrium. In a useful approximation, the expansion is divided by a "quitting surface" into a continuum isentropic regime of thermodynamic equilibrium and a collision-free molecular-flow regime [165, 170].

Earlier theoretical works with classical models indicated that the terminal speed ratio is [165]

$$S = \alpha \left(\sqrt{2} \frac{P_0}{kT_0} d \left(\frac{53C_6}{kT_0} \right)^{1/3} \right)^\beta, \quad (4.18)$$

where the parameters α and β are given in Table 4.1. For He the onset of strong quantum effects, when the expanded gas is cooled below about 1 K, complicate the dependence of the speed ratio on P_0d [171, 172]. As P_0d increases the effect of the enhanced quantum cross-section leads to a significant divergence from the classical treatment and the achievable terminal speed ratios are significantly larger than for other species. The theory predicts that the speed ratio can increase to 700 if condensation does not occur [171]. Speed ratios greater than 1000 have been reported [173]. The experimental values [173] exceed the theoretically predicted values [171], probably due to the inadequacies in the interaction potential assumed in the calculations, since the speed ratio is extremely sensitive to the interaction potential.

An important point that must be considered in the free-jet design is the choice of the pump and the source diameter. The flux rate, Φ is limited by the pumping speed which is proportional to P_0d^2 (see Equation 4.4). Whereas speed ratio is proportional to P_0d . Thus, for maximum attainable speed ratio with a limited pumping speed, d must be as small as possible.

4.2 Characteristics of He Beams

As seen in the last section, the nozzle diameter is important not only for the intensity and flow rate of the source but also the speed ratio of the beam. Therefore, the effective nozzle diameter is an important quantity for comparison with theory. For instance it is assumed above that the flow reaches to the sonic speed at the nozzle exit. In fact,

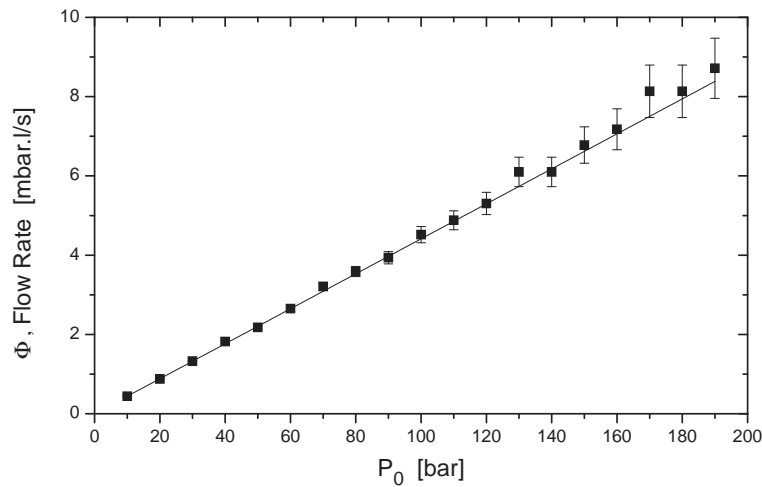


Figure 4.2: The flow rate measurement of He gas in a water tank at the temperature of 297 K. The error increases as the flow rate increases because the measured time to fill a certain volume decreases. The calculated effective orifice diameter is $9.9 \pm 0.4 \mu$.

this is true only for an ideal converging nozzle and, although we keep on using the term nozzle, the source used in this work is a sharp-edged orifice. Pitot tube studies with different types of source geometry have shown that while a short converging source provides a nearly uniform, ideal, planar sonic surface at the exit, a sharp-edged orifice presents a convex surface at a distance of $x/d \sim 0.25$ from the exit along the centerline [174]. Secondly, the effective orifice diameter is slightly reduced because of boundary layer effects in the entry section [161].

The effective diameter of the source can be determined by flow rate measurements. The flow rate is measured with the nozzle outside the vacuum chamber by connecting a tube to the nozzle and inserting the other end of the tube into a water tank. The flow-rate through the nozzle at a constant pressure was determined by measuring the time to replace a certain volume of water. In Figure 4.2 the measured flow-rate values at different source pressures are plotted. Using the slope of the curve in the figure and Equation 4.4 the effective nozzle diameter is calculated as $9.9 \pm 0.4 \mu$. It is slightly less than the nominal nozzle diameter (10μ) as expected. However, the difference is small and the error bars are large; hence, we will keep on using the nominal diameter as the effective diameter.

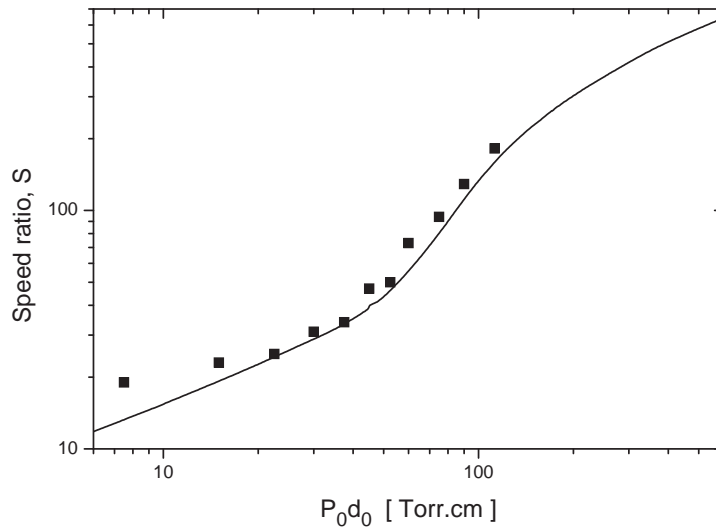


Figure 4.3: The measured and calculated speed ratios of He beam at $T_0=300$ K as a function of $P_0 d$. The calculated data (solid line) is from ref. [175].

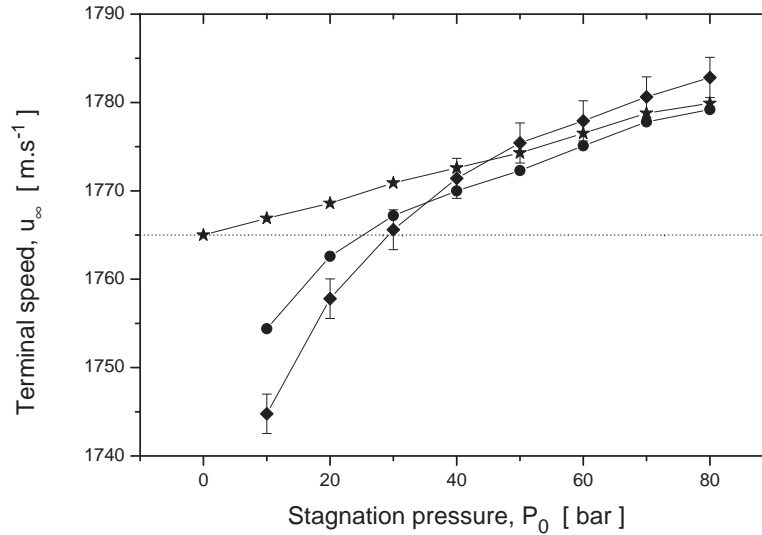


Figure 4.4: The pressure dependence of the measured and calculated terminal velocities of a He beam with $T_0=300$ K. The measured beam speed ($-\diamond-$) is compared with calculated terminal velocities of the ideal-gas expansion from Equation 4.19 (dotted lines) and real gas expansion from $u = \sqrt{2H_0/m}$ ($-\star-$) and from Equation 4.21 ($-\bullet-$). $d=10 \mu$. $P_B=2.3 \times 10^{-4}$ - 2.0×10^{-3} mbar.

In Figure 4.3 the speed ratios of He beam measured here are compared with predicted values [171] as a function of P_0d . As P_0d increases, the enhanced speed ratio due to the increased quantum cross section becomes evident. The measured speed ratios are systematically larger than the theoretical values. The reason is that we assumed that the terminal velocity distribution is Maxwellian. However, the terminal velocity distribution has a long tail and can be described more precisely with a sum of two Boltzmann distributions, hence with two different speed ratios [176, 177]. For a better approximation the weighted-average of two speed ratios can be used in order to compare the theory and experiment with a better precision [178]. The reason of a beam with two families of particles with different temperatures, so called "bimodal distribution", is attributed to the strong collision energy dependence of the cross section [178]. Since colder atoms experience larger cross sections, they expand faster and thus become colder.

As seen in Equation 4.5, with increasing Mach number the internal temperature of the beam approaches zero and the beam velocity reaches (see Equation 4.6) the value of

$$u_\infty = \sqrt{\frac{2\gamma kT_0}{(\gamma - 1)m}} \quad . \quad (4.19)$$

This is the highest achievable terminal velocity of an ideal gas and a good approximation for high P_0d values.

The terminal velocity of the beam can be described with the energy balance. The total energy of beam takes the form

$$H_0(P_0, T_0) = \frac{1}{2}mu^2 + \frac{3}{2}kT_{\parallel} + kT_{\perp} \quad , \quad (4.20)$$

where H_0 is the enthalpy of a molecule in the source, and u , T_{\parallel} and T_{\perp} are beam velocity, the parallel and perpendicular temperature of the beam at any point in the expansion, respectively. At large distances downstream, the perpendicular temperature becomes negligibly small due to the geometrical cooling and some authors ignore it in the energy balance [179]. A better approximation is to set the perpendicular temperature $T_{\perp} = T_{\parallel}$, which is valid for the sudden freeze point, since further cooling of T_{\perp} does not contribute to the parallel speed and temperature [170, 172, 180]. Using Equation 4.13 and 4.20, the terminal beam velocity can be expressed in terms of measured speed ratio as

$$u_\infty = \sqrt{\frac{2H_0}{m}} \left[1 + \frac{5}{2}S^{-2} \right]^{-1/2} \quad . \quad (4.21)$$

Note that for ideal gas enthalpy and very large speed ratios this equation is reduced to Equation 4.19.

In Figure 4.4 the pressure dependence of the terminal beam velocity for the stagnation temperature of 300 K is provided. In the figure the terminal velocities according to Equation 4.21 are plotted for infinite and actual speed ratios. Since the enthalpy and the speed ratio of the He beam increase with increasing pressure, the terminal velocity increases. The realistic enthalpy values are taken from the ref. [175]. The calculated and measured values agree well at high pressures. The discrepancy at low pressures can be explained in addition to errors from the approximate definition of speed ratio and stagnation temperature, with highly complicated realistic effects, such as perpendicular temperature, viscosity and thermal conductivity effects, source geometry, skimmer effects, etc. Nevertheless the error is less than 0.5%.

In Figure 4.5 the dependence of the intensity on the vertical and horizontal positions of the nozzle with respect to the skimmer are shown. The intensities are constant across the skimmer. As the skimmer diameter is small (400 μ) with respect to the nozzle-skimmer distance (10 mm), the offset angle of the beam from the centerline is only 20 mrad and can be neglected. As mentioned above the peaking factor of the free jet sources is only about two and the angular density distribution is a broad $\cos^2(\theta)$ distribution [161,170]. The width of the slope in the figure is defined by the collimation and the diameter of the sudden freeze zone. The symmetric and well behaving intensity profiles in the figure ensure the nonexistence of clogging and misalignment problems. In earlier experiments asymmetric intensity profiles were observed and it turned out to be due to the misalignment of an aperture downstream.

In Figure 4.6 the beam intensity as a function of the nozzle-skimmer distance from 2 mm to 15 mm for the stagnation temperatures of 297 K and 96 K is shown. When the nozzle approaches the skimmer the intensities increase first, but when it gets too close to the skimmer, beam-skimmer interactions become significant and the intensity drops. Ideally, the measured beam intensity (beam density at the detector) is proportional linearly to the beam density at the skimmer entrance, which is proportional inversely to the square of the nozzle-skimmer distance, X_{NS} . The exact prediction of measured intensity is highly complicated and depends on many other factors such as skimmer interferences, Mach-number focusing, and background attenuation. Several models have been developed to predict the measured intensities which are valid at different and only limited operating conditions [156, 162, 181]. At large nozzle skimmer-distances the skimmer interference is rather minimal and inverse-square dependence of the intensity on the X_{NS} is valid. In addition to this, there is also the attenuation of the

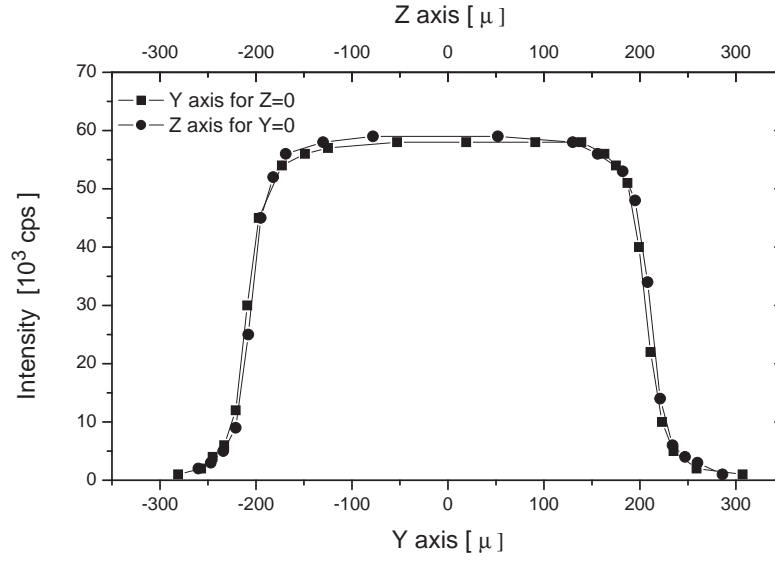


Figure 4.5: The beam intensity dependence of He beam on nozzle position in horizontal (y-axis: squares) and perpendicular (z-axis: circles) directions. The diameter of the skimmer orifice, $d_s=400 \mu$. $d=10 \mu$. $P_0=100$ bar, $T_0=297$ K. $X_{NS}=10$ mm. $P_B=2.2 \times 10^{-3}$ mbar. $S=79$.

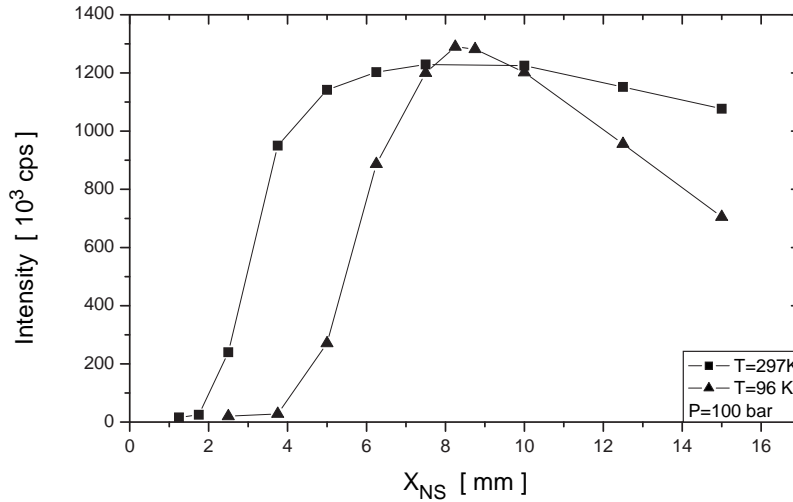


Figure 4.6: The dependence of the intensity of He beam on nozzle-skimmer distance at two different source temperatures. For $T_0=96$ K (triangles), $P_B=3.2 \times 10^{-3}$ mbar and for $T_0=297$ K (squares), $P_B=2.2 \times 10^{-3}$ mbar. $P_0=100$ bar. $d=10 \mu$.

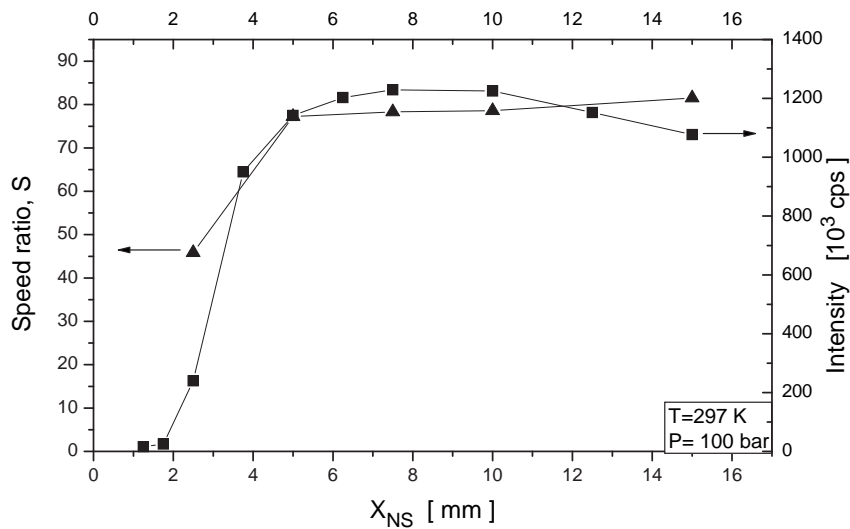


Figure 4.7: Speed ratio (triangles) and intensity attenuation (squares) of He beam due to the nozzle-skimmer distance. $P_0=100$ bar, $T_0=297$ K. The conditions are same as in Figure 4.6.

beam at large X_{NS} distances due to the background scattering. In Figure 4.6 the decrease of the intensity with increasing X_{NS} for the cooled beam is steeper than for the room temperature because the background pressure is higher and the average beam velocity is smaller. The background gas attenuation simply obeys Beer's law but the effective total collision cross section needs a careful consideration [182]. In Figure 4.7 the dependence of the measured speed ratio on the nozzle-skimmer distance is shown. The attenuation of the speed ratio is similar to the attenuation of the intensity. At large distances, there is no effect of skimmer interference on the speed ratio and it remains nearly constant. The background attenuation has also no effect on the speed ratio. This is obvious that the scattering processes mostly remove the atoms out of the central beam without affecting the velocity distribution of the rest beam.

The skimmer interference is the main problem to be avoided in beam experiments. There are different approaches adopted to correlate the skimmer interference with the beam parameters. It has been shown that the skimmer interferences are negligible if the Knudsen number at skimmer entrance, $Kn_s = \lambda/d_s > 2$ [183], where d_s is the diameter of the skimmer and λ is the mean free path of the He atoms in the beam at the skimmer entrance and can be calculated by using the isentropic beam expansion equations

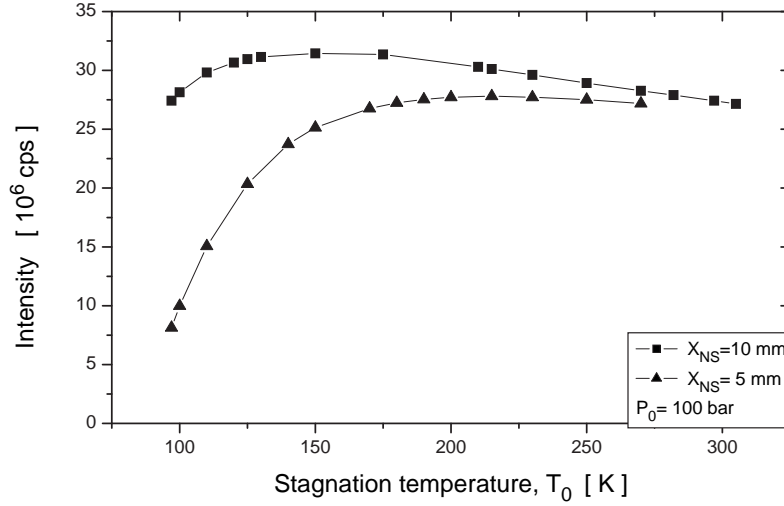


Figure 4.8: Stagnation temperature dependence of He beam intensity. $P_0=100$ bar. $X_{NS}=10$ mm (squares), $X_{NS}=5$ mm (triangles). $d=10 \mu$. The diameter of the iris is 1.0 mm. The intensities are corrected according to the normal operating conditions of the detector (see Section 3.1.7).

given above. At the nozzle-skimmer distances where the intensities tend to decrease significantly for the stagnation temperatures of 297 and 96 K, the Knudsen number at skimmer entrance is equal to 5 and 4, respectively. An exact correlation requires involving specific geometry of the skimmer. As a second approach [184,185], it has been found that the skimmer-induced increase in perpendicular temperature is negligible when Kn_s/M_s is greater than 0.3. Here M_s is the Mach number at the skimmer entrance. In our case, at the skimmer distances where skimmer-induced intensity loss become significant when $Kn_s/M_s=0.03$ (for 297 K at 5 mm) and $Kn_s/M_s=0.02$ (for 96 K at 8 mm).

In Figure 4.8 the dependence of the beam intensity on the source temperature for a given source pressure and for two nozzle-skimmer distances is shown. Note that the flow rate is inversely proportional to the square-root of the stagnation temperature (see Equation 4.2) and the efficiency of the detector is inversely proportional to the beam speed (see Section 3.1.7); thus measured intensity should be inversely proportional to the stagnation temperature. However, due to the increasing background scattering and skimmer interference with decreasing temperature, this is not observed in Figure 4.8.

On the other hand, with a careful choice of the nozzle-skimmer distance it is possible to have a beam which is insensitive to operating conditions. This is the main advantage of using diffusion or turbomolecular pumps and operating at low background pressures which is referred to as Fenn type of source [162]. A low cost alternative of this source is the so-called Campargue source, which operates at high background pressures [158]. The main disadvantages of this the Campargue sources, are the critical design of the skimmer, high sensitivity of operating conditions and the requirement of one extra differential pumping stage.

The nozzle-skimmer distance of 10 mm is preferred for surface scattering experiments and Figure 4.8 serves as a reference data for estimating the exact reflection from surfaces in the following chapters. Therefore the measured intensities in Figure 4.8 are corrected for the normal operating conditions of the detector as given in Section 3.1.7, although the measurements provided in Figure 4.8 like all direct ($\theta_{SD}=180^\circ$) beam experiments were carried out with a reduced detector efficiency (see also Section 3.1.7).

4.3 Internal Relaxation and the Overall Characteristics of n-D₂ Beam

In the free-jet expansion of polyatomic gases the internal degrees of freedom must be considered. Since the temperature of the gas, T , rapidly cools and becomes much lower than T_0 vibrational and rotational degrees of freedom relax as long as the internal degrees of freedom remains in contact with the translational thermal bath. The extent of the coupling between the internal and translational temperatures will depend on the number of collisions needed for relaxation and the number of collisions undergone by a molecule during the expansion until the collisions become infrequent and the vibrational and rotational relaxation processes are frozen in. The rate of rotational cooling can be approximated by a linear relaxation model which states that the rate of cooling from the rotational temperature T_R to the translational temperature T is given by [186]

$$\frac{dT_R}{dt} = -\frac{T - T_R}{\tau} \quad , \quad (4.22)$$

where τ is the relaxation time which can be replaced by $Z_R \cdot \tau_{hs}$, where τ_{hs} is the average time between the collisions of hard sphere molecules and Z_R is the adjustable parameter to be determined and represents the number of hard sphere collisions required for

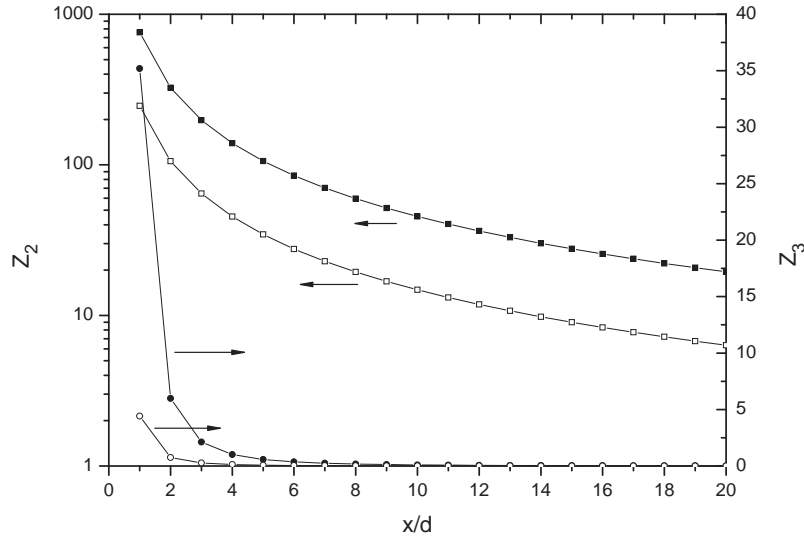


Figure 4.9: The number of two-body (squares) and three-body (circles) collisions remaining in the expansion versus reduced distance along the beam centerline for D₂ by using Equations 4.14 and 4.17. Legend: For P₀=120 bar and T₀=300 K, Z₂: -■-, Z₃:-●-. For P₀=10 bar and T₀=108 K, Z₂: -□-, Z₃:-○-. $\gamma=5/3$. $d=10 \mu$. $\sigma(T_0) = 1.89\pi r_m^2 (\varepsilon/T_0)^{1/3}$, where $\varepsilon=38$ K and $r_m=3.44 \text{ \AA}$.

energy transfer from rotational energy quantum into the translational energy. The use of isentropic equations decouples the kinetics from the flow properties. Then the first part of Equation 4.22 can be replaced by $u(dT_R/dx)$ where u is the flow velocity and x is the distance along the streamline. This equation can then be integrated in terms of the isentropic expansion defined with Equations 4.5-4.11. From the measured terminal rotational temperatures Z_R values can be calculated with this model. If the relaxation is efficient then the beam density, temperature, and velocity can be approximated with isentropic equations for a fully relaxed diatomic gas with $\gamma=7/5$. Since in the case of H₂ or D₂, the relaxation is inefficient, the expansion can be treated as a monatomic gas [187]. A better approximation is to couple the relaxation and the flow properties. In this case the energy balance is adjusted at each energy step and the deviation from the isentropic equations is taken into account [179, 188].

In Figure 4.9 the number of remaining two-body and three-body collisions of a D₂ expansion are plotted as a function of reduced distance (x/d) for two stagnation conditions. As seen in the figure the significant part of the collisions occurs within a few

Table 4.2: Rotational and vibrational energy values of the H₂, HD and D₂ molecules. The rotational and vibrational energy levels are expressed as $E_J = k\theta_R J(J + 1)$ and $E_\nu = \hbar\omega_0(\nu + 1/2)$, where θ_R is the characteristic rotational temperature and ω_0 is the vibrational eigenfrequency. [189]. Z_R is the collision number for rotational relaxation in the room temperature beam [187,190].

J	n-H ₂ (meV)	HD (meV)	n-D ₂ (meV)
0	0.00	0.00	0.00
1	14.69	11.06	7.41
2	43.94	33.11	22.20
3	87.47	66.00	44.29
4	144.90	109.51	73.60
$\hbar\omega_0$	545.7	472.8	386.3
θ_R	85.4 K	64.2 K	43 K
Z_R	300	30	150

diameters of the source. With increasing (x/d) the collision rates decrease rapidly. The total number of binary collisions experienced during the expansion is typically of order of 10^2 to 10^3 . Hence, any kinetic process which requires this number of collisions (Z_R) will relax and approach equilibrium. Large polyatomic molecules generally have much smaller vibrational relaxation numbers of only 1-10 collisions and so that for these molecules vibrational cooling will be almost complete [179]. Rotational relaxation is usually much faster due to the smaller energy level spacing. For H₂, D₂, and HD, where the rotational energy spacing is the largest compared to all other molecules, at room temperature about 300, 150, and 30 collisions are required for rotational relaxation, respectively [187,190]. In Table 4.2 the rotational energy levels of hydrogenic molecules are listed. Note that there is a direct correlation between the energy level spacings and the collision number for rotational relaxation. Besides the smaller level spacings due to the allowed transitions between the odd and even levels, the rotational relaxation of the HD is favored by the displacement of the center of mass from the geometrical center of the molecule. Since the first vibrational energy levels for hydrogenic molecules are relatively high (see Table 4.2), the vibrational relaxation of a small diatomic like hydrogen requires around 10^4 collisions and thus, the amount of vibrational cooling will be negligibly small [191].

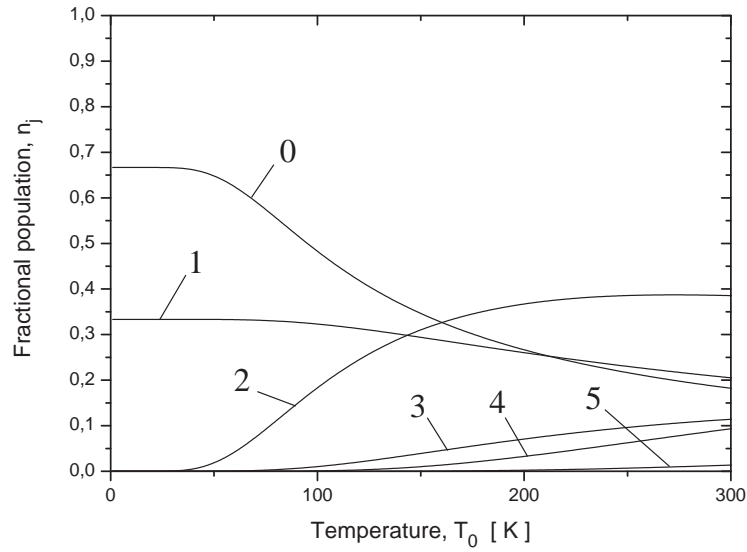


Figure 4.10: Fractional populations of rotational levels for n-D₂ as a function of temperature. n-D₂ (2/3 o-D₂ + 1/3 p-D₂).

The rotational temperatures of the H₂ and D₂ beams can be determined experimentally either by measuring the populations of the rotational states [192–194] or by estimating the final rotational energy remaining in the molecules by comparing the measured final velocity distributions of the beam [186, 187, 190, 195]. Similar to the atomic case discussed previously, energy balance can be expressed for molecules in the adiabatic expansion by

$$H_0 = \frac{1}{2}mu_\infty^2 + \frac{5}{2}kT_\infty + E_{R\infty} \quad , \quad (4.23)$$

where H_0 is the enthalpy of the gas at the source, u_∞ is the terminal beam velocity, T_∞ is the terminal translational temperature and $E_{R\infty}$ is the terminal rotational energy of the beam. For ideal diatomic gas H_0 is $\frac{7}{2}kT$ and E_R is kT . However, this is only valid when $T \gg \theta_R$, where θ_R is the characteristic rotational temperature of the molecule. This is not the case for hydrogenic molecules in the medium temperature range which have large rotational temperatures as seen in Table 4.2. At equilibrium the average rotational energy of the molecules at a temperature of T is given by

$$E_R(T) = \sum_{J=0}^{\infty} E_J n_J(T) \quad , \quad (4.24)$$

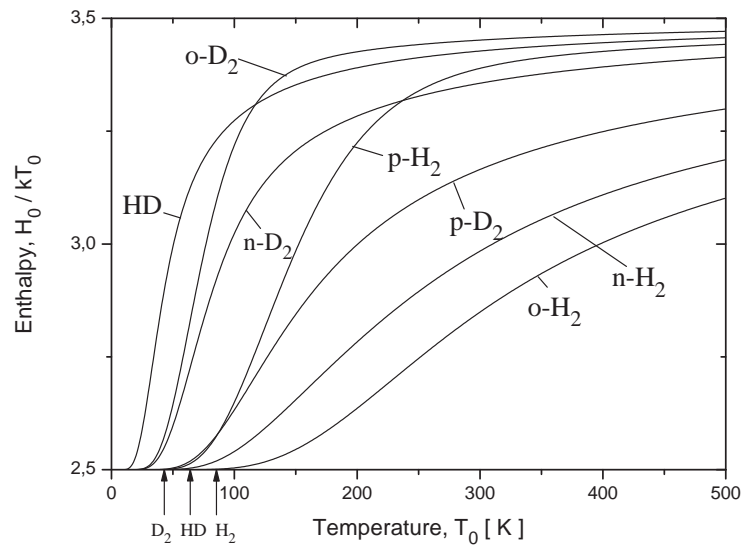


Figure 4.11: The reduced enthalpies (H_0/kT_0) of different species and forms of hydrogenic molecules as a function of temperature. The upper and lower y-axes correspond to the values of ideal diatomic ($7/2$) and monatomic gases ($5/2$), respectively. Arrows indicate the characteristic rotational temperatures.

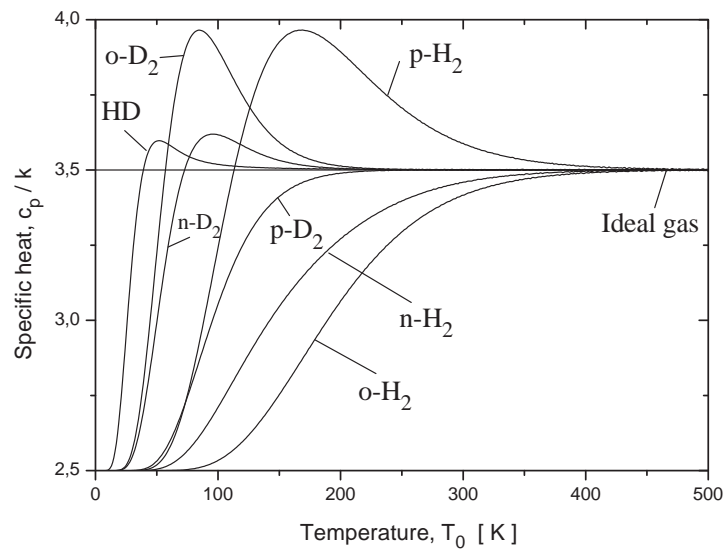


Figure 4.12: Specific heats of hydrogenic molecules as a function of temperature. Ideal diatomic gas ($7/2$) is plotted with a straight line. The lower y-axis corresponds to the value for ideal monatomic gas ($5/2$).

where n_J is the fractional population of the molecules in the rotational level J given by [196]

$$n_J = \frac{(2J+1) \exp[-E_J/kT]}{\sum_{J=0}^{\infty} (2J+1) \exp[-E_J/kT]} \quad . \quad (4.25)$$

For n-D₂ (n-H₂) the average rotational level populations $n_J^{(n)}$ must account for the different contributions of the ortho and para species. The statistical weights of p-H₂ (J=even) and o-H₂ (J=odd) are 1/4 and 3/4; and of p-D₂ (J=odd) and o-D₂ (J=even) are 1/3 and 2/3, respectively¹. Thus average rotational level populations for n-D₂ (n-H₂) become

$$n_J^{(n)} = 2/3(3/4)n_J^{(o)} + 1/3(1/4)n_J^{(p)} \quad . \quad (4.26)$$

Here E_J in Equation 4.25 is defined with the lowest allowed rotational level. In Figure 4.10 the fractional populations (or occupation probability) of the rotational levels for n-D₂ as a function of temperature are shown. Note that at low temperatures almost only the lowest energy levels are occupied.

The enthalpy of the gas in the source reservoir, H_0 is the sum of translational energy and rotational energy. The latter can be now easily calculated by using Equation 4.24, and thus

$$H_0 = \frac{5}{2}kT_0 + E_R(T_0) \quad . \quad (4.27)$$

The enthalpies of different hydrogenic gases as a function of temperature are plotted in Figure 4.11. Similarly the specific heat can be expressed as

$$c_P = \frac{5}{2}k + k(dE_R/dT) \quad , \quad (4.28)$$

and is plotted in Figure 4.12. As seen in both figures, the molecules have for $T_0 < \theta_R$ monatomic like behavior and for $T_0 \gg \theta_R$ diatomic like behavior.

In Figure 4.13 the measured terminal velocity of the n-D₂ beam as a function of stagnation pressure at 300 K is shown. The solid line shows the maximum velocity, namely the case where the whole initial enthalpy (obtained from Figure 4.11) converted into the directed flow energy. The difference between the maximum and actual velocity is due to the rotational and random translational energy of the beam and it decreases with increasing stagnation pressure. The speed ratio of the D₂ beam as a function of pressure is plotted in Figure 4.14. Note that the cooling rate of D₂ molecule through supersonic expansion is relatively weak in comparison to He atom. At room temperature and 120 bar He beam reaches a speed ratio of S=129 while D₂ has S=41.

¹HD has no ortho- or para-form so that all transitions are allowed and Equation 4.25 is sufficient.

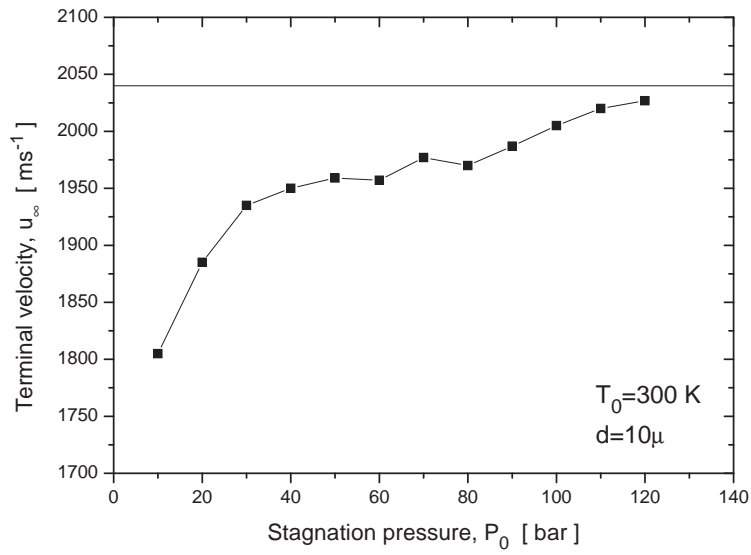


Figure 4.13: The terminal velocity of D_2 beam versus stagnation pressure. Solid line shows the maximum terminal velocity $u = \sqrt{2H_0/m}$. $T_0=300$ K , $d=10 \mu$.

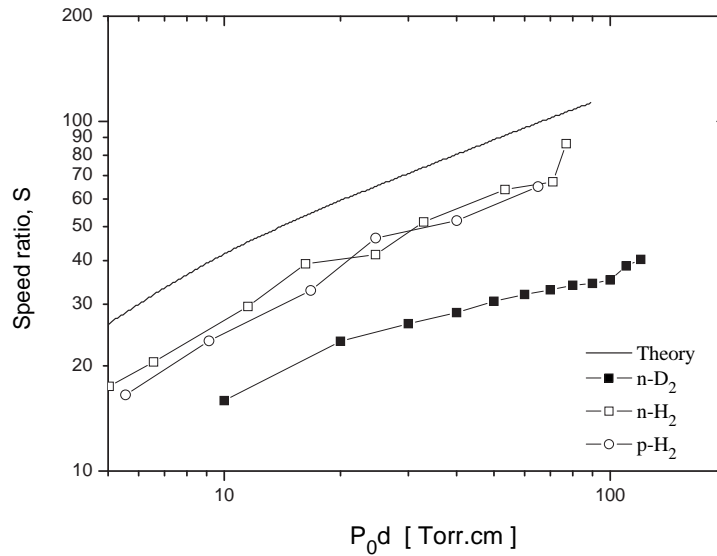


Figure 4.14: Speed ratio of D_2 beam as a function of $P_0 d$ (-■-) for $T_0=300$ K, $d=10 \mu$. Speed ratios of n- H_2 (-□-) and p- H_2 (-○-) for $T_0=293$ K, $d=5.6 \mu$ and calculated speed ratio without rotational relaxation (solid line) [195].

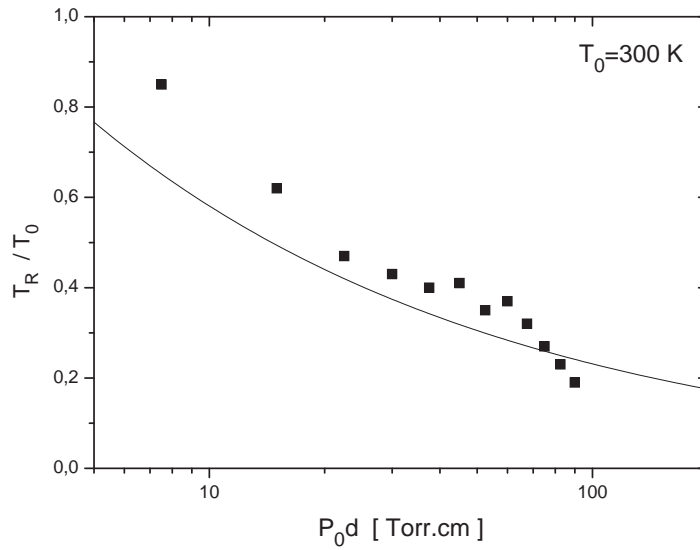


Figure 4.15: Rotational temperature of the D₂ beam calculated by energy balance given in Equation 4.23. The solid line is the best fit line of previous experiments as provided in Equation 4.29. $T_0 = 300$ K, $d = 10$ μ .

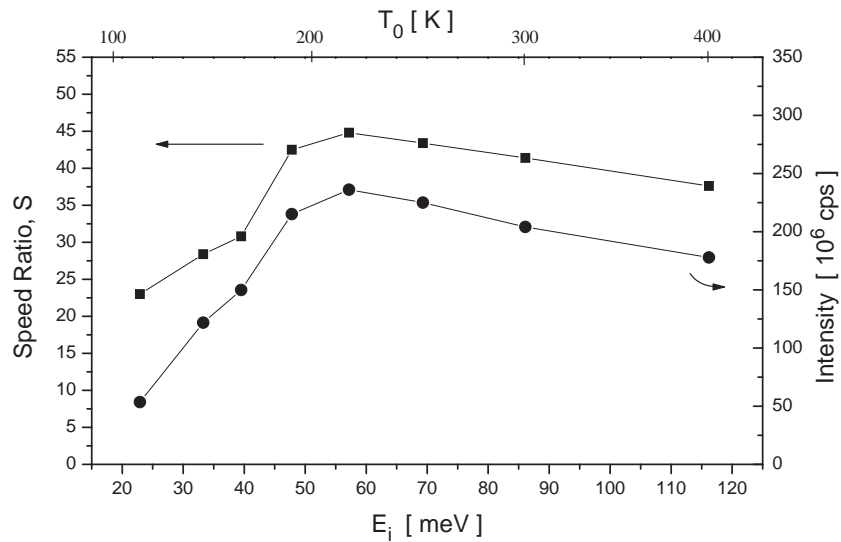


Figure 4.16: The speed ratio, S (in squares) and the intensity (in circles) of the D₂ beam between the beam energies of 20-120 meV. The stagnation pressure is 120 bar. Iris diameter is 2.5 mm. $X_{NS} = 7.5$ mm. The intensity as a function of beam energy serves as a reference data for absolute reflection probabilities from a surface in the following chapters.

The measured speed ratios of n-H₂ and p-H₂ and calculated speed ratio by Winkelmann are shown for comparison [172, 195]. The theoretical speed ratio is calculated quantum mechanically for a Lennard-Jones (12,6) potential with a well depth of 3.42 meV and an equilibrium distance of 3.10 Å and assuming that there is no rotational relaxation. The speed ratios of hydrogen species are significantly lower than the theoretical values and the discrepancy becomes more evident for the D₂ gas. This can be explained in terms of rotational relaxation which heats the beam up and reduces the terminal speed ratio. For D₂ the relaxation rate is larger than for H₂, thus the speed ratio is lower.

Using the energy balance considerations above the rotational temperatures are calculated as shown in Figure 4.15. In the expanded molecular beam the occupation of the rotational states of the molecules show a nearly Boltzmann distribution, thus the populations of the rotational states can be determined with Equation 4.25 or similarly with the use of plots in Figure 4.10. Previous investigations demonstrated that the rotational distributions can be characterized by an effective rotational temperature T_R , which can be expressed with an empirical fit for n-D₂ as [197]

$$\log(T_R/T_0) = -0.40 \cdot \log[P_0 d \cdot T_{ref}/T_0] + 0.16 \quad , \quad (4.29)$$

and for para- and normal-H₂ as

$$\log(T_R/T_0) = -0.44 \cdot \log[P_0 d / \sqrt{T_0}] - 0.32 \quad , \quad (4.30)$$

where $T_{ref} = 293$ K is a reference temperature and $P_0 d$ is given in units of Torr cm. For comparison, in Figure 4.15, Equation 4.29 is also plotted. The discrepancy between the measured rotational temperature values and the empirical best fit line is reasonable. Note that the best fit line given in Equation 4.29 estimates the rotational temperature within 10% of error [197]. One of the error sources in our calculation of the rotational temperature from the energy balance is that the enthalpy values (H_0) for zero pressure is used. At 120 bar and 300 K the enthalpy diverges from zero-pressure enthalpy by only less than 2% [198] and will enhance the measured rotational temperatures by about 20% and for lower pressures it becomes rapidly insignificant. This explains why the calculated rotational temperatures at high pressures decrease steeper in Figure 4.15. From the figure, the rotational temperature, at stagnation pressure of 120 bar and temperature of 300 K, is 72 K and using Figure 4.10 the fractional populations of the rotational levels n_0 , n_1 , and n_2 are 58, 33, and 8% , respectively.

In Figure 4.16 the speed ratio and the intensity of the D₂ beam as functions of stagnation temperature and translational energy are shown. As seen in the figure

the speed ratio and the intensity decrease simultaneously when the energy is less than 50 meV ($T_0 < 190$ K). This sudden "worsening" of the beam is partly due to the skimmer effects similar to the He case. At $P_0=200$ K, $Kn_s/M_s=0.02$, which is similar to the values at the onset of strong skimmer interferences for He gas (see also Section 4.2). The second reason is that, unlike He under the similar conditions [199], the cluster formation plays a significant role in the speed ratio and beam intensity due to the surplus energy originating from clustering and also the energy balance given in Equation 4.23 is not valid, which is the subject of the following section.

4.4 Cluster Formation in n-D₂ Beams

With its strong cooling effect, the free-jet expansion is also suitable for creating weak van der Waals complexes. The first observation of condensation was made by Becker *et al.* [200]. They observed unexpected changes of the intensity, velocity and speed ratio of H₂, N₂, and Ar beams with decreasing stagnation temperature and increasing stagnation pressure and attributed their observation to condensation effects. At sufficiently low temperatures and high densities, dimers form via three-body collisions. The formation of trimers requires collisions between two dimers when there is sufficient dimer density. Once sufficient dimers and trimers are formed two-body collisions are sufficient to produce massive condensation. Our main interest in the present work is on dimers and clusters of small sizes, in contrast to previous works on the formation of large H₂ [201–206] and D₂ clusters [207]. The understanding of the dimerization process in the free-jet expansion is of particular interest for a variety of motivations: It provides a simple system for understanding of cluster growth. It is desirable to produce dimer beams without larger complexes for surface scattering and reactive collisions. It is sometimes desirable to avoid clustering at all, which limits the beam performance in molecular beam experiments.

Several criteria were developed for correlating the onset of condensation [208, 209] and different nucleation models have been proposed which provide empirical estimates of dimer concentrations for specific cases [210, 211]. Gordon *et al.* adapted a recombination model suggested by Bunker in order to predict terminal dimer concentrations [3]. The recombination model suggests a two-step mechanism for dimer formation where a virtual orbiting intermediate complexes are first formed then stabilized by collisions with a third body [212]. Knuth proposed a relatively simple model for extracting local recombination coefficients from the measurements of the terminal dimer mole frac-

tions from free jets of rare gases using a sudden-freeze model [1]. This model provides straightforward scaling parameters which define the influence of thermodynamics and kinetics on the terminal dimer concentration. For relatively low dimer concentrations, the dimer concentration is given as [1, 213]

$$\frac{x_2}{x_1} = 3.5^C B \Gamma^{C+1} \quad , \quad (4.31)$$

where x_2 and x_1 are, respectively, dimer and monomer mole fractions, B and C are constants and Γ is the scaling factor given in the form

$$\Gamma = K_1^q K_2^{1-q} \quad , \quad (4.32)$$

where $q = C/(C + 1)$, K_1 and K_2 are kinetic and thermodynamic parameters, respectively and are given by

$$K_1 = n_0 \sigma^3 \frac{d}{\sigma} \left(\frac{\varepsilon}{kT_0} \right)^{5/4} \quad , \quad (4.33)$$

$$K_2 = n_0 \sigma^3 \left(\frac{\varepsilon}{kT_0} \right)^{3/2} \quad . \quad (4.34)$$

Here n_0 is the number density in the source, σ is the zero-potential radius, and ε is the well depth of the interaction potential. The value of the q may have values between 0 and 1 depending on the experimental conditions. For $q=0$, the terminal dimer mole fraction is a function only of K_2 . Hence, only thermodynamic is relevant and there is no dependence of $\frac{x_2}{x_1}$ on d . In other words, the terminal dimer mole fraction is the same as in the source conditions. For the case $q=1$, the terminal dimer mole fraction is dominated by production during the free-jet expansion and the initial concentration of dimers is negligible. From the analysis of the available data of terminal dimer concentrations from free-jet expansion of rare gases [209,210,214,215], it is found that $q=0.4$.

The dimer concentrations in the source, for $x_1 \simeq 1$, can be given by [217]

$$x_2 = n_0 K_D = n_0 2^{2/3} \left[\frac{\hbar^2}{2\pi m k T_0} \right]^{3/2} \sum_J (2J + 1) \exp\left[-\frac{E_J}{kT_0}\right] \quad , \quad (4.35)$$

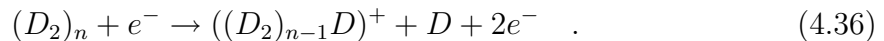
where K_D is the equilibrium constant, m is the mass of the monomers and E_J is the energy of rotational levels. The dimer concentrations in the source for the used source conditions are provided in Table 4.3.

Table 4.3: The dimer mole fractions in the source calculated by using Equation 4.35. The rotational eigenenergies of o-D₂- o-D₂, E_J for $J=0, 1, 2$ and 3 are, respectively, 8.75 K, 7.32 K, 4.60 K and 0.712 K [216].

P ₀ (bar)	T ₀ =108 K	T ₀ =140 K	T ₀ =160 K	T ₀ =180 K	T ₀ =220 K	T ₀ =300 K
10	7.0×10^{-5}	3.7×10^{-5}	2.7×10^{-5}	2.0×10^{-5}	1.2×10^{-5}	5.6×10^{-6}
20	1.4×10^{-4}	7.3×10^{-5}	5.3×10^{-5}	4.0×10^{-5}	2.4×10^{-5}	1.1×10^{-5}
30	2.1×10^{-4}	1.1×10^{-4}	8.0×10^{-5}	5.9×10^{-5}	3.6×10^{-5}	1.7×10^{-5}
40	2.8×10^{-4}	1.5×10^{-4}	1.1×10^{-4}	7.9×10^{-5}	4.8×10^{-5}	2.2×10^{-5}
50	3.5×10^{-4}	1.8×10^{-4}	1.3×10^{-4}	1.0×10^{-4}	6.0×10^{-5}	2.8×10^{-5}
60	4.2×10^{-4}	2.1×10^{-4}	1.6×10^{-4}	1.2×10^{-4}	7.2×10^{-5}	3.3×10^{-5}
70	4.9×10^{-4}	2.6×10^{-4}	1.9×10^{-4}	1.4×10^{-4}	8.4×10^{-5}	3.9×10^{-5}
80	5.6×10^{-4}	3.0×10^{-4}	2.1×10^{-4}	1.6×10^{-4}	9.6×10^{-5}	4.5×10^{-5}
90	6.3×10^{-4}	3.3×10^{-4}	2.4×10^{-4}	1.8×10^{-4}	1.1×10^{-4}	5.0×10^{-5}
100	7.0×10^{-4}	3.7×10^{-4}	2.7×10^{-4}	2.0×10^{-4}	1.2×10^{-4}	5.6×10^{-5}
110	7.7×10^{-4}	4.1×10^{-4}	2.9×10^{-4}	2.2×10^{-4}	1.3×10^{-4}	6.1×10^{-5}
120	8.4×10^{-4}	4.4×10^{-4}	3.2×10^{-4}	2.4×10^{-4}	1.4×10^{-4}	6.7×10^{-5}

4.4.1 Experiment

Mass-resolved intensity and velocity distributions of n-D₂ beam were made at stagnation temperatures of 108, 140, 160, 180, 220 K and at pressures between 10-120 bar. Mass spectra were measured in the range 1-40 a.u. The nozzle-to-skimmer distance was fixed at 7.5 mm. Figure 4.17 shows a typical mass spectrum for a stagnation pressure of 120 bar and a source temperature of 140 K. The detector resolution decreases as the mass number increases. The electron impact energy is 160 eV. Although the background-mass spectrum was subtracted, there are still some small fingerprints of the background vacuum. Also two satellite peaks around the D_2^+ peak is due to the defocusing of the ions which is caused due to the reduced efficiency of the detector by worsening the ion optics. Since it is the largest peak and the resolution is high for low masses, it is only observed for the D_2^+ peak. As seen from the figure the odd ion numbers are the greatest peaks, which is consistent with the most probable reaction by electron impact [2]



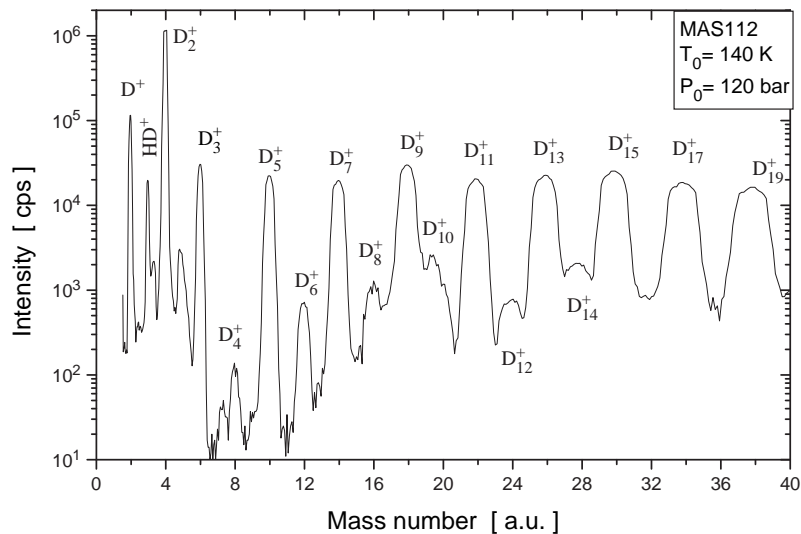
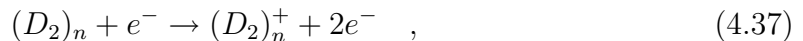


Figure 4.17: Mass spectrum for n-D₂ beam at P₀=120 bar and T₀=140 K. Ionization energy is 160 eV. The background mass spectrum (see Figure 3.13) is subtracted. $d=10 \mu$.

In the mass spectrum the mass-4 (D_2^+), mass-6 (D_3^+), mass 10 (D_5^+), mass-14 (D_7^+), etc. peaks originate from the existing monomers (D_2), dimers ($(D_2)_2$), trimers ($(D_2)_3$), tetramers ($(D_2)_4$), etc., respectively. The reaction



which leads to even ion numbers, has a probability of one to two orders of magnitude less than the reaction in Equation 4.36 as seen in Figure 4.17. Another possible reaction which may occur inside the detector is [2]



It is found that at the room temperature conditions where dimers are negligible (300 K and 10 bar) the intensity of D_3^+ (mass-6) amounts about 0.8×10^{-4} of the monomer peak intensity². This measured intensity at mass-6 is partly due to the reaction and partly due to the existing dimers in the beam. Thus, the reaction in Equation 4.38 is negligible, provided that the dimer mole fraction in the beam is more than 10^{-4} of the monomer.

²For 300 K and 120 bar dimer intensity is 7×10^{-4} of the monomer peak intensity.

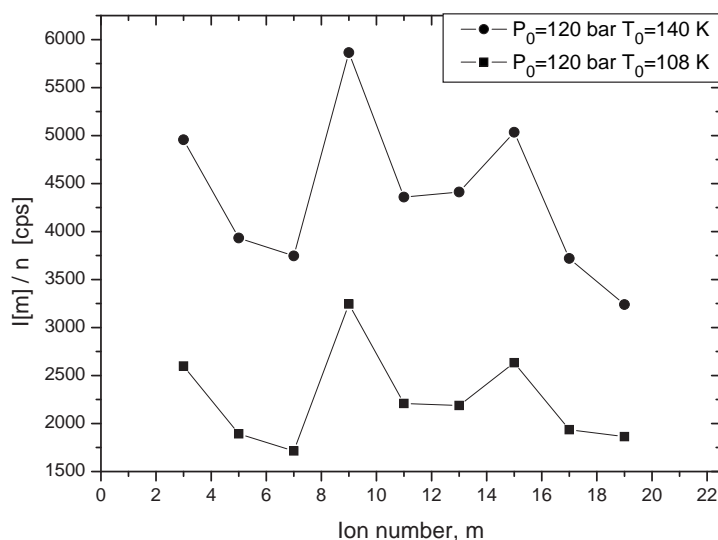


Figure 4.18: The intensities of ions D_m^+ as a function of ion number. The intensities are divided by the parent cluster size number n , where $n=(m+1)/2$. Since the resolution of mass spectrum significantly changes in the given mass range, the peak areas are used to determine the intensity. Circles stand for $P_0=120$ bar $T_0=140$ K and squares stand for $P_0=120$ bar $T_0=108$ K. $V_{cathode}=160$ V. $d=10$ μ .

The ionization cross sections of small clusters are approximately equal to the cluster size times the ionization cross section of a simple molecule [218]. In Figure 4.18 the intensities of the ion peaks as a function of the ion number of D atoms (m) is plotted for two mass spectra. Since these ions are mainly attributed to the reaction given in Equation 4.36, the intensities are divided by the parent cluster size number n , where $n=(m+1)/2$. At these conditions much larger clusters ($\text{mass} \gg 40$ a.u.) should exist and for a small range of mass spectra mole fractions of clusters should not change significantly unless a certain cluster is particularly stable. For $T_0=108$ K the intensities are less than for $T_0=140$ K because at lower temperatures larger clusters are possible so that the mole fraction of an individual cluster size is smaller. As seen Figure 4.18 the intensities of ions D_9^+ and D_{15}^+ exhibit maxima. Experimentally [219] and theoretically [220] it is reported that H_9^+ (mass-18 for D_2) is especially stable forming an equilateral triangle (H_3^+) with three H_2 molecules positioned at the outside of the triangle on the lines from the center through the midpoints of the sides. Since the ion D_9^+ is particularly stable, the fragmentation of its parent cluster ($(D_2)_5$) is favorable

and has a larger ionization cross section. The reason for higher cross section of D_{15}^+ is, to our knowledge, not clear and should be investigated theoretically. Also the stability of the clusters should be investigated for an unambiguous conclusion.

In Figures 4.19-4.22 the stagnation pressure dependence of intensities at constant stagnation temperatures of 220 K, 180K, 160 K, 140 K and 108 K is shown. In these figures only the intensities of the ion fragments D_2^+ , D_3^+ , D_5^+ and D_7^+ are plotted. The pressure dependence of the intensities shows very different trends for different temperatures. At low temperatures and high pressures, a "saturation" of intensities is observed. This effect appears when the all possible clusters reach at about same intensity and not observed at high temperatures, for instance $T_0=220$ and 180 K. The monomer intensities saturate much earlier than of the clusters.

In order to calculate the mole fraction of dimers, the relative ionization efficiencies of monomers and dimers, and the dimer enrichment due to the Mach-number focusing must be taken into account. Hence, the dimer mole fraction, for low cluster concentrations, as a function of measured intensities given as

$$\frac{x_2}{x_1} = \frac{I(6)}{I(4)} \frac{1}{2\alpha} \quad (4.39)$$

Here $I(4)$ and $I(6)$ are the measured intensities at masses 4 and 6 a.u. The relative ionization probability of dimers is adjusted by the factor of 2. α is the effect of Mach-number focusing which adjusts relative enrichment of the species at the detector to the mole fractions at the skimmer which results from the unequal speed ratios of different species in the beam. A simple analytical form of the α is given as [221]

$$\alpha = \frac{1 - \exp[-S_{\perp 2}^2 \xi_{max}^2]}{1 - \exp[-S_{\perp 1}^2 \xi_{max}^2]} \quad (4.40)$$

where $S_{\perp 2}$ and $S_{\perp 1}$ are the perpendicular speed ratios of the dimer and monomer at the skimmer³, and ξ_{max} is the flow divergence (the skimmer radius divided by the nozzle-skimmer distance). Under moderate conditions (where there is no massive condensation) the value of α is found to be between 1.2 and 1.9.

In Figure 4.23 the terminal dimer mole fractions are plotted as a function of the scaling parameter given in Equation 4.32. The only appropriate data for comparison is H_2 terminal dimer fractions measured by Van Deursen *et al.* [2, 219, 222] and is also plotted⁴. As seen H_2 and D_2 dimer mole fractions show linear dependence with the

³We assumed that the S_{\perp} is the same as the parallel speed ratio, which is determined by TOF.

⁴There is also limited data of H_2 dimer mole fractions reported by Winkelmann [172], however according to the data dimer mole fractions decrease with increasing pressure even much before the onset of massive condensation which cannot be true, and thus it is not shown here.

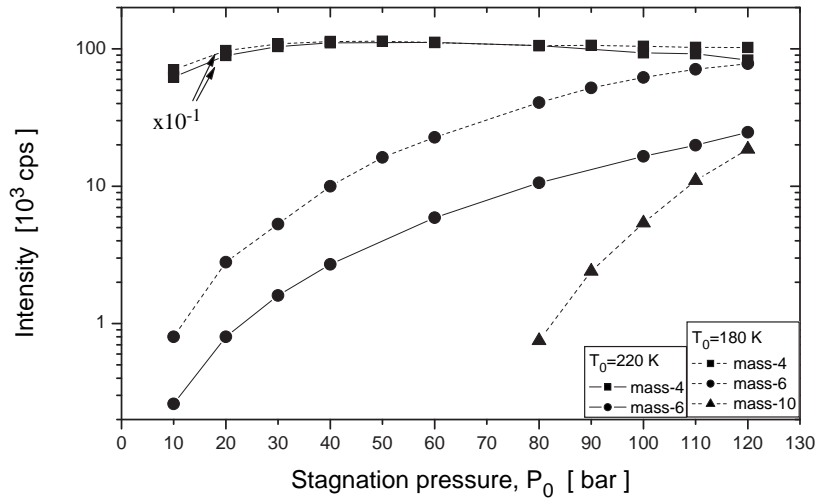


Figure 4.19: The intensities of the ion fragments (D_2^+ : \blacksquare), dimers (D_3^+ : \bullet), and trimers (D_5^+ : \blacktriangle) at $T_0=220$ K (solid lines) and 180 K (dashed lines). The intensities of the monomers is divided by 10. $d=10 \mu$.

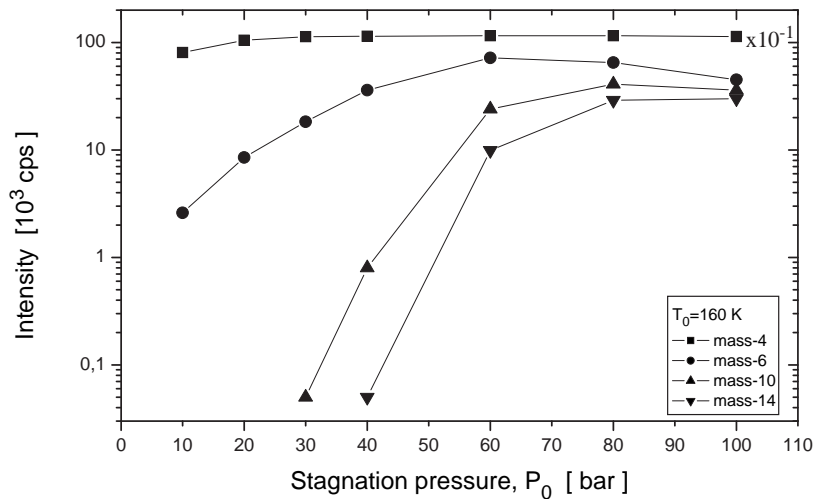


Figure 4.20: The intensities of the ion fragments (D_2^+ : \blacksquare), dimers (D_3^+ : \bullet), trimers (D_5^+ : \blacktriangle) and tetramers (D_7^+ : \blacktriangledown) at $T_0=160$ K. The intensities of the monomers is divided by 10. $d=10 \mu$.

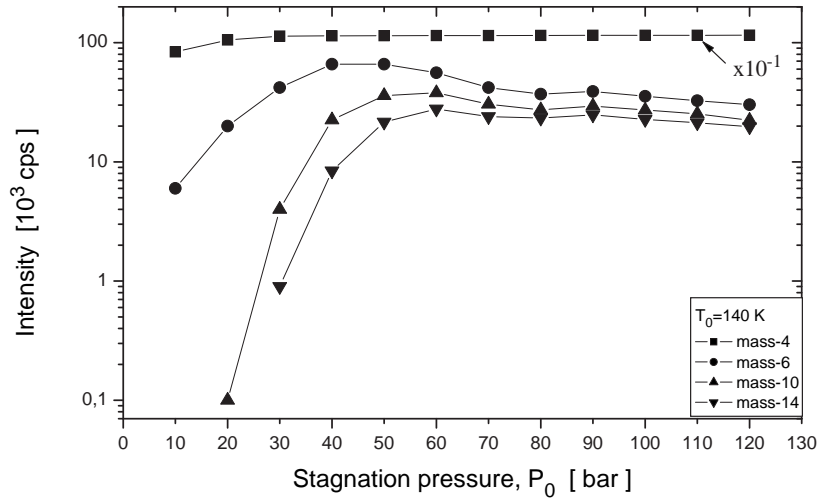


Figure 4.21: The intensities of the ion fragments (D_2^+ : \blacksquare -), dimers (D_3^+ : \bullet -), trimers (D_5^+ : \blacktriangle -) and tetramers (D_7^+ : \blacktriangledown -) at $T_0=140$ K. The monomer intensity is divided by 10. $d=10 \mu$.

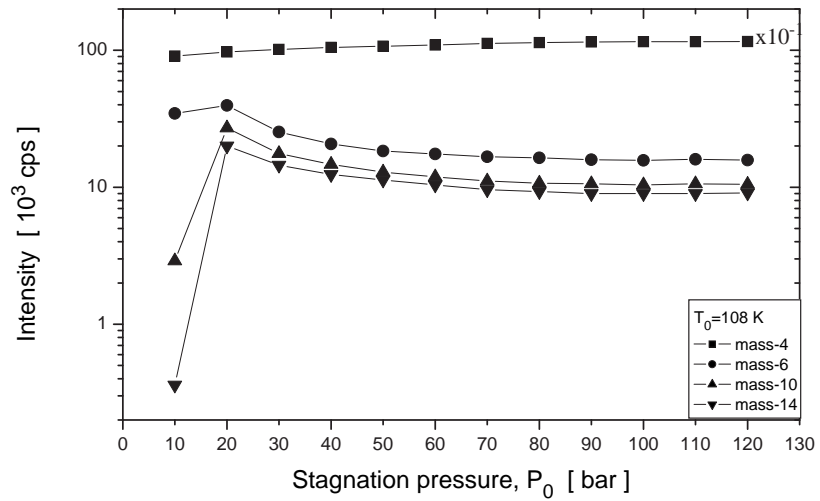


Figure 4.22: The intensities of the ion fragments (D_2^+ : \blacksquare -), dimers (D_3^+ : \bullet -), trimers (D_5^+ : \blacktriangle -) and tetramers (D_7^+ : \blacktriangledown -) at $T_0=108$ K. The intensities of monomers divided by 10. $d=10 \mu$.

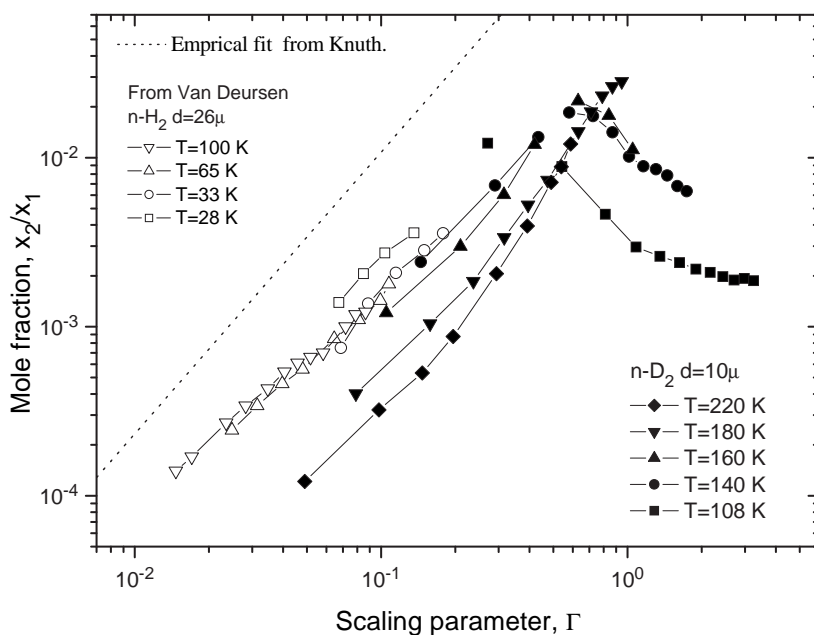


Figure 4.23: Mole fractions of H_2 and D_2 dimers as a function of scaling parameter, Γ , defined in Equation 4.32. Hydrogen data is from refs. [2, 219, 222] (the orifice diameter is 26μ). The empirical fit of scaling factor for monatomic gases [1] is plotted as a straight dotted line. For H_2 and D_2 (ε/k) is equal to 38.0 K; and σ is 2.915 Å and 2.948 Å, respectively [169].

scaling parameter unless there is massive condensation. The H_2 dimer mole fractions lie on the same curve whereas D_2 dimer mole fractions increase, thus approach to H_2 values with decreasing stagnation temperature for the same scaling parameter value. As discussed previously, the characteristic rotational temperature of the H_2 molecule is 85.4 K whereas of the D_2 molecule is 43 K. The stagnation temperatures of H_2 data are between 28 and 100 K, which are less than or comparable with the characteristic rotational temperature of H_2 . Thus, no rotational relaxation of the H_2 molecules during the expansion is expected at these low stagnation temperatures and the H_2 molecules behave like a monatomic gas. Whereas, since the D_2 measurement are at high stagnation temperatures rotational relaxation has a bigger effect by increasing the temperature of the gas, thus reducing the formation of the dimers.

As seen in Figure 4.23 at high stagnation pressures the dimer mole fractions tend to decrease or at least the increase slows down, due to the formation of trimers and larger

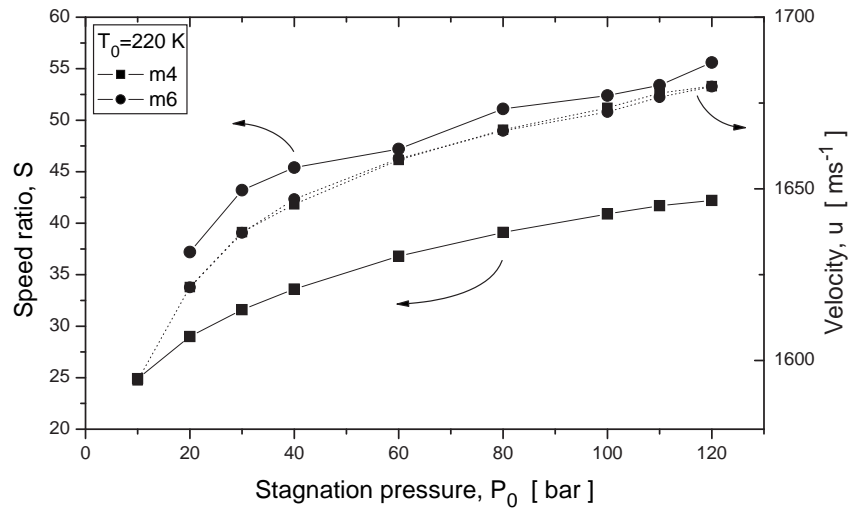


Figure 4.24: Pressure dependence of the speed ratios (solid lines) and terminal velocities (dotted lines) of the n -D₂ monomers (■) and dimers (●) at $T_0=220$ K. The speed ratios of monomers dimers have a constant ratio of $S_2/S_1 = \sqrt{2}$. The velocities of the dimers and monomers are almost the same. $d=10 \mu$.

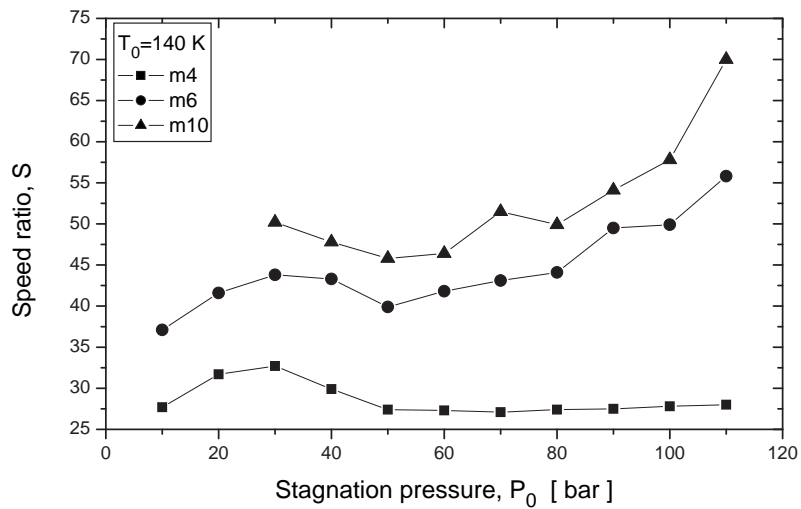


Figure 4.25: Stagnation pressure dependence of the speed ratios of the n -D₂ monomers (D_2^+ :■), dimers (D_3^+ :●), trimers (D_5^+ :▲) at $T_0=140$ K. $d=10 \mu$.

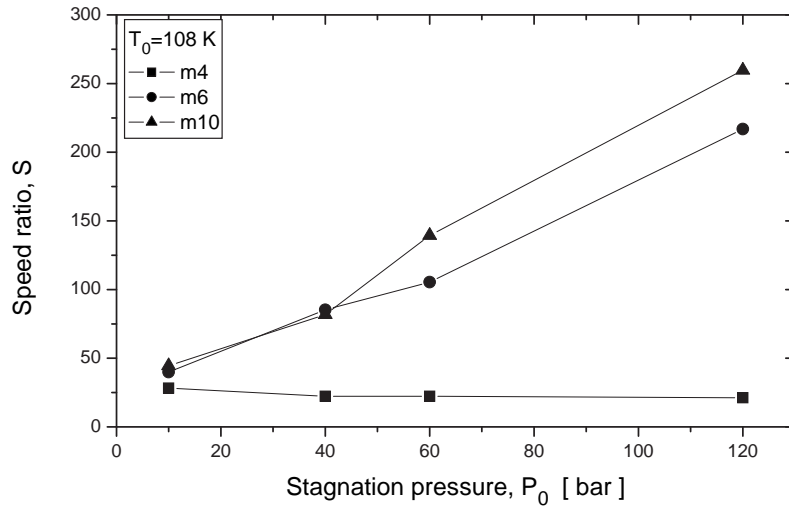


Figure 4.26: Stagnation pressure dependence of the speed ratios of the n - D_2 monomers (D_2^+ :■), dimers (D_3^+ :●), trimers (D_5^+ :▲) at $T_0=108$ K. $d=10$ μ .

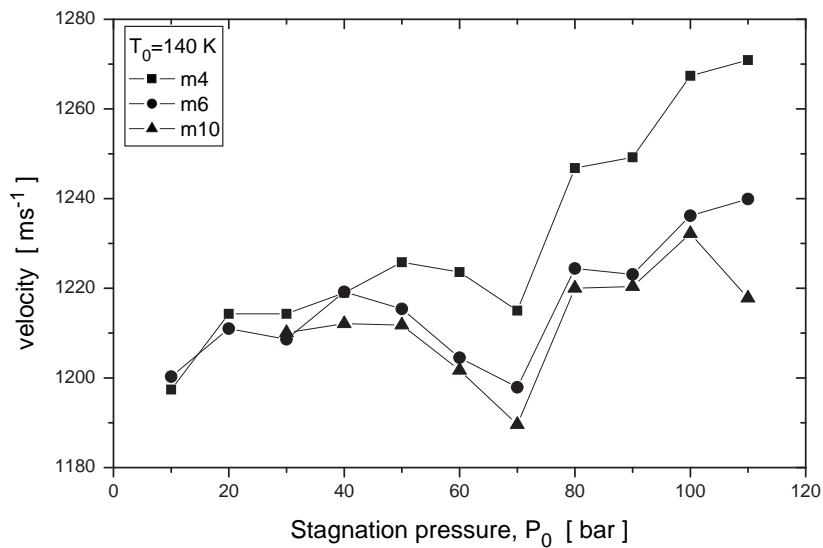


Figure 4.27: The terminal velocities of the n - D_2 monomers (D_2^+ :■), dimers (D_3^+ :●), trimers (D_5^+ :▲) as a function of stagnation pressure at $T_0=140$ K. $d=10$ μ .

clusters, namely at where massive condensation sets on. In Figure 4.23 the H₂ dimer mole fractions are plotted only up to where they start to diverge from linear behavior. For D₂, dimer mole fractions are plotted for all conditions in order to demonstrate the effects of the massive condensation. For D₂ data the plot lines are interrupted where trimer to dimer ratios are more than 10% which also corresponds the conditions where plots tend to diverge from the linear behavior. Hence we assign the onset of massive condensation as trimers reach 10% of dimers which occur at $\Gamma=0.4-0.8$. Van Deursen suggested a criterion for the onset of massive condensation as [219]

$$n_0\sigma^3 \left(\frac{d}{\sigma}\right)^{0.55} \left(\frac{\varepsilon}{kT_0}\right)^{5/4} < 0.5 \quad . \quad (4.41)$$

In the present case this factor is found to be less than 1.5 to avoid the formation of trimers. The discrepancy is due to two reasons. Firstly, the D₂ dimer fraction are less than H₂ dimer fractions which means also formation of trimers should be retarded. Secondly, the value of this factor depends highly on the definition of what is "negligible", where here it is found that up to 10% of trimer/dimer ratio (about 0.1% of monomers), the dimer mole fractions are not affected by the trimer formation.

In Figure 4.24 the pressure dependences of the speed ratios and velocities of the monomers and dimers for stagnation temperature $T_0=220$ K are shown. Both monomers and dimers have the same velocity and the speed ratios differ by about a factor of $\sqrt{m(D_4)/m(D_2)}$ which indicates that both have about the same beam temperature (see Equation 4.13). Note that there is no saturation of the dimer intensity for this stagnation temperature and the intensities of higher clusters are too low to be determined accurately (see Figure 4.19). However, the features change dramatically for the lower stagnation temperatures. In Figures 4.25 and 4.26 the speed ratios of the beam at 140 K and 108 K, respectively, are shown. The speed ratios at 140 K (in Figure 4.25) decrease between 30 and 50 bar first, and then increase at higher pressures. In Figure 4.26 at 108 K, for dimers and trimers speed ratios increase significantly with the pressure increase; however, the speed ratio of monomers decreases. Hence, a significant beam temperature difference between monomers and clusters at high stagnation pressures and low stagnation temperatures, namely a "temperature lag" between the beam species is observed.

Also similar to the beam temperature, an effect of "velocity lag" between the monomers and the clusters can be seen as shown in Figure 4.27. For all species the velocities show increasing trend with increasing stagnation pressure, however, velocities decrease between 40 and 70 bar. Here there are two competing effects: The heat

released in cluster formation leads to an increase in the velocities while the enthalpy decreases with increasing pressure by about 2% [198]. The velocities of molecules and clusters differ at high stagnation pressures, namely the clusters are slower than the molecules. This effect can be seen more clearly in TOF spectra given in Figures 4.28, 4.29 and 4.30. With decreasing stagnation temperature and increasing stagnation pressure, the temperatures of the monomers, dimers and trimers are at equilibrium first, then the monomers get hotter and faster and the dimers and the trimers get cooler and slower whereas the dimers and the trimers differ also each other; and finally the dimers and the trimers are in equilibrium and significantly slower and cooler than the monomers.

These effects can be understood as follows: Dimers are formed in three-body collisions where two partners get together and the third molecule carries away the surplus energy of dimer formation. This leads to an increase in the velocity and internal temperature of the monomers. With increasing stagnation pressure and decreasing stagnation temperature the amount of the clusters formed in expansion increases, releasing more surplus energy, which is transferred to the monomers. In the case of massive condensation, the dimers exist sufficiently. As the formation of or fragmentation of larger clusters needs two-body collisions which freeze much later than three-body collisions, clusters remain in thermal and kinetic equilibrium during the expansion. However, after the formation of the clusters, their further acceleration by the monomers is not effective compared with the self-acceleration of the monomers.

4.5 Conclusions

In this chapter the overall expansion properties of He and n-D₂ gases are characterized. The knowledge of incident beam intensities for scattering experiments is highly valuable in the surface scattering experiments for the determination of the surface reflectivity and of the diffractive and rotational transition probabilities. The estimation of the actual incident beam intensities is highly complicated and the approximations based on the source parameters and the apparatus geometry will lead mostly erroneous results.

Maxima in the intensities of ion fragments originating from the clusters (D₂)₅ and (D₂)₈ is observed. For (D₂)₅ this is attributed to the particular stability of ion D₉⁺ [220] leading a larger cross-section of the reaction: (D₂)₅ + e⁻ → D₉⁺ + D + 2e⁻. For (D₂)₈ it is not clear yet.

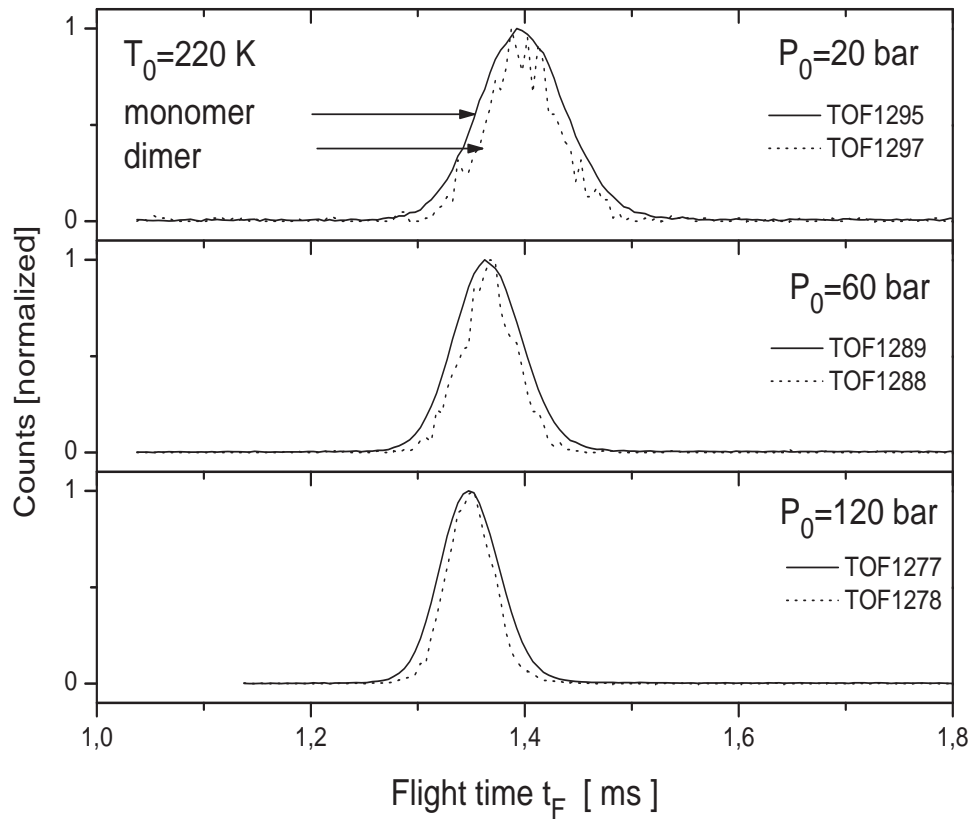


Figure 4.28: TOF spectra of the $n\text{-D}_2$ monomers (solid lines) and dimers (dotted lines) at stagnation temperature of 220 K and at stagnation pressures of 20, 60, and 120 bars. The flight distance is 2266 mm. $d=10 \mu$.

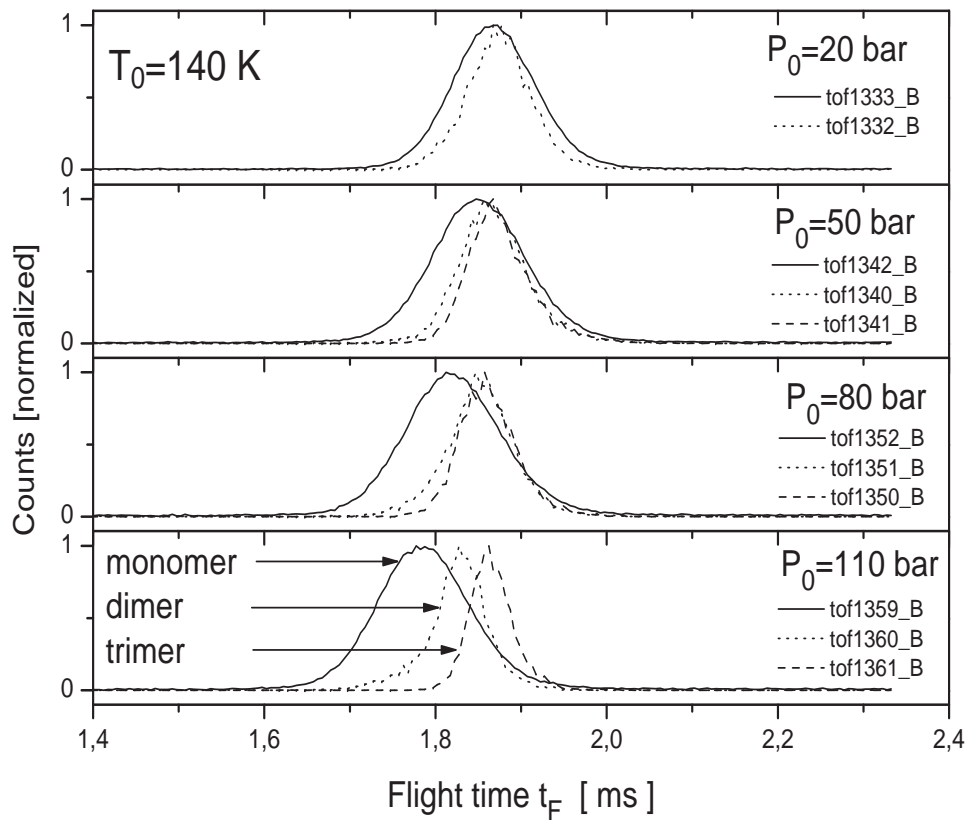


Figure 4.29: TOF spectra of the $n\text{-D}_2$ monomers (solid lines), dimers (dotted lines), and trimers (dashed lines) at $T_0=140$ K and at pressures of 20, 50, 80, and 110 bars. The flight distance is 2266 mm. $d=10 \mu$.

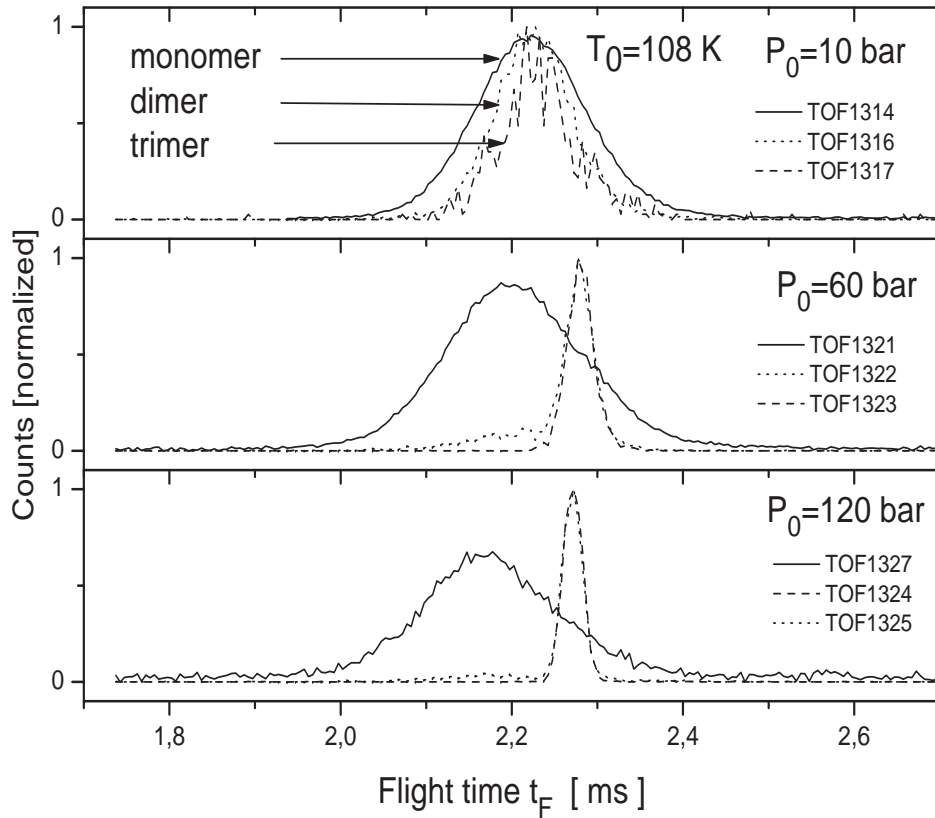


Figure 4.30: TOF spectra of the $n\text{-D}_2$ monomers (solid lines), dimers (dotted lines), and trimers (dashed lines) at $T_0=108$ K and at pressures of 10, 60, and 120 bars. Note that at pressures higher than 10 bar, massive condensation is observed. The flight distance is 2266 mm. $d=10 \mu$.

The formation of small clusters in n-D₂ beam at relatively high stagnation temperatures and pressures is investigated. It is observed that with decreasing stagnation temperature the dimer mole fractions increase systematically at the same scale parameter, which takes both thermodynamics and kinetics of isentropic expansion. At stagnation temperatures of 160, 140, and 108 K the dimer mole fractions are similar to the H₂ data, which were carried out for lower temperatures. The lower amount of terminal dimer mole fractions at higher stagnation temperature recalls the effect of temperature lag (the decrease of the speed ratio) due to the rotational relaxation diverging from the isentropic expansion of monatomic gases. Most of the rotational relaxation [186] and also three-body collisions [143], thus dimer formation take place within a few diameters of the nozzle downstream as shown in Figure 4.9. It is not clear, how far relaxations affect the formation of dimers which requires solving coupled equations of translational relaxation, rotational relaxation, and dimerization.

In the analysis of the terminal velocities and temperatures of individual species by TOF spectra, it is observed that with increasing concentrations of the clusters, velocity and temperature lag emerge between the monomers and the clusters. Such a velocity and temperature difference, so called "velocity and temperature slip" have been also widely observed in free-jet of mixtures⁵ [223]. The kinetic theory analysis of this phenomenon is rather complicated⁶ and requires collision time scales governed by combinations of the collision cross sections of three pairs, namely inter and intra-species pairs [143]. In a supersonic-expansion of a mixture the heavier species fail to keep up with the rest due to insufficient collisions. In the case of the cluster formation, the surplus heat from condensation is transferred from the heavier species to the lighter ones, which increases firstly the beam temperature, which is next, up to some extent, converted into the directed flow velocity of lighter species, which finally also leads to acceleration of heavier species if the remaining number of collisions are sufficient; and if not the clusters fail to keep pace with the lighter molecules.

In these studies the potential sources of error were not investigated. The possible distortions of the dimer mole fractions by the skimmer interferences were neglected. In the extreme case; for stagnation condition 120 bar and 108 K, Kn_s/M_s is equal to 0.01, which suggests a strong skimmer interference. How skimmer interference would influence the final dimer mole fractions is unclear. For instance, the scattering of clusters can lead to fragmentation of the clusters. Another source of error is the selective

⁵Since its origin is somewhat different, we preferred calling the difference "lag" instead of "slip".

⁶For clusters it is even more complicated.

attenuation by the background gas. The beam composition may change due to the different cross sections for the background gas. Both skimmer interference and selective attenuation by background gas should be investigated by measuring the final dimer fraction by changing the nozzle-skimmer distance and changing the background pressure.

5. Preparatory Experiments for He-Microscopy

Atom optics has attracted considerable attention in recent years [45,224–226]. One of the main challenges for further applications is the realization of optical elements for neutral atom beams. Recent efforts to focus neutral beams of attempts have mainly concentrated on atoms and molecules which can be manipulated by using static electromagnetic and optical fields [45,227]. These standard techniques cannot be used for focusing neutral, ground state ^4He atoms of thermal energies [140]. As mentioned in Chapter 1, a HAS-scanning microscope will complement the existing surface probe tools and focusing of thermal He atoms is of great technological and scientific interest.

Focusing of neutral He atoms has been accomplished by means of Fresnel zone plates [47] and bent-crystal mirrors [48]. With Fresnel zone plates the focusing of a beam of He atoms with a wavelength of $\sim 0.9 \text{ \AA}$ down to a spot size of 2μ has been reported [47]. The theoretical limits of the focused spot size are set by the chromatic dispersion of the beam velocity distribution and diffraction limited resolution of zone plate, which make nominally a few hundred nanometers [228]. The focused beam intensity is limited by the transmissivity and the size of free standing Fresnel zone plate. The total diameter of the zone plate used in the experiments [47,229] was 0.27 mm and the transmission was found to be about 34% [230]. Moreover, only one third of the transmitted beam is focussed, while the undiffracted and defocused beam lead to a broad background around the central maximum which is difficult to remove with further collimation and reduces the intensity-to-background ratio.

The use of a bent-crystal surface can be the solution of this limitation where several millimeters of diameters of incident beam can be focused. For instance, with the focusing of an incident beam of 5 mm diameter with an ideal and perfect surface an intensity gain with a factor of 3×10^3 can be realized compared to the Fresnel zone plates. However, the principal disadvantages are intensity loss due to diffractive, ther-

mal and inelastic effects. Additionally technical challenges have to be overcome, for instance; bending a crystal accurately into an ideal Cartesian shape¹, manufacturing atomically flat surfaces with low defect densities and large domain sizes, being homogeneous over millimeters, preferably being unreactive to contaminants for wide-spread applications and keeping it clean inside the apparatus for long periods of time [232].

Thin Si(111):H(1×1) crystal surface has emerged as a promising candidate satisfying the prerequisites of an atomic reflective mirror [233–237]. The successful focusing of He atoms, by means of a 50- μ -thick hydrogen passivated Si(111) crystal bent with an electric field, to a spot diameter of 210 μ has been reported [48]. Theoretical investigations concluded that a spot size of 200 nm can be achieved with single thin crystals clamped with an elliptical frame and under electrostatic pressure generated by electrodes of optimized geometry [129, 232] and with utilization of a one micron diameter skimmer [133]. This approach is regarded as the best candidate for focusing of a beam achromatically with a large aperture. The Si(111):H(1×1) crystals can be prepared with *in-situ* hydrogenation [238, 239] and with *ex-situ* wet chemical etching method [240, 241]. In contrast to *in-situ* method, the wet chemical etching provides an atomically flat and low-defect density surface which is a prerequisite for focusing purposes.

One of the main motivations in building this apparatus (see Chapter 3) was focusing of the neutral He atoms by means of an atomically flat Si(111):H(1×1) single thin crystal. The apparatus was designed to be highly flexible in order to allow an optimization of the best reflection geometry (scattering angle, beam divergence) and a demagnification ratio of 5:1 (source-to-mirror: mirror-to-detector). Additionally, special precautions were taken to ensure that the vacuum is free of hydrocarbon contamination (see also Section 3.1.3). Only turbo-molecular pumps are installed for all chambers providing an oil-free pumping and for the source chamber allowing the use of micro-skimmers, since the minimum focused spot (image) size is also limited by the skimmer (object) size.

In this chapter the first experiments of transportation, storage in the beam apparatus and testing the reflection quality of the crystals with He scattering are reported. These experiments serve as prefatory experiments to test the reliability of *ex-situ* prepared Si(111):H(1×1) crystals as a focusing element towards the realization of a HAS-microscope.

¹An ideal mirror without aberrations can be represented by an elliptical surface of revolution, so called Cartesian ellipsoid, with object and image points at the foci [231].

5.1 Experiment

The unreconstructed Si(111) surface is terminated by tetrahedrally coordinated silicon atoms with one dangling surface bond and its termination is highly unstable. The cleaved Si(111) surface reconstructs at room temperature to a (2×1) structure and at higher temperatures to a (7×7) structure [242, 243]. Hydrogenation with the wet chemical etching methods of the Si(111) surface passivates the surface with hydrogen atoms yielding a surface structure of a simple bulk truncation with the exception of the uppermost lattice sites which are capped with hydrogen atoms [240, 241, 244, 245]. Hence the dangling bonds are eliminated and the surface structure has the same symmetry like the unreconstructed Si(111) surface which is shown in Figure 5.1.

The crystals used in this experiment are fabricated in Cambridge and transported to Göttingen. The details of the fabrication and transportation are reported elsewhere [232, 246, 247]. The experiments are conducted with polished, n-type silicon crystals ($0.5 \times 10 \times 10$ mm) with a miscut angle of 0.1° . The optimized etching process and cleaning protocols resulted, as observed by AFM, in a clean and passivated surface with broad, zigzag shaped steps of about 200 nm spacing [232]. The samples are put in a specially designed stainless steel box immediately after fabrication and the box is evacuated with an oil-free membrane pump and flushed with pure argon² gas several times in a clean room. Finally it is filled with a slight over-pressure of Ar and sealed. The AFM checks of samples kept in the transportation box for 25 hours showed that the atomic terraces had retained their smoothness and the edges were well defined [232].

After the chemical preparation in a clean room the samples are transported within 24 hours to Göttingen and mounted into the target chamber and the vacuum chamber is subsequently pumped down within 30 minutes according to the clean-pumping down procedures described in Section 3.1.3. The sample holder, shown in Figure 5.2, offers a quick-fix connection with the target manipulator and with electrical and cooling feedthroughs. It is designed for only these preliminary experiments. All pieces are mounted onto a Vespel³ base plate. Vespel is chosen because it is vacuum compatible and easy to machine. The crystal is pressed with four clamps onto the sapphire disk. The sapphire provides both electrical and at high temperatures thermal isolation from the copper head and a good thermal contact when the crystal is cooled. Upper fixing

²Messer Gresshiem; 99.999% purity, <2 vpm O_2 , <3 vpm H_2O .

³Vespel® (SP-1) is a high performance and vacuum compatible polyimide material manufactured only by DuPont, DE, USA.

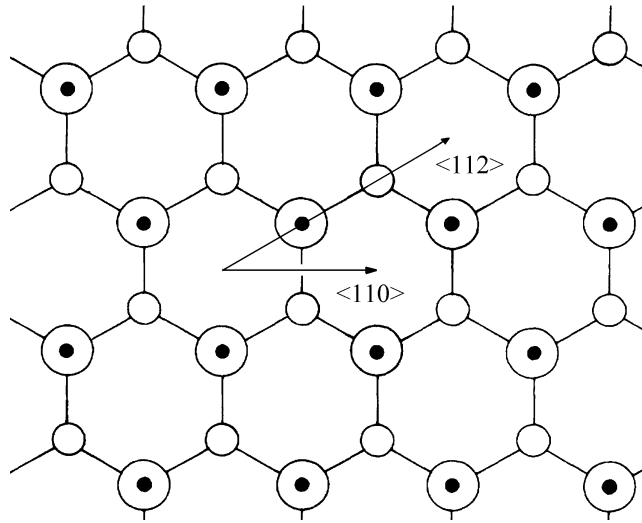


Figure 5.1: The top view of the Si(111):H(1 \times 1) surface. The filled circles represent hydrogen atoms, large and small open circles show first layer and second layer Si ions, respectively. The bonds between the neighboring atoms are shown with lines. High-symmetry directions are marked with arrows. The reciprocal lattice vectors \mathbf{G} along the $\langle 110 \rangle$ and $\langle 112 \rangle$ directions are 3.27 \AA^{-1} and 1.89 \AA^{-1} , respectively.

clamps also serve for contacting the thermocouple with the crystal surface. A tantalum sheet is placed between the crystal and the sapphire plate. The 50μ -thick, home-made tantalum sheet with zigzag pattern is fixed and electrically connected with two separate clamps. The sample cooling is realized with a copper braid with a copper block head pressed onto the sapphire plate from the backside. A clamp fixing the copper plate provides a quick fix ensuring a good thermal contact. A C-type (W5% Re:W26% Re) thermocouple [248] is chosen because more conventional K-type thermocouple contains nickel which causes a reconstruction of the silicon surface [138,249]. Although the Si(111):H(1 \times 1) surface is found to be inert, remaining clean over several months at 10^{-6} mbar [48], the hydrocarbon compounds are highly reactive with the surface chemisorbing to form Si-C bonds [232]. For this reason special precaution must be taken in order to ensure an oil-free vacuum (see Section 3.1.3). The sample holder is cleaned with detergent and acetone under ultrasonic agitation. Hot filaments in the target chamber and neighboring chambers are turned off to protect the crystal from electron emission and the glass windows are covered to avoid the UV-light in the vacuum chambers. Exposure of UV light or electrons in the 2 to 10 eV energy range is sufficient to break the Si-H bond, leading to reconstructions of the Si(111):H(1 \times 1)

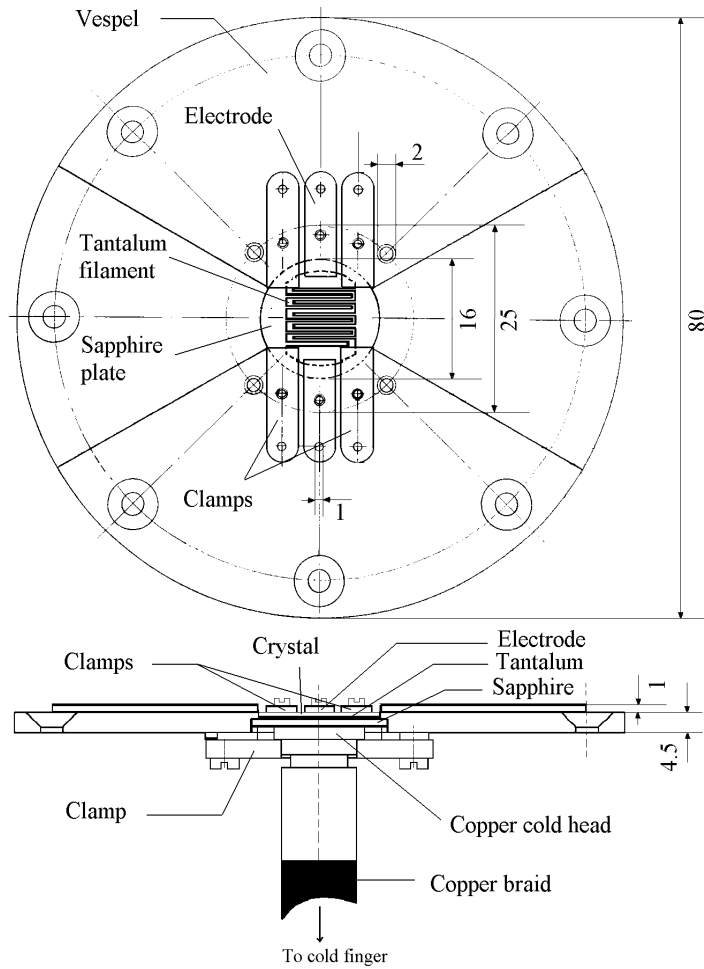


Figure 5.2: Schematic top view and side view of the Si(111):H(1×1) sample holder. The crystal is not depicted in the top view scheme to show the tantalum sheet. The thermocouple (not shown in the figure) is pressed on the crystal with the clamps after the crystal is mounted. The clamp on the backside serves to connect the cold head after the holder is mounted onto the target manipulator.

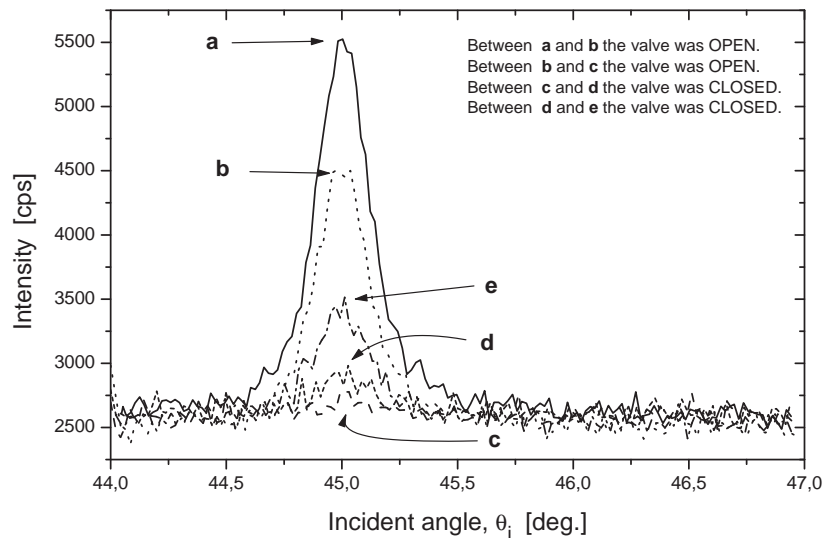


Figure 5.3: Angular scans of the specular peak for He-Si(111):H(1 \times 1) in the $\langle 110 \rangle$ direction. Crystal-B. $P_0=100$ bar, $T_0=298$ K, Iris=1 mm. When the beam entrance valve is kept open the specular peak intensity deteriorates and when the valve is kept closed the intensity recovers but not to the original value. Between the scans **a** and **b** the valve is left open for 2 hours and intensity decreased by 30% ; between **b** and **c** the valve is left open for 23 hours and the peak was almost disappeared; between **c** and **d** the valve is left closed for 5 hours and the intensity has recovered slightly; between **d** and **e** the valve is left closed for 15 hours and the intensity reached 30% of the initial value.

surface [250, 251].

Three samples have been tested in the course of this project and are labelled as Crystal-A, B, and C. The first crystal (Crystal-A) showed no coherent reflection at first. Upon slight heating (about 50 °C) a very small specular reflection is observed (see also Table 5.1) and the specular peak intensity disappeared completely within two days. This indicated that there was still some contamination in the target chamber. To remove the contamination the manipulator and glass window with Viton sealing were taken out and all pieces of the manipulator were cleaned with acetone and the chamber was baked without the manipulator and the glass window up to 150 °C. A mass spectrometer was mounted to the target chamber to check the vacuum quality. The chamber was baked out again after the manipulator is remounted.

Crystal-B exhibited much better specular intensity (see Figure 5.3), however a signif-

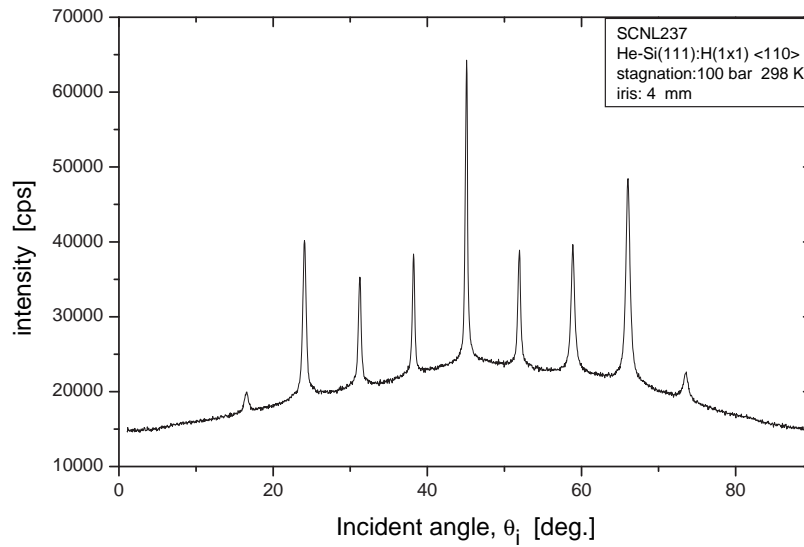


Figure 5.4: Angular scan of He diffraction from Si(111):H(1×1) along the $\langle 110 \rangle$ direction. Crystal-C. $P_0=100$ bar, $T_0=298$ K, $k_i=11.19 \text{ \AA}^{-1}$. Iris= 4 mm. $T_s=298$ K. $\theta_{SD}=90^\circ$. The incident intensity is given in Figure 4.8; note that the iris diameters are different.

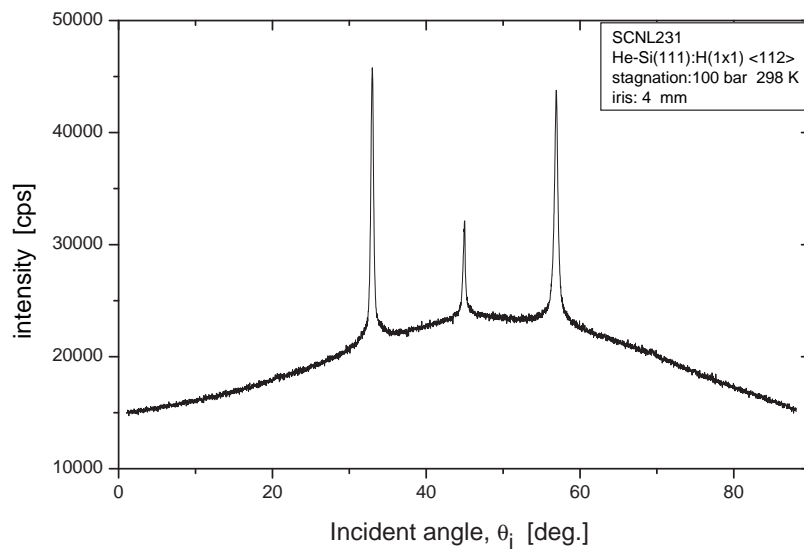


Figure 5.5: Angular scan of He diffraction from Si(111):H(1×1) along the $\langle 112 \rangle$ direction. Crystal-C. $P_0=100$ bar, $T_0=298$ K, $k_i=11.19 \text{ \AA}^{-1}$. Iris= 4 mm. $T_s=298$ K. $\theta_{SD}=90^\circ$.

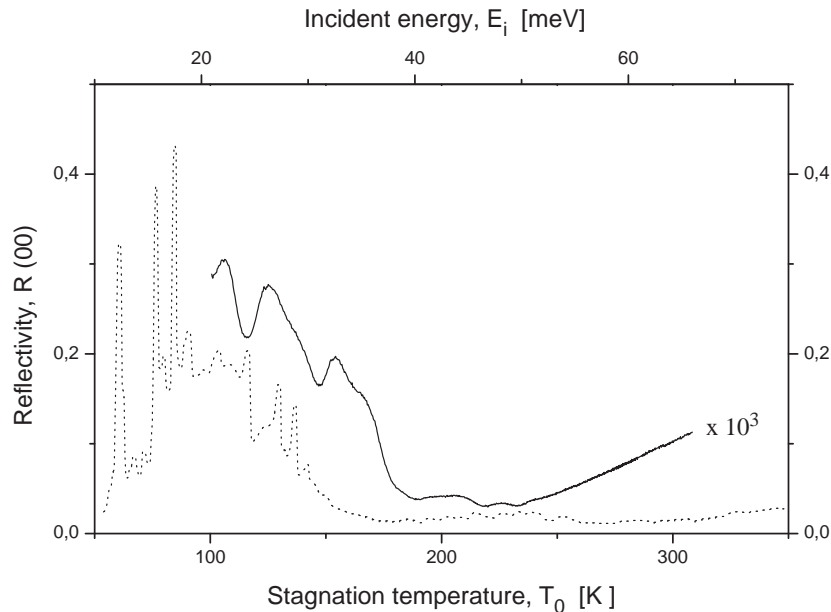


Figure 5.6: The stagnation temperature dependence of the specular peak reflectivity (peak intensity/incident intensity) along the $\langle 110 \rangle$ direction. Crystal-C. $\theta_i=45^\circ$. $P_0=100$ bar. Incident energies are found by interpolating several incident energy values at constant source temperatures by TOF, which give the incident energy corresponding to a stagnation temperature within an error of ± 2 meV. The reflectivity is found by comparing the initial specular peak intensity (within the 24 hours after the crystal put in) with the incident beam intensity provided in Figure 4.8. Theoretical values are provided with dotted lines [233]. The sharp peaks and dips at low incident energies are due to the selective adsorption resonances. Note that the experimental values are multiplied by a factor of 10^3 for comparison and the SAR peaks and dips are smoothed due to the energy spread of the incident beam.

icant and fast decay of the specular peak intensity was observed indicating impairment of the crystal surface: As seen in Figure 5.3 leaving the beam entrance valve connecting the iris chamber and the target chamber (see Figure 3.1) open between the measurements leads to significant decrease of specular peak intensity, thus has a detrimental effect on the crystal quality. When the valve was kept closed a slight recovery of the crystal was observed. This indicated that iris and chopper chambers⁴ are leading to a contamination. The iris and chopper chambers were cleaned and baked out with cleaning procedures similar to that of the target chamber. Also the iris made of plastic was replaced with a stainless steel one in order to avoid any possible organic contami-

⁴Both chambers are practically one chamber.

nation from the iris. A separate mass spectrometer is installed in the chopper chamber to check the cleanliness of the vacuum. The pressure of the chopper chamber after the bake out was lower than 1×10^{-10} mbar and the mass spectrum showed no sign of contamination.

Crystal-C showed high specular and diffractive intensity sufficient for further experimentation. The angular scans along the two high symmetry axes are shown in Figure 5.4 and 5.5. To our knowledge these measurements are the best resolved diffraction profiles from the Si(111):H(1×1) surface. Along the $\langle 110 \rangle$ direction up to fourth order diffraction peaks are observed. The surface corrugation leads maxima for zeroth and third order peaks. Along the $\langle 112 \rangle$ direction only first order diffraction peaks are clearly and second order diffraction peaks are barely observed. Strong surface corrugation leads maxima for the first order diffraction peaks and suppresses higher order peaks. In Figure 5.6 the beam stagnation temperature dependence of the specular peak reflectivity, $R(00)$ is shown in the range of 100-330 K⁵. The observed sharp peak and dips indicate selective adsorption resonances. The bound state energies for He-Si(111):H(1×1) are given in ref. [252]. The theoretical values [233] calculated by Buckland are also provided in the figure for comparison. The theory is done by CC-calculations using a hybrid potential (Born-Meyer form + cubic polynomial + z^{-3}) with a well depth of 7.54 meV [233]. The discrepancy between the experimental and theoretical values is about 10^3 and is due to the Debye-Waller factor whereas the calculations are carried out for a rigid surface and due to the surface defects since HAS is highly sensitive to the surface defects due to the large scattering cross sections [35]. The observed diffraction peaks and SAR features attest that the surface has a well ordered (1 × 1) symmetry with the lattice structure shown in Figure 5.1.

Nevertheless, there are three undesired features observed from the HAS measurements:

- Firstly, the crystal was slightly deformed in shape. This is clear from the fact that over the whole surface the angular position of the specular peak changes within 0.6° in tilting angle (β) and 0.2° in polar angle (θ_i). The crystal deformation is due to the strong pressure applied by the fixing clamps.
- Secondly, although the angles are optimized for each x-y positions, the measured specular intensity varies over the surface. In Figures 5.7 and 5.8 the x and y scans (moving the crystal in horizontal and vertical directions, respectively) of the specular

⁵ $R(00)$ is the ratio of the specular peak intensity and the incident beam intensity as given by Equation 7.7.

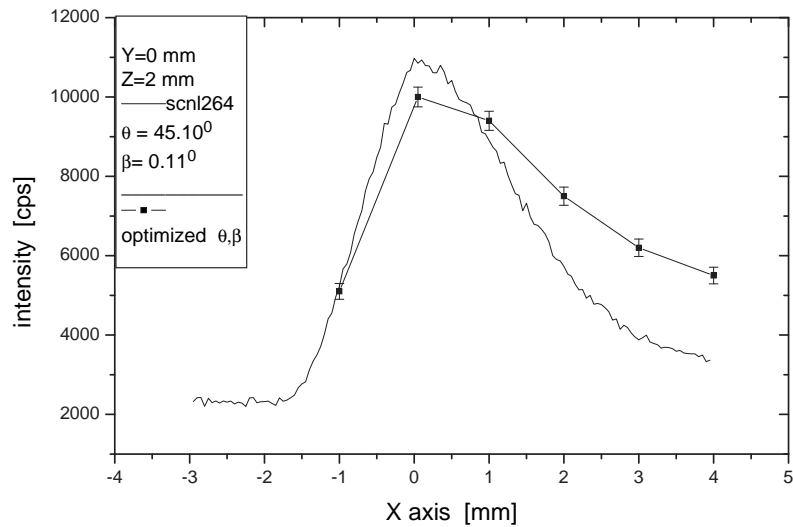


Figure 5.7: The intensity of the specular peak depending on x position for two cases where one scan is carried out at fixed angle (—) and one scan carried out by optimizing the polar and tilt angle at each x position (---). Crystal-C. $\theta_i=45^\circ$. Note that the maximum of the optimized scan is less than the maximum of unoptimized scan due to the detrimentation of the crystal reflectivity. Iris diameter is 0.7 mm.

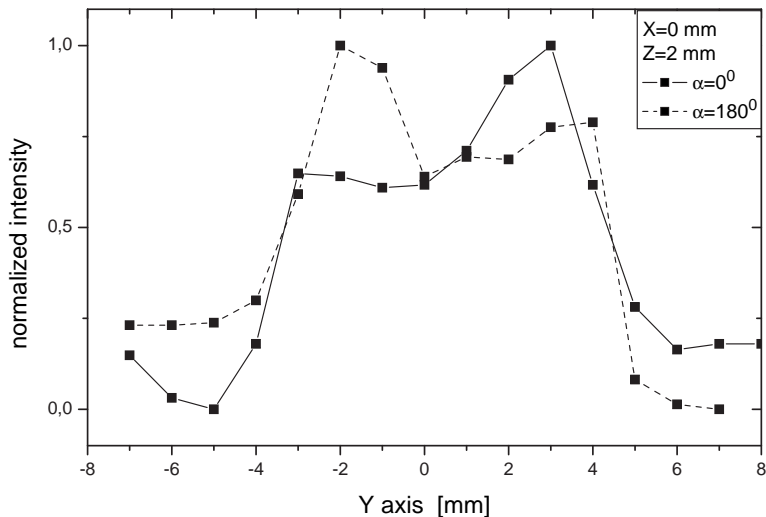


Figure 5.8: The intensity of the specular peak depending on y position with optimized polar and tilting angles and for $\alpha=0^\circ$ (solid line) and $\alpha=180^\circ$ (dashed line). Crystal-C. Iris=0.7 mm. $\theta_i=45^\circ$.

peak intensity are shown. The reflectivity of the crystal varies up to 50% over the crystal surface on a x and y line indicating that the quality of the surface varies significantly over the surface. When the crystal is rotated around the direction normal to the surface by 180° it gives the same but mirrored profile (see Figure 5.8), indicating that the varying intensity is not due to the misalignment and is purely an artifact of the surface reflectivity ⁶.

The fabrication of Si(111):H(1×1) surface comprises long subsequent procedures of wet-chemical cleaning, re-oxidation, etching and passivation which requires stirring the solution to dislodge evolving bubbles in the solution which might have failed for the particular sample and for a certain region of the surface [253,254]. Additionally, at the final stage of anisotropic etch to smooth the surface the stirring of the etchant is not performed as it is regarded to have disadvantageous effects [232]. In wet-chemical methods the homogeneity of chemical processes over the entire surface of cannot be always guaranteed and such problems may lead to a lack of homogeneity of the surface defect density on the resulting surface. Although the AFM analysis indicated no clue of inhomogeneity [232, 246], HAS experiments provide an ultimate test of the surface quality over several millimeters with its superior sensitivity to surface defects and roughness.

- Thirdly, a decrease of reflectivity $40\% \pm 10$ per week is observed. This was a surprising result since extreme precautions were taken for the cleanliness of the vacuum. When the crystal is heated at about 50 °C the specular intensity extinguished within 30 minutes absolutely and when the heating is turned off it recovered partially to about 50% of the intensity before the heating. The detrimental heating of a clean surface, however, could only occur over 400 °C [232], leading to hydrogen desorption. Hence, it indicates a source of contamination which is enhanced due to the heating of the sample holder or an augmentation of the reactivity of the contamination which already exists on the surface.

The mass spectrum of the target chamber showed no clue of contamination at first look as provided in Figure 5.9. Although most of the potential organic contaminations, such as pump oils, have much larger masses than the provided mass range, they exhibit many ion fragments at low masses [255]. The sensitivity of the mass spectrometer is about 4×10^8 (V/mbar)⁷ and the minimum detectable partial pressure is about 10^{-12}

⁶Both these effects are not observed with cleaved LiF crystals, i.e. see Figure 6.3, thus the effects are purely due to the silicon crystal.

⁷The analog output of the mass spectrometer is in volts and read through a Keithley multimeter and GPIB interface with computer.

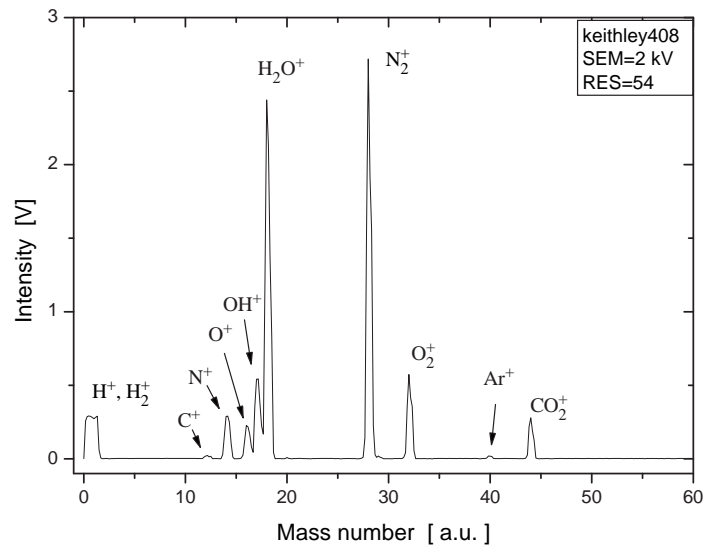


Figure 5.9: The mass spectrum of the target chamber with crystal holder in the range of 0-60 a.u. $P_{TC}=3.4\times 10^{-8}$ mbar.

mbar. The minimum detectable pressure is increased by a factor of 100 by reducing the mass resolution and increasing the multiplier voltage of the spectrometer; and measuring 60 points (1 sec/point) per mass unit and smoothing the measured curve (averaging each point with 50 adjacent data points).

With this enhanced sensitivity additional small peaks indicating contamination in vacuum are observed, as shown in Figure 5.10. The mass spectra of the vacuum with and without the sample holder mounted but with same pumping histories showed significant differences. The mass spectrum without the sample holder has small peaks at 55 and 57 one day after the pumping down and they disappear after several days. However the mass spectrum with the sample holder has large peaks at 58 and 55 one day after the pumping down and they are observable even after 5 months of pumping. The observed peaks are typical fingerprints of hydrocarbon compounds. This shows that the sample holder made of Vespel is the source of contamination.

The observed peaks can be originating from the Vespel material itself or from species absorbed from the air or contacting materials on the Vespel surface. For instance, the Vespel piece was cleaned with acetone after it was machined and mass-58 ($(\text{CH}_3)_2\text{CO}^+$) is one of the main peaks of acetone in the mass spectrum. There is no data available for absorption and desorption rate of solvents for Vespel. Polyimide materials

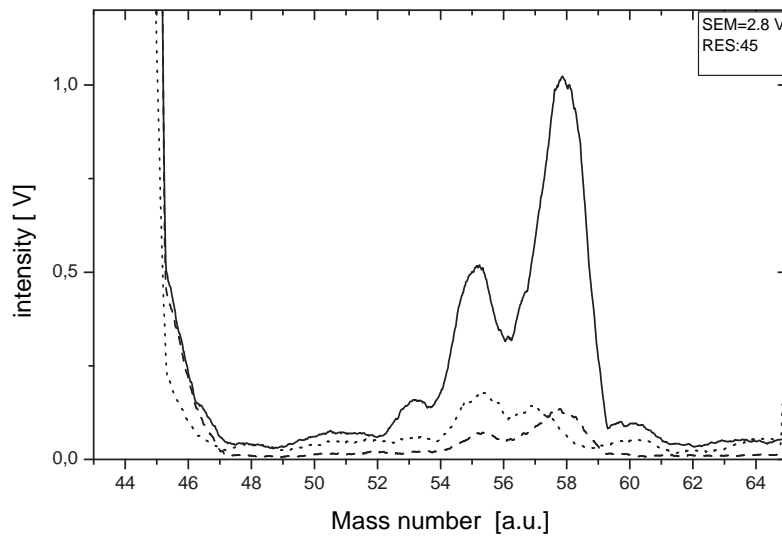


Figure 5.10: The mass spectra of the target chamber with enhanced sensitivity in the range of 43-65 a.u. showing the fingerprints of contamination. Solid line: Mass spectrum with sample holder after one day of pumping ($P_{TC}=1.9\times 10^{-7}$ mbar). Dashed line: Mass spectrum with sample holder after 5 months of pumping ($P_{TC}=3.4\times 10^{-8}$ mbar). Dot line: Mass spectrum of empty vacuum chamber after one day of pumping ($P_{TC}=1.6\times 10^{-7}$ mbar).

are characterized by a ring-shaped molecular structure containing Nitrogen. To our knowledge there is no discrete mass spectrum data of the outgassing of Vespel to compare with. The outgassing rate of the Vespel after a 12-hour bake out is about 10^{-10} torr·liters· s^{-1} · cm^{-2} (less than of the Viton) and after 5-hour air exposure the outgassing rate is about 10^{-7} torr·liters· s^{-1} · cm^{-2} (10 times more than of the Viton) [256]. The main outgassing species from Vespel are water and CO_2 which are already existent in vacuum without the holder and slight increase in the total pressure with the holder can be assigned to these. High temperature mass-spectra direct-probe analysis showed a major peak at mass-59 at the temperature of $740^\circ C$ [257]. However the major volatile substances at room temperature can be pretty different. It is well known that vacuum elastomers have high gas permeability and high desorption rates compared with metal, glass and ceramics [258]. Mass integrated mass spectrum measurements show that the outgassing rate of Vespel (after one hour bake at $100^\circ C$) for masses larger than 41 a.u., which is predominantly volatile species, is less than 17 ppm/s but significantly larger than for the Viton-A with the similar sample history [259].

Table 5.1: The summarized results of three samples. The intensities are the very first measurements of each crystal and for specular peak along the $\langle 110 \rangle$ direction, for iris diameter of 1 mm and the inelastic background is subtracted.

Sample	Intensity, $I(00)$	Observation	Conclusion
Crystal-A	400 cps upon heating by 50 °C.	Fast deterioration of the surface	Contamination from the crystal chamber
Crystal-B	3000 cps.	Deterioration of the surface when the beam entrance valve opened	Contamination from the iris and chopper chamber
Crystal-C	2500 cps	Slow deterioration of the surface	Contamination from the Vespel piece.

The partial pressure of the contaminants is estimated from Figure 5.10 approximately⁸ as 10^{-14} mbar. This pressure corresponds to an exposure of 10^{-2} Langmuirs per week [72]. The strong attenuation of the He beam is a well known process and the cross-sections of adparticles are about 100 \AA^2 [23, 260]. The observed degradation of specular peak intensity by 40% per week is in good agreement with the predicted exposure rate, if it is assumed that the intensity decrease is proportional to the adatom density.

5.2 Conclusions

The observed effects and their reasons for the three investigated samples are summarized in Table 5.1 in tabular form. These results are promising and indicate that the cleanliness of the crystal surface can be maintained for long transportation and short-term air exposure in ordinary laboratory conditions. The surface quality was high and sufficient to carry out He scattering experiments. The He atom scattering from surface showed intense diffraction peaks and sharp selective adsorption profiles. All these indicate that the manufacturing and transportation steps, which are crucial for the development of focusing mirror, are satisfactory.

It has been observed that the cleanliness of vacuum and the selection of materials

⁸The partial pressures are calculated from the ratio of total intensity of all peaks in the mass spectrum and the total pressure measured by pressure gauge without taking the different ionization probabilities of gas species into account.

for use in vacuum parts is very crucial. Generally the use of polymers and rubbers, although they are regarded as clean and vacuum compatible, should be avoided or their use must be kept at a minimum due to the extreme sensitivity of Si(111):H(1×1). The indispensable parts such as Viton and Teflon sealings must be well outgassed. For the sample holder Macor can be used instead of Vespel; it is more difficult to machine, however less porous and has lower outgassing rates.

The reflectivity of the fresh crystal is measured to be about

$$R(00) = \frac{I(00)}{I_0} \simeq 1 \times 10^{-4} \quad , \quad (5.1)$$

for room temperature beam ($E_i \simeq 65$ meV). Here $I(00)$ and I_0 are the measured specular peak and incident beam intensities, respectively. This value is reasonable according to theoretical considerations: The estimated transition probability of the specular peak from CC-calculations is about $P(00)=0.02$ [234]. In addition to this, the thermal attenuation of the elastic peaks must be considered since theoretical calculations were carried out for a static surface. The thermal vibrations of the atoms at the Si(111):H(1×1) surface have been theoretically investigated [261, 262]. The perpendicular mean square amplitude of H atoms at room temperature at the surface is determined as $\langle u_z^2 \rangle = 0.0177 \text{ \AA}^2$ [261]. One can write the thermal attenuation in Equation 2.47 for specular reflections as

$$2W = 4k_{iz}^2 \langle u_z^2 \rangle \quad . \quad (5.2)$$

Here k_{iz} is the perpendicular component of the wave vector of the incident atoms. At a first approximation acceleration of impinging atoms due to the potential well depth can be ignored (see also Section 2.4). Assuming that the thermal attenuation of scattering atoms is only due to the vibrations of surface H atoms, the thermal attenuation of the specular peak is calculated to be about $e^{[-2W]} = 0.012$ by using Equations 2.46 and 5.2 and for $k_i = 11.2 \text{ \AA}^{-1}$. Thus the estimated reflectivity for an ideal surface is

$$R(00) = P(00) \times \exp[-2W] = 2.4 \times 10^{-4} \quad . \quad (5.3)$$

Considering the further reduction of coherent intensity due to the effects of the surface steps and defects the estimated reflectivity gets closer to the measured value. However, the theoretically estimated reflectivity can be erroneous. For instance, as shown in Figure 5.6, for liquid nitrogen cooled beam ($E_i \simeq 20$ meV) the intensity is increased only by a factor of 3, however the theory predicts an enhancement of the reflectivity by a factor of 10 as shown in Figure 5.6. The discrepancy between the experimental

and theoretical values is much larger for the low incident energies. Thus, the theoretical calculations must be revised with a best-fit potential in the light of the angular distributions of diffraction peaks and the incident energy dependent specular intensity measurements provided above.

Compared to the other crystal surfaces the reflectivity of the Si(111):H(1×1) crystal surface is rather poor. The specular reflectivity of the LiF(001) surface with a He beam of incident energies of 65.8 meV and 18.2 meV was found to be 0.3% and 3%, respectively (see Figures 6.6 and 6.8). For metal surfaces the specular reflectivity is mostly higher than for the LiF(001) surface with a factor of 10 to 100, because the corrugation sensed by the He atom on metal surfaces is small, resulting in negligible diffraction peak intensities and the specular peak is the only dominating peak.

The obtained reflectivity of Si(111):H(1×1) surface can be improved with better crystal preparation, transportation methods and vacuum conditions, particularly when the use of vacuum elastomers are avoided. Also the theoretical reflectivity may be different than the estimated value here where a more realistic interaction potential can lead to a higher or lower specular reflectivity. Taking the number of open channels into account⁹, the theoretically calculated specular peak reflectivity of 2% (without DW factor) [234] for the room temperature beam is reasonable unless there is a strong rainbow effect. Also the actual DW factor can be somewhat higher than the estimated value due to the contribution of heavier Si atoms. However, it is difficult to calculate this contribution. Thus, although small improvements in the both theoretical and experimental reflectivity of the Si(111):H(1×1) surface are possible, these are not expected to be more than by an order of magnitude. In the work reporting that the specular intensity should be 20-30% of the incident beam [234] for the liquid nitrogen cooled beam, does not correspond to the reality where, partially, the interaction potential should be refined and mainly the DW factor was simply overlooked.

Although the reflectivity decreased slowly due to the contamination in vacuum, the given reflectivity here is the reflectivity of the freshly installed crystal. A much better reflection or a more clean surface is not expected, unless the fabrication and transportation methods are improved or there was an unnoticed and accidental contamination during the fabrication or transportation in the present experiments.

⁹The number of open channels can be estimated approximately as $\frac{\pi k_i^2}{\sigma}$ which gives the ratio of accessible area and the area of Brillouin zone (σ) on the reciprocal lattice plane. For a room temperature beam $k_i \simeq 11 \text{ \AA}^{-1}$ and for Si(111):H(1×1) surface $\sigma \simeq 6.3 \text{ \AA}^{-2}$. Thus the coherently scattered intensity is distributed over about 60 open channels equally when the corrugation effects are excluded.

6. Thermal Expansion of the LiF(001) Surface

Until now the attention paid to surface relaxation, thermal expansion and vibrations focusses mainly on the direction normal to the surface [263–273]. At the surface, compared to the bulk, it is expected that anharmonicity is enhanced due to the reduced coordination and thus a relaxation normal to the surface plane is expected. The difference between the bulk and the surface phonons of alkali halides have already been investigated [274–276]. However all these calculations are based on the harmonic approximation. Using the quasiharmonic approximation of an unrelaxed slab, Chen *et al.* calculated that the mean-square amplitudes (MSA) of thermal vibrations perpendicular to the surface of the LiF(001) at crystal temperatures above 300 K are for negative and positive ions, respectively, 65% and 35% higher than in the bulk [275]. The lattice-dynamical models with simple anharmonic model potentials showed that at high temperatures the thermal expansion normal to the surface can be approximated as¹ [277–279]

$$\frac{\alpha_s}{\alpha_b} = \frac{3 \langle u_z^2 \rangle_{surface}}{4 \langle u_z^2 \rangle_{bulk}}, \quad (6.1)$$

where α_s and α_b are the thermal expansion coefficients of the surface and the bulk. This is a simple consequence of the reduced coordination. Although this expression mostly does not provide good agreement with the experiments [263, 278] due to the lack a realistic potential and due to the surface relaxation and reconstruction, it gives an idea of the enhanced surface vibrations and thermal expansion.

As a result of the reduced coordination the surface vibrations are also expected to be anisotropic and mean-square amplitudes parallel to the surface are predicted to be enhanced [274–277]. Similar calculations by Chen *et al.* showed that the MSA of thermal vibrations along the surface of the LiF(001) are about 30% larger than the

¹A general expression of the coefficient of linear expansion is given in Equation 6.9.

bulk values [275], which are similar to the MSA in surface normal. In order to extend such theoretical investigations to the thermal expansion parallel to the surface, a more realistic treatment of the system is necessary in which vacancies and steps are included. The calculations of surface distortions of stepped and kinked NaCl crystal surfaces showed surface atom displacements in the order of 5-10% of the lattice constant parallel to the surface [280–282]. Although these calculations are based on static potentials, they give an idea about how a discrepancy between the surface lattice constant and the bulk lattice constant may appear. Furthermore, the creation and annihilation of surface defects and their rearrangement with increasing temperature can enhance the static displacements of surface atoms, thus enhancing the thermal expansion of the surface. Conversely, they may also compensate the lattice constant discrepancy resulting from the enhanced anharmonicity of surface atoms.

The precise determination of surface lattice constants is necessary for the accurate measurement of surface parameters which are \mathbf{G} -vector dependent such as the bound state energies, or the dispersion of surface phonons. Moreover, the knowledge of the relaxation parallel to the surface, can provide a better insight into surface related phenomena, such as adsorption and the relaxation perpendicular to the surface of alkali halide surfaces, which is still in progress [60, 61].

The surface anharmonicity parallel to the surface has been experimentally investigated only in a few studies. Frank *et al.* measured the thermal expansion of surfaces using selective adsorption resonances of H and D atoms on NaF(001) and LiF(001) [4, 57]. They observed a thermal shift of the selective adsorption resonance positions which is related to the change in \mathbf{G} vector and concluded that the thermal expansion surface coefficients of surfaces (α_s) were about two times larger than the bulk values (α_b) at high temperatures. Watanabe *et al.* measured the position of the diffraction peaks of the LiF(001) by using HAS and concluded also that α_s was higher by a factor of 3.6 than α_b [5]. There are other reports mentioning that the α_s for other surfaces are somewhat different than the bulk values: Glebov has reported that the α_s coefficient of AgBr(001) measured with HAS was 13% larger than the bulk value [283]. Traeger measured, also with HAS, α_s coefficient of KCl(001) surface as 27% less than the bulk value given in the literature [284]. Nestrenko *et al.* carried out LEED experiments on Si(111), Ge(111) and GaAs(110) and reported that α_s s were larger than α_b s by factors of 8, 4 and 3, respectively [285].

In this chapter, the diffraction of He atoms on LiF(001) along the $\langle 100 \rangle$ and the $\langle 110 \rangle$ directions is measured by rotating the crystal and keeping the detector at a fixed angle. The lattice constant is calculated from the elastic diffraction peaks observed by

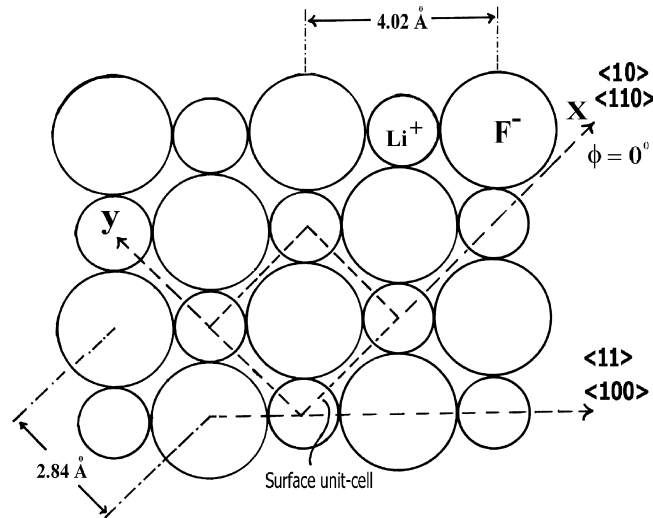


Figure 6.1: The geometrical structure of the LiF(001) surface. The bulk fcc lattice of the rock salt crystals form a square checkerboard two-dimensional net of alternating Li^+ cations and F^- anions. The x and y directions have been defined to lie along the $\langle 110 \rangle$ directions.

in-plane scattering of He atoms and determining the momentum of He atoms with TOF. With careful consideration and control of the experimental precision, the lattice constants at different surface temperatures, $a(T)$ and the thermal expansion coefficient of the surface lattice, $\alpha(T)$ are determined with unprecedented accuracy. In the next section, the properties of the LiF(001) surface are discussed first. Then, the experimental procedure and results are presented. Finally, the results are discussed and compared with the previous results.

6.1 LiF(001) Surface

The LiF crystals were purchased from the company Korth Kristalle². The crystals are cleaved in air into 3-4 mm slices from larger slabs of cross-section of 10x10 mm. The cleavage results in a clean "almost" single-faceted surface of (100) orientation. The structure of the LiF(001) surface is shown in Figure 6.1 and the general bulk and surface properties are given in Table 6.1.

²Karl Korth Kristalle GmbH, Altenholz, Germany. To our experience, not all cleaved crystals have a good surface quality, namely sometimes the cleavage ends up with several facets. The crystals ordered in 2002 had bad quality after cleavage. The crystals used were purchased from the same company but about ten years ago.

Table 6.1: The properties of LiF crystal and its (001) surface. Remarks: (a) at room temperature from ref. [286]; (b) from ref. [287]; (c) with He from ref. [288]; (d) with He from ref. [289]; (d) without Armand correction [290]; (f) with H from ref. [76]; (g) with He from ref. [291] (this is just the bulk value divided by $\sqrt{2}$); (h) with He in this work (Section 6.2.3); (i) with D₂ in this work (Section 7.3); (j) for the untreated surface from ref. [292]. In the Armand correction, the possibility of the interaction of the scattering atom with more than one surface atom is taken into account and the Debye temperatures are corrected according to the scattering geometry [290].

Density	$2.635 \times 10^3 \text{ kg m}^{-3}$
Lattice constant	4.0262 \AA^a
Bulk Debye temperature	734 K^b
Melting Temperature	1115 K
Surface Debye Temperature	$335 \pm 33 \text{ K}^c$, $350 \pm 50 \text{ K}^d$ (513 K^e), $415 \pm 44 \text{ K}^f$ (610 K^e), 520 K^g , $478 \pm 10 \text{ K}^h$, $577 \pm 50 \text{ K}^i$
H ₂ O adsorption energy	$200 \pm 50 \text{ meV}^j$

Surface Cleanliness: In the earlier years, the cleanliness of the alkali halide surfaces was a matter of question regarding both gas-surface and epitaxial growth studies [57, 69, 293]. The ellipsometric measurements of Bayh *et al.* on large single alkali halide crystals indicated that on the LiF surface, cleaned under poor vacuum conditions (10^{-6} torr), four layers of adsorbed water formed and the first monolayer was still present at temperatures as high as 770 K [294]. These results led most of the researchers working in the gas-surface field with alkali halides to believe that they had actually probed the properties of thin epitaxial water films arranged in the same structure as the surface and unrealistic gas-surface potentials were justified with this argument [62, 69, 87, 295]. However, attempts to duplicate and extend these earlier measurements subsequently failed and totally different results were obtained, reporting that no ellipsometric variations were observed for alkali halide surfaces exposed to water partial pressures in the range of 1 to 10^{-6} torr and it has been concluded that alkali halides have water-free surfaces after baking out at temperatures of 620-720 K and residual pressures of less than 10^{-9} torr [296]. More persuading and systematic evidence for the inertness of the LiF surface was supplied using secondary ion emission spectroscopy (SIMS) by Estel *et al.* [292]. They investigated (001) planes of

LiF, NaF and NaCl under UHV conditions with a variety of cases: air and vacuum cleaved; with and without bake-out; and with and without exposure of water at various crystal temperatures. They concluded that the cleaved crystal surfaces are free of water and hydroxide layers under UHV conditions. Water can be adsorbed on unannealed LiF surfaces at a partial pressure of 10^{-9} torr below 200 K. The adsorption energy for LiF(001) is 200 ± 50 meV [292]. Thicker layers of water will grow according to the Volmer-Weber mechanism. Baked out crystals (18 hours at 700 K), however, are found to be virtually inert to hydroxylation and water adsorption is possible only under extremely forced conditions. The inertness of the annealed crystals is attributed to the removal of active sites, such as surplus Li^+ metal ions on the surface [292]. This evidence is supported by other observations [297, 298], which had negated the previous opinion that alkali halide surfaces are hard to clean and showed that, particularly water insoluble alkali halides (NaF, LiF), following a proper bake out, are hard to contaminate.

Surface Relaxation: The clean alkali halide surface exhibits both relaxation and rumpling, where the top layers of anion and cations do not lie in the same plane but are separated from each other slightly in the direction of surface normal. The relaxation is compatible with a (1×1) surface of rock salt type and no reconstruction is reported for the LiF(001) surface³. Relaxation and rumpling of the (100) surface of alkali halides were first predicted theoretically by Benson *et al.* [300–302]. They predicted that at top layer of LiF(001) the lithium ions should relax by 0.12 \AA inwards, however the convergence of calculations involving the relaxation of more than one layer failed and made the results doubtful. The first evidence came from the detailed analysis of experimental results of McRae *et al.* [303] by Laramore *et al.* [304]. They found that certain features of the LEED intensity profiles measured by McRae *et al.* strongly suggest that the Li^+ and F^- subplanes in the uppermost layer are separated by about 0.25 \AA at 573 K. Relative to the ideally terminated surface, the top Li^+ and F^- sublayers at 573 K are contracted about 0.35 \AA and 0.1 \AA towards the bulk, respectively. Recently, Vogt *et al.* carried out LEED experiments on alkali halides [60, 305] and concluded that the rumpling is rather small at the LiF(001) surface at 20 K [60], in contradiction to earlier results [304] but in agreement with theoretical calculations [306–310]. The fluorine ions found to (with rather large error bars) remain at their bulk positions and the lithium sublayer is contracted by $0.02\pm 0.10 \text{ \AA}$. However,

³An anomalous reconstruction of the NaCl(001) surface is observed only once [299]

more recently and more precisely, Roberts *et al.* reported larger relaxation values from a LEED analysis of multilayer LiF(001) thin films grown on Pt(111) at 115 K [61]. They observed an "intralayer" corrugation between the Li⁺ and F⁻ subplanes as 0.24 ± 0.04 Å in the uppermost layer and 0.07 ± 0.04 Å in the second layer. The "interlayer" spacing between the top and the second layer was determined as 1.77 ± 0.06 Å and the second interlayer spacing is found to be same as the bulk value ($=2.01$ Å) within the error bars. One possible explanation for the results of Robert *et al.* could be that the investigated thin films are more relaxed than the cleaved surfaces of massive crystals. In contrast, Mills *et al.*, using low energy positron diffraction, reported that the surface ions remain at positions similar to the bulk within the error bars of 0.01 Å [311]. Although all theoretical and experimental works report, qualitatively, a rumpling at the LiF(001) surface due to the asymmetric relaxation of Li⁺ ions towards the bulk, the magnitude of the relaxation (both intralayer and interlayer) is still not clear.

Step and Defect Density: The dynamics of cleavage and the resulting morphology of alkali halide surfaces has been studied extensively [312–318]. It is well known that cleaved surfaces of alkali halides contain many steps of heights down to a few atomic dimensions [313–316]. The dislocation density is estimated in the range $10^4 - 10^5/\text{cm}^2$ [313, 314]. Flush-shaped step configuration of dimensions of 50-500 nm are observed, however their appearance depends strongly on the cleavage conditions [314–316]. These results are in agreement with the measurements of HAS experiments, in which terrace widths broader than 30 nm were estimated [319, 320]. Mass spectrometer studies by Gallon *et al.* showed that dissociation of surface atoms occurs upon cleavage of the LiF, NaF and KCl, although different in character for each crystal [321]. The time development of the partial pressure curves of surface atoms was assigned by the authors to the non-stoichiometricity of the dissociation. This effect was most pronounced for LiF, where the decay of the fluorine signal was much slower than of the lithium signal. Although no quantitative analysis has been given, non-stoichiometric dissociation after the cleavage indicates that there should be some advacancies and adatoms in considerable density. In contrast, AFM studies on cleaved LiF surfaces have demonstrated that the surface has defect-free terraces [322].

6.2 Experiment

In the HAS scattering experiments, the diffraction profiles are measured at constant surface temperatures. The fluctuation of the surface temperature was ± 1 K during a specific diffraction scan. Diffraction patterns are recorded between 110-720 K crystal temperature in +20 K steps of a heating series and -20 K steps of a cooling series, thus providing $a(T)$ values for $\Delta T_s = 10$ K. The lowest crystal temperature is limited by the liquid nitrogen cooling of the sample. The upper temperature is limited by the loss in peak intensity. Although it is possible to see diffraction peaks at 800 K, the experiment is carried out only up to 720 K because of the reduced precision due to the decreasing intensity at high temperatures. The lattice constant is calculated by measuring the first order diffraction peaks and taking the mean value of the lattice constant calculated from each diffraction peak. Second order diffraction peaks are not taken into account because of their much lower intensities. Also the specular peak position is determined at each measurement because the heating of the crystal holder results in small shifts of the angular positions of the diffraction profile by up to 0.05° as seen in Figure 6.2. According to the shift of the specular peak position, the values of diffraction peak positions are corrected. When the crystal temperature is set to a new value it takes several hours to stabilize the angular positions of the peaks because the entire crystal holder temperature changes and the crystal normal according to the target manipulator shifts. To avoid the long waiting times the angular scans for the diffraction and the specular peaks are taken only in a small angular region, and as quickly as possible so that the error due to the slow shift of the peak positions is minimized.

6.2.1 Surface Preparation

The LiF crystals are cleaved in air and put into the vacuum chamber within 5 minutes as described in Section 3.1.6. The cleavage in air results in a clean and atomically flat surface so that the elastically scattered beam was good enough to do experiments without any annealing. However a significant loss of the signal was observed when the crystal was cooled under 200 K as a result of water adsorption at active sites. The background pressure of the crystal chamber was between 1×10^{-9} and 3×10^{-8} mbar during the experiments depending on whether the crystal is cooled or heated. Therefore, to anneal the defects the crystals were baked out for 15 hours at 800 K. Although this treatment had little effect on the scattered signal at room temperature,

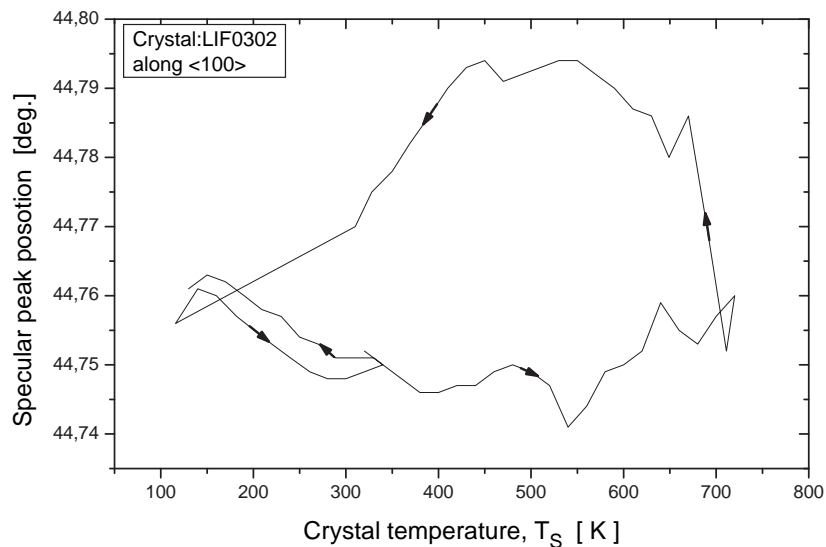


Figure 6.2: The shift of the specular peak position during the measurement at different crystal temperatures. The arrows show the sequential temperature direction of the experiment. Namely, the crystal temperature is gradually ($\Delta T_s=20$ K) increased from 320 K up to 720 K, decreased down to 116 K and then increased again up to 340 K, and finally decreased down to 130 K. The hysteresis of the specular peak depends on the cooling and heating rate and the waiting time at a constant temperature.

it did lead to a significant increase in signal when crystal was cooled, which is in accordance with previous works [292, 297, 298] and with discussions above.

Two crystals used in this thermal expansion experiments were labelled as LIF0302 and LIF0702. The quality of the cleavage, namely facets was tested by observing the specular peak intensity as the crystal is moved in x- and y- directions (upwards and sideways on surface plane). In Figure 6.3, a x-scan of the specular peak is shown. The intensity is almost constant when the whole beam spot falls onto the crystal surface. Thus, it shows a single faceted surface. A multiple-faceted surface would result in varying specular intensity with changing x-position due to the splitted specular peaks at a constant x-position⁴ and would make it difficult to determine the peak positions accurately.

As discussed in Section 3.2.3 the shape of the diffraction peaks is determined by both the instrumental resolution (geometrical resolution and beam monochromaticity) and

⁴These effects were observed for a few samples.

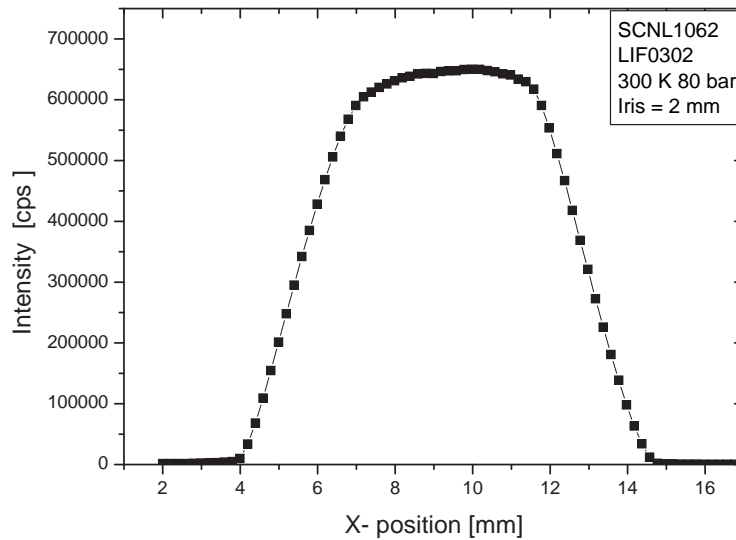


Figure 6.3: X-scan of the specular peak of the crystal LIF0302. The profile attests that the cleavage resulted in a single-faceted surface. The iris diameter is 2 mm and the incident angle is, $\theta_i=45^\circ$, leading to an elliptical spot of dimensions 2.7 mm and 3.7 mm on the surface, along y and x axes, respectively.

the domain size of the surface probe. The broadening of the specular peak is, however, independent of the beam monochromaticity. The specular peak width is determined by introducing two 200 μ -wide slits defining the beam divergence and detector opening as shown in Figure 6.4. The results of specular peak scans of both crystals and in the $\langle 100 \rangle$ and $\langle 110 \rangle$ directions are listed in Table 6.2. The average domain sizes are calculated using Equation 3.32. This model, however, is a rough estimate and presumes that all contributions of broadening have Gaussian form. A more accurate method would require defining a realistic slit function and deconvoluting the measured peak with it. Moreover, since the surface domains on the surface are not well defined, a more realistic analysis is difficult. Taking all these sources of error into account, it is concluded that the average domain sizes of the cleaved LIF0302 and LIF0702 crystals are about 140 ± 40 nm and 230 ± 80 nm, respectively. The results indicate that average domain size may change from cleavage to cleavage and it is also possible that the average domain sizes depend on the direction. These value are similar to the results from electron microscopy studies of cleaved alkali halides [315, 316].

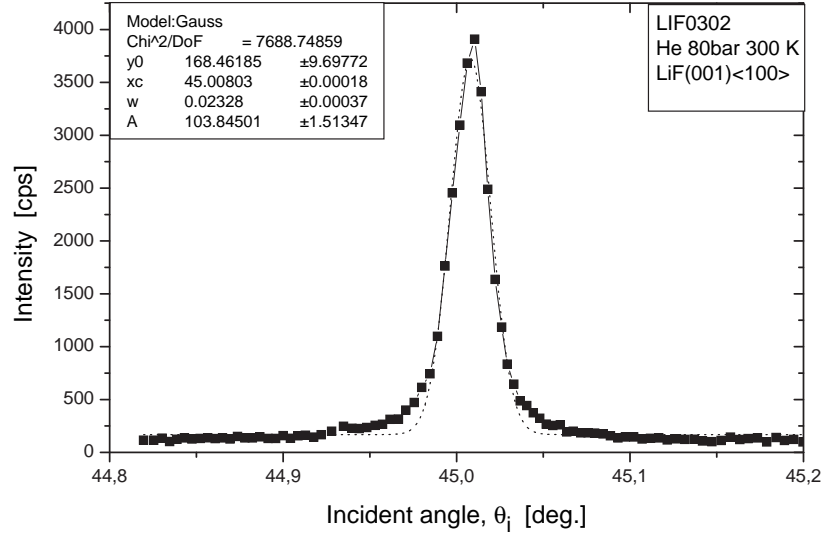


Figure 6.4: The profile of the specular peak with the 200 μ -wide beam and detector slits with angular steps of 0.005°. Crystal:LIF0302 in the $\langle 100 \rangle$ direction. $P_0=80$ bar and $T_0=300$ K. Crystal temperature is 297 K. The fitted Gaussian peak is shown with dotted-lines and its parameters are provided in the caption.

Table 6.2: The peak width results of specular peak scans and the calculated average domain size for each peak width using Equation 3.32. Wavelength of the incident He beam is, $\lambda=0.56$ Å. The instrumental peak width is 0.015°, which is defined by the collimating slits.

Crystal	Azimuth	Peak width	Av. Domain size
LIF0302	$\langle 100 \rangle$	0.023°	130 nm
LIF0302	$\langle 110 \rangle$	0.022°	150 nm
LIF0702	$\langle 100 \rangle$	0.019°	210 nm
LIF0702	$\langle 110 \rangle$	0.018°	250 nm

6.2.2 Precision Considerations

The lattice constants are measured from the Bragg conditions of the elastic peaks given in Equation 2.6, which can be expressed for a constant total scattering angle $\theta_{SD}=90^\circ$ as,

$$G = \frac{2\pi}{a} = k_i[\cos \theta_i - \sin \theta_i] \quad , \quad (6.2)$$

where k_i is the wave vector of the incident beam and θ_i is the incident angle where the diffraction peak observed. Therefore, the exact determination of the lattice constant requires the precise determination of both the wave vector of the atomic beam and the angular positions of the elastic peaks and the error of the lattice constant can be given as

$$\frac{\delta a}{a} = \frac{\delta k_i}{k_i} + \delta \theta_i \frac{[\sin \theta_i + \cos \theta_i]}{[\sin \theta_i - \cos \theta_i]} \quad (6.3)$$

The precision of incident wave vector determined by TOF depends on the accuracy of flight distance (L_{CD}), the fluctuation of the source temperature and the accuracy of the measured TOF peak position. The precision of the angular measurements depends on the measurement of the total angle θ_{SD} , adjustment of the azimuthal and tilting angles, the quality of the beam collimation and the accuracy of the determination of the diffraction peak positions. The largest error sources are systematic (or static) errors, such as the flight distance and adjustment of the azimuthal angle and the beam collimation. The TOF spectra showed no systematic changes and also the diffraction peak intensity ratios remained almost constant at different crystal temperatures. Thus the azimuthal angle and the flight distance do not change upon heating and they remain constant once the flight distance is calibrated and the beam collimation and the azimuthal angle of the crystal are adjusted after mounting the crystal. Therefore they do not contribute the error of the thermal expansion coefficient, $\alpha(T)$. For the latter only the relative changes and statistical errors are important. Hence, in the discussion of the precision of the lattice constant, it is needed to discriminate the "absolute" and the "relative" error of the $a(T)$.

TOF Accuracy: The measurements are carried out at a constant source temperature of $300.00 \pm (< 0.05)$ K. In Figure 6.5 a typical TOF spectrum of the specular peak is shown. During the experiments many TOF spectra are taken to observe the stability. All measured values of the time-of-flight were determined to be within $t_F = 1.2718 \pm 0.0002$ ms. The error bar is due to the temperature fluctuation and goodness of the fit. As discussed in Section 3.2 the flight length (chopper-to-detector distance) is given

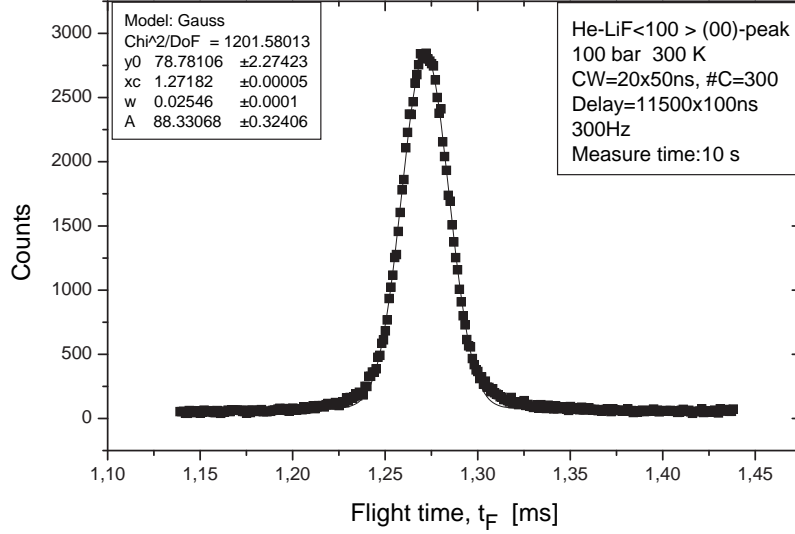


Figure 6.5: The TOF spectrum of the specular peak. The source temperature and pressure are $T_0=300$ K and $P_0=100$ bar, respectively. The $t_F=1.2718$ ms $L_{CD}=2266$ mm and the $k_i=11.2295$ \AA^{-1} and speed ratio is about 94. Although the TOF bins are $1\mu\text{s}$ (black squares), the peak position can be determined with Gaussian fit curve with an error of 0.05 μs and about a hundred TOF spectra taken during the experiments had the same peak position within the error of 0.2 μs .

as $L_{CD} = 2266 \pm 2$ mm⁵. The incident beam wave vector is then given by

$$k_i = \frac{m}{\hbar}u = \frac{m}{\hbar} \left(\frac{L_{CD}}{t_F} \right) . \quad (6.4)$$

Thus, the absolute and relative errors of the wave vector are given as

$$\left[\frac{\delta k_i}{k_i} \right]_A = \frac{\delta L_{CD}}{L_{CD}} = \pm 8.8 \times 10^{-4} \quad \left[\frac{\delta k_i}{k_i} \right]_R = \frac{\delta t_F}{t_F} = \pm 1.6 \times 10^{-4} . \quad (6.5)$$

Here $\delta L_{CD} = \pm 2$ mm is the calibration error of the flight length and $\delta t_F = \pm 0.0002$ is the accuracy of the peak position in TOF spectrum⁶.

⁵The detector position, L_D is set to 300 mm and L_{CD}^0 is found to be 2566 mm (see Section 3.2) when in situ TOF calibration is made for $\theta_{SD}=90^\circ$. Although this value is similar to the measured L_{CD}^0 for $\theta_{SD}=180^\circ$ within the error range, it can slightly change for the scattering configuration, thus a new calibration is required.

⁶The finite detector length and chopper slit width contribute to the TOF width but has no direct effect on the accuracy of TOF.

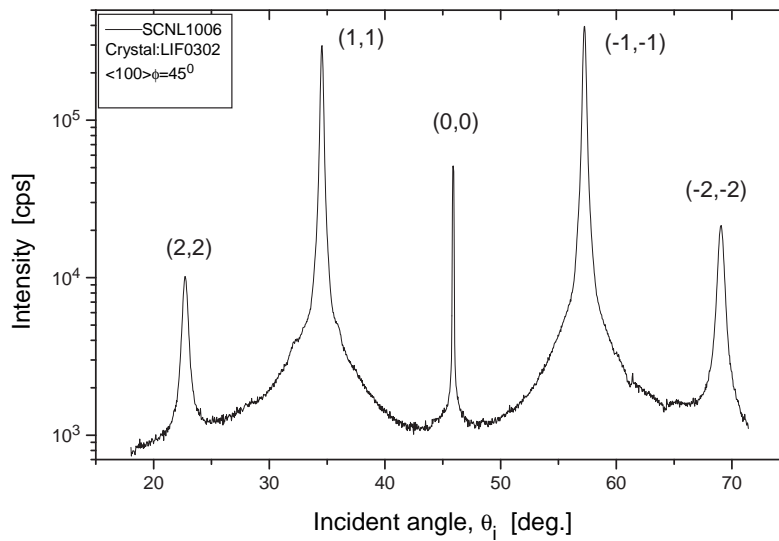


Figure 6.6: Typical incident angular scan of LiF(001) in the $\langle 100 \rangle$ direction with a He beam of $k_i = 11.2295 \text{ \AA}^{-1}$ ($T_0 = 300 \text{ K}$ and $P_0 = 80 \text{ bar}$). $\theta_{SD} = 90^\circ$. The corresponding m, n values of each peak is given in parenthesis. $T_s = 297 \text{ K}$. Iris: 1 mm.

Angular Accuracy: The total scattering angle is determined by measuring the direct beam position at 180° and rotating the detector to 90° . The detector angle decoder is highly precise and one motor step correspond to an angular movement of 6.6×10^{-6} degrees, thus the error due to the detector angle is negligibly small. There can be small errors due to the adjustment of the collimation which may change the total scattering angle or distort the shape of the diffraction peaks. It is difficult to estimate the quality of the collimation quantitatively. However, as the beam path is 3 meters long with apertures of a few millimeters, in the worst case any misalignment can lead to very few milliradians of error. The beam collimation is carefully adjusted and the observed peaks are highly symmetric, thus the actual error should be much smaller.

The azimuthal angle, ϕ of the crystal surface symmetry axis is found by optimizing the highest intensities of the diffraction peaks within an error of $\delta\phi = \pm 0.15^\circ$. The misalignment of the azimuthal angle causes an offset between the scattering plane and the symmetry axis of the surface. For a simple geometrical consideration where scattering plane and scan plane have an azimuthal angular difference of $\delta\phi = 0.15^\circ$ and leading an error of $\sin(\phi)$ in the measured G value, the error of the lattice constant, due to the adjustment of the crystal orientation is estimated to be $[\frac{\delta a}{a}]_A = \pm 2.6 \times 10^{-3}$.

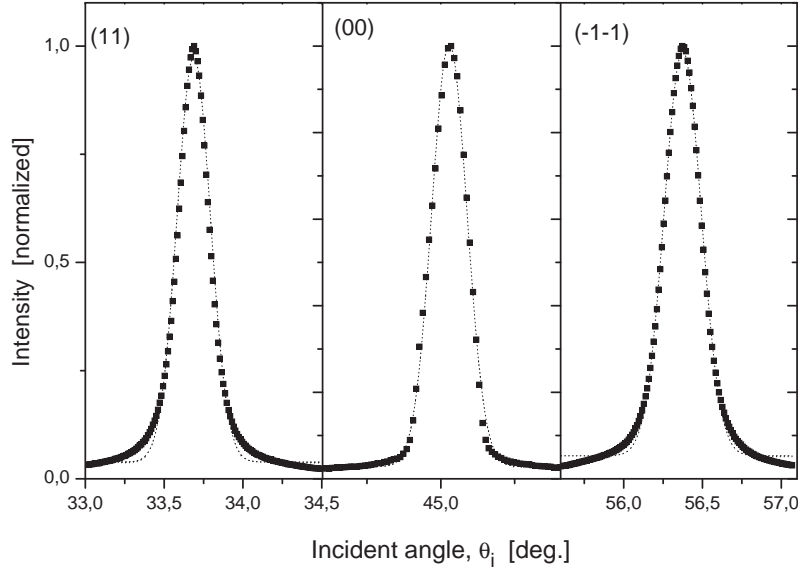


Figure 6.7: Typical scans of the specular and first order diffraction peaks in the $\langle 100 \rangle$ direction at a crystal temperature of 300 K. Although the angular step size is 0.01° , the fitting of a Gaussian curve (dotted lines) gives the peak positions with an accuracy of 0.001° . The positions of the (11), (00), and (-1-1) peaks are 33.688, 45.029, and 56.374 degrees, respectively. The lattice constant from the (11) and (-1-1) peaks are determined to be $a=4.0239 \text{ \AA}$ and $a=4.0225 \text{ \AA}$, respectively, and the mean value is $a=4.0232 \text{ \AA}$.

In fact, the exact error from azimuthal angle is more complicated due to the finite width of the peaks. The azimuthal movement of the crystal manipulator is not very precise and the given value for the error of the azimuthal angle is the precision of the scale of the target manipulator for azimuthal movement. Actually the azimuthal angle adjustment of the crystal depends highly on experience and the measured data from different crystals and along different symmetry axes indicate that the lattice constant error is less than the given value above as will be seen below (for instance in Figures 6.11). The reproducible error due to the adjustment of the azimuthal angle is found to be as

$$\left[\frac{\delta a}{a} \right]_A = \pm 8 \times 10^{-4} \quad . \quad (6.6)$$

A typical angular distribution of the diffraction profiles in the $\langle 100 \rangle$ direction is shown in Figure 6.6. The lattice constant measurement at a certain temperature is done with a quick scan of the specular and the 1st order diffraction peaks as shown in Figure 6.7. The incident angle decoder is highly precise. One tooth of the decoder

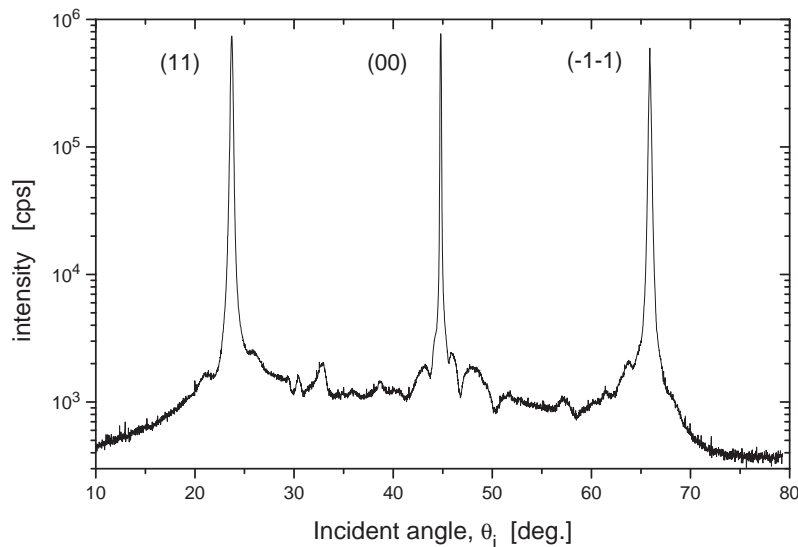


Figure 6.8: Incident angular scan with the cooled beam He beam. LiF(001) $\langle 100 \rangle$. The selective adsorption resonances are strongly pronounced. $P_0=100$ bar, $T_0=97.7$ K; $k_i=5.91\text{\AA}^{-1}$. $T_s=297$ K. Iris: 1 mm. $\theta_{SD}=90^\circ$.

gearing corresponds to an angular interval of 5.36×10^{-4} degrees. One step of the motor is about 1.5×10^{-3} degrees and the step motor has a backlash of about 1° . All angular scans are done increasingly in order to avoid the backlash. The resolution of the apparatus can be changed by inserting slits and an adjustable iris aperture in the beam path. As mentioned in Section 3.2.3 the specular peak FWHM can be changed from 0.015° up to 0.30° , regarding to the desired intensity and resolution. Although higher angular resolution was achievable, in the lattice constant measurements the FWHM of specular peak is determined to be 0.12° . With this resolution the intensity was enough to measure the peak positions up to 720 K precisely and quickly. It takes about 15 minutes to measure three peaks (sequentially (11), (00), and (-1-1) peaks) with angular steps of 0.01° . The averaging of the lattice constants determined from two diffraction peaks somewhat compensates the shift of the specular peak within this time. Although the angular steps are rather large, fitting a Gaussian curve to diffraction peak profiles allows determining the peak positions with much higher accuracy: After repeating several scans at same conditions, the reproducible error of the peak positions are found to be about $\pm 0.001^\circ$. The statistical error due to the angular precision, using

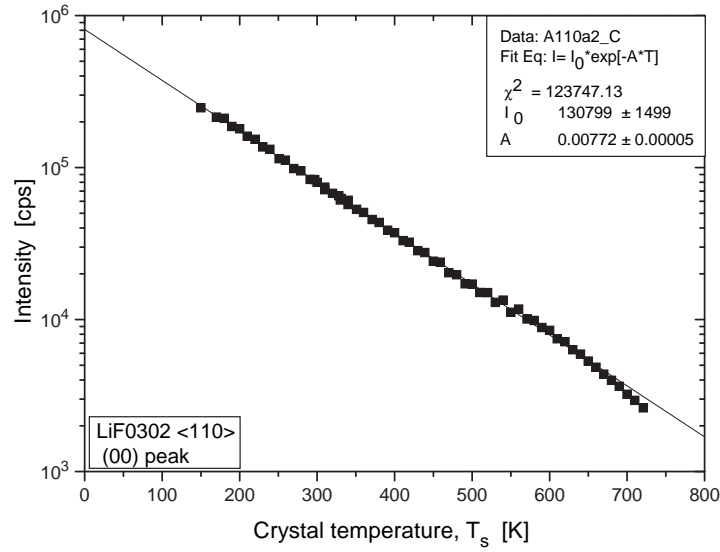


Figure 6.9: Thermal attenuation of the specular peak intensity. $\theta_i=45^\circ$ and $E_i=65.9$ meV. A slight divergence from the exponential form is observed at crystal temperatures above 600 K.

Equation 6.3, is

$$\left[\frac{\delta a}{a} \right]_R = \pm 0.9 \times 10^{-4} \quad . \quad (6.7)$$

The measured lattice constant from the angular scan shown in Figure 6.7 at 300 K is $a=4.0232$ Å. The systematic or absolute error from the wave vector and angular accuracies is $\delta a=\pm 0.0068$ Å. And the total statistical error is $\delta a=\pm 0.0010$ Å. The lattice constant of the bulk crystal at room temperature is given in the literature as $a=4.0262$ Å [286]. There is no error given for the bulk value. The given bulk value and the measured surface value is in accordance within the experimental error range.

In addition to the angular and beam wave vector errors, there are other possible error sources. The He is not an "absolutely non-interacting" probe in determining the surface structure. It can also interact with the surface potential and with the surface phonons. In Figure 6.8 the angular scan with a He beam of low incident energy is shown. Between the elastic peaks several selective adsorption resonance (SAR) peaks and dips are observed. SAR interferences in the neighborhood of elastic peaks may affect the shape and thus the determined position of the specular or a diffraction peak. However, with the room temperature beam the SAR effects are not pronounced significantly as seen in Figure 6.6.

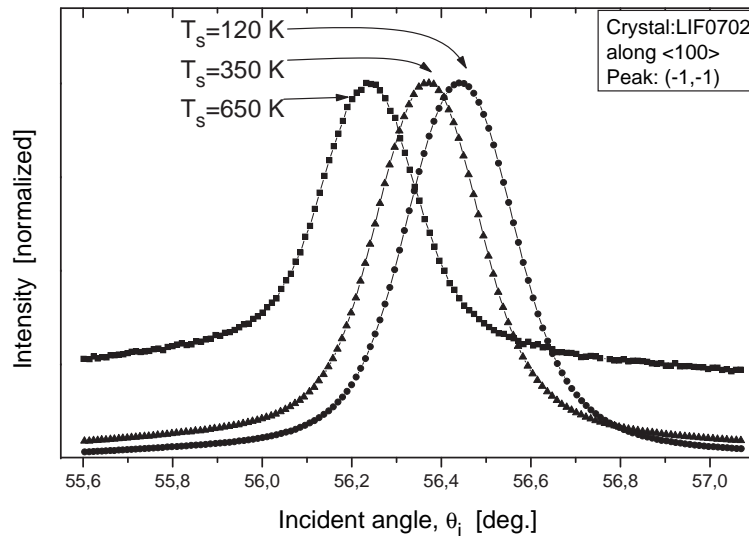


Figure 6.10: The (-1,-1) peak of the LiF(001) crystal at different crystal temperatures. The effect of shifting of the peak towards smaller angles with increasing temperature is clearly seen, which indicates that the lattice expands. The intensities are normalized. The real intensities are 1.60×10^6 cps, 0.707×10^6 cps, 0.36×10^5 cps at $T_s = 120$ K (-●-), 350 K (-▲-), and 650 K (-■-), respectively. The increasing offset of the peaks with increasing temperature is as a result of the increasing proportion of the background due to the inelastic scattering.

6.2.3 Debye-Waller Factor

In Figure 6.9 the thermal attenuation of the specular peak is shown. The intensity profile fits to a straight line in log-scale rather well. As discussed in Section 2.4, the Debye-Waller factor accounts for the decrease in the intensity with increasing crystal temperature as a function of $\exp[-2W(T_s)]$. From the plot in Figure 6.9 it is found to be as $-2W/T_s = 7.72(\pm 0.05) \times 10^{-3}$. However, this value is found to be reproducible for different measurements within the error range of $\pm 0.3 \times 10^{-3}$. Using Equation 2.50 the measured surface Debye-Waller factor for the effective mass 25.9 amu, which is the mass of the unit cell, and for the potential well depth of 8.03 meV [82], is determined from the present He-LiF(001) experiments as

$$\Theta_D = 478 \pm 10 \text{ K.} \quad (6.8)$$

This value is similar to the earlier values (without Armand correction) in Table 6.1.

Since the thermal attenuation of the reflectivity is highly in accordance with DW

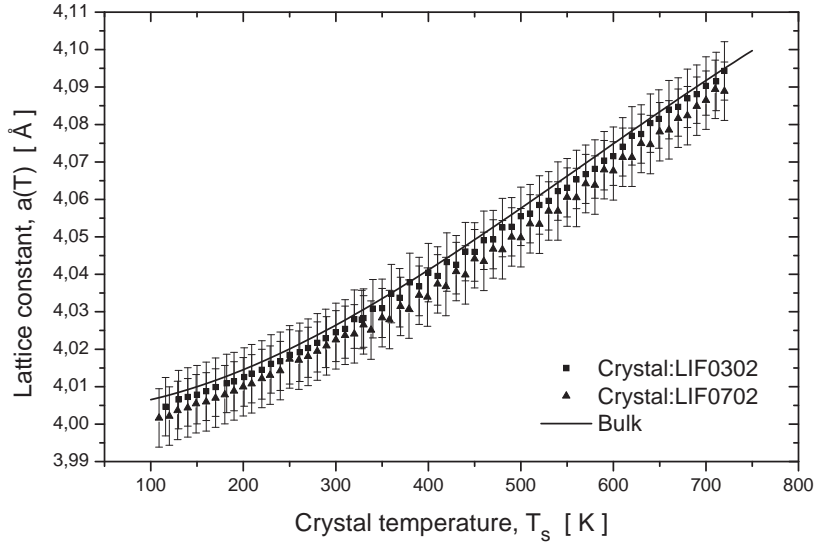


Figure 6.11: The lattice constants measured at different surface temperatures for both crystals. The total error bars are also shown. The difference between two crystals is about 0.002 \AA which is due to the adjustment error of the azimuthal angle. The lattice constant of the bulk is also provided: It is obtained by fitting a second-order polynomial to the thermal expansion coefficients provided in Figure 6.13 and integrating it with Equation 6.9 and by using the reference point $a(298 \text{ K})=4.02617 \text{ \AA}$ from ref. [325].

model, it is possible to make a further conclusion that the defect formation with the increasing surface temperature is insignificant. Moreover, a broadening of the specular peak and an emergence of a broad tail around the elastic peaks with increasing temperature are not observed in the present HAS experiments, which would have indicated significant existence of defects [25, 323, 324]. Such a significant decrease of the reflectivity diverging significantly from the thermal attenuation is reported by Vitali *et al.* [288]. They observed a slight drop in the 550-750 K range, which can be quantitatively assigned to anharmonic terms and which is also observed in Figure 6.9. Moreover they observed a sudden drop in the specular peak intensity at temperatures above 750 K which cannot be explained in terms of anharmonicity and assigned this effect as the onset of surface disorder. Although they admitted that the results should be considered rather preliminary and the conclusion is speculative, it supports the conclusion that at least up to 750 K, the surface remains well-ordered and the defect density does not increase significantly.

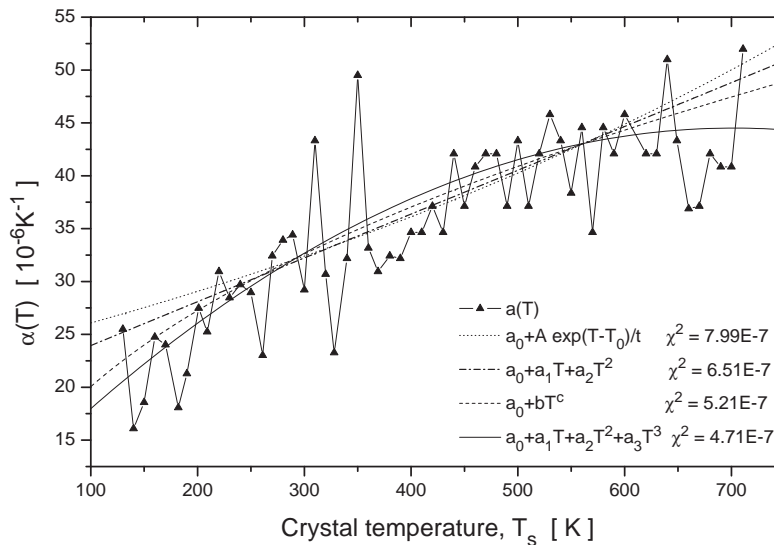


Figure 6.12: The thermal expansion coefficient of the sample LIF0302 obtained from Figure 6.11 and Equation 6.9. The derivatives of the different fit functions to the $a(T)$ curve in the previous figure are compared. The χ^2 -test gives third order polynomial as the best fit function of the lattice constant. The differentiation of the $a(T)$ curve ($\Delta a(T)/\Delta T$) is also shown ($-\blacktriangle-$).

6.2.4 Thermal Expansion Coefficient

An example of typical profiles of a diffraction peak at different crystal temperatures along the $\langle 100 \rangle$ direction are shown in Figure 6.10. The shift of the diffraction peak $(-1-1)$ at different crystal temperatures is clearly seen. The calculated lattice constants, $a(T)$ from the average values of the lattice constant determined from the positions of the $(-1-1)$ and (11) diffraction peaks, are plotted in Figure 6.11. The experiment is repeated for two different crystals. The offset of two $a(T)$ curves from two different samples is about 0.002\AA and is due to the adjustment error of crystal orientation as discussed above. Also the lattice constant of the bulk is provided for comparison. The bulk and surface values are in good agreement. Increasing slopes of two curves are apparent which indicates increasing thermal expansion coefficient. The $a(T)$ curves in Figure 6.11 can be fitted to different functions. These curves are smooth enough not only to determine a constant value of the surface thermal expansion coefficient, but also its temperature dependence, namely $\alpha_s(T)$. As the $a(T)$ changes only 2% in the

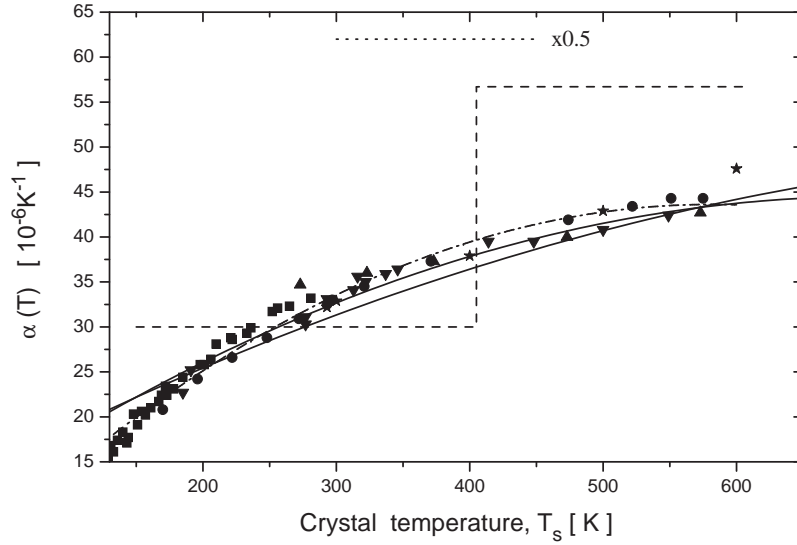


Figure 6.13: The comparison of the surface thermal expansion coefficients α_s and bulk thermal expansion coefficients α_b . α_s s for two independent crystals (solid lines) are obtained from the derivatives of the best-fit third-order polynomials as in the previous figure. The bulk values and their sources are: (■) from ref. [326]; (●) from ref. [327]; (▲) from ref. [328]; (▼) from ref. [329]; and (★) from ref. [330]. For the details of specimens and used methods see the references and for further data see ref [326, 331]. A second-order polynomial curve (dashed-dotted line) is fitted to the bulk values shown in the figure. For comparison, the surface thermal expansion coefficients measured by Watanabe *et al.* (dotted lines) [5] and by Frank *et al.* (dashed lines) [4] are also provided. Note the α_s value measured by Watanabe *et al.* are scaled by factor two and the reported value is $\alpha_s=124\pm 17 \times 10^{-6}/\text{K}$.

whole temperature range, the $\alpha(T)$ can be defined as

$$\alpha(T) = \frac{1}{\bar{a}} \frac{da(T)}{dT} \quad , \quad (6.9)$$

where $\bar{a}=4.05\text{\AA}$ is the mean value of $a(T)$ over the temperature range 100-800 K. The $\alpha(T)$ derived from the different fit functions are plotted in Figure 6.12. The fit functions to the $a(T)$ and their goodness of the fit are given in the figure. Also the differentiated curve of experimental $a(T)$ ($\Delta a(T)/\Delta T$ from the Figure 6.11) is plotted. Large fluctuations of the $\alpha(T)$ obtained from the differentiation of $a(T)$ are due to the small steps of ΔT (10 K). In Figure 6.13 best fit curves from two samples are plotted in solid lines. The fit curves are 3rd order polynomial, which smooth the $\alpha(T)$ without losing the trend of the temperature dependence of the experimental thermal

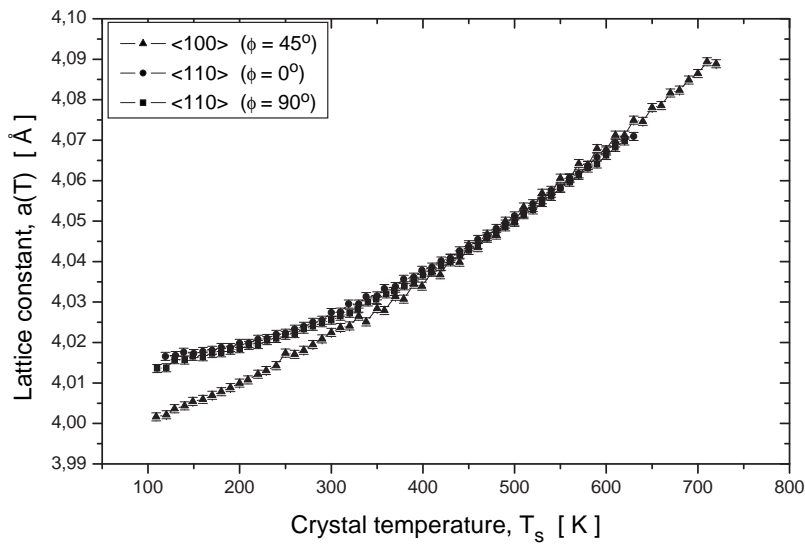


Figure 6.14: The comparison of the lattice constant measured from the different symmetry directions. The lattice constant curves measured in the $\langle 110 \rangle$ directions diverge from the one in the $\langle 100 \rangle$ direction at low temperatures significantly. Only the statistical error bars are shown. $T_0=300$ K.

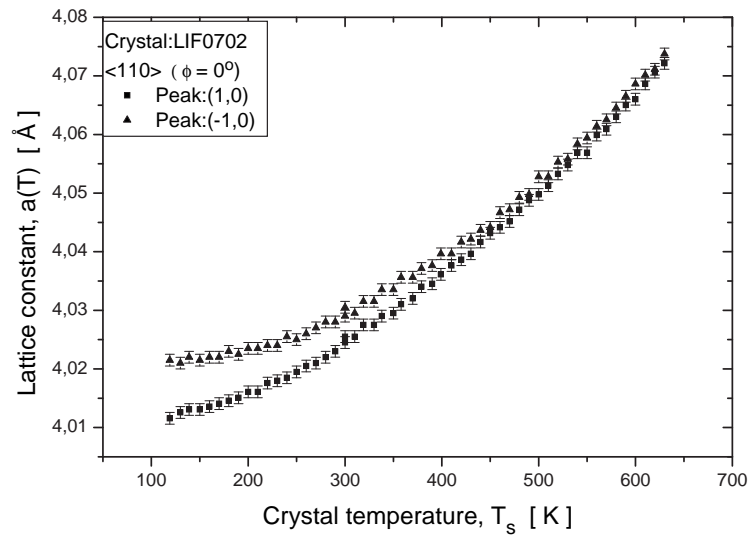


Figure 6.15: The comparison between the lattice constant measured from (1,0) and (-1,0) diffraction peaks. There is a discrepancy at low crystal temperatures. Only the statistical error bars are shown. $T_0=300$ K.

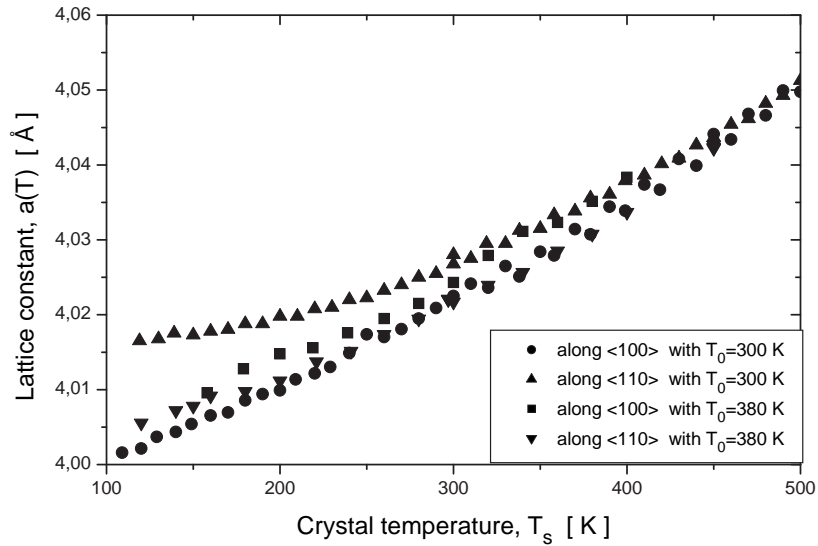


Figure 6.16: The lattice constant vs. crystal temperature curves with two different stagnation temperatures. k_i values at $T_0=300$ K and $T_0=380$ K are 11.26 \AA^{-1} and 12.77 \AA^{-1} , respectively. The anomaly is only observed along the $\langle 110 \rangle$ when the stagnation temperature is, $T_0=300$ K.

expansion coefficients. The difference of the curves are rather small indicating that the results are reproducible within error bars of $\pm 5 \times 10^{-6} \text{ K}^{-1}$. In order to compare the surface thermal expansion the bulk values from different works are also provided in the figure. The bulk and surface thermal expansion curves in the given temperature region are identical within the experimental error.

The thermal expansion results presented above are from two scattering experiments along the $\langle 100 \rangle$ symmetry axis for two sample crystals. Also scattering experiments along the $\langle 110 \rangle$ direction are carried out for both crystals. An anomaly was observed along this direction at low temperatures for both samples. As shown in Figure 6.14 the curve of $a(T)$ measured along the $\langle 110 \rangle$ direction diverges at low crystal temperatures from the one measured along the $\langle 100 \rangle$ direction by about 0.015 \AA . Not only the mean value of $a(T)$ (mean value obtained from the (10) and (-1-0) diffraction peaks) but also the $a(T)$ s measured from the (-1,0) and (1,0) diffraction peaks diverge from each other by about 0.01 \AA , when they are plotted separately as in Figure 6.15. Nevertheless, if the incident beam energy is changed the discrepancy disappears. In Figure 6.16 the measured lattice constants in both symmetry axis measured with different beam

energies are compared. The divergence is observed only along the $\langle 110 \rangle$ direction at the stagnation temperature of 300 K. There is no clear explanation for this effect yet. The effect emerges at low crystal temperatures and it is incident energy dependent, so that it may be due to the selective adsorption resonances (SAR), which are less smeared out and more clearly seen when the inelastic scattering background is reduced, namely at low surface temperatures. SAR of a certain bound state can correspond to the neighborhood of the 1st order diffraction peaks and can shift the measured position of the diffraction peaks. Often SAR lead to strong peaks and dips distorting the shape of the elastic peaks, however in this case a very shallow bound state can cause broader effect, which remain unnoticed but shifts the position of elastic peak determined by a Gaussian curve fit.

6.3 Conclusions

The lattice constant of the LiF(001) surface is determined with a precision of $\delta a = \pm 0.0078 \text{ \AA}$. The measured temperature dependence of the lattice constant is found to agree with the bulk value within the experimental error. The main sources of errors are due to the flight path distance calibration and the azimuthal angle adjustment. As the statistical error of the measured lattice constant is much smaller ($\delta a = \pm 0.0010 \text{ \AA}$) it is possible to determine not only an average value of the thermal expansion coefficient, but also its temperature dependence. The best-fit lines of the thermal expansion coefficients measured from two different crystals are similar to the fitted line of the bulk values within an error of 10%. The results have demonstrated that the thermal expansion of the LiF(001) surface is identical to the expansion of the bulk in contradiction with the earlier reports of a greater thermal expansion on the LiF surface [4, 5]. The sample preparations of earlier reports are similar to this work. The discrepancy with the present results can be attributed to the lack of precision in previous results: Frank *et al.* [4] obtained two average thermal expansion coefficients from only three measured lattice constant values at surface temperatures of 150 K, 405 K, and 610 K by observing rather broad selective adsorption minima (see also Figure 6.13). Watanabe *et al.* [5] determined an average thermal expansion coefficient in the temperature range of 300-450 K. Although the best-fit straight line to the data resulted in the thermal expansion coefficient as $\alpha_s = 124 \pm 17 \times 10^{-6} / \text{K}$, which is larger than the bulk value by a factor of 3.6, the measured data range is small (150 K) and the measured lattice constants are scattered within an error band of 0.1 \AA , so that

it is also even possible to plot a straight line which would result a thermal expansion coefficient which is less than the bulk value.

Additionally, in the HAS from surfaces, the scattered atoms are not only probe particles but also an object of the surface scattering phenomena at the same time, inelastic effects can lead to erroneous results, as observed in the scattering along the $\langle 110 \rangle$ with the room temperature beam, which has not been clarified yet.

The cleaved (001) surface of LiF crystals have smooth surfaces of sufficiently large terraces with low defect density and the LiF crystal is rather hard, thus the surface cannot be distorted in a convex shape. These features rule out any possible enhanced anharmonicity parallel to the surface and the positions of the surface atoms along the surface plane remain in consistent with the positions of the bulk atoms.

7. The Scattering of D₂ from LiF(001)

After the pioneering reports of the observation of well-defined diffraction of H₂ from LiF, NaCl, and NaF by Stern and his coworkers in the early 1930's [50,51], comparative studies of the scattering of H₂ and D₂ from LiF were reported only much later in 1970 by O'Keefe *et al.* [69,332]. In both works diffractive scattering and selective adsorption resonances (SAR) were observed. In their experiments O'Keefe *et al.* observed an increasing inelastic-scattering background in going from He to H₂, and to D₂ and attributed this to the rotational excitation of the molecules. Rotational transitions were first observed in angular distributions for H₂, HD and D₂ from MgO by Rowe *et al.* [333,334] and subsequently for H₂ from LiF(001) by Boato *et al.* [295]. Later, H₂ scattering from MgO(001) by Kolodney *et al.* [335] and D₂ scattering from LiF(001) by Brusdeylins *et al.* [336] were reported. Recently Traeger carried out extensive angular distributions and TOF experiments of n-H₂ and p-H₂ from LiF, NaCl, KCl, and MgO [284]. The comparative analysis of the diffractive scattering of normal- and para-H₂ have demonstrated that magnetic-quantum number transitions play an important role in the scattering process of hydrogenic molecules from alkali halides [54] confirming the earlier predictions [7,70].

Compared to atomic scattering from a surface, the scattering of molecules is experimentally more difficult due to the increased background and the additional open channels related to the rotational excitation of the scattered molecules. From the theoretical point of view, the understanding and the analysis of the molecular scattering is much more challenging since internal states and the anisotropy of the molecule affect the scattering process. On the other hand, the study of molecule scattering from surface can provide the basis for understanding the much more complicated chemisorption interaction in molecular scattering from reactive metal surfaces.

The first prediction of the existence of the rotational transitions was reported by Logan [337] wherein a simple quantum mechanical treatment of a rigid-rotator was described. With the advances in theoretical understanding, and computational tech-

niques and power, various methods have been developed: Reflection of a prolated ellipsoid from a flat surface was studied by Halbritter [338]. Garibaldi *et al.* extended the Eikonal approximation for scattering from a hard corrugated surface [78] to the scattering of H_2 and HD from $LiF(001)$ [64]. Goodman *et al.* applied the CCGM method [339] to the molecular case [340]. Close-coupling calculations of the scattering of hydrogenic molecules were first made by Wolken [62, 63] and later by Drolshagen *et al.* [68] and Brusdeylins *et al.* [336]. Gerber *et al.* investigated the scattering of H_2 - $LiF(001)$ for relatively high impact energies using the sudden approximation [90]. Recently, a time-dependent Hartree method was applied to H_2 - $LiF(001)$ by Capellini *et al.* [341] and also by Ehara *et al.* [342].

In all the methods mentioned above, the magnetic quantum number transitions in the scattering and rotational state transitions are either forbidden or only weakly allowed and the effect of the quadrupole-electrostatic interactions is overlooked. The hard corrugated wall approximation [64] is only valid for low corrugation and potential well depth and electrostatic term cannot be represented in the interaction potential. These assumptions hold better for molecular scattering from metallic surfaces and the model is highly effective for the interpretation of the experiments [88]. In the close-coupling calculations which were historically the most influential one, the Δm_j transitions were forbidden [62]. Furthermore, Boato *et al.*, without a detailed analysis, concluded from their experimental results that m_j is approximately conserved [295]. However, Hill's calculations pointed out that the scattering and rotational transitions processes for H_2 - $LiF(001)$ are strongly affected by the interactions between the quadrupole moment of the molecule and the electric field of ions at the crystal surface [65], which can cause a reorientation of the molecules thereby leading to Δm_j transitions. Recently, extensive calculations of Kroes and his coworkers based on the close-coupling wave packet method (CCWP) demonstrated that the quadrupole-electrostatic interactions contribute significantly to the scattering and RID transition probabilities and, moreover, that m_j transitions make a large contribution [7, 70]. The experimental evidence came from the observation of strong differences in the diffraction peaks of n- and p- H_2 [54].

In this chapter the scattering experiments of D_2 from $LiF(001)$ are presented. Firstly, the experimental details and the procedures for the analysis of the experimental results and the data reduction are explained. Drift-TOF experiments are presented in Section 7.2 for the detailed investigation of the interaction potential. The so determined experimental potential-well depth will be used in the next section where scattering experiments with different crystal temperatures are carried out in order to gain more

insight into the effect of thermal attenuation of the surface. In Section 7.4 the effects of the incident beam energy on the diffraction and RID transition probabilities are discussed. The experiments are carried out with a fixed source-to detector (or total scattering) angle, $\theta_{SD}=90^\circ$. In Section 7.5 the scattering experiments with changing total scattering angle are presented. From the angular scans the developments of the probabilities with changing incident angle are determined, which is a novelty in "high resolution" molecule-surface scattering experiments. In Section 7.6 the results of scattering of D_2 dimers from LiF(001) are presented.

7.1 Experiment

The crystal preparation is described in Chapter 6. The experiments are carried out with n- D_2 at stagnation pressure of 120 bar and stagnation temperature of between 100 and 400 K. The incident beam intensity and the beam energy spread at different stagnation temperatures are described in Figure 4.16. The initial distributions of internal rotational states can be determined by estimating the terminal rotational temperatures from Equation 4.29 and using Equation 4.25 or Figure 4.10 which give the occupation probabilities of internal states corresponding to a rotational temperature. An iris diameter of 2.5 mm is used, which leads to a beam divergence of 0.12° and a specular peak width (FWHM) of about 0.15° in the incident angular distributions. Angular scans are carried out with angular steps of 0.05° . Such a scan with finite angular steps cannot fully follow the shapes of the especially narrow peaks such as the specular and some RID peaks and the measured peak heights may vary significantly as data points do not correspond mostly the peak maxima. Thus, to determine peak intensity the points were interpolated by fitting them to a Gaussian peak shape. This procedure was tested by repeating the measurements at the same conditions with smaller angular steps. Integration times of 0.5 seconds were used to measure the signal at each angular step. When the intensities were found to be too low the integration times were increased to 1 second per step. All the signal intensities in this chapter were converted to counts per second (cps).

Typical scans for a constant total scattering angle of $\theta_{SD}=90^\circ$ are shown in Figures 7.1 and 7.2 in the $\langle 100 \rangle$ and $\langle 110 \rangle$ scattering directions, respectively. The peaks are always observed at the predicted positions when both the population of the initial states and the transition probabilities are sufficiently large. And also if the peaks do not overlap with another peak and if they are not too broad to be resolved. In the $\langle 100 \rangle$

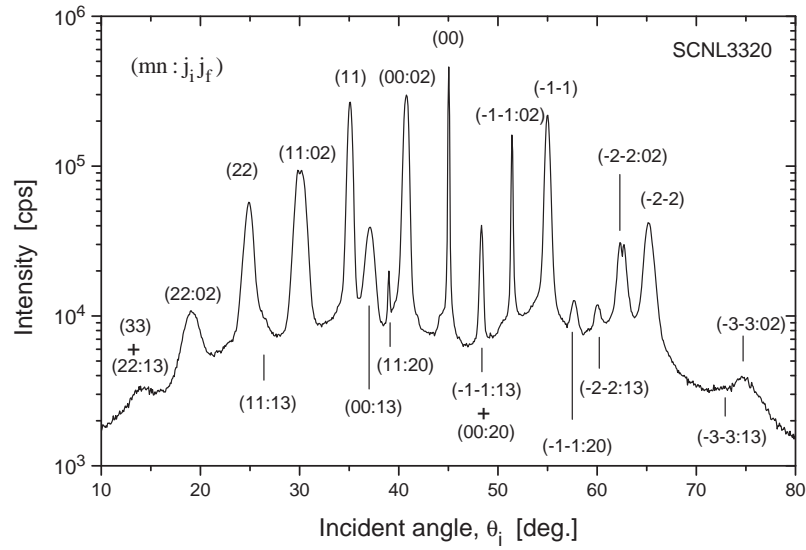


Figure 7.1: The incident angular scan for D_2 - $LiF(001)$ along the $\langle 100 \rangle$ direction. $T_s=130$ K, $T_0=300$ K and $P_0=120$ bar. $E_i=85.3$ meV ($k_i=12.8 \text{ \AA}^{-1}$) and $\theta_{SD}=90^\circ$.

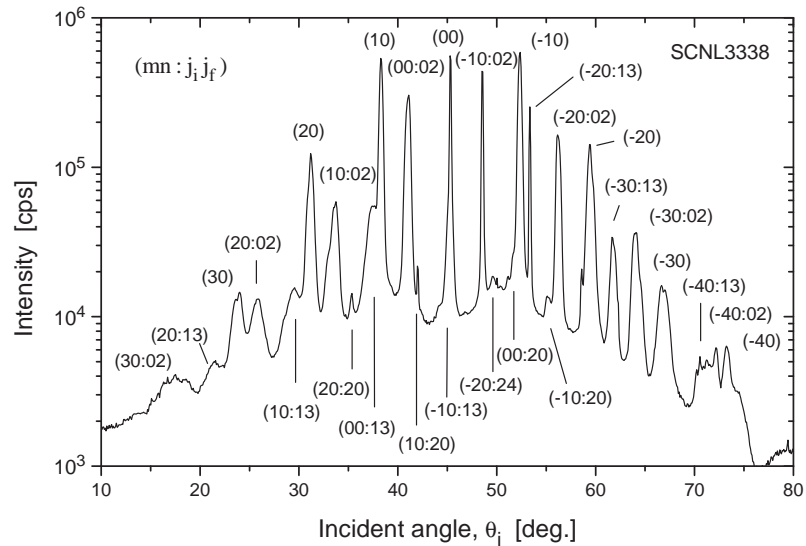


Figure 7.2: The incident angular scan for D_2 - $LiF(001)$ along the $\langle 110 \rangle$ direction. $T_s=130$ K, $T_0=300$ K and $P_0=120$ bar. $E_i=85.3$ meV ($k_i=12.8 \text{ \AA}^{-1}$) and $\theta_{SD}=90^\circ$.

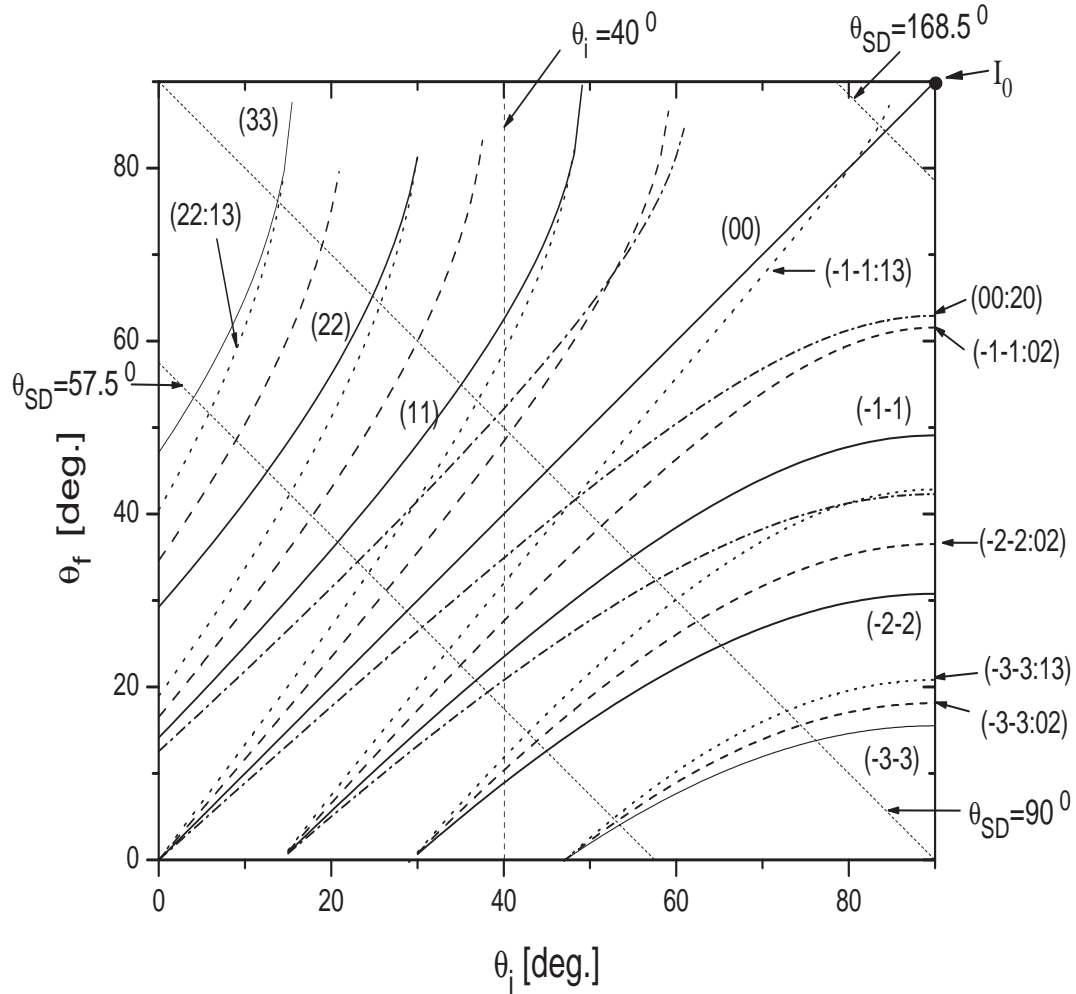


Figure 7.3: Typical angular scan lines and the kinematical conditions of the major observed peaks for initial and final angles for D_2 -LiF(001) with an incident beam wave vector of $k_i=12.8 \text{ \AA}^{-1}$ ($E_i=85.3 \text{ meV}$) along the $\langle 100 \rangle$ direction. Constant- θ_{SD} incident angular scan lines for $\theta_{SD}= 57.5^\circ$, 90° , and 168.5° (short-dotted lines) and constant- θ_i angular scan line for $\theta_i=40^\circ$ (short-dashed line) are shown. $(mn:j_i j_f)$ represents the RID peak for a transition from an initial rotational state j_i to a final rotational state j_f coupled with the diffraction peak (mn) . The legend of diffraction and RID peaks: solid lines: elastic diffraction peaks, dashed lines: $(0 \rightarrow 2)$ RID peaks, dotted lines: $(1 \rightarrow 3)$ RID peaks, dashed-dotted lines: $(2 \rightarrow 0)$ RID peaks. Note that all RID peaks merge with their elastic peaks at low incident angles and rotational transitions to higher states lie at lower incident angles with respect to their elastic peaks. (m,n) and $(-m,-n)$ peaks are symmetric according to the specular peak. At $\theta_i=\theta_f=90^\circ$ the incident beam, I_0 is observed.

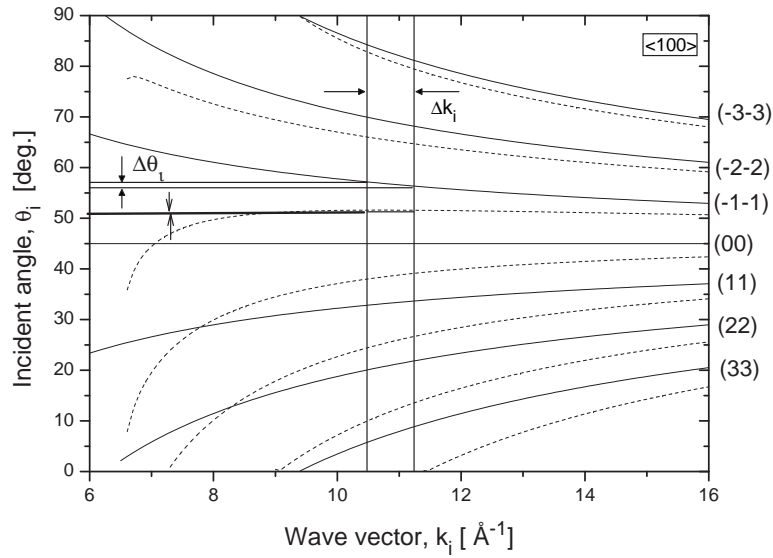


Figure 7.4: Wave vector dependence of the incident angle of the elastic (solid lines) and $(0 \rightarrow 2)$ inelastic peaks (dashed lines) for D_2 - $LiF(001)$ along the $\langle 100 \rangle$ where $\theta_{SD} = 90^\circ$. The peak widths, $\Delta\theta_i$ of the $(-1-1)$ diffraction peak and its RID peak are illustrated for the case of a finite beam energy spread of Δk_i is shown at $k_i = 10.9 \text{ \AA}^{-1}$. Note that the inelastic peak is narrower than the elastic peak because the inelastic peak depends very little on the incident wave vector.

direction more than 17 peaks are clearly resolved and several more appear as shoulders. In the $\langle 110 \rangle$ direction there are about 27 peaks. The greater density of the peaks is due to the smaller \mathbf{G} and the overlapping of peaks is more likely. All peaks can be identified by the kinematical conditions given in Equations 2.6 and 2.7. A qualitative identification of the peaks in the angular scans reveals that the elastic peaks of plus and minus order lie symmetrically with respect to specular peak and inelastic peaks for transitions to higher rotational levels lie at lower incident angles with respect to their parent elastic peaks. In Figure 7.3 the elastic peaks and major RID peaks for scattering from $LiF(001)$ along the $\langle 100 \rangle$ direction are plotted according to the kinematical equations. According to Figure 7.3 the peaks are expected whenever the scan line for $\theta_{SD} = 90^\circ$ intersects with a kinematical line. Note that the peaks $(00:20)$ and $(-1-1:13)$ and the peaks (33) and $(22:13)$ are at the same angles for the $\theta_{SD} = 90^\circ$ -scan line so that observed peaks at about 48° and 14° in Figure 7.1 are each the sums of two peaks. In both scattering directions, some $(2 \rightarrow 0)$ deexcitation rotational transitions are also

observed. Note that the fractional population of the level $j_i=2$ in the incident beam is only 8% percent at the given stagnation conditions so that the deexcitation peak intensities are low but the transition probabilities are comparable with the transition probabilities of $(0\rightarrow 2)$ and $(1\rightarrow 3)$.

It is also seen that the peak widths are very different. Even some peaks are as narrow as the specular peak (such as the $(-1-1:02)$, $(11:20)$ or $(-20:13)$ peaks). This can be understood by examining the kinematical conditions for the peaks. In Figure 7.4 the incident energy dependence of the incident angles for some elastic and RID peaks is illustrated. It is seen, for instance, that the position of the $(-1-1:02)$ peak becomes almost independent of wave vector (like the specular peak) when the k_i greater than about 8.5 \AA^{-1} . Therefore, despite the energy spread, these peaks appear to be very sharp. This effect is called *kinematic rotational focusing* [334,343]. Kinematical focusing is also seen for phonon excitations [146].

7.1.1 Calculation of Probabilities

In order to compare the experiment with the theory some considerations must be taken into account such as the external and the instrumental effects which affect the measured data in addition to the investigated physical phenomenon. In the case of the molecular scattering from the surface, the influences of the instrumental broadening, finite crystal temperature, the energy spread of the beam, and initial distributions of the internal states on the measured intensities of diffraction and rotational transitions must be extracted, since the theoretical analysis provides diffraction and transition probabilities at ideal conditions and for a static surface.

As seen in the previous section the peaks demonstrate quite different widths associated with their dependence on incident beam energy. Secondly, as discussed in Section 3.2.3 and provided with Equation 3.32, the instrumental broadening significantly changes for different scattering geometries. Thus, principally, all peaks must be deconvoluted from the broadening due to the finite instrumental resolution and the beam energy spread. However, this is a very time consuming procedure when many peaks are observed and the scattering geometry is changed frequently, and deconvoluting of each peak requires independent treatment. Therefore, in this work another method is adopted: The effects of the instrumental and chromatic broadening of the peaks can be circumvented by taking the area of the peaks instead of peak heights. This is a reasonable approximation so long as the beam divergence is kept constant and unless the intensity fluctuates abruptly within the energy spread of the incident

beam. Thus, the intensities given in this chapter, except the angular scans, are defined as the peak areas determined by Gaussian fitting and subtracting the background. Similarly, the incident intensity on the crystal should be corrected according to the finite beam divergence, whereas the incident intensities given in Figure 4.16 are taken at constant angle of $\theta_{SD}=180^\circ$. The peak area intensity of the incident beam I_0 is calculated by scanning the incident beam with the detector angle. The obtained peak area is divided by a factor of two, while scattered beam intensities are obtained by changing the incident angle, since one degree of the incident angle corresponds to two degrees of the detector angle. Thus, the peak intensities in Figure 4.16 must be divided by a factor of 7.2, which is the ratio of the peak height to the peak area, to obtain the peak area intensity of the incident beam.

Because of the finite size of the crystal, at high incident angles the whole beam which passes through the iris does not reflected from the crystal since the crystal surface has a finite size of 8 mm¹. Therefore, the intensity of peaks with incident angles higher than 66 degrees must be corrected with a geometrical factor, η which describes the ratio of the beam that falls on the crystal surface to the total incident beam².

As discussed in Section 3.1.7 the detection probability of the detector is inversely proportional to the particle velocity. Although the incident beam intensity at different beam energy is directly measured and can be used for the comparison of the intensity of the elastic peaks, the intensities of the inelastic peaks must be corrected because those molecules which undergo a rotational transition have different final velocities, thus different detection probabilities. As mentioned above, since the theoretical treatments for the calculation of the diffraction and RID probabilities are carried out with a static lattice, the thermal attenuation of the scattered beam at the finite surface temperature must also be taken into account. The simplest way is correcting the intensities with Debye-Waller factors as discussed in Section 2.4. The validity of the DW analysis for D_2 -LiF(001) system is investigated in Section 7.3.

Taking all of the above considerations into account the probabilities of diffraction and RID peaks are calculated for comparison with the theory. For instance, if the measured peak area intensities for a rotational transition ($j_i \rightarrow j_f$) related with a re-

¹In fact, the crystal size is 10x10 mm, but along $\langle 100 \rangle$ direction two supporting clamps cover 2 mm length of the crystal surface.

²This is not the same commonly used constant, α which accounts for the ratio of the beam spot on the surface seen by the detector at a constant initial and final angle [42]. As in the present case the crystal is rotated the finite beam spot size on the crystal surface contributes in the instrumental broadening and, thus, is taken into account by integrating the peak area.

reciprocal lattice vector \mathbf{G}_{mn} is defined as $I(mn:j_i j_f)$, the transition probability from an initial rotational state j_i to a final rotational state j_f correlated with the \mathbf{G} -vector is calculated as

$$P(mn : j_i j_f) = \frac{I(mn : j_i j_f)}{I_0 \cdot n(j_i) \cdot \eta} \cdot \sqrt{\frac{E_i + \Delta E}{E_i}} \cdot \exp [2W(\theta_i, E_i, E_f, T_s)] \quad , \quad (7.1)$$

where ΔE ($=E_f - E_i$) is energy loss due to the rotational transition. The first term stands for the ratio of the measured beam intensity to the incident beam intensity with the corrections of ratio of the incident beam falling onto the crystal and fractional population of the rotational state j_i in the incident beam. The second term corrects the different detection probability of the RID peaks. The third term takes the thermal attenuation of the beam into account.

However, it should be kept in mind that this equation provides an experimental probability averaged over the magnetic quantum number (m_j), since the molecules are not state-selected and changes in the m_j of the molecules cannot be detected. Thus, for inelastic peaks the $P(mn:j_i j_f)$ can be obtained theoretically by averaging over m_{j_i} and summing over m_{j_f} :

$$P(mn : j_i j_f) = \frac{1}{2j_i + 1} \sum_{m_{j_i}, m_{j_f}} |S[00, j_i m_{j_i} \rightarrow mn, j_f m_{j_f}]|^2 \quad , \quad (7.2)$$

where S is the transition matrix element. For the elastic diffraction peaks the probabilities are a weighted average of all initial rotational states. So that it is necessary to define a general transition probability for elastic diffraction peaks in order to compare the experimental values with the theory:

$$P(mn) = \sum_{j_i} P(mn : j_i j_i) \cdot n(j_i) \quad . \quad (7.3)$$

The equations above are used in the following sections, however, mostly the ratio of the probabilities will be used because of the following reasons. Firstly, using DW approximation is only an approximate method as will be discussed in Section 7.3 and taking the ratios of the peaks somewhat cancels the DW factors. The second and the most important reason is that the measured intensities can be significantly reduced due to the surface defects and steps. Although the step and the defect densities of the LiF(001) surface are relatively low (see Section 6.1), the defects have large cross-sections and may reduce the intensities significantly and it is very difficult to estimate this reduction in the present case.

It is useful and commonly preferred method to compare a RID peak with the associated elastic peak (m,n), which can be defined as

$$R(mn : j_i j_f) = \frac{I^*(mn : j_i j_f)}{I(mn) \cdot n_j} , \quad (7.4)$$

where the ratio of the peak intensity with respect to elastic peak intensity $I(mn)$ is taken. Here both inelastic and elastic diffraction intensities are peak area intensities. The asterisk denotes that the RID intensities are corrected due to the different detection probability of the RID peaks. The theoretical correspondence of this equation is

$$R(mn : j_i j_f) = \frac{P(mn : j_i j_f)}{P(mn)} . \quad (7.5)$$

Similarly, for elastic peaks we define,

$$R(mn) = \frac{P(mn)}{P(00)} , \quad (7.6)$$

where $P(mn)$ is defined in Equation 7.3. In the investigation of selective adsorption resonances (also used in Chapter 5), the intensity of the specular peak is compared with the incident beam intensity by defining reflectivity as

$$R(00) = \frac{I(00)}{I_0} , \quad (7.7)$$

which gives a comparison of the specular peak with the incident beam without any detailed correction of intensities.

7.2 Selective Adsorption Resonances

As discussed in Section 2.5, the molecules can be resonantly trapped in the well of the molecule-surface interaction potential. This results in an effective attenuation of the reflected beam when kinematical conditions, given in Equation 2.51, corresponding to resonant trapping, are satisfied. The experimental data for selective adsorption resonances (SAR) of H₂ on LiF(001) were first reported by Frisch and Stern [51] but their interpretation remained unclear at that time. An analysis of their data by Tsuchida yielded three bound states (see Table 7.1) [344]. Later O'Keefe *et al.* reported SAR observations both for H₂ and D₂ [69]. The results of both groups were reanalyzed by Le Roy and the observed values of H₂ and D₂ were assigned to certain eigenenergies as given in Table 7.1 [6]. Le Roy concluded that the measurements of both groups and

Table 7.1: Survey of experimental values of bound state energies, $|\epsilon_\nu|$ (in meV) taken from the literature. The footnotes denote (a) the experimental values measured by Frisch and Stern [51] and corrected by Tsuchida [344]. (b) The experimental results of O’Keefe *et al.* [69]. Both results have been reanalyzed by Le Roy and the reported values were assigned to the eigenstates as listed here [6]. From the $|\epsilon_\nu|$ he calculated the best fit well depth to be $D=37.7(\pm 4.4)$. (c) The theoretically calculated values by Wolken where he used the experimental values marked with * and Equations 2.20 and 2.21 resulting in the parameters of $D=38$ meV and $\alpha=1.18$ Å^{-1} [63, 345].

ν	$(\text{H}_2)^a$	$(\text{H}_2)^b$	$(\text{H}_2)^c$	$(\text{D}_2)^b$	$(\text{D}_2)^c$
0		30(± 6)	30.9	31(± 6)	32.9
1	-17(± 1)	19(± 4)*	19.0	19(± 4)	23.8
2	-10(± 1)	10(± 2)*	9.9		16.2
3	-4(± 1)		3.8	11(± 2)	10.1
4			0.5		5.4

for both molecules agree with each other when isotope effect is taken into account and he calculated a best-fit well-depth of $D=37.7(\pm 4.4)$ meV. Although these results were doubtful, where particularly for D_2 any maxima and minima were barely observed and the obtained eigenenergies were similar to the H_2 [69], they are used for the empirical potentials in the theoretical works [63, 345].

In this section the investigation of SAR of D_2 molecules on $\text{LiF}(001)$ surface by drift-TOF measurements are presented. Because of the broad energy spread of the incident D_2 beam it is difficult to observe the resonances without TOF resolution. In the drift-TOF technique where the incident beam energy is resolved with TOF technique and the beam energy is changed in a broad band, the energy resolution is not limited by the energy spread of the primary beam [121]. The energy dependence of the reflection coefficient of the specularly scattered beam, $R(00)$ is measured as the temperature of the source is changed from $T_0=100$ K up to 180 K. The total measurement time is 3000 seconds and the stagnation temperature is increased linearly by 0.1 K steps during the TOF run. The direct beam TOF spectrum is also measured as a function of temperature under the conditions, thus incident energy dependent reflection coefficient can be calculated using Equation 7.7.

In Figure 7.5 the drift-TOF spectra of the specular peak for $\theta_i=45^\circ$ in the $\langle 100 \rangle$ direction ($\phi=45^\circ$) and the direct beam (where $\theta_{SD}=90^\circ$) are shown. One can imagine

as if a beam of a broad and smooth velocity distribution represented by the dashed-line is incident on the surface and the velocity distribution of the reflected beam is given by the solid-line which is quite different and shows strong fluctuations presumably due to the resonances at certain incident energies. At these energies where kinematical conditions are satisfied the molecules may be trapped into the bound states of the attractive potential well, mediated with a diffraction or rotational transition and be delayed or inelastically scattered out of the specular peak leading to dips and peaks in the intensity profile.

Identifying the energy levels is not simple because there are several possible \mathbf{G} -vectors and which may be responsible for the resonance. Secondly, since it is an interference effect, especially when the rotational transitions are allowed [121, 346], there is no qualitative way of predicting whether the resonance is a peak or a dip and it is not easy to identify, for instance, whether a dip is a real resonance or an artifact of the neighboring peaks. Thirdly, a molecule can be trapped into a bound state with the help of a simultaneous rotational transition. In this case the determined energy level will be as if it is $|\epsilon_\nu| + \Delta E_{rot}$ instead of $|\epsilon_\nu|$ as given in Equation 2.51. Furthermore, with increasing incident energy, the opening of new diffraction and rotational transition channels can also lead to sudden changes of the specular peak intensity. Therefore, it is necessary to change other parameters leading to different kinematic conditions for a certain bound-state energy, such as, incident angle or azimuthal angle of the scattering plane. Hence, principally, the evaluation of the positions of the peaks and dips in the energy spectra can be followed, the fake peaks and dips can be excluded and the \mathbf{G} -vector and ΔE_{rot} can be identified and $|\epsilon_\nu|$ can be calculated. In Figure 7.6 the drift-TOF spectra for incident angles of 40° , 45° , and 50° are plotted as a function of incident energy. The $R(00)$ values are obtained by dividing the drift-TOF spectra of specular peaks with the drift-TOF spectrum of the direct beam. As it is seen the profiles of the intensities change strongly and it is difficult to follow the shift of any peaks. This is due to the more than a hundred possible channels³ and presumably their strong coupling with each other.

Therefore, an indirect method is carried out for estimating the resonance energies: Firstly, the bound state energies, ϵ values from all peaks and dips in Figure 7.6 using

³For instance, the number of open channels can be estimated approximately as $\frac{\pi k_i^2}{\sigma}$ which gives the ratio of accessible area and the area of Brillouin zone (σ) on the reciprocal lattice plane. For a trapping into a bound state energy level of 30 meV with an incident energy of 40 meV, there are 86 open channels where $k_i^2 = \frac{2m}{\hbar^2}(E_i + |\epsilon_\nu|)$. This number is enhanced by a factor 2 due to the accessible rotational transitions of (0→2) and (1→3).

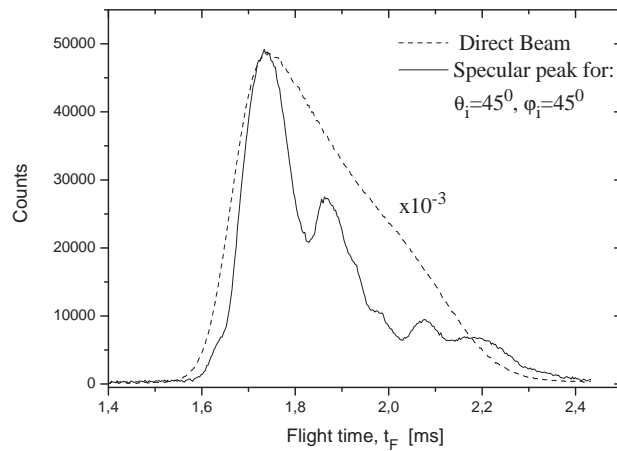


Figure 7.5: Drift-TOF spectra of the direct beam (dashed line) and specular peak (solid line) at incident angle of 45° for D_2 -LiF(001) along the $\langle 100 \rangle$ direction. The source stagnation pressure is 120 bar and the source temperature is changed linearly between 100-180 K. Total TOF measurement time is 3000 s. Note that the direct beam is multiplied by the factor of 10^{-3} .

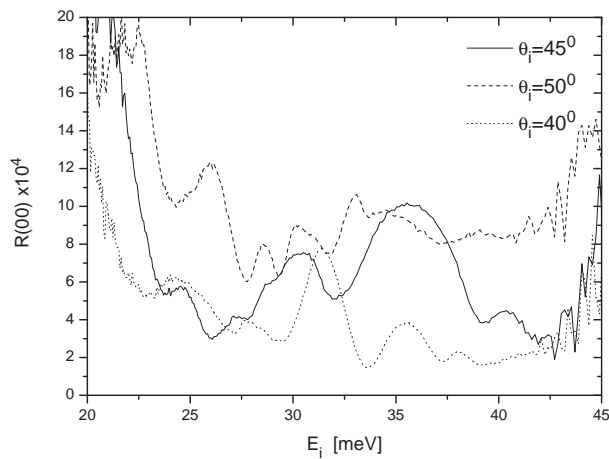


Figure 7.6: $R(00)$ values at the incident angles of 40° (dotted line), 45° (solid line), and 50° (dashed line). These $R(00)$ values were obtained by dividing the drift-TOF spectra of the specular peaks (for $\theta_i=45^\circ$ shown in Figure 7.5) with drift-TOF spectra of the direct beam (shown in Figure 7.5) and the similar drift-TOF spectra for D_2 -LiF(001). The flight time scale is converted into incident energy scale.

Equation 2.51 for all \mathbf{G} which can involve in the SAR process are calculated in the range of $(m,n)=(\pm 3,\pm 3)$. Then frequency distributions of calculated ϵ values for energy bits of 0.5 meV are plotted as given in Figure 7.7. There are some clustering of data in Figure 7.7 at certain energies. Naturally, bound state energies less than zero is nonsense and also energies higher than about 30 meV are also not expected where the potential well depth should not be much greater than 40 meV. The most frequent energy is identified at about 28 meV which should be probably the most observable or significant bound state, namely ϵ_0 . One remarkable point is that peaks higher than 28 correspond to lower energy peaks with a difference of 22.2 meV (which is the ΔE_{rot} for $(0 \rightarrow 2)$ transition). In the figure these peaks and their corresponding energy of -22.2 meV are shown. When these peaks are shifted by -22.2 meV they overlap with other peaks.

In Figure 7.8 the frequency distribution spectrum of the energies obtained by shifting the part of the spectrum in Figure 7.7 above 31 meV by -22.2 meV is plotted. There are 5 peaks which are explicitly distinguished, namely: at (1)28.7, (2)23.4, (3)16.8, (4)11.6, (5)9.0 meV. Comparing the results with the ones in Table 7.1, the values are slightly lower than the previous measurements. These peaks can be used to calculate the parameters of interaction potentials. For a Morse potential the calculated parameters are listed in Table 7.2. Identifying the first peak as binding energy ϵ_0 is reasonable. The second peak cannot be identified as ϵ_1 when the first one identified as ϵ_0 so that it must be skipped. There are three cases considered where the observed peaks are identified as different eigenvalues of the potential well in Table 7.2. In Case-A, peaks at 28.7 meV and 16.8 meV are assigned to the bound state levels ϵ_0 and ϵ_1 , respectively. In Case-B, peaks at 28.7 meV, 16.8 meV and 11.6 meV are ascribed to the bound state levels ϵ_0 , ϵ_1 and ϵ_2 , respectively. In Case-C, peaks at 28.7 meV, 16.8 meV and 9.0 meV are assigned to the bound state levels ϵ_0 , ϵ_1 and ϵ_2 , respectively. From the assigned bound states (ϵ_ν^{exp}) the best fit parameters α and D of the Morse potential is obtained. Using the obtained Morse potential parameters, their bound energy levels (ϵ_ν^{theo}) are calculated. The bound states to a given set of parameters were compared to the experimental values, and the best-fit potential parameters are estimated by the standard deviation factor,

$$\sigma = \frac{1}{\sqrt{N}} \sqrt{\sum_{\nu} [\epsilon_{\nu}^{exp} - \epsilon_{\nu}^{theo}]^2} \quad (7.8)$$

Although Case-A fit very well, Case-C is also reasonable and is preferred where the 1., 3., and 5. peaks are identified as ϵ_0 , ϵ_1 and ϵ_2 . The potential depth calculated for

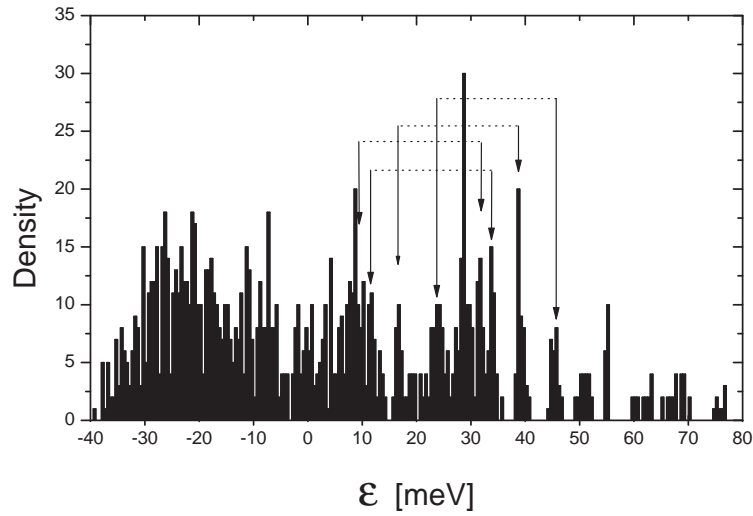


Figure 7.7: The density of bound state energies calculated from all the dips and peaks in Figure 7.6 and for all G-vectors within the range of $(m,n)=(\pm 3,\pm 3)$ by using Equation 2.51. The peaks higher than 30 meV and corresponding to lower energy peaks with a difference of 22.2 meV are marked with arrows.

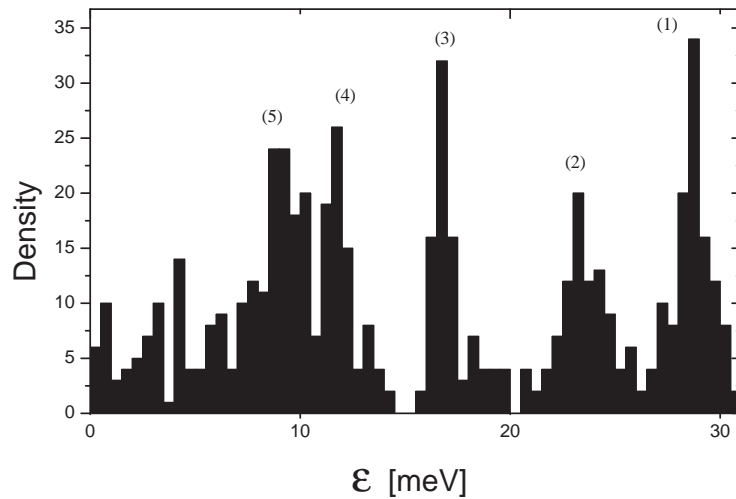


Figure 7.8: Density of calculated energies after shifting the part of the spectrum in Figure 7.7 above 31 meV by -22.2 meV. The peaks are at (1)28.7, (2)23.4, (3)16.8, (4)11.6, (5)9.0 meV.

Table 7.2: The comparison of different cases A, B, and C where the peaks assigned to bound states and compared with the Morse potential by using Equation 2.21. The case C is preferred.

Parameters	A	B	C
ϵ_0^{exp} (meV)	-28.7	-28.7	-28.7
ϵ_1^{exp} (meV)	-16.8	-16.8	-16.8
ϵ_2^{exp} (meV)		-11.6	-9.0
D (meV)	35.8	33.7	35.3
α (\AA^{-1})	1.74	1.41	1.65
ϵ_0^{theo} (meV)	-28.7	-28.0	-28.6
ϵ_1^{theo} (meV)	-16.8	-18.3	-17.2
ϵ_2^{theo} (meV)	-7.5	-10.6	-8.8
ϵ_3^{theo} (meV)	-2.0	-1.6	-1.9
σ	0.03	1.09	0.29

the case is $D=35.3$ meV. This agrees well in the error bars with estimated D value by Le Roy. The determined resonance energies and resulting potential depth is about 2-3 meV less than the previously predicted and measured values with the exception of Kroes potential, which has a depth of 31 meV for H_2 [7].

The excluded peaks, such as 2. and the 4. peak may indicate a splitting of the resonances due to the different rotational states. The anisotropic potential should lead to resonances which depend on the j_i and m_i of the incoming molecules. Such a energy level splitting is observed in the SAR studies of H_2 -Ag(110) [347] and should also be observed for LiF. The 1., 3., and 5. peaks probably belong to $j_i=0$. Note that 2/3 of the beam is in $j_i=0$. Hence, the obtained potential well is the laterally and angularly average interaction-potential. The unidentified peaks may belong to $j_i=1$, $m_i=\pm 1$, which makes the second largest population of the incident beam. Thus, bound state energy levels at 23.2 meV (2.peak) and 11.6 meV (4. peak) can be assigned to the ϵ_0 and ϵ_1 levels of rotational state $j_i=1$, $m_i=\pm 1$.

7.3 Debye-Waller Factor Analysis

The theoretical methods used for elastic surface scattering calculations mostly assume a static surface model where the surface atoms are at rest and rigid, while experi-

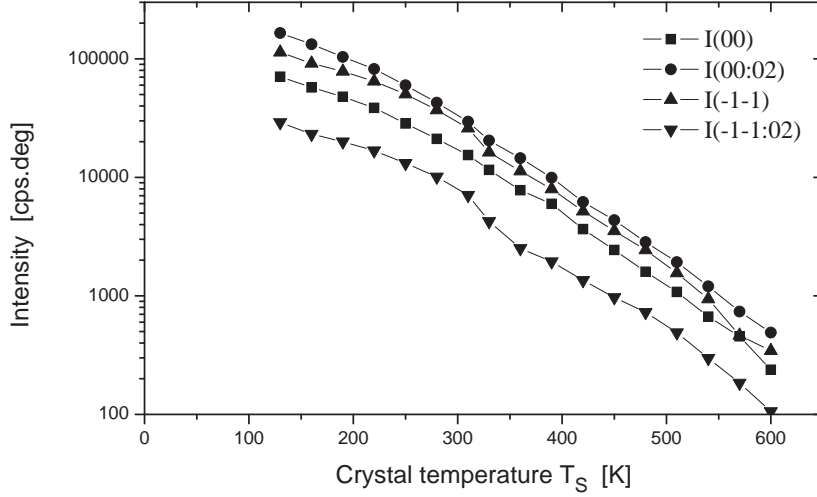


Figure 7.9: The surface temperature dependence of the intensities (peak area) of the peaks (00)(-■-), (00:02)(-●-), (-1-1)(-▲-) and (-1-1:02)(-▼-) for D_2 -LiF(001) along the $\langle 100 \rangle$ direction. $E_i=85$ meV ($k_i=12.8 \text{ \AA}^{-1}$). $\theta_{SD}=90^\circ$.

ments are carried out usually with crystals at room or liquid nitrogen temperatures. When the experimental and the theoretical elastic and RID probabilities are compared, zero-point and thermal vibrations of the surface atoms have to be taken into account. Debye-Waller analysis provides a simple method to investigate the attenuation of peak intensities by thermal attenuation due to the vibrations of the surface atoms as discussed in Section 2.4. Once DW factor is known, it is possible to estimate the peak intensities from surface of zero temperature from the measured peak intensities from a surface of finite temperature. DW factors for He and atomic hydrogen on LiF(001) are listed in Table 6.1. Moreover, the coupling of the rotational transitions with surface phonons is an important point [343, 348]; if the rotational transitions are enhanced with phonons significantly, a static model would not suffice to explain the observed RID intensities. In this section, the crystal temperature dependence of peak intensities is investigated in order to obtain Debye-Waller factors and also phonon inelastic effects on the rotational transitions are discussed.

Constant- θ_{SD} scattering experiments were carried out similar to the angular scans in Figures 7.1 and 7.2 in $\langle 100 \rangle$ and $\langle 110 \rangle$ scattering directions for surface temperatures between 130 K and 600 K. High signal-to-background ratios allow determining the

major peak intensities up to the given temperatures. In Figure 7.9 the temperature dependence of the intensities of some sample peaks is given. The thermal attenuation is similar for other peaks. The lines are not first-order exponential which would be the case for an ideal DW analysis. Thus, the attenuation of the intensities with temperature do not agree with the DW model very well. At surface temperatures higher than 300 K the slope of the curve increases. This is probably due to the influences of multi-phonon effects and anharmonicity of the surface vibrations [290]. In Tables 7.3 and 7.4 the best-fit curve slopes $2W(T_s)/T_s$ of all peaks for two surface temperature ranges are given. The extrapolated intensities at 0 K, I^0 are found with using the slope of the curves are calculated only from data points between $T_s=130-310$ K. Surface Debye temperatures are calculated using the well depth measured in the previous section ($D=35.3$ meV) and Equations 2.46 and 2.50. The average value of Debye temperature Θ_D is obtained, by excluding the values with high uncertainty (marked with †), as

$$\begin{aligned}\Theta_D &= 577 \pm 50 \text{ K}; \text{ for } 130 \text{ K} \leq T_s \leq 310 \text{ K}, \\ \Theta_D &= 479 \pm 24 \text{ K}; \text{ for } 330 \text{ K} \leq T_s \leq 600 \text{ K}.\end{aligned}\tag{7.9}$$

Here the error bars are the standard deviation of the scattered Θ_D values and actual full ranges of the Θ_D values are about two times larger than the given error bars. Thus, in the analysis to compare the theory and the experiment, calculating back the zero temperature intensities from experimental results due to the obtained Debye temperature with high error bars, is not better than taking the peak ratios unless the peaks have a large incident angular difference. For instance, using the intensities measured from a room temperature surface, the exact probabilities to be determined by using Equation 7.1 have errors up to 100% , whereas the ratios to be determined by using Equation 7.4 will have errors of less than 50% .

As the temperature increased there is no significant broadening of peaks. Also for RID peaks there is no observation of a shifting of peak positions or much different DW factor which would have indicated a significant role of the surface temperature in rotational excitation as observed in molecular scattering from metal surfaces [349,350]. Allison *et al.* has reported that rotational transitions of D_2 and H_2 on $LiF(001)$ are dissipative rather than diffractive [348]. However, after extensive TOF analysis of D_2 from NaF , Brusdeylins *et al.* concluded that phonon excitations with and without rotational transition involvement have about the same probability [343]. The similarity of DW factors of all peaks in the present experiments supports this argument. Hence, a scattering model independent of phonon inelastic transitions using a static lattice is a good approximation for D_2 - $LiF(001)$.

Table 7.3: The surface temperature dependence of the peak intensities for D₂-LiF(001) along the $\langle 100 \rangle$ direction with $\theta_{SD}=90^\circ$. The peak positions and the probabilities are also given. The probabilities ($P=P(mn : j_i j_f)$) are obtained by using the extrapolated intensities to 0 K (I^0). At the peak (-1-1:13) there is also a small contribution of (00 : 20). The incident beam energy is $E_i=85$ meV and incident intensity is $I_0=28.4 \times 10^6$ cps.deg. The Debye temperatures (Θ_D) are obtained for two temperature ranges of the $-2W/T_s$ values by using Equation 2.46. The values marked with † have large errors due to the low intensity of the peaks.

(mn: $j_i j_f$)	θ_i [deg]	I^0 [cps.deg]	$P \times 10^3$	$-2W \times 10^3 / T_s$ (T_s range[K])	Θ_D [K]
(22:13)	13.94	12874	1.0	15.6(130-190)	445†
(22:02)	19.03	60964	3.2	13.0(130-330)	490†
(22)	24.83	260676	9.2	12.5(130-310):14.5(330-450)	510:473†
(11:02)	30.03	433314	23.0	10.8(130-310):13.9(330-510)	540:476
(11)	35.04	461632	16.2	9.26(130-310):14.7(330-600)	600:476
(00:13)	37.02	82962	6.7	7.83(130-310):16.1(330-510)	653:455
(11:20)	38.95	8044	4.0	9.04(130-360)	626†
(00:02)	40.70	520290	26.6	8.65(130-310):13.0(330-600)	602:491
(00)	45.00	196474	6.9	7.90(130-310):12.7(330-600)	652:514
(-1-1:13)	48.29	35082	2.8	8.65(130-310):11.2(330-510)	580:510
(-1-1:02)	51.38	71780	3.8	6.91(130-310):10.3(330-600)	666:546
(-1-1)	54.96	294562	10.4	7.21(130-310):12.7(330-600)	679:512
(-1-1:20)	57.66	11370	5.1	9.18(130-310)	627
(-2-2:13)	60.00	5710	0.4	6.46(130-310)	653†
(-2-2:02)	62.44	56570	2.8	7.95(130-310):13.5(330-480)	608:467
(-2-2)	65.19	106774	3.7	8.89(130-310):14.9(330-420)	604:466†
(-3-3:02)	74.84	15262	1.5	9.15(130-250)	552†

Table 7.4: The surface temperature dependence of the peak intensities for D_2 - $LiF(001)$ along the $\langle 110 \rangle$ direction with $\theta_{SD}=90^\circ$. The peak positions and the probabilities are also given. The probabilities ($P=P(mn : j_i j_f)$) are obtained by using the extrapolated intensities to 0 K (I^0). The Debye temperatures (Θ_D) are obtained for two temperature ranges of the $-2W/T_s$ values by using Equation 2.46. The values marked with † have large errors due to the low intensity of the peaks.

$(mn:j_i j_f)$	θ_i [deg]	I^0 [cps·deg]	$P \times 10^3$	$-2W \times 10^3 / T_s (T_s \text{ range [K]})$	Θ_D [K]
(30:02)	17.02	19145	1.0	11.9(130-210)	512†
(30)	23.50	67292	2.4	13.6(130-330)	489†
(20:02)	25.46	70284	3.7	14.6(130-330)	464†
(10:13)	29.28	85061	6.8	13.8(130-270)	472†
(20)	30.87	341771	12.0	12.3(130-300):14.7(330-480)	518:474
(10:02)	33.25	216887	11.4	12.8(130-300):15.0(330-450)	498:459
(00:13)	37.05	237304	19.0	9.69(130-300):12.8(330-450)	558:485
(10)	37.98	826819	29.0	11.6(130-300):15.2(330-540)	537:469
(00:02)	40.70	715597	37.5	11.5(130-300):14.4(330-540)	523:467
(10:20)	41.69	6239	2.8	8.02(130-210)	667†
(00)	45.00	376451	13.3	9.51(130-300):13.1(330-540)	594:506
(-10:02)	48.23	289034	15.2	9.28(130-300):13.4(330-540)	577:480
(-10)	52.01	918901	32.1	10.5(130-300):14.7(330-540)	564:477
(-20:13)	53.02	140506	11.3	9.55(130-300):13.5(330-540)	547:459
(-20:02)	55.90	341218	17.9	11.1(130-300):14.7(330-540)	522:453
(-20)	59.13	361785	12.7	10.7(130-300):15.6(330-540)	555:460
(-30:13)	61.46	60588	4.9	9.38(130-300):13.4(330-450)	540:452
(-30:02)	63.74	99010	5.2	9.13(130-300):14.2(330-480)	566:454
(-30)	66.54	68337	2.4	9.30(130-300):13.5(330-390)	589:490†

7.4 Scattering with Different Incident Beam Energies

In this section experiments with a constant source-to-detector angle and with different incident beam energies are discussed. In all the following results, the detector angle $\theta_{SD}=90^\circ$, the surface temperature $T_s=297$ K and the stagnation pressure $P_0=120$ bar. In Figures 7.10 and 7.11 some of the angular distributions of intensity vs. angle of incidence in the directions of $\langle 100 \rangle$ and $\langle 110 \rangle$, respectively, are presented for several incident energies and wave vectors. The complete presentation of the angular scans can be found in Appendix-B. The relative populations of the rotational states in the incident beam are listed in Table A.1. In the $\langle 100 \rangle$ direction for an incident energy of $E_i=21.3$ meV there are only specular and first order diffraction peaks. The diffraction peaks are significantly broad and even slightly asymmetric due to the broad energy spread of the incident beam and strong dependence of the peak positions on the wave vector as seen in Figure 7.4. Note that also the background is much higher at lower angles. Probably a small portion of beam has an energy of more than $\Delta E(0 \rightarrow 2)=22.2$ meV and goes through rotational transitions which appears as a very broad background at lower incident angles. With increasing incident energy rotational transitions are observed as far as the incident energy slightly above the transition energy. For instance, in the $\langle 110 \rangle$ direction and incident energy of 23.3 meV the (-20:02) peak is observed. For higher incident energies (1 \rightarrow 3) rotational transitions are also observed ($\Delta E(1 \rightarrow 3)=36.9$ meV) where 1/3 of the incident beam is in $j_i=1$. (2 \rightarrow 4) transitions can be observed only with the highest incident energy because of the high transition energy ($\Delta E(2 \rightarrow 4)=51.4$ meV) and low population of $j_i=2$ in the incident beam. For the angular scans -c and -d in Figures 7.10 and 7.11, respectively, 5% and 17% of the incident molecules are in $j_i=2$. In the scattering process from a surface, not only rotational excitations, but also rotational deexcitations are possible. Although (2 \rightarrow 0) transitions are principally possible at all incident energies, they are only observed at high energies, because at low energies (low stagnation temperatures) the population of the $j_i=2$ state is negligible. (3 \rightarrow 1) rotational transition is never observed since even at the highest stagnation temperature $T_0=400$ K ($E_i=116$ meV) the population of the rotational state $j_i=3$ is only 2%.

The relative intensities of the diffraction peaks with respect to the specular peak intensity, $R(mn)$ for both symmetry directions are shown in Figures 7.12 and 7.13 as a function of incident beam energy. Since the (m,n) and (-m,-n) peaks are kinematically symmetric, their intensities must be identical. Slight differences of 10-20% in the intensities of symmetric diffraction peaks are observed due to the inaccurate adjust-

ment of azimuthal and tilt angles. The average intensities of the symmetric peaks are plotted in the figures in order to reduce the alignment uncertainties. For all diffraction peaks, the ratio $R(mn)$ first increases as the E_i increases, then reaches a maximum and subsequently decreases. This is due to two competing processes. Firstly, as the E_i increases the corrugation "seen" by the molecules increases, which leads, generally, to an increase of the intensities of the diffraction peaks. Secondly, with increasing E_i the number of open channels increases and the outgoing flux is distributed over more channels thereby leading to a decrease in the intensities of the individual diffraction peaks. To compare the diffraction ratios between the two symmetry directions, in $\langle 110 \rangle$ the diffraction ratios are slightly larger than in $\langle 100 \rangle$. This is something against the intuition where along $\langle 100 \rangle$ also Li ions are lined! This demonstrates that such qualitative explanations like above are crude and mostly invalid, particularly when the interaction potential is deep and the corrugation is strong.

As the simplest quantitative approach, the Eikonal approximation provides for the estimation of peak intensities, explicit Bessel functions of corrugation and perpendicular momentum change which leads oscillatory behavior of intensities with changing perpendicular momentum change, Δk_z . Thus at certain conditions the peak intensities exhibit strong fluctuations and maxima, so called rainbow effects.

Similar rainbow effects are also observed for H₂-LiF(001) [284]. Traeger observed that $R(11)$ for p-H₂ along the $\langle 100 \rangle$ direction reaches a maximum value of about 6 at about incident energy of 60 meV. The position of the maximum is remarkably similar to the one for D₂-LiF(001). On the other hand, she observed in the $\langle 110 \rangle$ direction that the $R(mn)$ were significantly lower and the energy dependence smoother. $R(11)$ for p-H₂ was in the range of 0.5 to 1.0 for the incident energies between 20-90 meV. p-H₂ ($j_i=0$ is 100%) is more likely to be compared with n-D₂ ($j_i=0$ is 2/3). Although the interaction potential for H₂ and D₂ is identical, it is very difficult to compare qualitatively both species due to the difference in mass where effective corrugation is related with incident energy for a soft potential and the number of open diffraction channels is related to the wave vector. Secondly and the most importantly, for D₂-LiF(001) RID peaks are as intense as the elastic peaks whereas for H₂-LiF(001) the rotational transition energies are two times larger and RID peaks are relatively much smaller and even mostly negligible. In order to compare the diffraction intensities in both cases, the diffraction intensities can be summed over the inelastic peaks, however this method is based on the presumption that the rotational transitions are decoupled from the diffraction which is not valid for D₂-LiF(001) as will be discussed below.

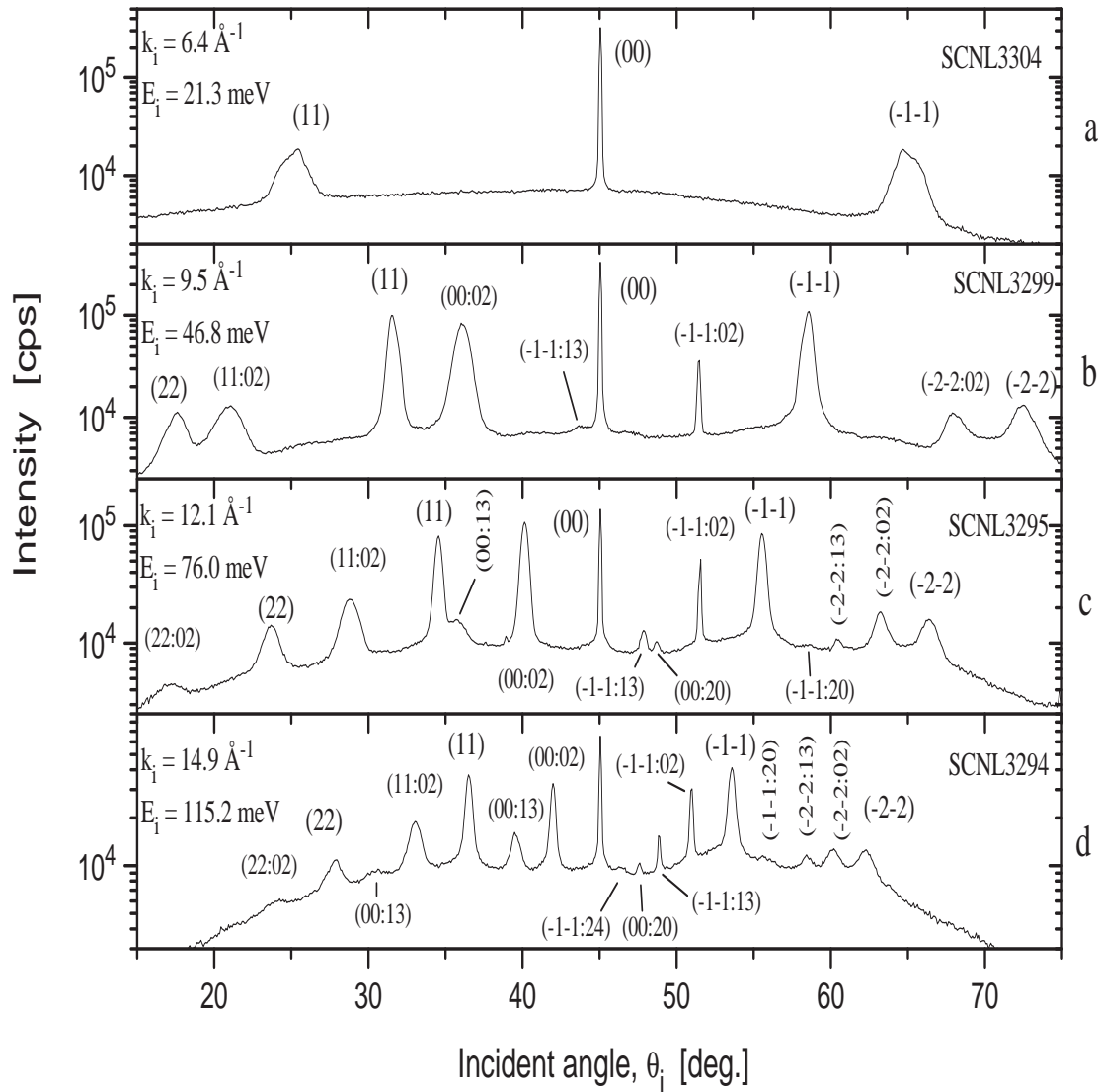


Figure 7.10: The incident angular scans at four different incident energies for D_2 -LiF(001) along the $\langle 100 \rangle$ direction. $\theta_{SD}=90^\circ$. The incident beam energy spread and initial relative populations of the rotational states are provided in Table A.1.

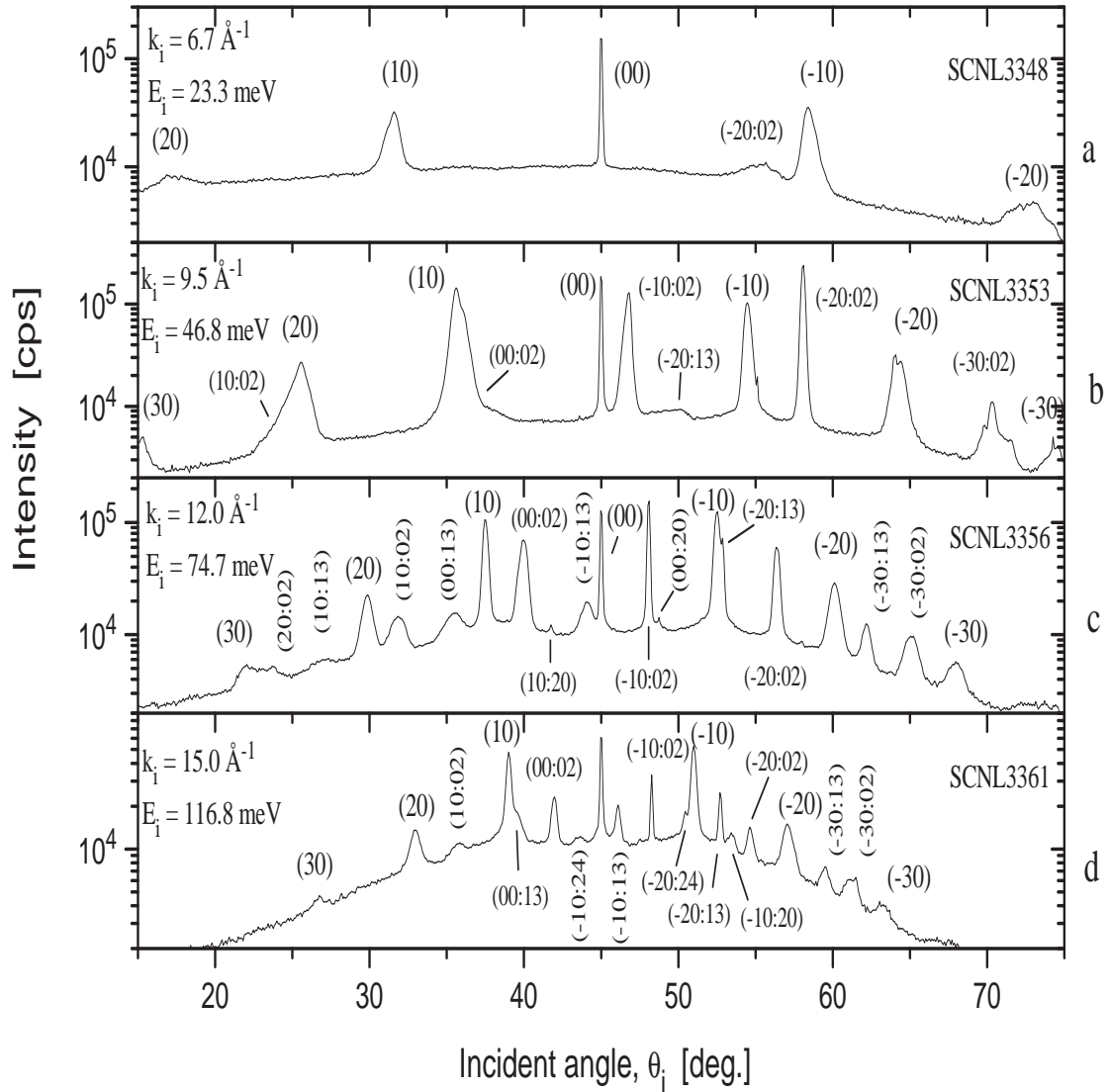


Figure 7.11: The incident angular scans at four different stagnation temperatures for D_2 - $LiF(001)$ along the $\langle 110 \rangle$ direction. $\theta_{SD}=90^\circ$. The incident beam energy spread and initial relative populations of the rotational states are provided in Table A.1.

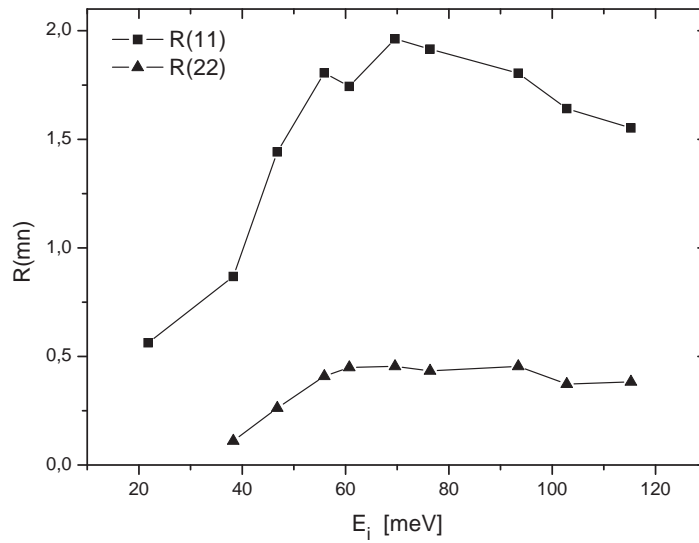


Figure 7.12: Ratios of diffraction peaks as a function of incident energy for D_2 -LiF(001) along the $\langle 100 \rangle$ direction. As the peak intensities the average peak-area intensities of symmetric peaks are taken. $\theta_{SD}=90^\circ$.

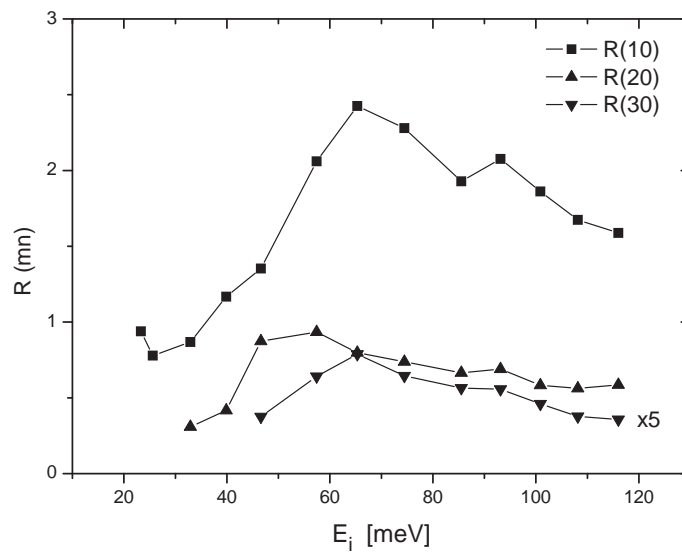


Figure 7.13: Ratios of diffraction peaks as a function of incident energy for D_2 -LiF(001) along the $\langle 110 \rangle$ direction. As the peak intensities the average peak-area intensities of symmetric peaks are taken. $\theta_{SD}=90^\circ$. Note that R(30) is multiplied by a factor of 5.

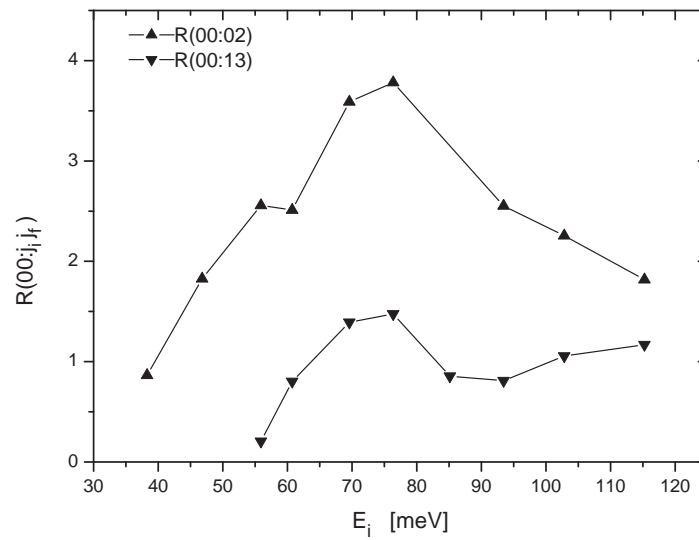


Figure 7.14: Incident beam energy dependence of the rotational transition ratios for D_2 -LiF(001) along the $\langle 100 \rangle$ direction. Ratio of the inelastic to elastic peaks $R(00:02)$ and $R(00:13)$ transition ratios are given. Note that $(0 \rightarrow 2)$ transition probability is 2 times larger than for $(1 \rightarrow 3)$. $\theta_{SD}=90^\circ$.

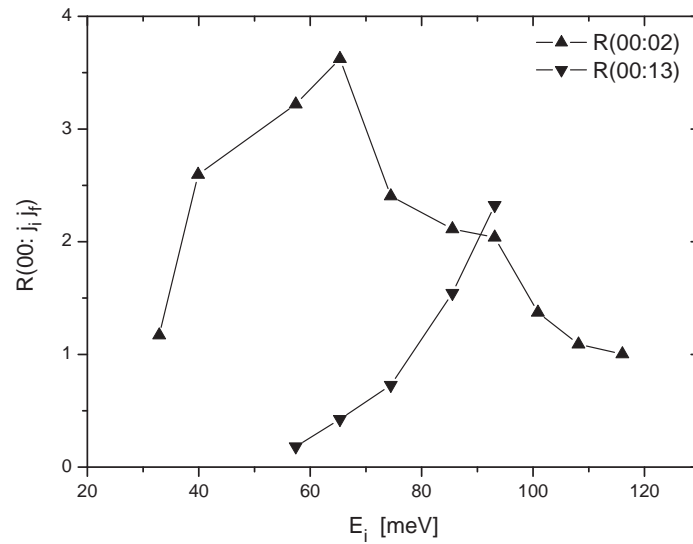


Figure 7.15: Incident beam energy dependence of the $R(00:02)$ and $R(00:13)$ transition ratios for D_2 -LiF(001) along the $\langle 110 \rangle$ direction. $\theta_{SD}=90^\circ$.

The incident energy dependence of the rotational transition ratios are plotted in Figures 7.14 and 7.15. The transition probabilities along the $\langle 100 \rangle$ azimuth for both the $(0 \rightarrow 2)$ and $(1 \rightarrow 3)$ transition reach a maximum at about $E_i = 70$ meV where $R(00:02)$ is two times larger than $R(00:13)$. The rotational rainbow structures are clearly observed. It is remarkable that both transitions have maxima at the same incident energy. However this is not a general rule. In $\langle 110 \rangle$ the transition probabilities are in the same order. But especially for $R(00:13)$ the energy dependence is very different. As seen in Figure 7.15 the $R(00:13)$ seems to have a maximum, if there is, at higher incident energies, however it is overlapped with other peaks at high incident energies.

In Figures 7.16 and 7.17 some of the ratios of the diffraction mediated rotational transitions with their parent diffraction peaks are shown. As seen apparently there is no correlation between the same rotational transitions of different diffraction and specular peak. The diffractive rotational transition ratios are found to be, mostly, less than the rotational transition ratios of the specular peak. This can be explained by the increased energy transfer from the normal motion for the diffraction peaks which competes with the energy exchange due to the rotational transition.

Therefore, it can be concluded that the rotational transition and diffraction are strongly coupled, where the decoupling should have had the following consequences: (a) $R(mn:j_i:j_f)$ for different (mn) should be the same; (b) the rotationally summed $R(mn)$ should be independent of molecular anisotropy; (c) the diffractively summed transition probabilities should be independent of surface corrugation.

One more evidence and an interesting implication of the strong coupling of diffraction and rotational transitions comes from the comparison of H_2 and D_2 scattering. As mentioned above, for H_2 -LiF(001) in the $\langle 110 \rangle$ there is no rainbow effect in diffraction observed [284], whereas for D_2 as seen in Figure 7.13 there is a strong rainbow effect is observed. This shows how rotational transitions significantly alter the diffractive features.

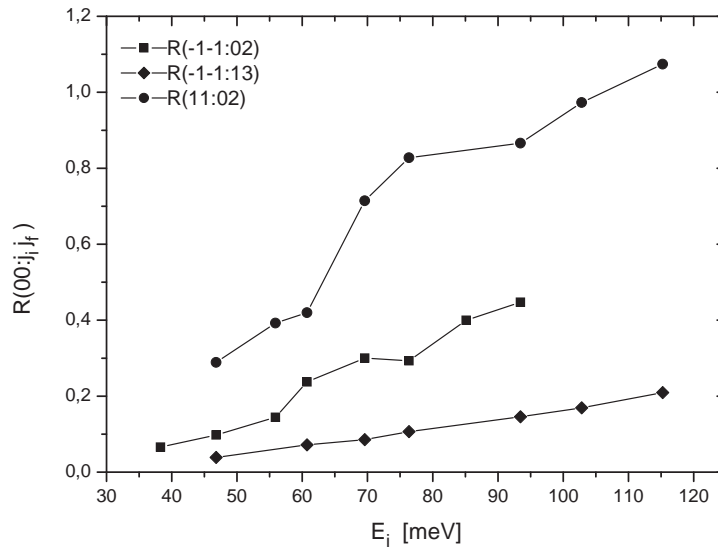


Figure 7.16: The ratios of diffractively mediated RID peaks with their parent elastic peaks for D_2 - $LiF(001)$ along the $\langle 100 \rangle$ direction as a function of incident beam energy. $\theta_{SD}=90^\circ$.

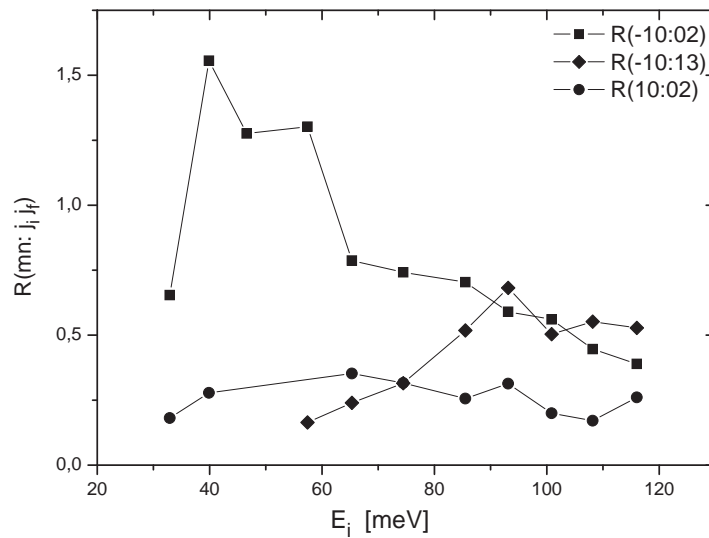


Figure 7.17: The ratios of diffractively mediated RID peaks with their parent elastic peaks for D_2 - $LiF(001)$ along the $\langle 110 \rangle$ direction as a function of incident beam energy. $\theta_{SD}=90^\circ$.

7.5 Constant Incident Angle Measurements

The rotatable detector feature of the apparatus allows for a variety of different possible molecular scattering experiments as discussed in Chapter 3. Not only the absolute reflectivity can be determined, thus, exact probabilities of the diffractive and rotational transitions, but also these can be measured at any initial and final angles. In principle, it is possible to rotate the detector while keeping the incident angle constant; or the final angle can be kept constant by rotating the detector and the crystal simultaneously. Although the latter technique could be useful for special purposes, the first one is highly desired and appreciated by theoreticians whereas previously most of the high resolution scattering data was taken for a constant total angle, θ_{SD} ($\theta_i + \theta_f = \theta_{SD}$). Additionally, observing the development of peaks with changing incident angle (decoupled from total angle restriction) will provide more insight into the scattering process. Hence, the flexibility of final and incident angles allows one to get the full picture of the scattering processes from a crystal. This can be done with the present apparatus in a variety of different ways. In Figure 7.3 constant- θ_{SD} and constant- θ_i scan lines are shown as a function of initial and final angles. Also the elastic peaks and major RID peaks for scattering from LiF(001) along the $\langle 100 \rangle$ direction are plotted according to kinematical conditions given in Equations 2.6 and 2.7. For instance, the detector can be rotated while keeping the incident angle constant which gives the intensities of all elastic and/or RID peaks for a given incident angle. However the rotation of the detector arm is too slow and it is necessary to break the vacuum during the scan to change the beam ports several times. Thus it would take several days to get one scan for a constant incident angle.

Another possible way would be to rotate the detector in small angular steps (0.1° - 0.2°) and at each step taking an angular scan by rotating the crystal; namely a incident angular (θ_i) scan which takes only about 15-20 minutes. The result would be a large matrix of intensity $[\theta_i, \theta_{SD}]$, which can be easily converted to the intensity matrix of $[\theta_i, \theta_f]$ providing a complete picture of the scattering process from the surface for all initial and final angles. With this three-dimensional data the development of the intensity of a certain peak can be analyzed or the intensities of all peaks at a constant incident angle can be extracted for theoretical comparison for any incident angle. Apart from the required time of several weeks for carrying out such an experiment and the problems of dealing with a huge amount of data, the problems of maintaining the required mechanical stability over such a long time finally led to abandoning this mode of operating. The following easier and more economic method, which also provides the

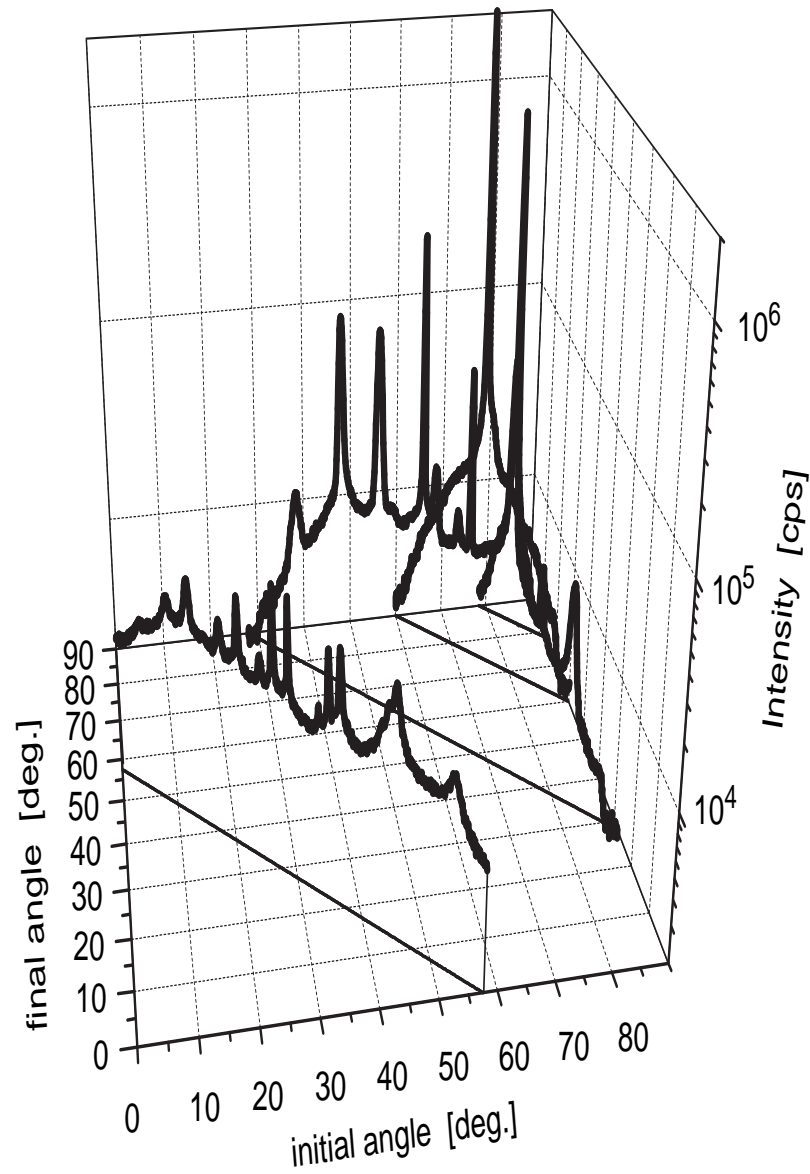


Figure 7.18: Incident angular scans at different constant total angles for D_2 - $LiF(001)$ along the $\langle 100 \rangle$ direction with total angles of $\theta_{SD}=57.5^\circ$, 118° , 150° , and 168.5° . $P_0=120$ bar and $T_0=300$ K. $E_i=85.3$ meV and $k_i=12.8 \text{ \AA}^{-1}$. The projection lines on the initial-final angle plane are also shown, which represent the scan lines as shown in Figure 7.3.

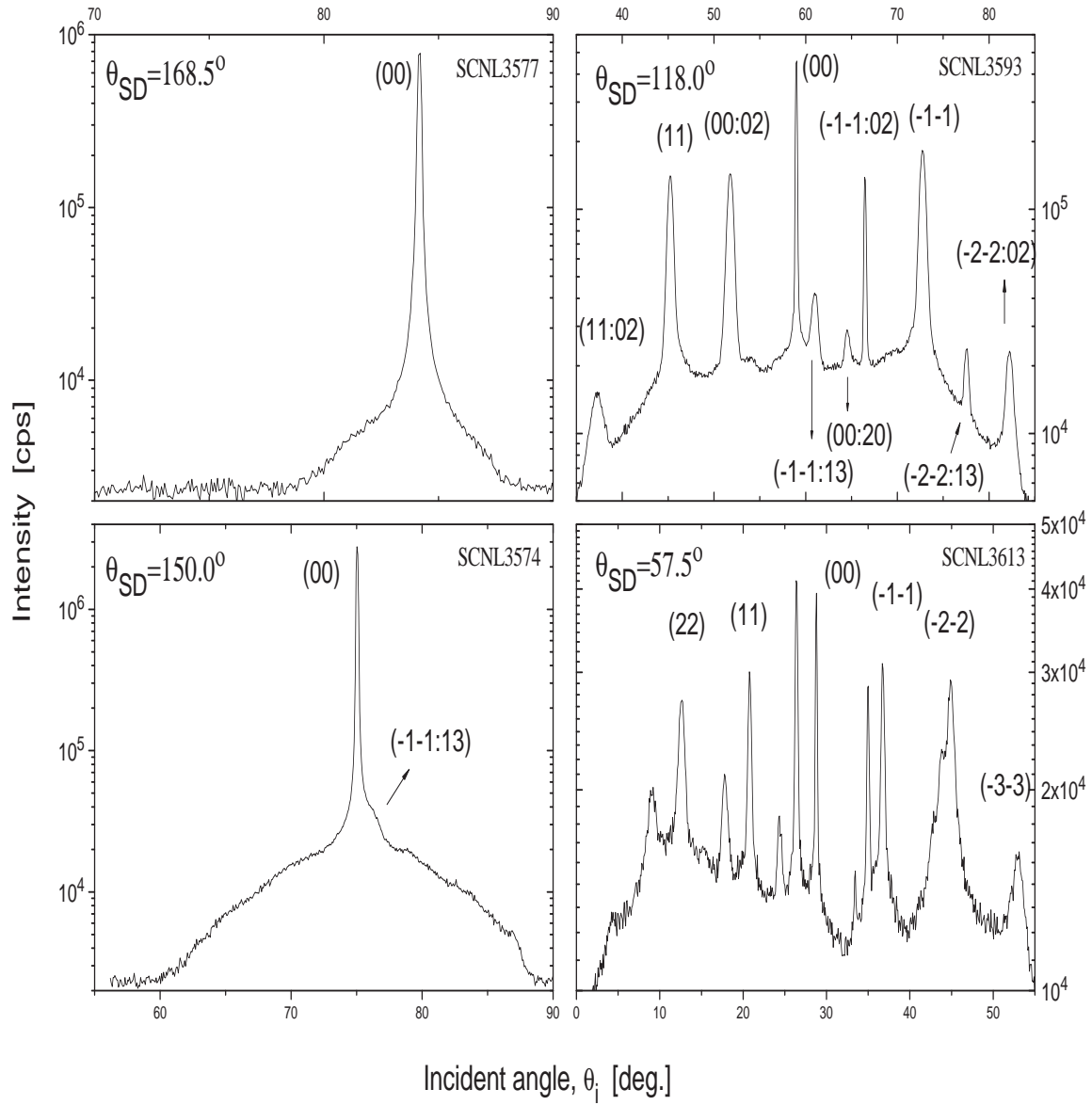


Figure 7.19: Incident angular scans at different total angles for D_2 -LiF(001) along the $\langle 100 \rangle$ direction. The scans are the same measurements in Figure 7.18. $P_0=120$ bar and $T_0=300$ K. $E_i=85.3$ meV and $k_i=12.8 \text{ \AA}^{-1}$.

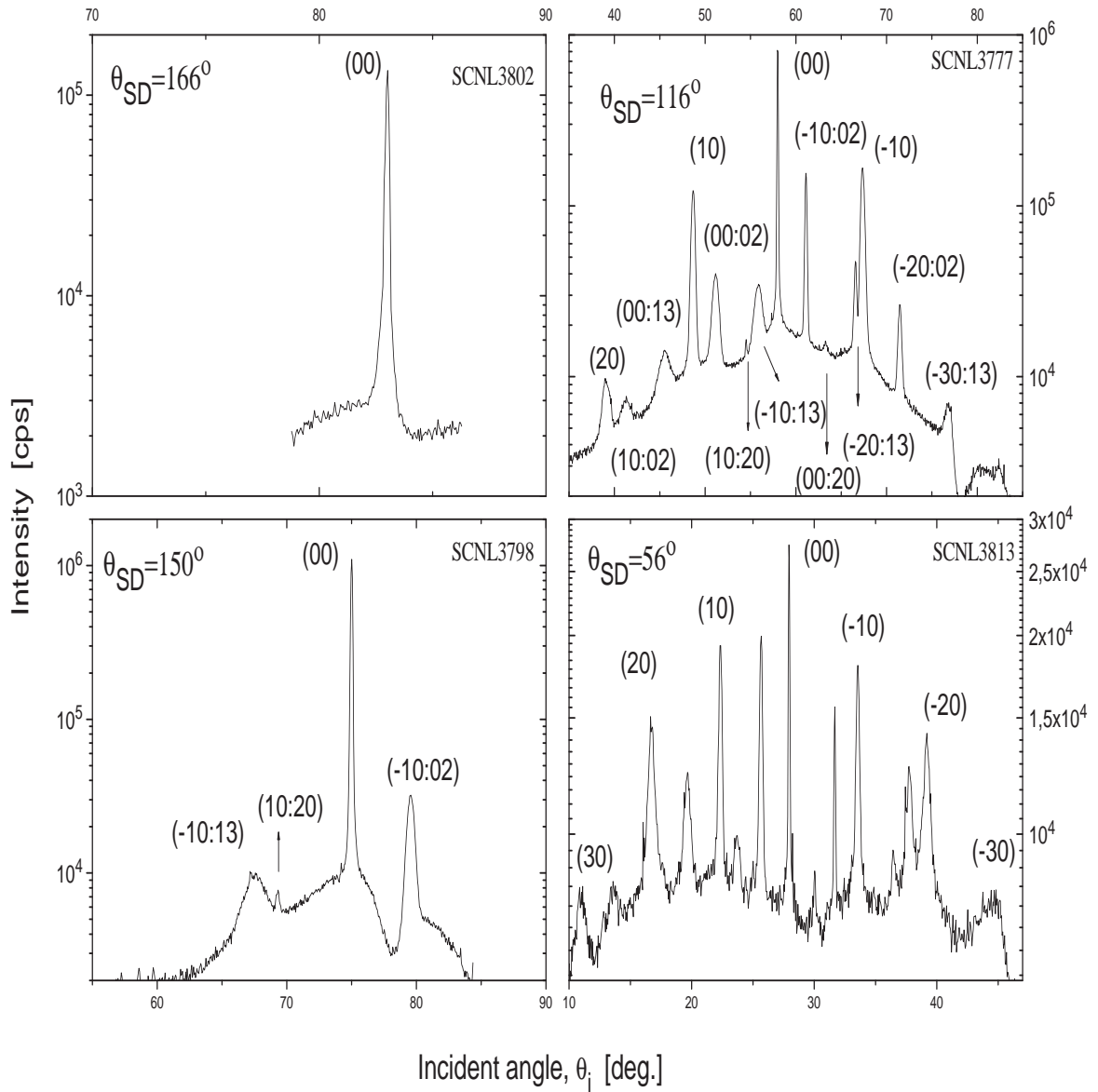


Figure 7.20: Incident angular scans at different total angles for D_2 - $LiF(001)$ along the $\langle 110 \rangle$ direction. $P_0=120$ bar and $T_0=300$ K. $E_i=85.3$ meV and $k_i=12.8 \text{ \AA}^{-1}$.

same whole picture was adopted. By taking several incident angular scans at constant detector angle in the range of $\theta_{SD}= 57.5^\circ$ and 168.5° with angular steps of 3° - 5° , it is possible to get the intensities of peaks at different incident angles (see Figure 7.3). The peak intensities for all peaks at a constant incident angle can be calculated by an interpolation of the intensity-incident angle plot. This is a reasonable method provided that the peak intensities change slowly and do not exhibit strong resonant features.

In this section the angular distribution of intensities with a variety of total scattering angles (θ_{SD}) are presented. The stagnation conditions were kept constant at 120 bar and 300 K, leading $E_i=85.3$ meV and $k_i=12.8 \text{ \AA}^{-1}$ and the populations of the rotational states of $n(j_i = 0)=58\%$, $n(j_i = 1)=33\%$, and $n(j_i = 2)=8$. The surface temperature was $T_s=297$ K.

In Figure 7.18 three-dimensional plots of intensities for four different total angles as functions of initial and final angles are given. With changing incident angle, the final angle also changes. The observed peaks can be identified with Figure 7.3. For clarity, only four angular scans are presented in the figure to give an overview of what constant- θ_{SD} angular scans mean. As the number of observed peaks changes from 1 to 20 and the peak intensities vary in a range of order of 3, it is difficult to get a physical insight and would be even more difficult when all the measured data had been presented.

The plots of intensity distributions as a function of incident angle only are more useful. In Figures 7.19 and 7.20 some of the measured angular scans in both symmetry axes are presented. The rest of the angular scans at all measured total angles are provided in Appendix-B. At the highest θ_{SD} angles only specular peak is observed and at the initial angles where the crystal surface "sees" the beam ($\theta_i < 90^\circ$) and the detector ($\theta_f < 90^\circ$) there is an inelastic background observed. Although there are some RID peaks kinematically possible at the highest detector angle in both directions, - for instance, as seen in Figure 7.3 the peak (-1-1:13), they are not observed due to the overlapping of peaks and, probably due to their low transition probabilities. With decreasing detector angle, the number of open channels and observed peaks increases and, as a consequence, the peak intensities decrease. However for the highest detector angles in both figures, the peak intensities are less than the ones for total angle of 150° . As discussed in Section 7.1.1, the reason is that at high incident angles, the actual amount of incident intensity decreases. For the lowest detector angles the RID peaks are not labelled in the figures where all RID peaks lie on the left of their parent elastic peaks. The RID peaks of (-2-2), (-3-3), and (-30) are merged with their

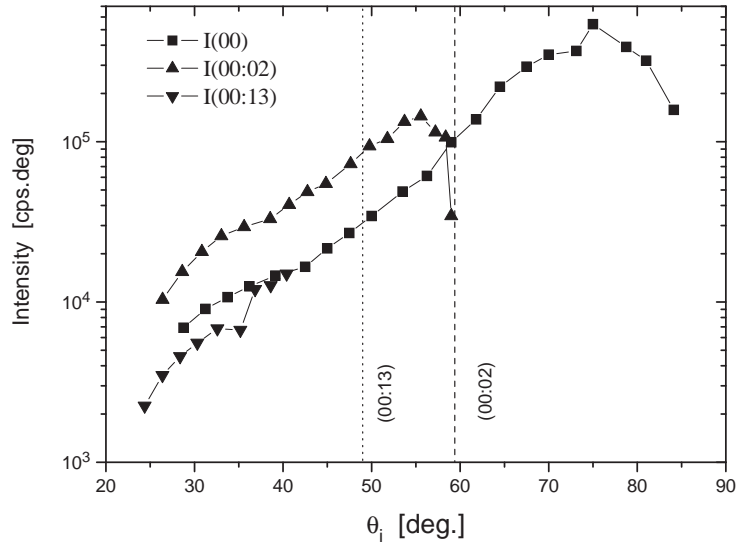


Figure 7.21: The peak-area intensities of specular peak and the rotational transitions for D_2 - $LiF(001)$ along the $\langle 100 \rangle$ direction ($\phi=45^\circ$). $P_0=120$ bar and $T_0=300$ K. $E_i=85.3$ meV and $k_i=12.8 \text{ \AA}^{-1}$. The dashed and dotted vertical lines show the critical angles for the (00:02) and (00:13) rotational transitions, respectively.

elastic peaks which is clearly seen in Figure 7.3. The reason is that the molecules scattered with large minus \mathbf{G} vectors bounce from the surface almost perpendicular. When they go through rotational transition they do not need to change their final angle significantly to compensate their total momentum change in order to conserve the parallel momentum.

Since each constant- θ_{SD} scan provides the intensities of individual peaks for different incident angles, the intensities of individual peaks can be extracted and plotted as a function of incident angle. In Figure 7.21 the measured intensities of specular peak and its rotational transitions in the $\langle 100 \rangle$ direction are plotted as a function of incident angle. All intensities increase with increasing incident angle due to the decreasing number of channels and decreasing DW factors. The intensity of the (0 \rightarrow 2) transition peak decreases abruptly as it approaches to the incident angle of about 60° . According to kinematical conditions (00:02) is not allowed above the incident angle of 59.4° which can be also seen in Figure 7.3. The critical angle for the (00:13) peak is 49.0° . At incident angles higher than the critical angle, the rotational transitions are not observed, since the momentum and energy conservation cannot be satisfied

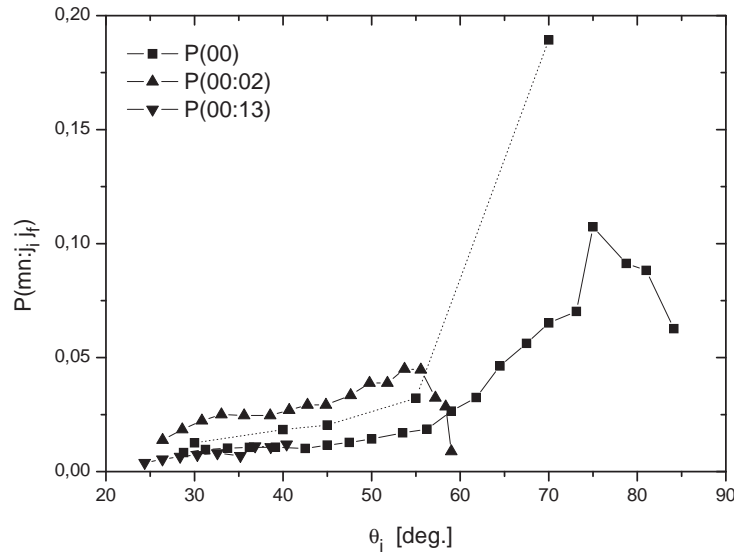


Figure 7.22: The probabilities of specular peak and the rotational transitions for D_2 -LiF(001) along the $\langle 100 \rangle$ direction ($\phi=45^\circ$) obtained from the data presented in Figure 7.21 using Equation 7.1. Theoretical values of $P(00)$ are presented as dotted lines. $E_i=85.3$ meV.

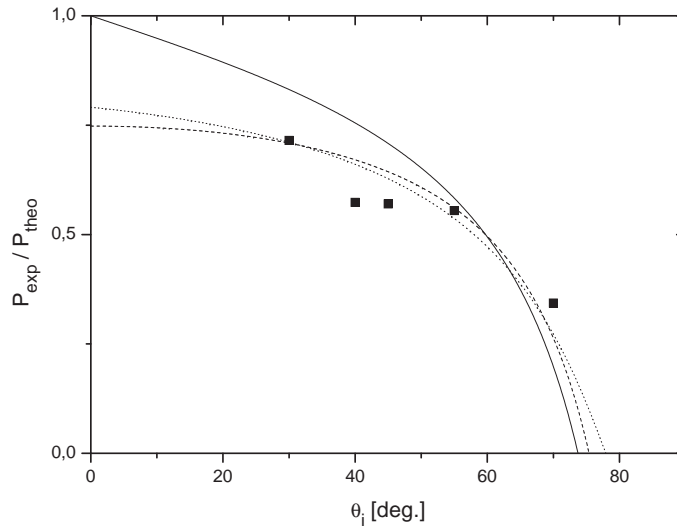


Figure 7.23: The ratio of experimental and theoretical probabilities of specular peak determined from the data in Figure 7.22 represented with filled squares. Solid line is the best-fit curve of Equation 7.11 resulting $L=6.9 H$. Dashed line is the best-fit curve of Equation 7.10 resulting $n_s \pi h^2=0.25$. Dotted line is the best-fit curve of the equation of multiplication of both Equations 7.11 and 7.10 resulting $L=18.2 H$ and $n_s \pi h^2=0.21$.

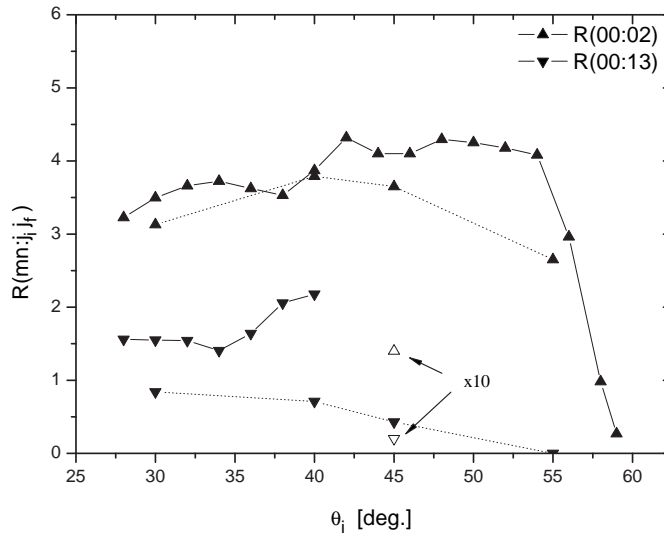


Figure 7.24: The ratios of inelastic transitions for D_2 - $LiF(001)$ along the $\langle 100 \rangle$ direction ($\phi=45^\circ$) obtained from the data in Figure 7.21 using Equation 7.4. Theoretical values are connected with dotted lines. The empty symbols represent the theoretical values (in the figure multiplied by a factor of 10) calculated without electrostatic term of the Kroes potential. $E_i=85.3$ meV.

simultaneously without phonons. Thus the region beyond the critical angle is kinematically forbidden zone. Unfortunately the (00:13) peak is overlapped with another peak for higher incident angles than 40° , so that its intensity cannot be extracted up to the critical angle. The specular peak intensity decreases at incident angles higher than 75° . This is mainly due to the decreasing actual amount of the incident beam on the crystal, namely decreasing factor η .

In Figure 7.22 the probabilities calculated from the intensity distributions in Figure 7.21 using Equation 7.1. Also theoretical values for only P(00) are presented. The theoretical values are calculated by using the Kroes potential and the CCWP method as described briefly in Sections 2.2.2 and 2.3 and in detail in refs. [7, 93]. For the calculations only $j_i=0$ and 1 states are taken into account because $j_i=2$ makes only 8% of the incident beam and it is computationally much more costly. Note that in the figure the theoretical probability values are about 2 times larger than the experimental ones. Of course, prediction of thermal attenuation of the surface with DW factor is poor as discussed previously. However, the discrepancy between the experimental and theoretical values is much larger than can be explained by the error of the DW factors.

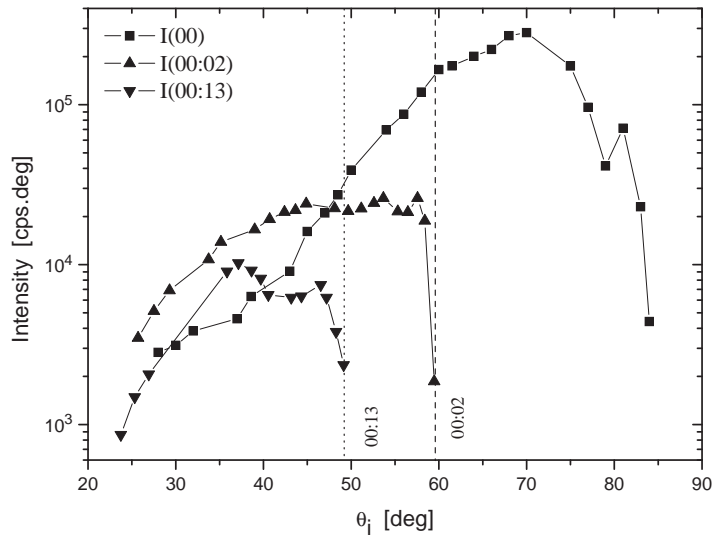


Figure 7.25: The peak-area intensities of specular and the associated rotational transition peaks for D_2 -LiF(001) along the $\langle 110 \rangle$ direction ($\phi=0^\circ$). $P_0=120$ bar and $T_0=300$ K. $E_i=85.3$ meV and $k_i=12.8 \text{ \AA}^{-1}$.

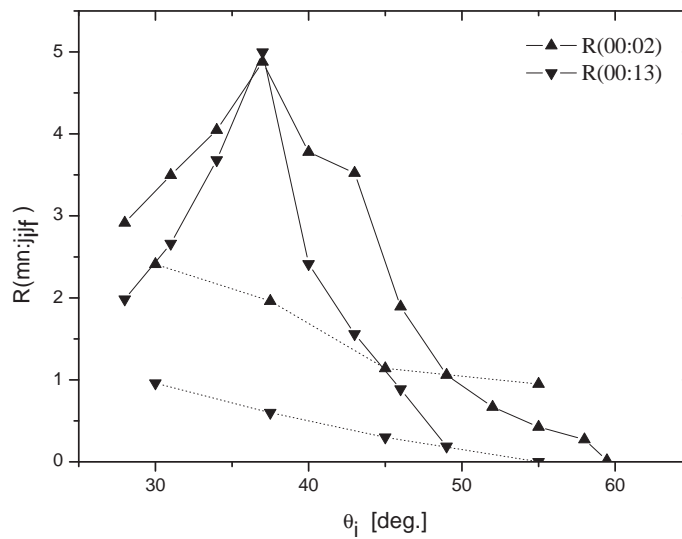


Figure 7.26: The ratios of the intensities of the rotational transition peaks to the specular peak for D_2 -LiF(001) along the $\langle 110 \rangle$ direction ($\phi=0^\circ$) obtained from the data in Figure 7.25. Theoretical values are connected with dotted lines. $E_i=85.3$ meV.

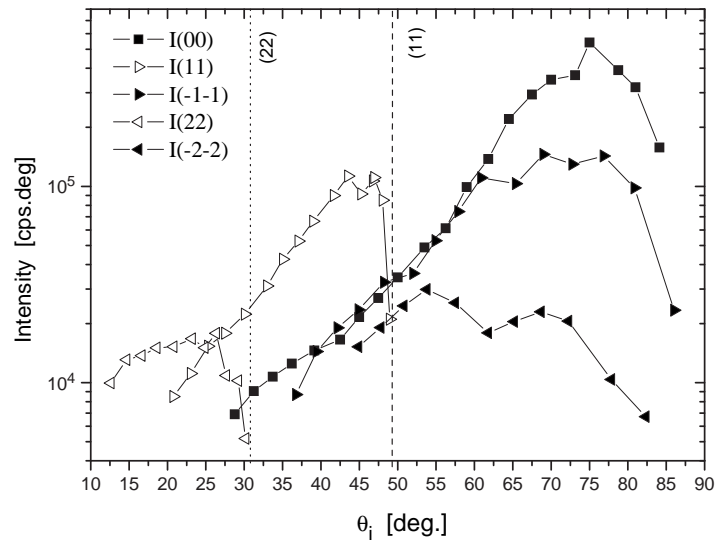


Figure 7.27: The peak-area intensities of specular and diffraction peaks for D_2 - $LiF(001)$ along the $\langle 100 \rangle$ direction ($\phi=45^\circ$). $P_0=120$ bar and $T_0=300$ K. $E_i=85.3$ meV and $k_i=12.8 \text{ \AA}^{-1}$.

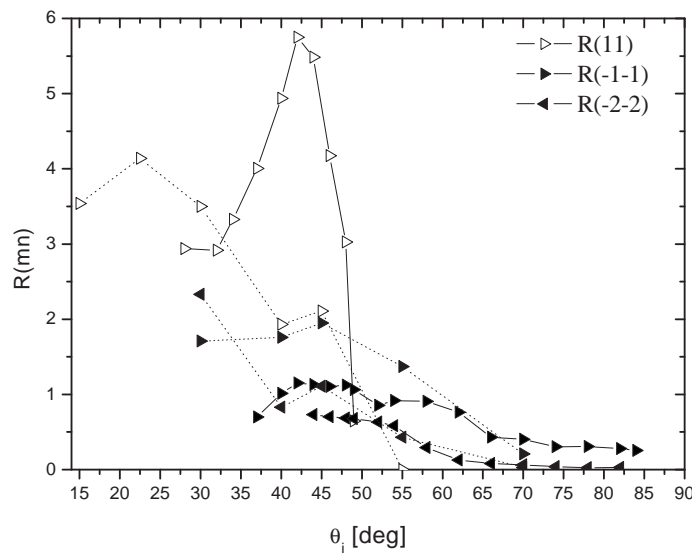


Figure 7.28: The ratios of diffraction peak intensities to the specular peak intensities for D_2 - $LiF(001)$ along the $\langle 100 \rangle$ direction ($\phi=45^\circ$) obtained from the data in Figure 7.27. Theoretical values are connected with dotted lines. $E_i=85.3$ meV.

The explanation is that even on the LiF(001) surface which has relatively low defect density and is an inert surface, there is still a significant amount of defects such as vacancies, steps, dislocations, adatoms, surplus ions, etc. These defects generally have very large scattering cross sections, diminishing a significant portion of the coherent intensity [35,36]. Assuming that the defects are isolated and randomly distributed on the surface with a density of n_s and have cross sections approximated with hemispheres of radius of h , the experimental probabilities can be estimated as [23]

$$P_{exp} = P_{theo} \left[1 - \frac{n_s \pi h^2}{\cos \theta_i} \right] , \quad (7.10)$$

where $\cos \theta_i$ accounts for influence of the incident angle for the specular peak for the "shadowed" clean surface⁴. For regular surface steps the measured probabilities of the specular peak will be [351]

$$P_{exp} = P_{theo} \left[1 - \frac{2H}{L} \tan \theta_i \right] , \quad (7.11)$$

where H is the effective step height and L is the average step length⁵. Note that in Figure 7.22 the discrepancy between the experimental and theoretical values increases with increasing incident angle and $P(00)$ decreases beyond $\theta_i=75^\circ$ even though the η factor has been taken into account. Both of these effects are in accordance with Equations 7.10 and 7.11. In Figure 7.23 the ratio of the experimental and theoretical probabilities of the specular peak ($\frac{P_{exp}}{P_{theo}}$) is plotted. Assuming that the discrepancy of the theoretical and experimental values are due to the steps a best-fit value of step length of $L=6.9 H$ is estimated. This result is unrealistic since steps heights should be a few angstroms and the average step width is several hundred angstroms (see also Chapter 6). The Equation 7.10 is also fitted to the data and a best-fit value of $n_s \pi h^2=0.25$ is obtained. Assuming the cross-section of the defects is 10 \AA^2 , the defect density should be 40 \AA^{-2} . By taking contributions of both defects and steps into account, best-fit values of $L=18.2 H$ and $n_s \pi h^2=0.21$ are obtained. These results are still not satisfactory since the best-fit curve predicts that the intensities should not be observed above the incident angle of about 75° whereas the intensities could be measured at least up to 85° . The probable reason is that Equation 7.11 presumes a regular and well defined steps. Moreover, the experimental and theoretical probabilities can have significant errors. The estimation of defect or step density would be more

⁴For $\cos \theta_i < n_s \pi h^2$, $P_{exp}=0$

⁵For $\tan \theta_i > \frac{L}{2H}$, $P_{exp}=0$. In the equation the interference effect is not taken into account.

feasible with He atoms where estimating DW factor and theoretical calculation of probabilities are much more precise and easier. Since the estimation of the effects of the defects and steps is difficult, as mentioned above, it is more reasonable to work with peak ratios (R) instead of probabilities (P) for the comparison of the theory and the experiment.

In Figure 7.24 the ratios of the rotational transition peaks to the specular peak determined by Equation 7.4 are given. The R-values are almost insensitive to the incident angle until they approach the kinematically forbidden zone. Theoretical values for the R(00:02) are in reasonably good agreement with the experimental values. For (00:13) there is a discrepancy of 50% at 30° which is not significant. At 55° R(00:13) is calculated as zero where it is kinematically also not allowed. In the figure at the incident angle of 45°, the calculated R-values without the electrostatic term of the interaction potential are shown. The rotational transitions are reduced by a factor of about 20 when the molecule quadrupole-surface electrostatic field interaction is ignored. This demonstrates the significant role of the electrostatic interaction in the rotational transitions.

In Figure 7.25 the intensities of the specular peak and its RID peaks in the $\langle 110 \rangle$ direction are shown. At incident angles of greater than 40° the RID intensities do not increase and even become almost constant or decrease. They decrease steeply as they approach their kinematically critical angles. The specular peak intensity exhibit a dip at the incident angle of 79°. As it can be seen in Figure 7.20 and in Appendix-B, the angular distribution of the intensities always show a dip at the incident angle of 78°. This is only observed in the $\langle 110 \rangle$ direction. Not only the intensity of the elastic and RID peaks, but also the inelastic background intensity is suppressed at this angle. The reason is unclear. In Figure 7.26 the ratios of the measured rotational transitions peak intensities to the specular peak intensity in the $\langle 110 \rangle$ direction are presented. The ratios for both (0→2) and (1→3) transitions show a strong dependence on the incident angle, unlike in the $\langle 100 \rangle$ direction, and have maxima at about 37°. The theoretical values are in agreement within 50% of error at 30° and above 45°. At 37° the observed enhancement in R-values cannot be reproduced by the theory.

The observance of maxima for both rotational transitions is a strong evidence of rotational rainbow effect. Diffractive rainbows are well-known features of atom-surface scattering and have been studied extensively within classical and quantum mechanical approximate methods [40, 78, 352, 353]. They arise from the extrema of the diffraction probability functions with respect to incident angle or energy. For the molecule-surface scattering rotational rainbows are also investigated [67, 354]. Similarly the extrema of

the excitation function lead to strong transition probabilities. However these methods are based on assumptions such as the interaction potential being independent of azimuthal angle of the molecule and/or rotational transitions being weak or decoupled from the diffraction. Indeed, *rotational rainbows* are separately treated from *surface rainbows* [67]. Whereas the former are assigned to the excitation of the rotational transitions due to the anisotropy of the molecule, the latter are related to the extrema of the diffraction intensities due to the corrugation of the surface.

In Figure 7.27 the intensities of the diffraction peaks in the $\langle 100 \rangle$ direction are plotted as a function of incident angle. The specular peak is also plotted for comparison. The diffraction peaks with positive \mathbf{G} -vectors decrease dramatically when they approach to the kinematically forbidden angle and finally disappear. The intensities of the diffraction peaks (-1-1) and (-2-2) tend to decrease at high incident angles relative to the specular peak. The intensity ratios extracted from Figure 7.27 are compared with the theoretical calculations in Figure 7.28. The R(11) ratio is almost constant at incident angles below 32° . The theory also predicts the same behavior and is in good agreement within 25% of error. However with increasing incident angles R(11) exhibits a strong rainbow effect, which the theory cannot reproduce. For other diffraction peaks there is no rainbow effect observed and the theoretical values fit rather well. For R(-1-1) the experimental values are about 50% less than the theoretical values and for R(-2-2) the theoretical and experimental values are in agreement within 30% .

In Figure 7.29 the diffraction peak intensities along the $\langle 110 \rangle$ direction are presented. The behaviors of the diffraction peaks are similar to the one in the $\langle 100 \rangle$ direction. At 78.2° the (-10) diffraction peak shows a strong minimum and it was barely observed and identified. As discussed before, this is due to the strong suppression of peak intensities at 78° . The attenuation of the specular peak is not as strong as the attenuation of (-10) peak because the specular peak is at 79° . In Figure 7.30 the measured and calculated R-values of the diffraction peaks are provided. The attenuation at 78° is ignored in determining the peak ratios. The R(10) exhibits a rainbow effect at about 40° . At the incident angles of 30° and 55° the agreement of the theoretical and experimental values is good, however the theory fails to reproduce the extremum between these angles. The agreement of theoretical and experimental R(20) values is rather poor. R(20) could be determined in a small angular region and seems to show also a rainbow effect below 30° . The behaviors of diffraction peaks with minus \mathbf{G} -vectors are smooth and the theory predicts reasonably similar values.

The diffraction peak ratios in both symmetry axes, generally tend to decrease with increasing incident angle. Qualitatively this can be explained as follows: With increas-

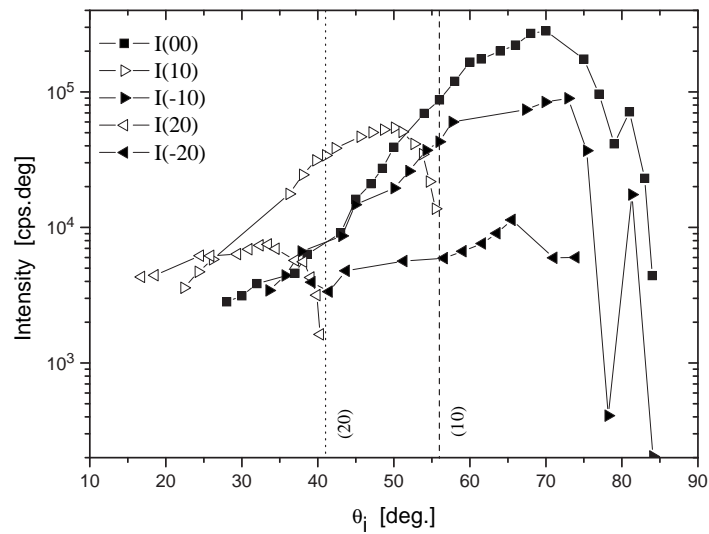


Figure 7.29: The peak-area intensities of specular and diffraction peaks for D_2 - $LiF(001)$ along the $\langle 110 \rangle$ direction ($\phi=0^\circ$). $P_0=120$ bar and $T_0=300$ K. $E_i=85.3$ meV and $k_i=12.8 \text{ \AA}^{-1}$.

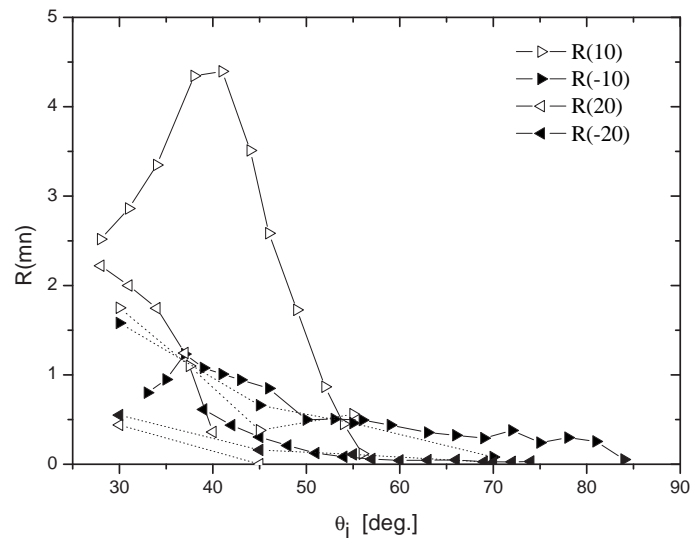


Figure 7.30: The peak ratios of the diffraction peaks for D_2 - $LiF(001)$ along the $\langle 110 \rangle$ direction ($\phi=0^\circ$) obtained from the data in Figure 7.29. Points connected with dotted lines are the calculated values. $E_i=85.3$ meV.

ing incident angle the perpendicular component of the incident energy is decreases, thus the penetration of the molecules into the repulsive region of the potential decreases (for instance, see Equation 2.23). The effective corrugation felt by the incident particle is thus reduced. Secondly, with increasing incident angle, for diffraction peaks the difference between the incident angle and final angle increases as can be seen in Figure 7.3. Since the initial and final states of the scattering particle become more separated the transition probabilities of the diffraction peaks decrease with increasing incident angle.

The rainbow effect is more pronounced for the (11) diffraction peaks. Although the Eikonal approximation is not valid for this case, it can be used for a qualitative explanation. Within this approximation the probability of elastic diffraction with \mathbf{G} -vector of indices (m,n) is given by [78]

$$P_{mn} = \frac{\cos \theta_f}{\cos \theta_i} J_{|m|}(\frac{\zeta_0}{2} \Delta k_z) J_{|n|}(\frac{\zeta_0}{2} \Delta k_z) \quad , \quad (7.12)$$

where $J_{|m|}$ and $J_{|n|}$ are the Bessel functions of order $|m|$ and $|n|$, Δk_z the change of the perpendicular component of the wave vector ($k_{iz} + k_{fz}$) and ζ_0 is the surface corrugation amplitude as described in Section 2.2.1. With increasing Δk_z the Bessel functions, thus the diffraction probabilities, increase monotonically for small Δk_z . For large Δk_z , provided that the corrugation is large, they oscillate and exhibit minima and maxima. For the same incident angle, the perpendicular component of the initial wave vector (k_{iz}) is the same for all diffraction peaks, however the diffraction peaks with positive \mathbf{G} -vector scattered with larger final angles as seen in Figure 7.3, thus they have larger perpendicular part of the final wave vector (k_{fz}). Since Δk_z is larger for positive m and n values, diffraction probabilities of positive indices must show have more extremal conditions.

In Figure 7.31 the intensities of the (-1-1) diffraction peak and of the associated rotational transitions and in Figure 7.32 the ratios of the RID peaks with respect to the diffraction peak in the $\langle 100 \rangle$ direction are presented. For the (1 \rightarrow 3) rotational transition the theory shows reasonable agreement at low incident angles. At the incident angles of 55° and 70° the discrepancy is about a factor 3 and 2, respectively. For the (0 \rightarrow 2) rotational transition the discrepancy is much more significant at low incident angles. Probably the (0 \rightarrow 2) transition exhibits rotational rainbow effect with a maximum at lower angles which, again, cannot be reproduced by the theory. Similar plots for the $\langle 110 \rangle$ direction are provided in Figures 7.33 and 7.34. For the (1 \rightarrow 3) transition the theory and the experiment are in good agreement within an error of 30% . At 70°

the theoretical value is zero as expected since the (1→3) transition is forbidden above 69°. For the (0→2) transition the theoretical value is similar to the experimental value at 45° but a factor 2 larger than the experimental value at the incident angle of 55°. The experimental R(-10:02) values at high incident angles increase significantly. Also the theoretical values increase, however much earlier and faster. This is due to the fact that both the (-10:02) and (-10) peak intensities decrease at high incident angles but the intensity of the (-10) decreases faster (see Figure 7.33).

Comparing the ratios of the rotational transitions associated with the (-10) diffraction and specular peaks in both symmetry axes, there is no correlation of ratios observed. This is an obvious evidence of the strong coupling of the diffraction and rotational transitions, since, as discussed in Section 7.4, in the case where diffraction and rotational transitions are decoupled, the ratios of the rotational transitions associated with different elastic peak must be identical.

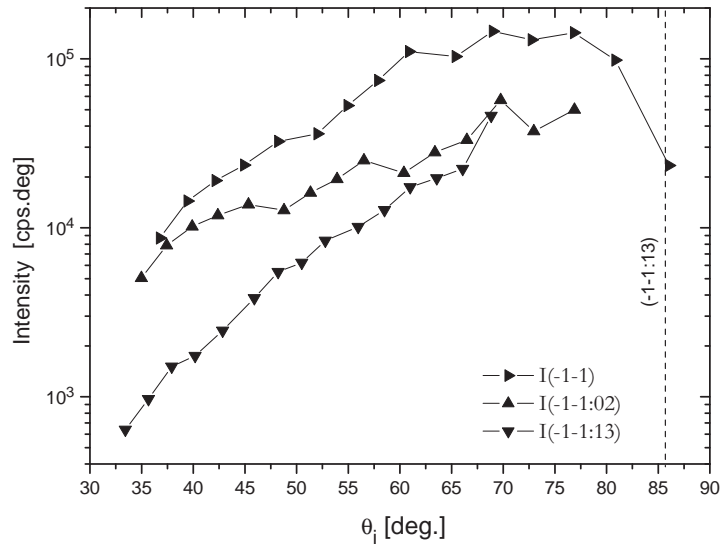


Figure 7.31: The peak-area intensities of (-1-1) diffraction peak and its related rotational transitions for D_2 -LiF(001) along the $\langle 100 \rangle$ direction ($\phi=45^\circ$). $P_0=120$ bar and $T_0=300$ K. $E_i=85.3$ meV and $k_i=12.8 \text{ \AA}^{-1}$.

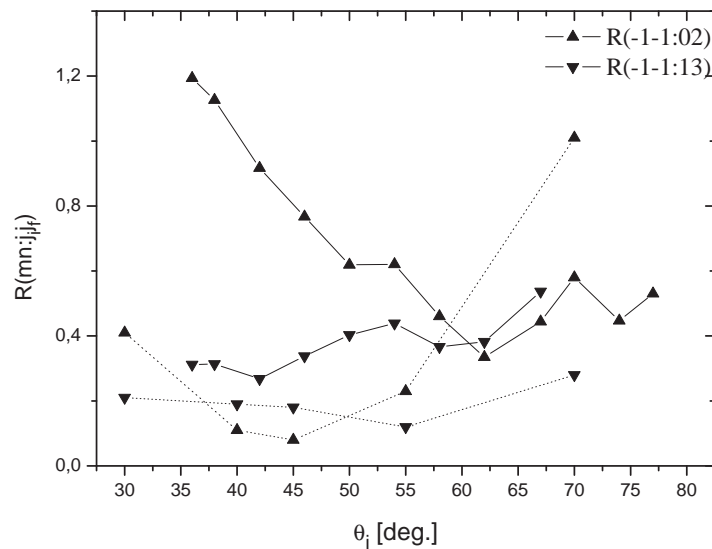


Figure 7.32: The calculated ratios of R(-1-1:02) and R(-1-1:13) peaks for D_2 -LiF(001) along the $\langle 100 \rangle$ direction ($\phi=45^\circ$) obtained from the data in Figure 7.31. The calculated values are given with dotted lines. $E_i=85.3$ meV.

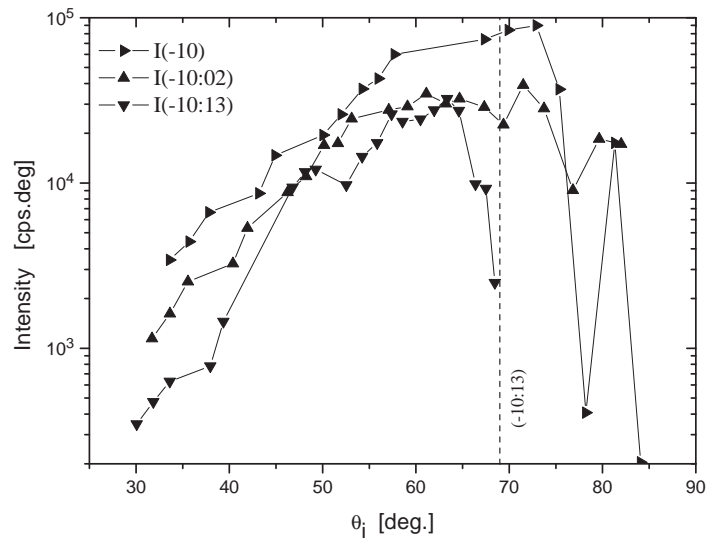


Figure 7.33: The peak-area intensities of (-10) peak and its rotational transition peaks for D_2 -LiF(001) along the $\langle 110 \rangle$ direction ($\phi=0^\circ$). $P_0=120$ bar and $T_0=300$ K. $E_i=85.3$ meV and $k_i=12.8 \text{ \AA}^{-1}$.

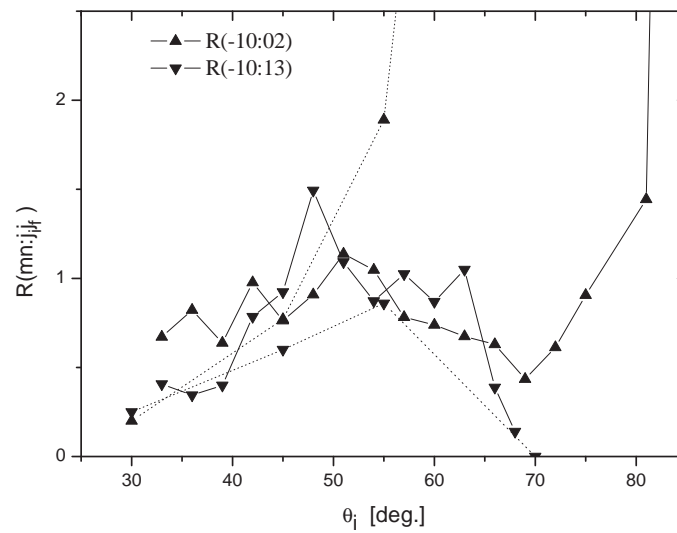


Figure 7.34: The ratios of the rotational transition peaks of the (-10) peak for D_2 -LiF(001) along the $\langle 110 \rangle$ direction ($\phi=0^\circ$) obtained from the data in Figure 7.33. Points connected with dotted lines are the calculated values. The experimental $R(-10:02)$ at 82° is 4.32 and the theoretical $R(-10:02)$ at 70° is 9.46. $E_i=85.3$ meV.

7.6 Scattering of D_2 Dimers from the LiF(001) Surface

As seen in Section 4.4, there is a significant amount of dimers and larger clusters in the incident beam. Observing a coherent scattering of the dimers from the surface would be an interesting experiment to investigate the dimer-surface interaction, which will bring more insight into inelastic energy transfer and thin film growth and adsorbate processes. Naturally, most of the weakly-bound dimers with an interaction potential of a few meVs will fragment when the surface temperature is high and the impact energy of dimer is significantly higher than the binding energy. However, similar to atomic and molecular scattering where most of the intensity is inelastically scattered from the room temperature surface, the small amount of elastically scattered fraction is coherent and lead to specular and diffraction peaks which provides information about the interaction potential. Indeed, coherent scattering of hydrogen dimers from LiF(001) has been reported by Tepper and Miller [355, 356]. They observed specular and first order diffraction peaks of the hydrogen dimers with an incident energy of 48 meV ($T_0=110$ K) scattering from a LiF(001) surface at 150 K. They estimated the surface corrugation as about 0.15 Å.

In this section, scattering of D_2 dimers from LiF(001) is investigated. As discussed in Section 4.4 stagnation conditions of $T_0=180$ K and $P_0=120$ bar provide the highest incident dimer intensity without any significant concentrations of trimers and larger clusters, ensuring that the observed scattered dimer beam is results purely from the incident dimer beam. In Figure 7.35 the angular scan of the specular peak of the dimers measured on mass 6 amu (for the D_3^+ fragment ion) is shown at an incident angle of 75° from a LiF(001) surface at 150 K. In order to reduce the background at mass-6 originating from C^{++} emitted from the hot cathode, the emission current is set to 1 mA and the cathode voltage is set to 40 V. Since the C^{++} signal is from double ionization peak, its intensity decreases faster than the single ionization probabilities with decreasing cathode voltage and 40 V was found to be providing an optimum signal-to-background ratio.

As seen in the figure the specular peak is barely observed. Note that the angular scan is 100 seconds per step. Under these circumstances it is impossible to observe diffraction peaks. Repeating the experiment at $T_0=110$ K did not increase the measured intensity. Although the incident energy is less at lower stagnation temperature which should lead to an increase in the survival probability of dimers during the impact, the incident dimer intensity gets also lower. The measured intensity of the specular peak of scattered dimers is 1 cps. The present construction of the apparatus (see also

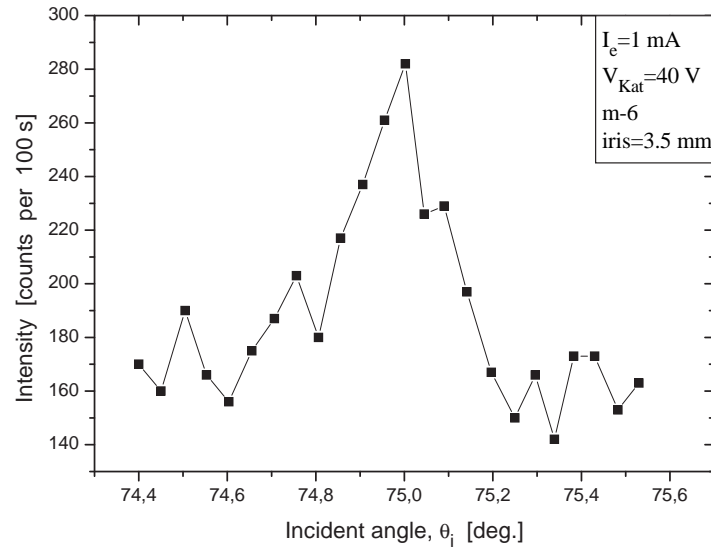


Figure 7.35: Angular scan of specular peak for $(D_2)_2$ -LiF(001). $\theta_{SD}=150^\circ$, $T_0=180$ K, $P_0=120$ bar and $T_s=150$ K. Detector settings: mass-6, $V_{Kat}=40$ V, $I_e=1$ mA. Incident dimer beam intensity, $I_0=4.8 \times 10^6$ cps.

Chapter 3) is not optimum for intensity measurements due to the long source-to-detector distances (~ 3 m). Tepper and Miller's apparatus was more compact (~ 60 cm) and had more beam divergence (0.5°) providing more incident intensity. On the other hand, they had no differential pumping stages where there is much more normal and diffused background at mass-3 originating from the natural abundance of D in hydrogen. Secondly, the binding energies of $(H_2)_2$ and $(D_2)_2$ are 0.37 and 0.85 meV, respectively [357], thus fragmentation of D_2 -dimer should be less probable. Nevertheless, they reported that they could observe the dimer diffraction peaks up to crystal temperatures of 300 K and also at source stagnation temperatures of 165 K. They estimated the survival probability of dimer (ratio of total elastically scattered dimers intensity with the incident beam intensity) as 5%. In our case, the incident intensity of the dimer beam is about 80×10^3 cps from Figure 4.19. In fact, taking the beam divergence (iris diameter) and detector settings into account it should be multiplied by a factor of 60 for the comparison. The survival probability of dimers during the scattering from fragmentation is estimated as about 10^{-7} . Hence, Tepper and Miller's results [355, 356] could not be reproduced.

7.7 Conclusions

Experiments with various techniques and the comparative theoretical analysis supplied valuable physical insights into the scattering and rotational transitions of D_2 from LiF(001). The theory with the Kroes-potential and the CCWP method is highly successful in predicting the probabilities of the diffractive and the rotational transitions. However, when strong rainbow effects are observed, the theoretical agreement is poor, thus Kroes-potential cannot predict rainbow effects. The reason is that the rainbow effects are highly sensitive to the surface corrugation and the anisotropic part of the potential.

For approximate methods molecular anisotropy or surface corrugation are the fit parameters, thus successful in reproducing the rainbow structures. However these approximate methods are not appropriate for the D_2 and H_2 -LiF(001) where either the coupling is ignored or weak [64], the magnetic quantum number transitions are forbidden [62] or an electrostatic term cannot be represented which is found to be playing a significant role in rotational transitions. Thus, the only way to further theoretical understanding is the further improvement of the used ab-initio interaction potential. The ambiguous components of the interaction potential should be improved, which is in progress.

The experiments with changing incident energy and, more unambiguously, with changing incident angle demonstrated that the rotational transitions and diffractive scattering are strongly coupled for D_2 -LiF(001) (at least, within the thermal incident energy range). The decoupling of diffraction and rotational transitions in the molecule-surface scattering has been discussed extensively and found to be quite well fulfilled in several approximate methods [66,89,107]. Drolshagen *et al.* investigated the decoupling conditions and concluded that for incident energies of 0.5-0.7 eV, the decoupling is valid if the corrugation (β) is small and at the same time corrugation anisotropy coupling ($\lambda \cdot \beta$) is smaller than the corrugation; and for small values of incident energies simple energetical threshold effects dominated over dynamical considerations [68]. Thus, the reason for the strong coupling in D_2 or H_2 -LiF(001) is the strong corrugation and low incident energy.

Although for D_2 -LiF(001) the separation of the surface and rotational rainbows is meaningless due to the strong coupling, some cautious conclusions can be drawn from the experiments: For instance, the diffraction rainbow is not observed for H_2 scattering in the $\langle 110 \rangle$ direction [284] whereas for D_2 scattering a diffraction rainbow in the same direction and similar conditions observed in Figure 7.13. Such an effect can be called

as *rotationally mediated diffraction rainbow*, which means the diffraction rainbow is caused by the rotational transitions. In general there is no correlation between the probabilities of the $(0 \rightarrow 2)$ and $(1 \rightarrow 3)$ rotational transitions, however remarkable similarities are observed in two cases. For changing incident energy, $R(00:02)$ and $R(00:13)$ in the $\langle 100 \rangle$ direction (see Figure 7.14) have maxima at the same incident energy. For changing incident angle $R(00:02)$ and $R(00:13)$ in the $\langle 110 \rangle$ direction (see Figure 7.26) have maxima at the same incident angle. Simultaneous maxima of excitation probabilities of different rotational transitions can be interpreted as *corrugation mediated rotational rainbow*.

Thermal attenuation of the diffraction and RID intensities showed that the Debye-Waller approximation has relatively poor agreement in comparison to He-LiF(001) and D_2 scattering from metal surfaces [88, 358]. There are several assumptions on which DW model is based on are not necessarily valid: The DW approximation is derived from the Born approximation whereas for D_2 -LiF(001) the interaction potential is strong and the corrugation is large. Secondly, multi-phonon exchange is very likely. As seen in Figure 7.9 the slope of the thermal attenuation increases with increasing surface temperature because multi-phonon excitations become significant at high surface temperatures. The scattering particle may simultaneously interact with several surface atoms which is more probable for molecule scattering.

The thermal attenuation of RID intensities are not different from the attenuation of the elastic peak intensities. This demonstrates that the contribution of phonons in rotational transitions is not significant. Significant coupling of phonons and rotational transitions are observed in molecular scattering from metal surfaces [349, 350] and for alkali halides in I_2 scattering from MgO(001) [359]. Allison and Feuerbacher carried out TOF analysis for D_2 and H_2 -LiF(001) and concluded that the rotational transitions should be dissipative rather than diffractive and directly coupled with phonon excitations [348, 360]. However, an extensive TOF analysis of D_2 from NaF(001) by Brusdeylins *et al.* indicated that phonon processes appear to take place with about the same probability, regardless of whether a rotational excitation takes place [343]. In this work, the angular distributions of diffraction and RID peaks are measured at different surface temperatures of a wide range. If the phonon participation were significant in rotational transitions, the rate of the decrease of the RID intensities with increasing surface temperature should have been somewhat less than the decrease of the elastic peaks and with increasing surface temperature the RID peaks should have become broader and shifted to smaller final angles due to the increased final energy. Hence, for D_2 -LiF(001) phonon and rotational excitations or deexcitations are decoupled, and a

rigid-surface treatment is valid and successfully accounts for the rotational transition probabilities.

Selective adsorption resonances are observed by measuring the drift-TOF spectra of the specular peak at different incident angles. Remarkable correspondences between several peaks with an energy difference of $\Delta E(0 \rightarrow 2)$ are observed and this is interpreted as *rotationally mediated selective adsorption*. With a reasonable assignment of the observed bound state energies -28.7, -16.8, and -9.0 meV to the zeroth, first, and the second bound state levels of a Morse potential, a potential well depth of 35.3 meV is obtained. Since the interaction potential is anisotropic, the bound states above belong to $j_i=0$ whereas the excluded bound states -23.4 and 11.6 meV, probably, belong to the initial states $j_i=1$, $m=\pm 1$. This is the first observation of the m -splitting of the SAR on alkali halides, nevertheless more direct and clear results are required for an obvious evidence. The estimated potential well is shallower than the previously estimated one which is 37.7 meV [6] and deeper than the well depth of the Kroes potential which is 31 meV [7]. Although, following the tradition, Morse potential is used, it is not necessarily the best one of the simple model potentials given in Section 2.2.1. Thus, a direct comparison of the obtained potential well with the Kroes potential is not feasible. The comparison can be made only by theoretically reproducing the selective adsorption resonances. Although it is difficult and computationally costly, this would be the ultimate test of the quality of the ab-initio potential.

The D₂-dimer scattering experiments showed that the coherent scattering probability of dimers are much lower than previously estimated [355,356]. Much lower surface temperatures and incident energies should be a prerequisite for a significant coherent scattering of dimers. The thermal attenuation of the elastic and the diffraction peaks cannot follow a simple DW behavior as asserted in ref. [356], and the coherent scattering should be rather strongly coupled with the surface phonons in a dissociative manner.

8. Summary and Outlook

In this work, a molecular beam apparatus with the novel concepts was developed. Its functionality was successfully demonstrated with the characterization experiments of the free-jet expansion of He and D₂ beams, investigation of clustering properties of the D₂ expansion and scattering experiments of He atoms and D₂ molecules from Si(111):H(1×1) and LiF(001) crystal surfaces. The results were discussed at the end of the each chapter in detail. The most important results and conclusions are summarized and proposals for the future-work based on these are made as follows:

Clustering properties of the D₂ beam: In the case of massive condensation, where the mole fractions of the clusters should be a smooth function, maxima were observed in the intensities of ions D₉⁺ and D₁₅⁺. The enhanced intensity of D₉⁺ was ascribed to the high stability of the ion [220]. For D₁₅⁺ signal it is not clear whether the ion is particularly stable or the parent cluster (D₂)₈ has an enhanced stability. This phenomenon, so called *magic numbers*, is highly interesting and can be investigated by transmission grating experiments [361] more systematically.

It was observed that with the terminal D₂ dimer mole fractions were reduced for high stagnation temperatures. This reduction became negligible at lower stagnation temperatures below 160 K and the dimer mole fractions at the same scaling parameter, Γ (in Equation 4.32) were similar to the H₂ dimer mole fractions which were measured at the stagnation temperature below 100 K. The reduction of the dimer mole fractions at high stagnation temperatures was attributed to the rotational relaxation, which heats up the beam. A quantitative investigation on the role of rotational relaxation in the clustering is complicated and requires solving coupled equations of the translational relaxation, rotational relaxation, and dimerization.

It was observed that with increasing mole fractions of the clusters, velocity and temperature lag emerged between the monomers and the clusters. This is in accordance with a two-step dimer formation mechanism [3] where the dimers form with the transfer

of the condensation heat to a third body, thus increasing the temperature and the velocity of the monomers.

The velocity lag can be used to create a beam of clusters without monomers by selectively chopping the beam.

Preparatory experiments with the Si(111):H(1×1) surface: In this work, it was demonstrated that it is possible to transport *ex-situ* prepared Si(111):H(1×1) crystals over the continent and to install in a HAS apparatus successfully for its implementation as an optical element for atom optics. The crystal surface exhibited high reflection sufficient for further experimentation. Diffractive scattering and selective adsorption resonances were observed, indicating that the crystal had an ordered surface with a low defect density. The reflectivity of the crystal for room temperature beam ($E_i \simeq 65$ meV) was found to be about 1×10^{-4} which is comparable with the theoretical predictions based on both diffractive scattering calculations from a rigid surface [233] and the thermal attenuation with a DW analysis [261]. It has been shown that, although Si(111):H(1×1) surface is relatively inert, extreme precautions must be taken for the cleanliness of the vacuum not only in the crystal chamber, but also in the neighboring chambers.

The intensity and the spot size of the focused beam are the most important issues when the focusing mirror to be used as the heart of a HAS scanning microscope. The reflectivity of the crystal can be increased in three ways: By cooling the beam, by cooling the crystal and by using reflection at higher incident angles. Using incident beam of lower energies does not increase the specular intensity significantly as seen in Figure 5.6. Cooling the mirror can be also used to increase the reflectivity by minimizing the DW factor. However, it will have the detrimental effect of increasing the adsorption of residual gas species on the surface. At higher incident angles the intensity of the specular peak will increase significantly due to the reduction of the number of open channels and the DW factor. However in that case the focusing will be technically difficult.

To compare the focusing of the He beams with the Si(111):H(1×1) crystal and with the Fresnel zone plate: Although the bent-crystal can focus a much broader intensity (about 10^3) than Fresnel zone plates, the gained intensity will be compensated with the poor reflectivity of the crystal. Apart from the technical difficulties of the realization of an ideal Cartesian surface of several millimeters for optimum focusing at later stages, other effects can reduce the achievable spot size. One problem for the focusing will be the finite domain sizes. Even extremely large steps sizes of several hundred

nanometers will be a limiting factor when a focusing of submicron spot size is intended. For instance, if the average surface domain size is $d=1000$ nm (which is an optimistic assumption), the wavelength of the atom is 0.05 nm (for the room temperature beam), and the mirror-to-detector distance is 30 cm (the shortest distance achievable for the present apparatus); then the broadening of the focussed spot ($\sim \lambda/d$) will be 15 μ . Additionally, when infinitesimal angular deflections are in consideration the effective cross sections of the defects can increase significantly, leading to an additional blurring of the focused spot. Hence, taking these considerations into account and the extreme necessary precautions for preserving the crystal which will limit its applications, the novelty of the method as an alternative to Fresnel zone plates is questionable.

Thermal expansion of the LiF(001) surface: The lattice constant of the LiF(001) surface and its temperature dependence were measured by the precise determination of the positions of the diffraction peaks. The results have demonstrated that the thermal expansion of the LiF(001) surface is identical to the expansion of the bulk which is in contradiction to the earlier reports on the LiF surface [4, 5]. This was attributed to the poor precision and/or narrow temperature range of these works.

In this study it was successfully demonstrated that the high resolution HAS can be used for the precise determination of lattice constants and the investigation of the surface anharmonicity; namely new application fields of the HAS. The lateral displacements of the surface atoms was measured with an error of 0.2% and this can be improved by a factor of 10 with small precautions, such as a better TOF calibration and implementation of a more precise target manipulator. Extending high resolution HAS experiments to other surfaces, especially, to the strongly relaxed, highly defected and reconstructed surfaces, multilayers and, adsorbates will supply significant insight into the structural and dynamical properties. Particularly interesting experiments will be observing how the surface lattice constant changes with increasing temperature before and after the surface reconstruction, i.e. [362–364] or lateral contraction of growing thin films with respect to the substrate, i.e. [365]

Scattering of D_2 from the LiF(001) surface: It was found that the theory with the Kroes-potential and the CCWP method is highly successful in predicting the probabilities of the diffractive and the rotational transitions. Particularly, neglecting the electrostatic term of the interaction potential led to low rotational transition probabilities. However, when rotational and diffractive rainbow effects were observed, the theoretical agreement was rather unsatisfactory. This was attributed to the fact that

the rainbow effects are highly sensitive to the surface corrugation and the anisotropic part of the potential.

The parts of the Kroes potential to be improved at the first stage are as follows [93]:

- Repulsive pair potentials: the parameters of the repulsive pair potential for the $\text{Li}^+\text{-H}_2$ repulsion energy were obtained from the self-consistent field (SCF) calculations on the interaction of $\text{Li}^+\text{-H}_2$ in the gas phase. This is a reasonable approximation since it has been shown that the surface Li^+ behave similar to the one in gas phase [94]. For the $\text{F}^-\text{-H}_2$ interaction the parameters were obtained using a combination rule by using the parameters of the interactions for He-Ar , $\text{H}_2\text{-Ar}$ and $\text{F}^-\text{-He}$ in the gas phase. However the surface F^- can behave quite differently than in the gas phase. A more accurate method would be determining the parameters from Hartree-Fock + Møller-Plesset calculations [366], using a model in which a F^- ion is surrounded by its nearest neighbor Li^+ ions, which are then embedded in a grid of point charges [94]

- Attractive pair potentials: The parameters of the induced dipole-induced dipole terms of the attractive pair potential were obtained from static polarizabilities in combination with the Slater-Kirkwood rule [95]. However, they can be determined more precisely using Hartree-Fock + Møller-Plesset calculations as discussed above.

Theoretical comparison of the data for scattering with different incident energies has not been done yet. The calculations require more computation times since for each data point two calculations at different incident angles must be made. This can be made after the refinement of the interaction potential.

A strong coupling between the rotational transitions and the diffractive scattering were observed, which led to interesting phenomena such as rotationally mediated diffraction rainbows and corrugation mediated rotational rainbows. The strong coupling was ascribed to the high corrugation of the interaction potential surface and relatively low incident energies. The existence of a possible decoupling at high incident energies should be investigated.

It was observed that the phonon and rotational excitations were decoupled which is in consistence with the conclusions of the Brusdeylins *et al.* [343].

Selective adsorption and also rotationally mediated selective adsorption resonances were observed. The determined bound state energies -28.7, -16.8, and -9.0 meV were assigned to the zeroth, first, and the second bound state levels of a Morse potential with a potential well depth of 35.3 meV.

The determined bound states of -23.4 and 11.6 meV were assigned to the initial rotational states of $j_i=1$. This is the first evidence of the rotational level splitting of the bound states for the D_2 or $\text{H}_2\text{-LiF}(001)$ system. However, the method of the de-

termination of the bound-energy levels was indirect and more clear results are awaited for the exact determination of the SAR levels. Particularly, repeating the similar experiments with lower incident beam energies ($T_0 < 100$ K) where there is much less open channels of resonances or no rotational transitions would provide better results.

A direct comparison of the obtained eigenenergies can be made with the Kroes potential by theoretically reproducing the selective adsorption resonances, however, this should be done after the improvement of the Kroes potential.

In the D_2 -dimer scattering experiments from the LiF(001) surface, it was observed that the coherent scattering probability of dimers were much lower than previous results [355,356]. Experiments with lower source stagnation temperatures and surface temperatures should give much more coherent scattering of dimers which will allow interesting experiments such as the observation of the diffractive scattering and a systematic analysis of the dissociative scattering.

A. Complete Data for D₂-LiF(001)

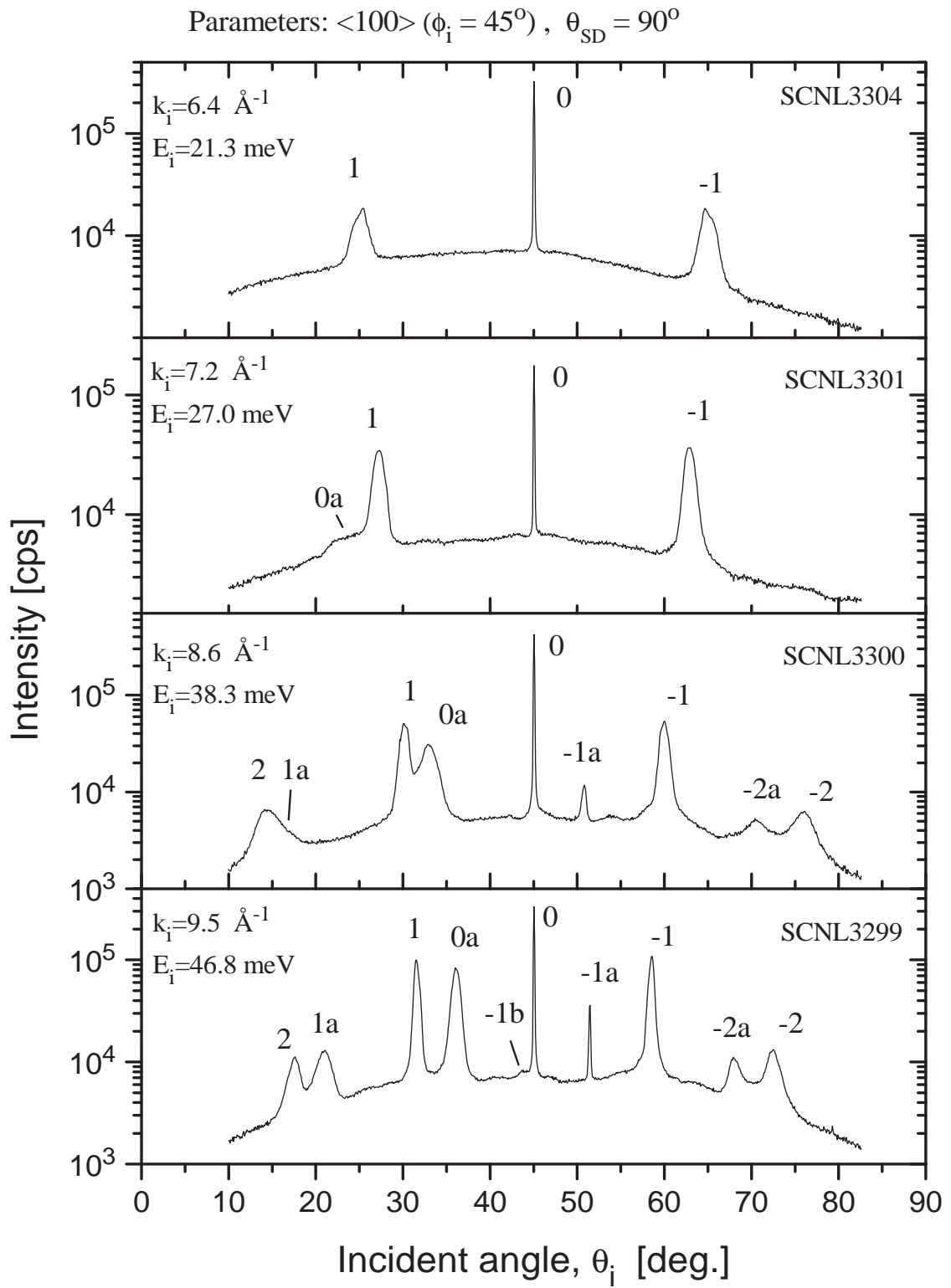
The complete data of angular distributions for different incident beam energies and detector angles in the $\langle 100 \rangle$ and $\langle 110 \rangle$ directions for n-D₂-LiF(001) are listed below.

The common parameters: $T_s=297$ K, $P_0=120$ bar. The angular distributions with different detector angles are carried out at the stagnation temperature, $T_0=300$ K. The rotational populations of the incident beam at some different stagnation conditions are given in Table A.1.

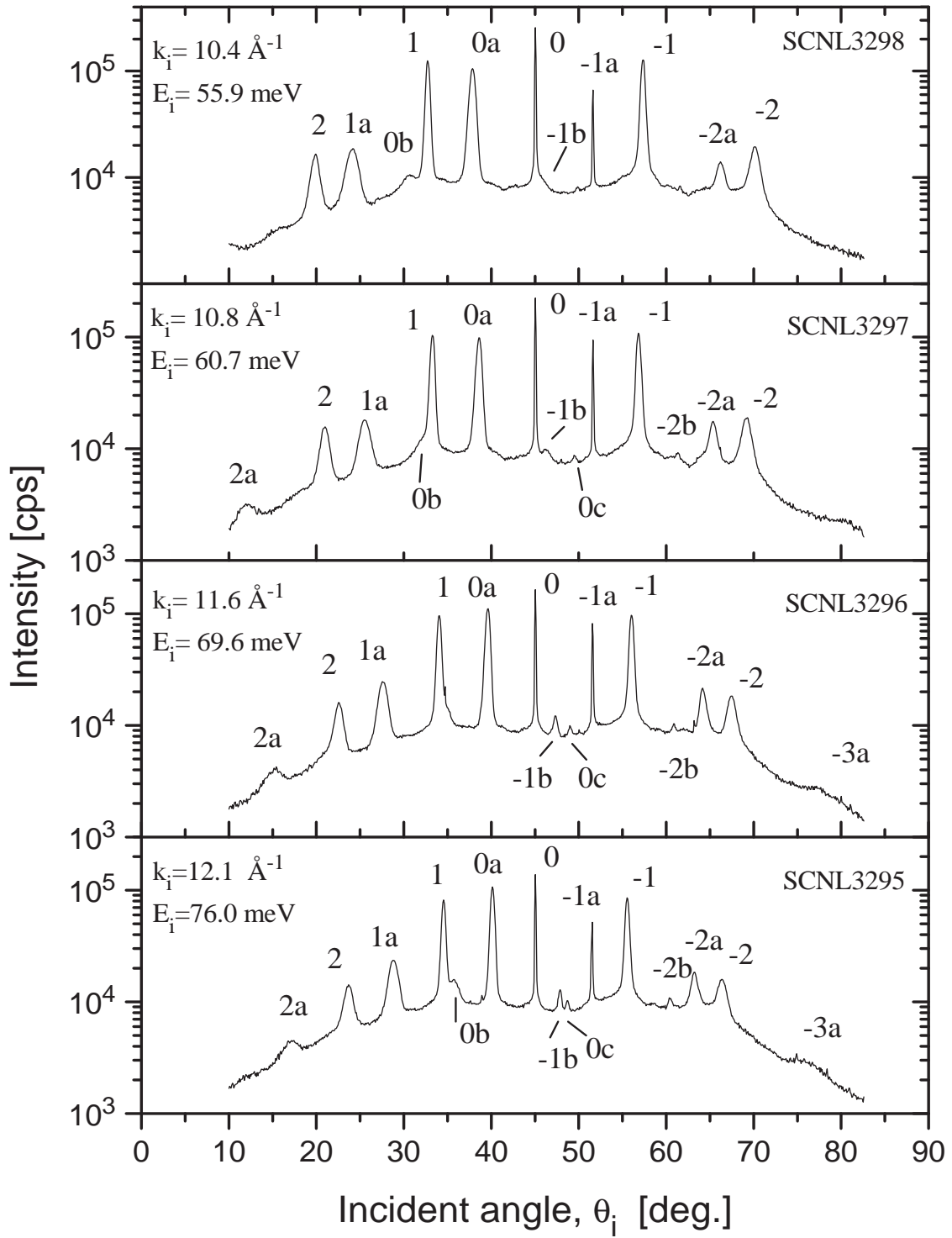
The legend of the rotational transitions: **a** is (0 \rightarrow 2), **b** is (1 \rightarrow 3), **c** is (2 \rightarrow 0) and **d** is (2 \rightarrow 4).

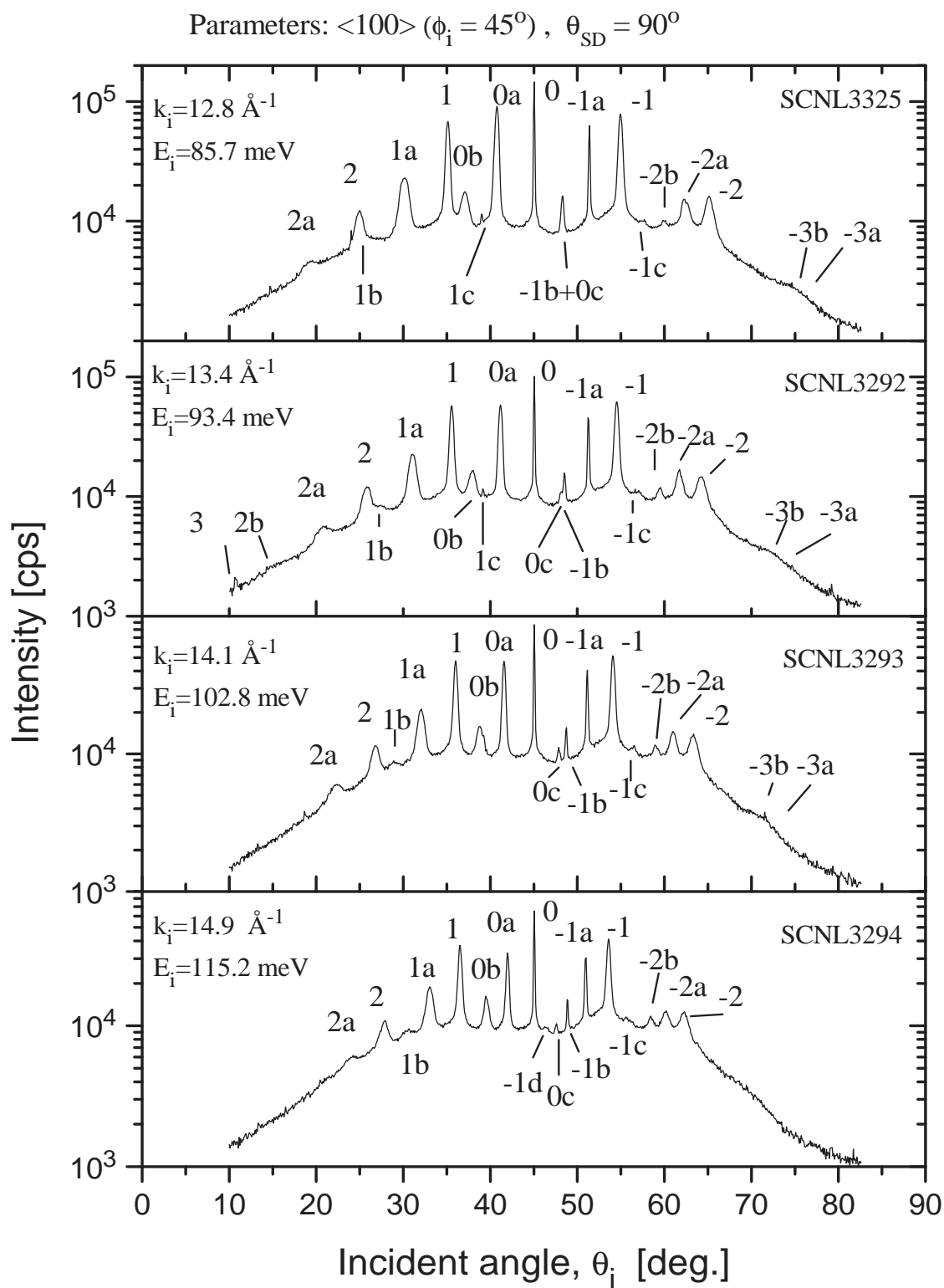
Table A.1: The fractional populations (n_j) of the rotational states, j_i (in %), the energy spread ($\Delta E_i/E_i$) (in %), and the peak-area intensity (I_0) of the incident n-D₂ beam at different stagnation temperatures and energies. $P_0=120$ bar, $d=10 \mu$. The beam energy and its spread is found by TOF measurements. The rotational temperatures (T_R) and distribution of rotational states are found by using Equations 4.29, 4.25 and 4.26.

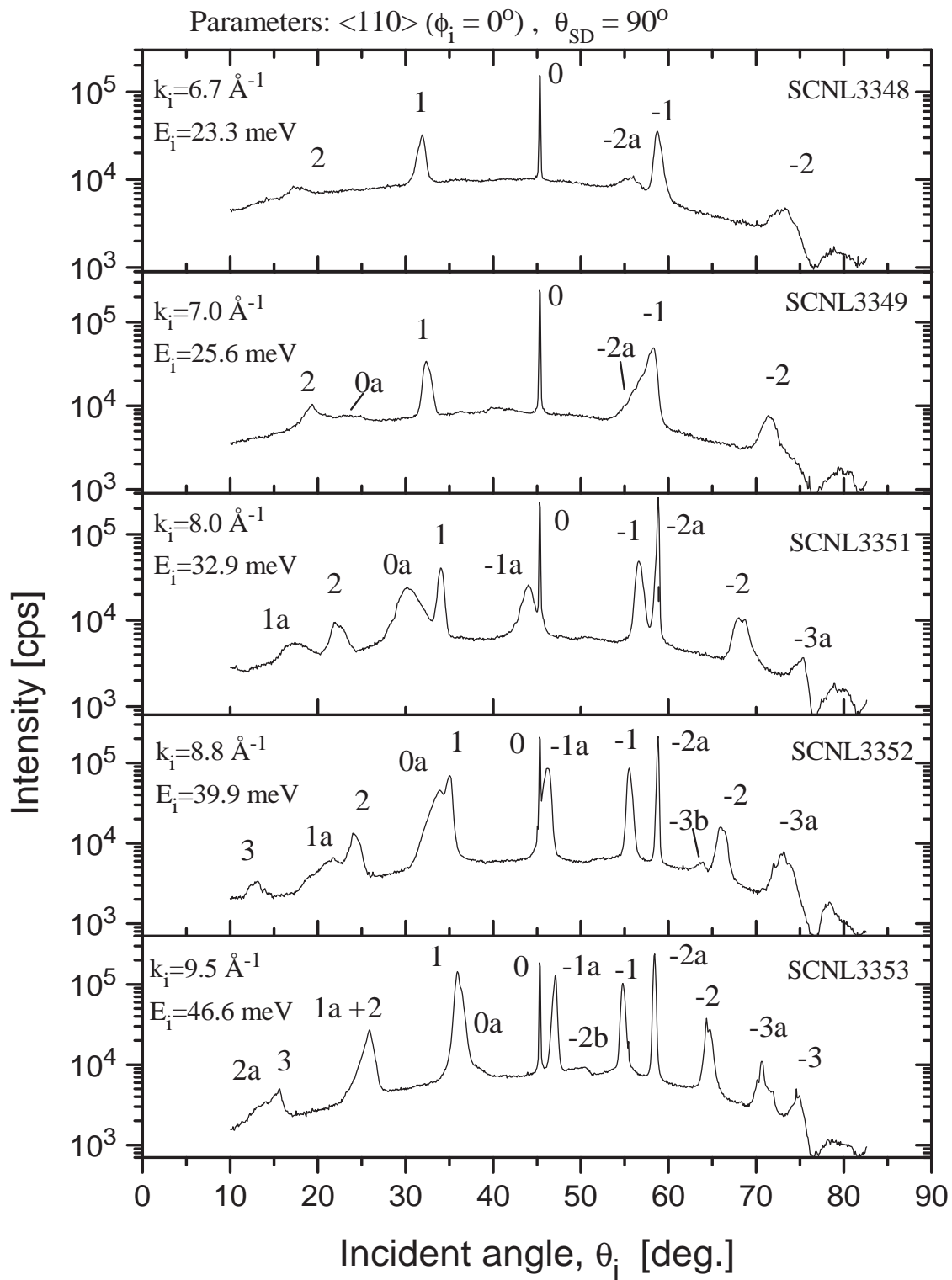
T_0 (K)	E_i (meV)	$\Delta E_i/E_i$ (%)	I_0 (10^6 cps·deg)	T_R (K)	$j_i=0$	$j_i=1$	$j_i=2$	$j_i=3$
400	115	8.8	24.8	108	46	32	21	1.3
360	103	8.0	26.3	93	51	33	16	0.7
300	85	7.9	28.4	72	58	33	8.1	0.2
250	70	7.0	31.4	56	63	33	3.2	-
210	56	7.1	32.8	44	66	33	0.9	-
180	47	6.8	30.0	35	66	33	0.2	-
120	27	16	12.7	20	67	33	-	-

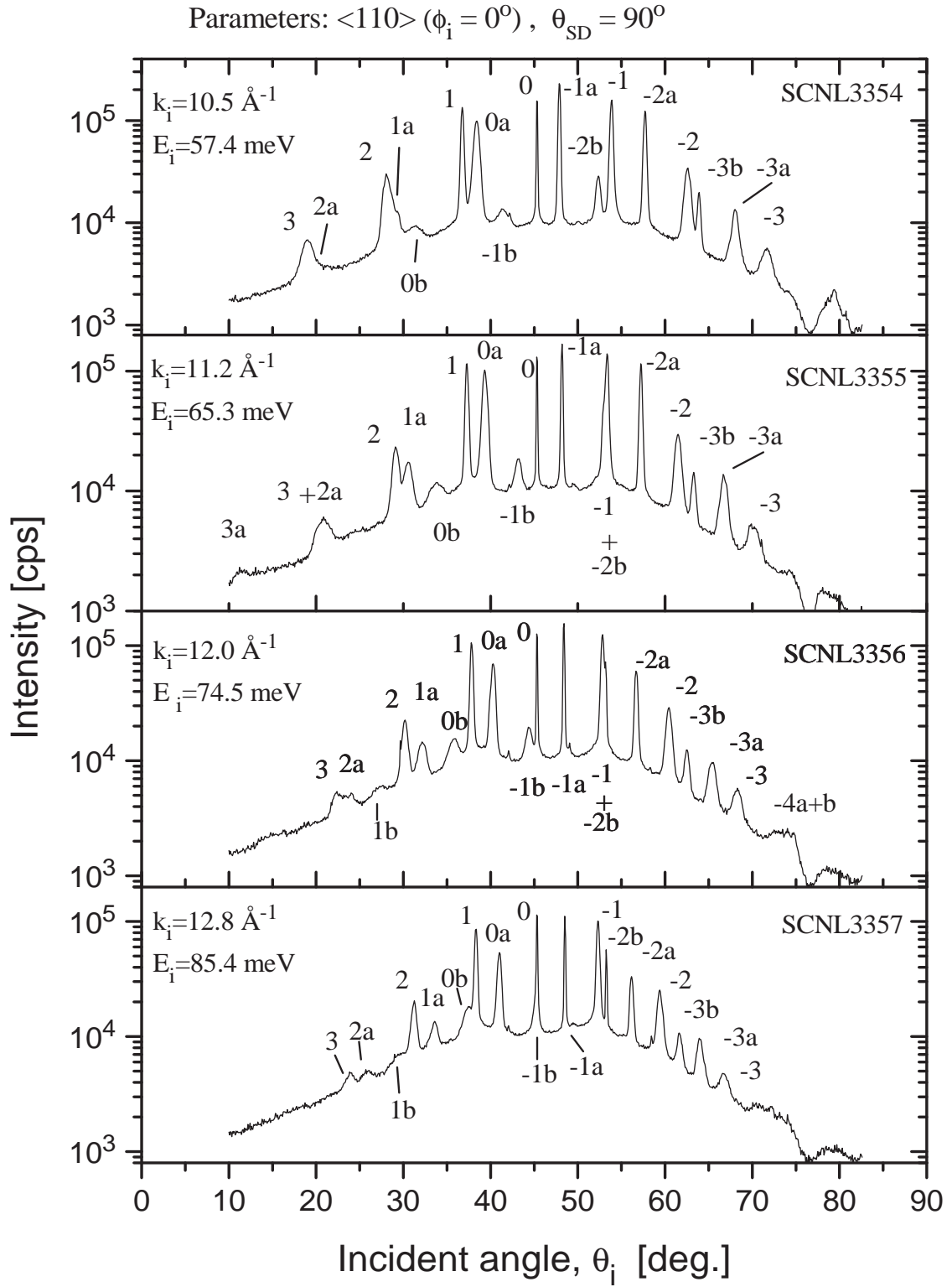


Parameters: $\langle 100 \rangle$ ($\phi_i = 45^\circ$), $\theta_{SD} = 90^\circ$

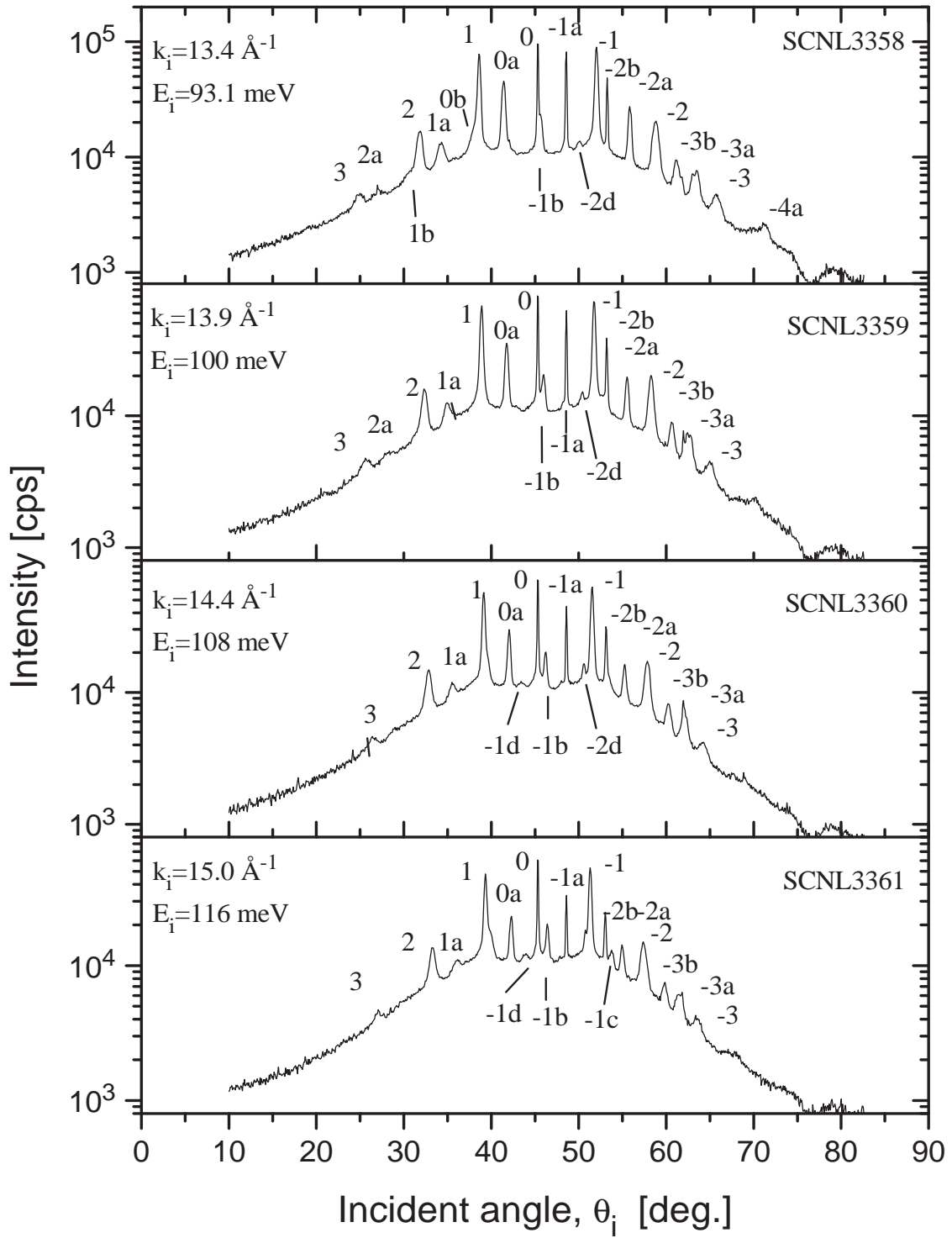


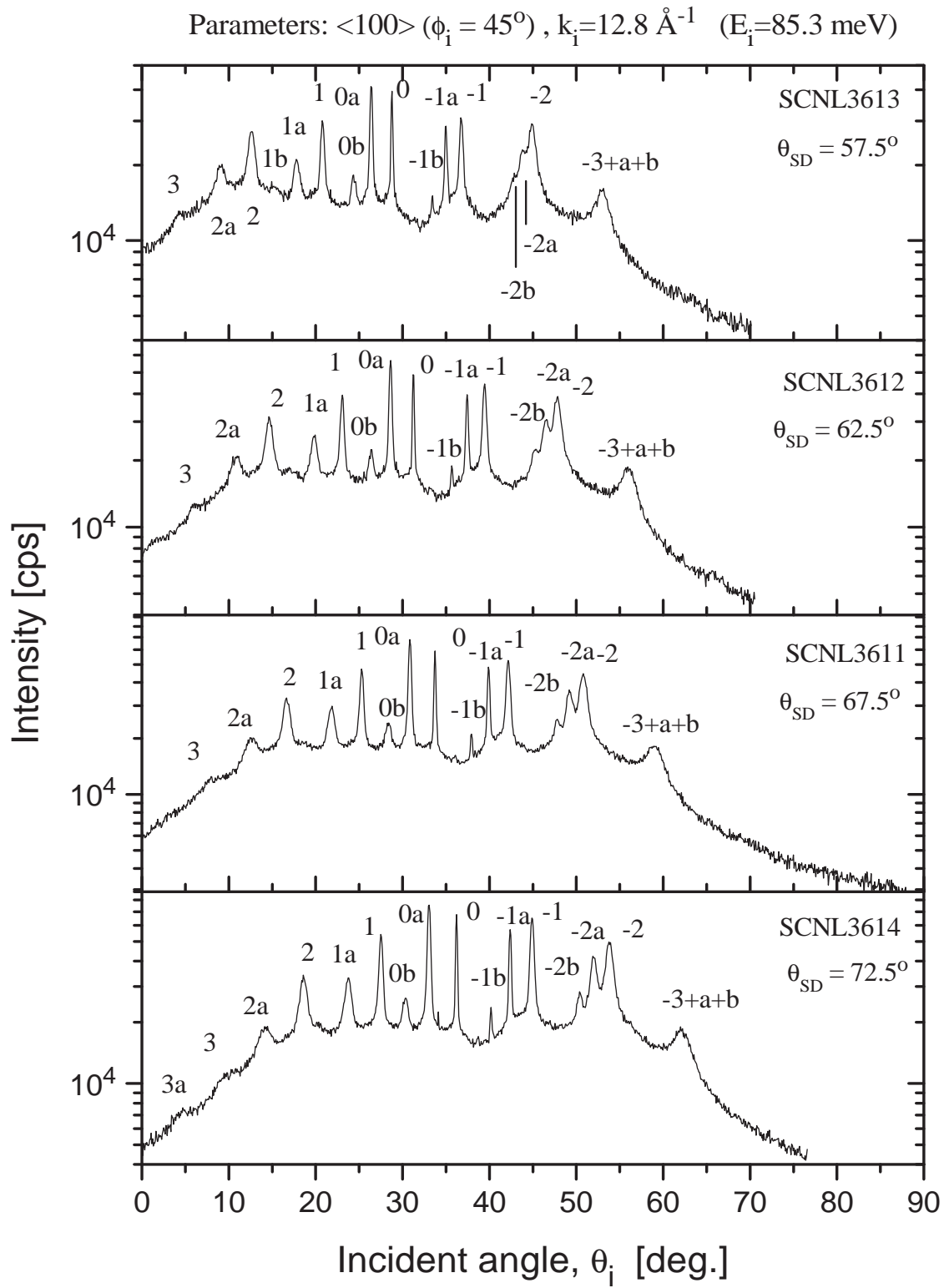


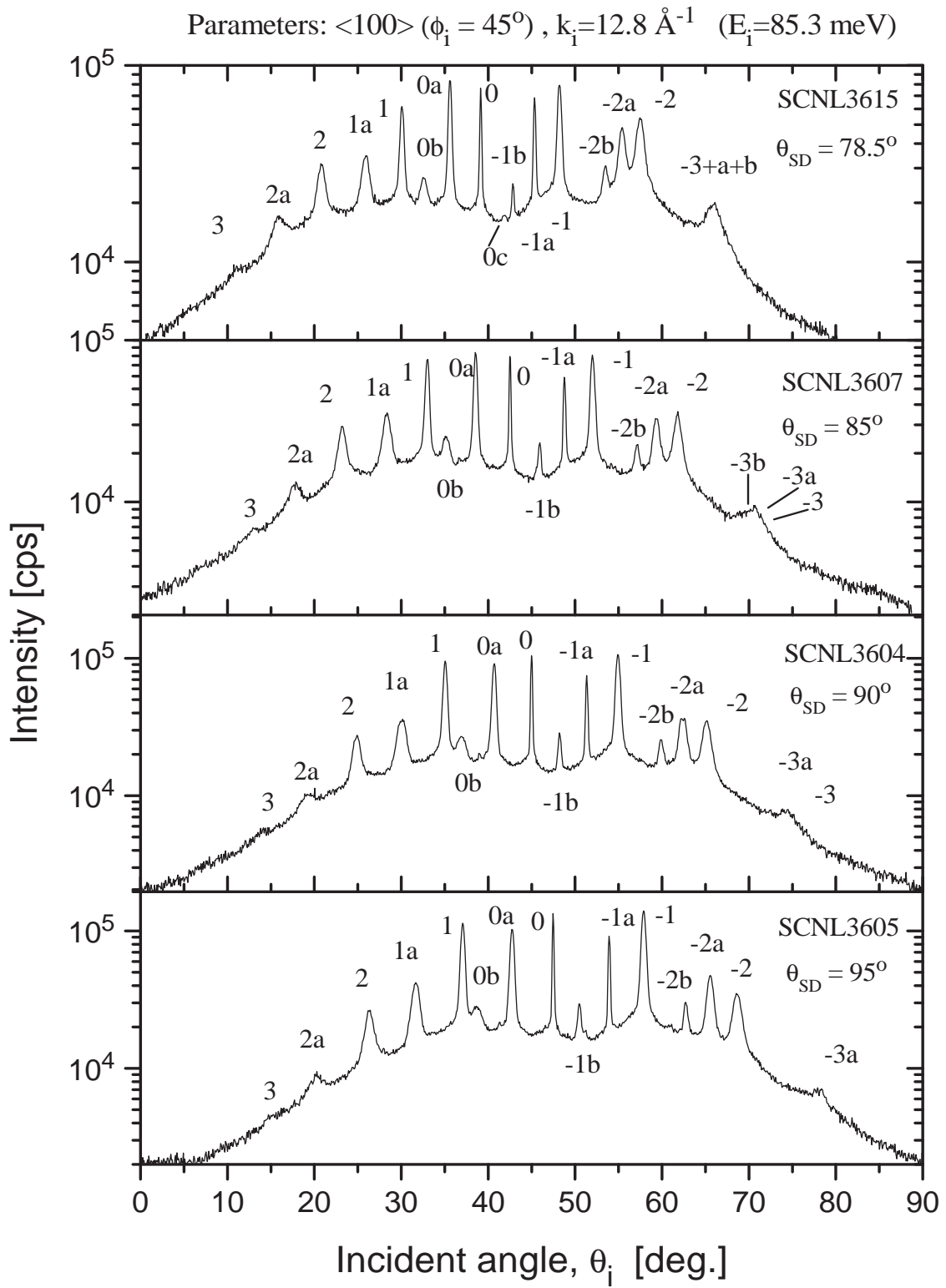


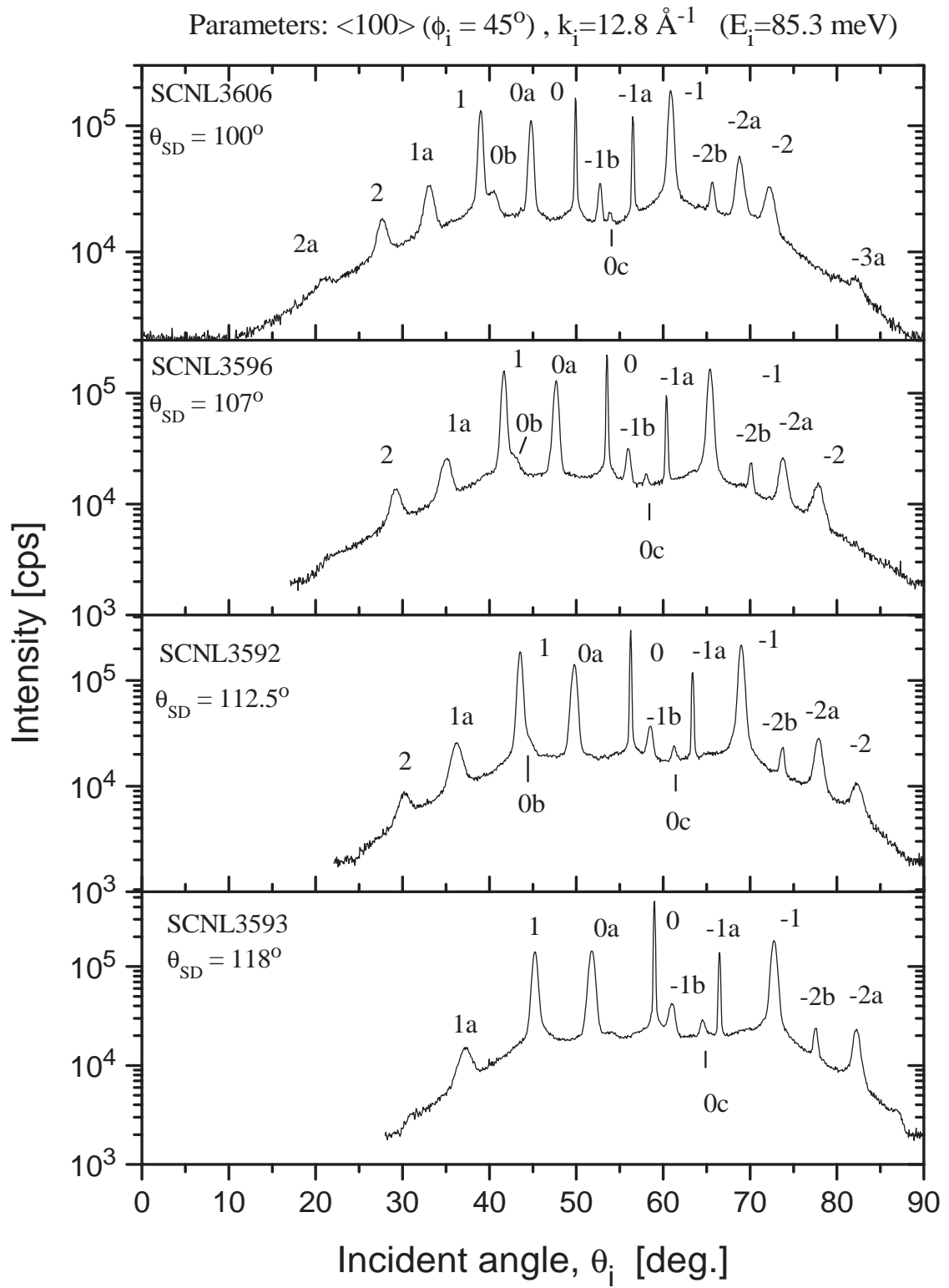


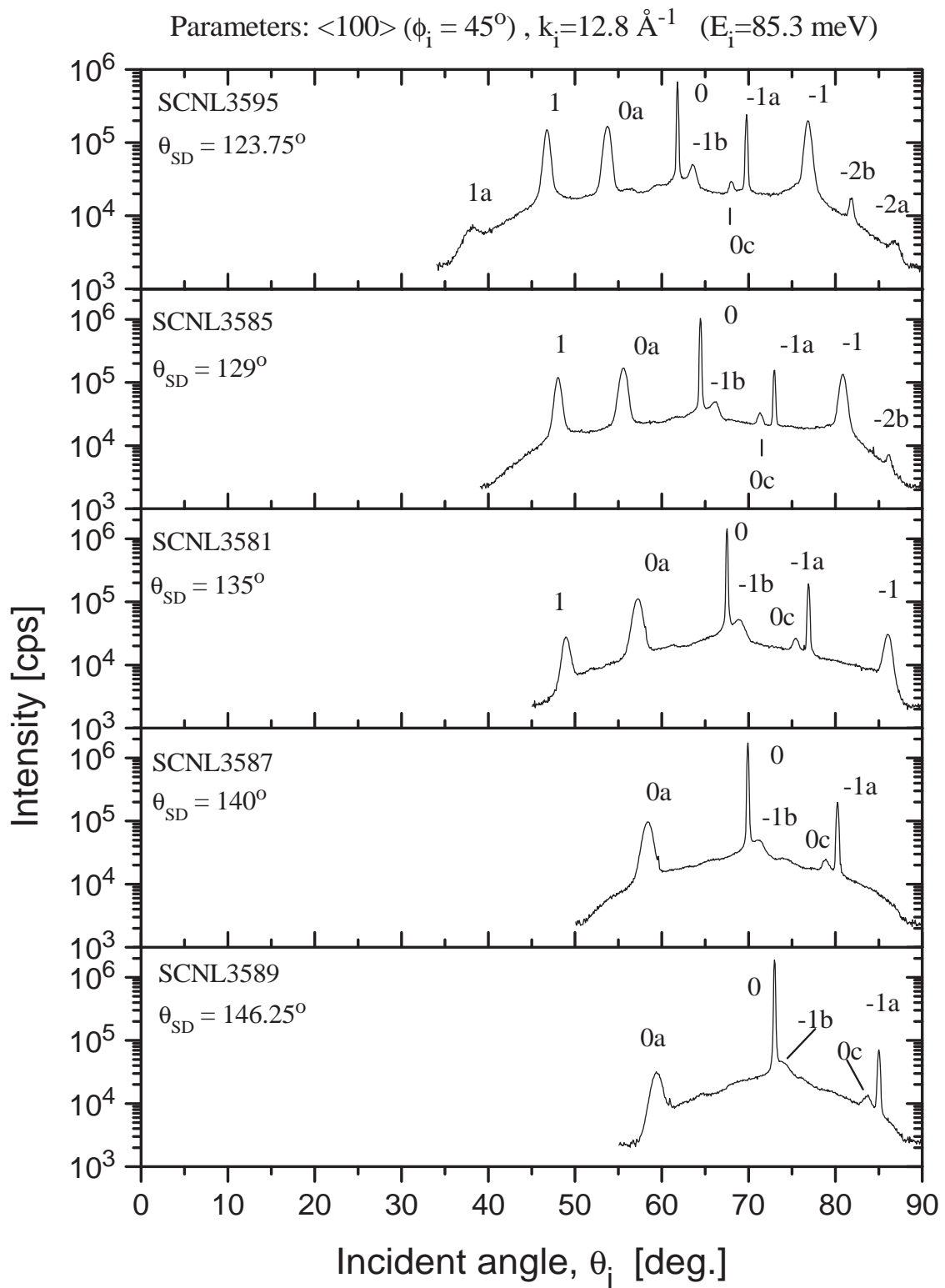
Parameters: $\langle 110 \rangle$ ($\phi_i = 0^\circ$), $\theta_{SD} = 90^\circ$

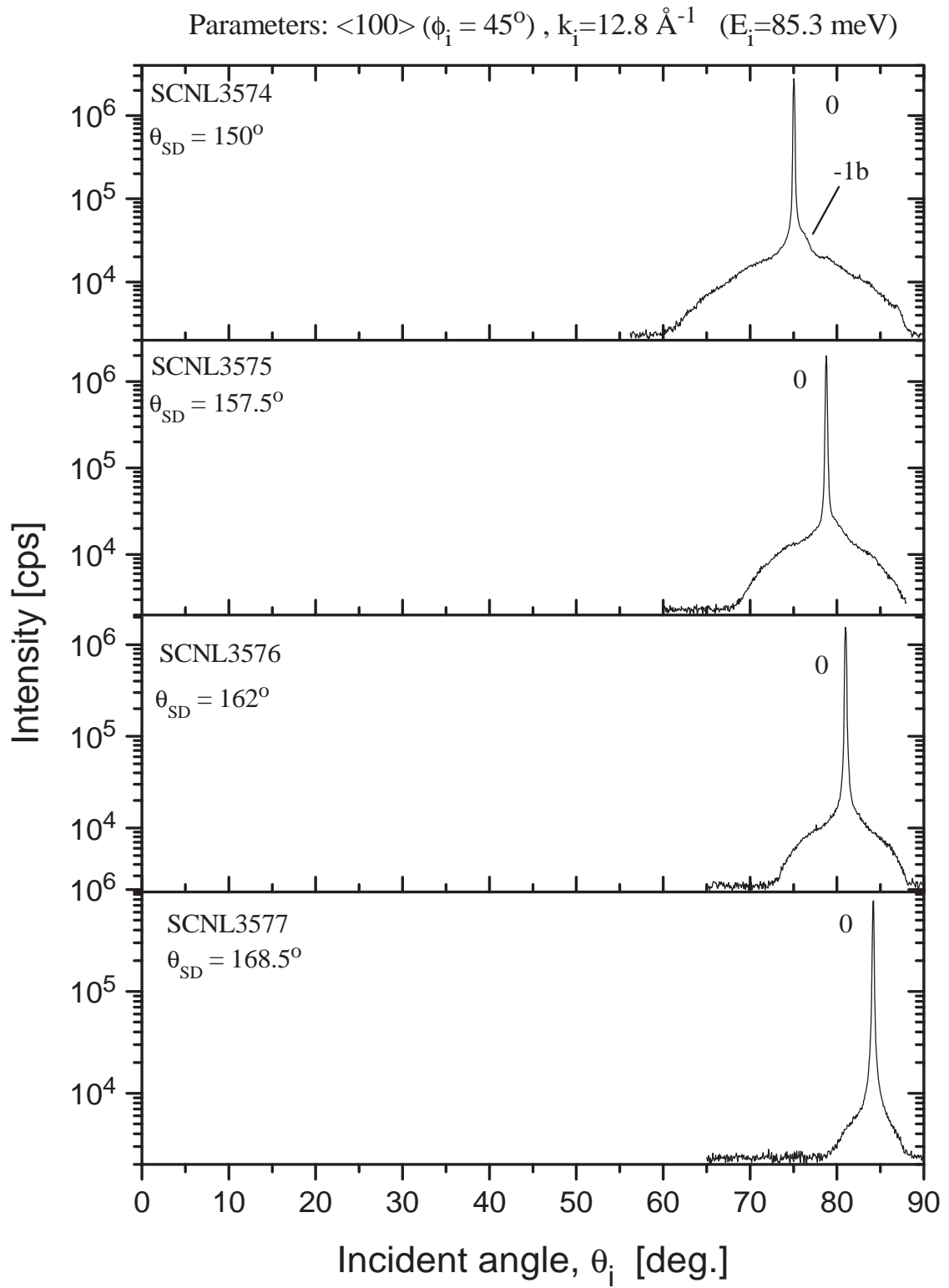




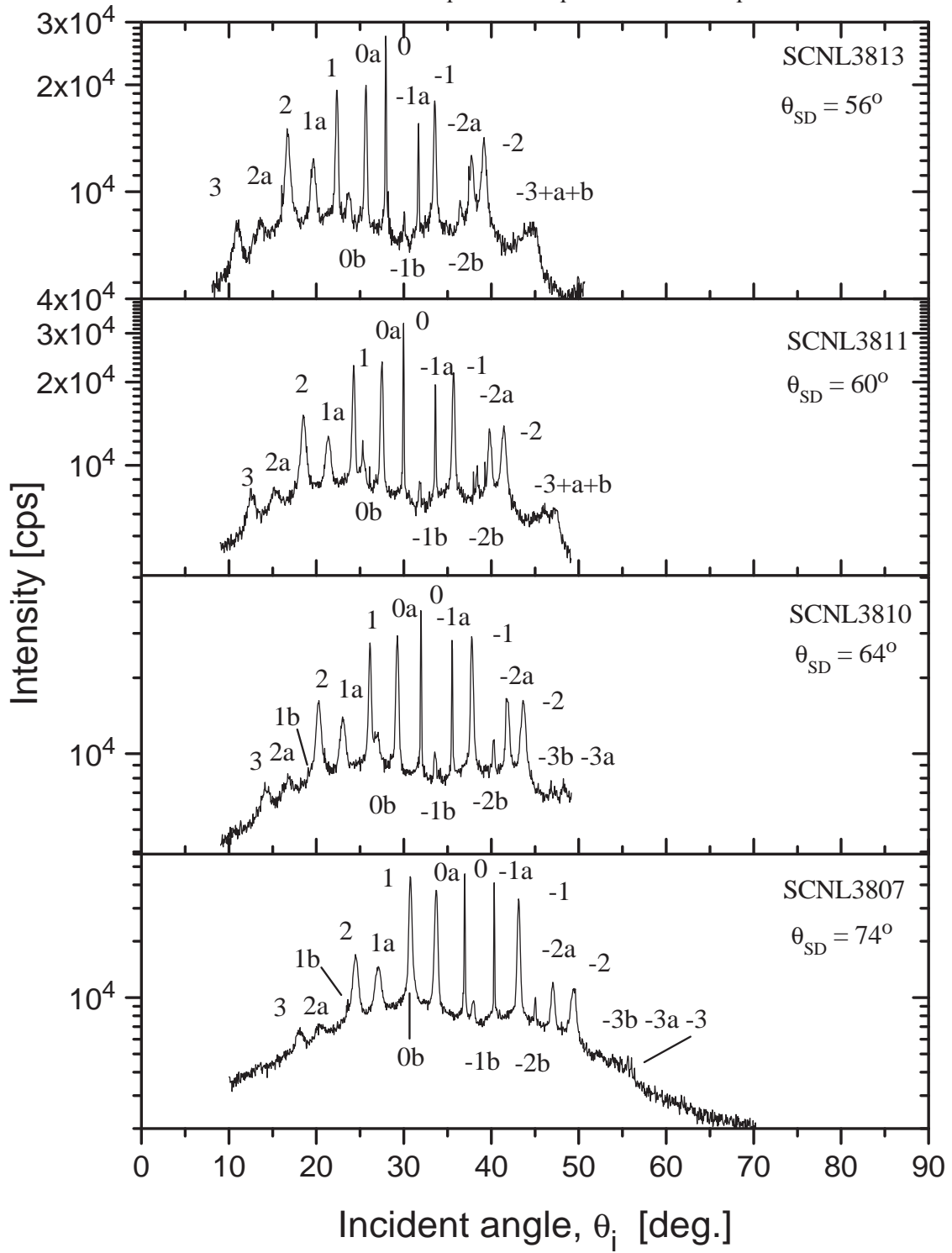


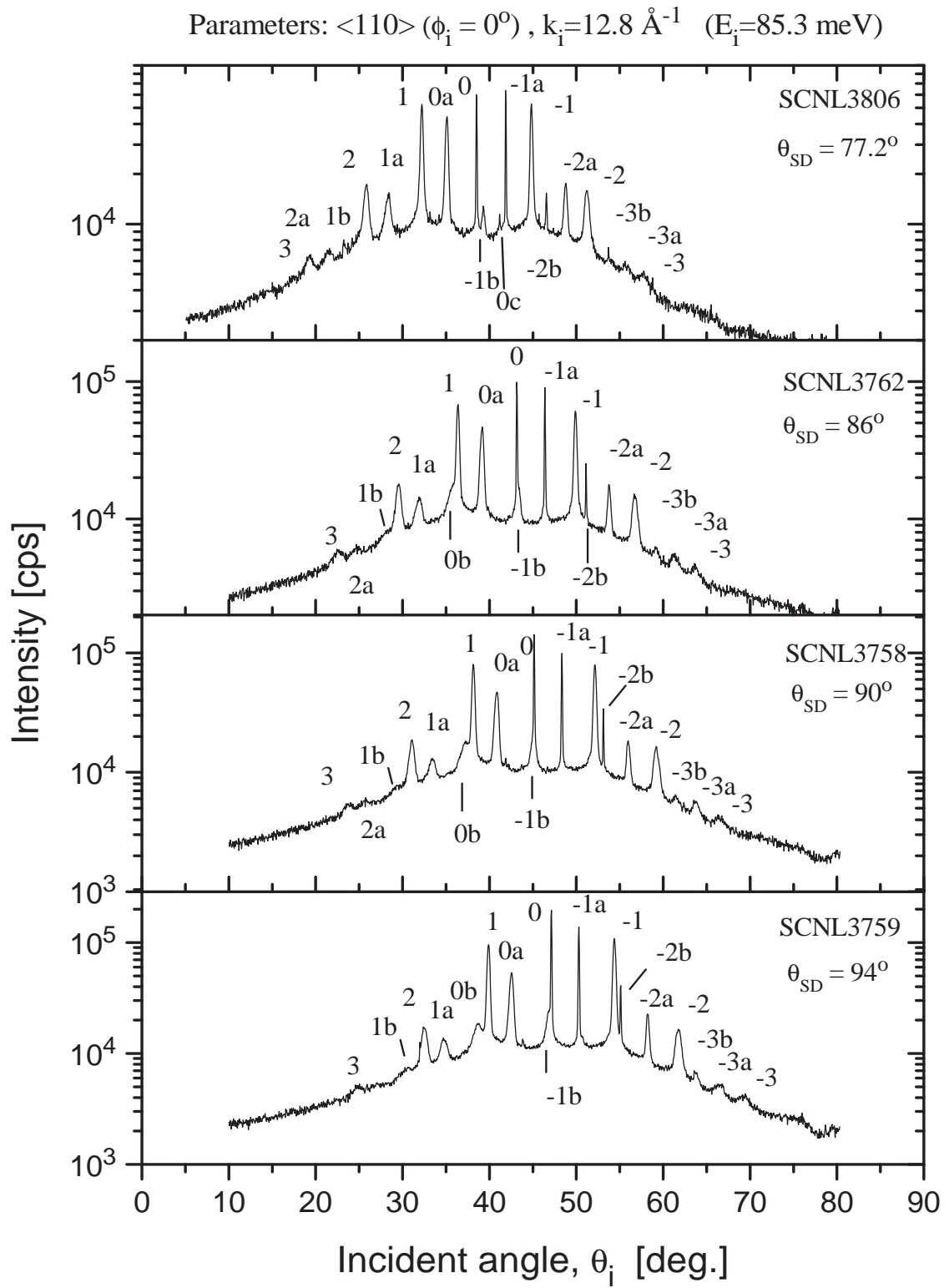




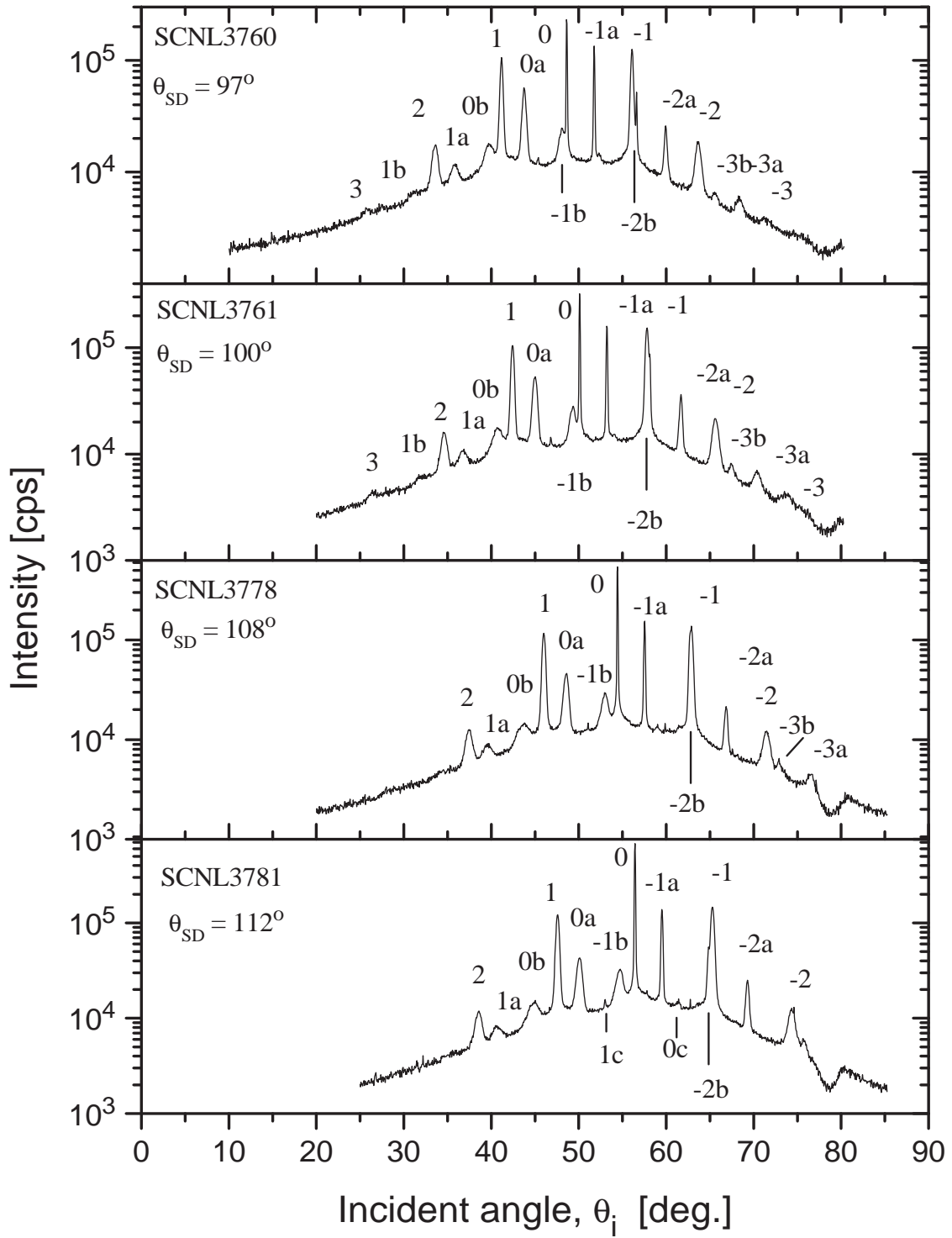


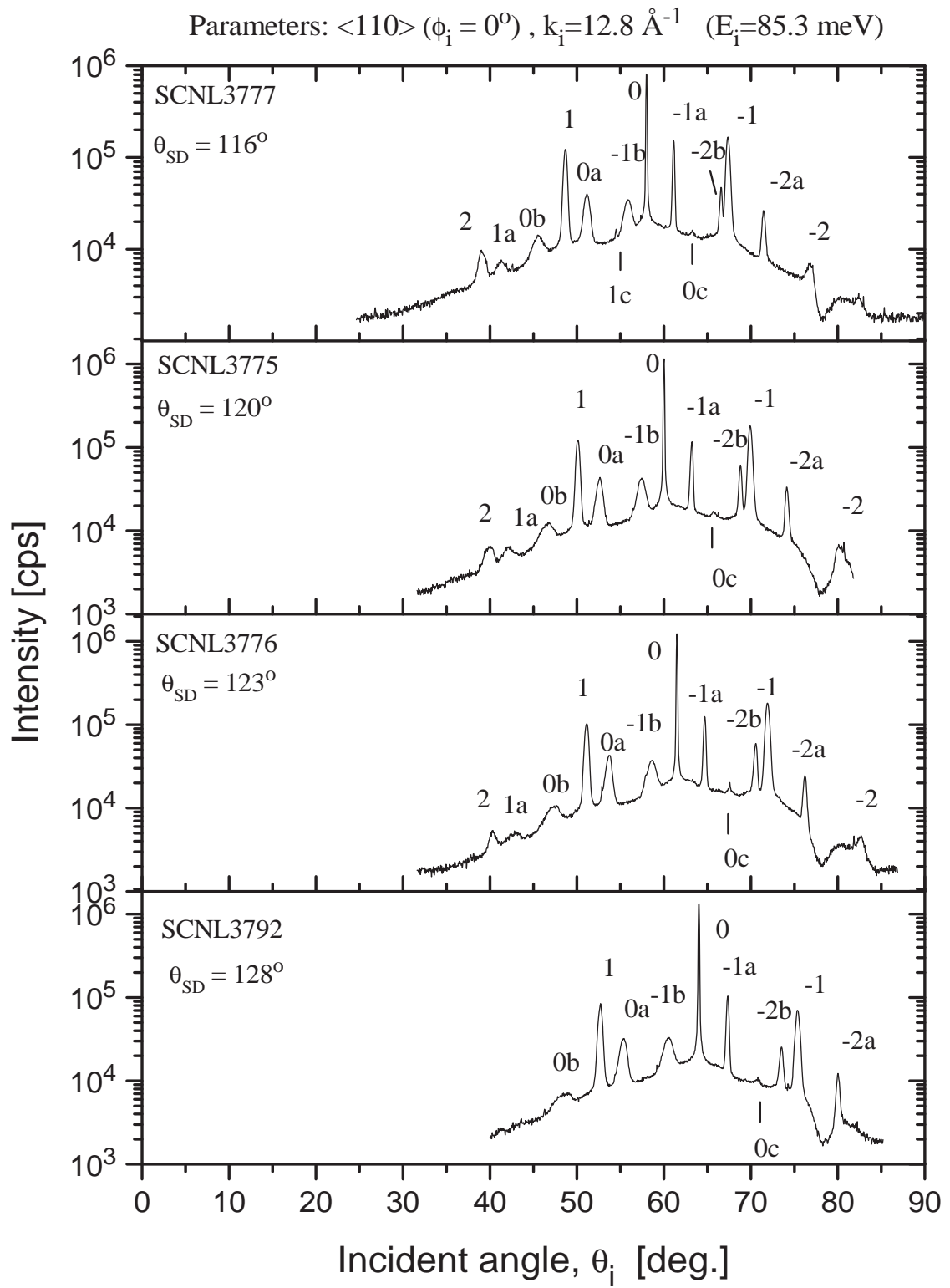
Parameters: $\langle 110 \rangle$ ($\phi_i = 0^\circ$), $k_i = 12.8 \text{ \AA}^{-1}$ ($E_i = 85.3 \text{ meV}$)



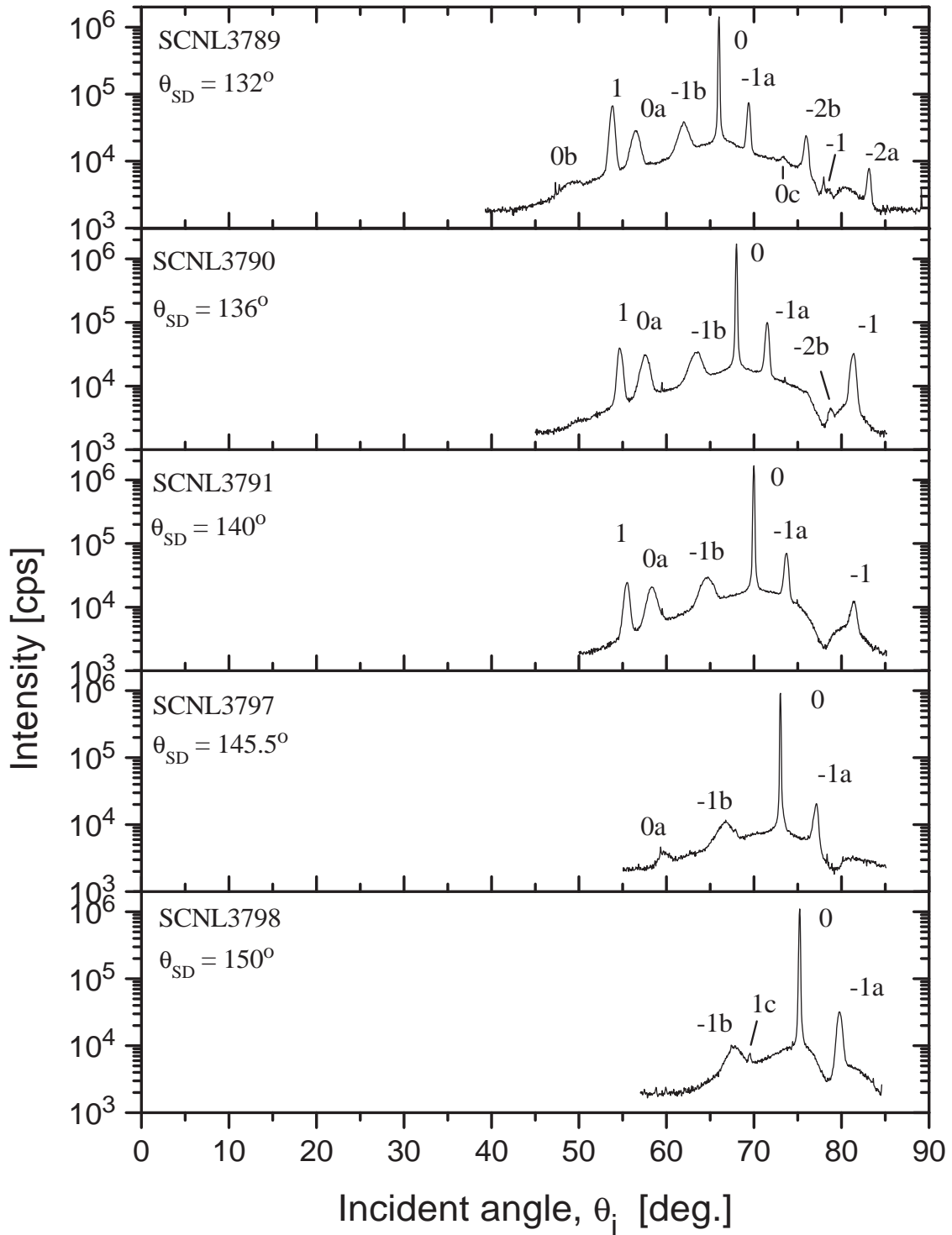


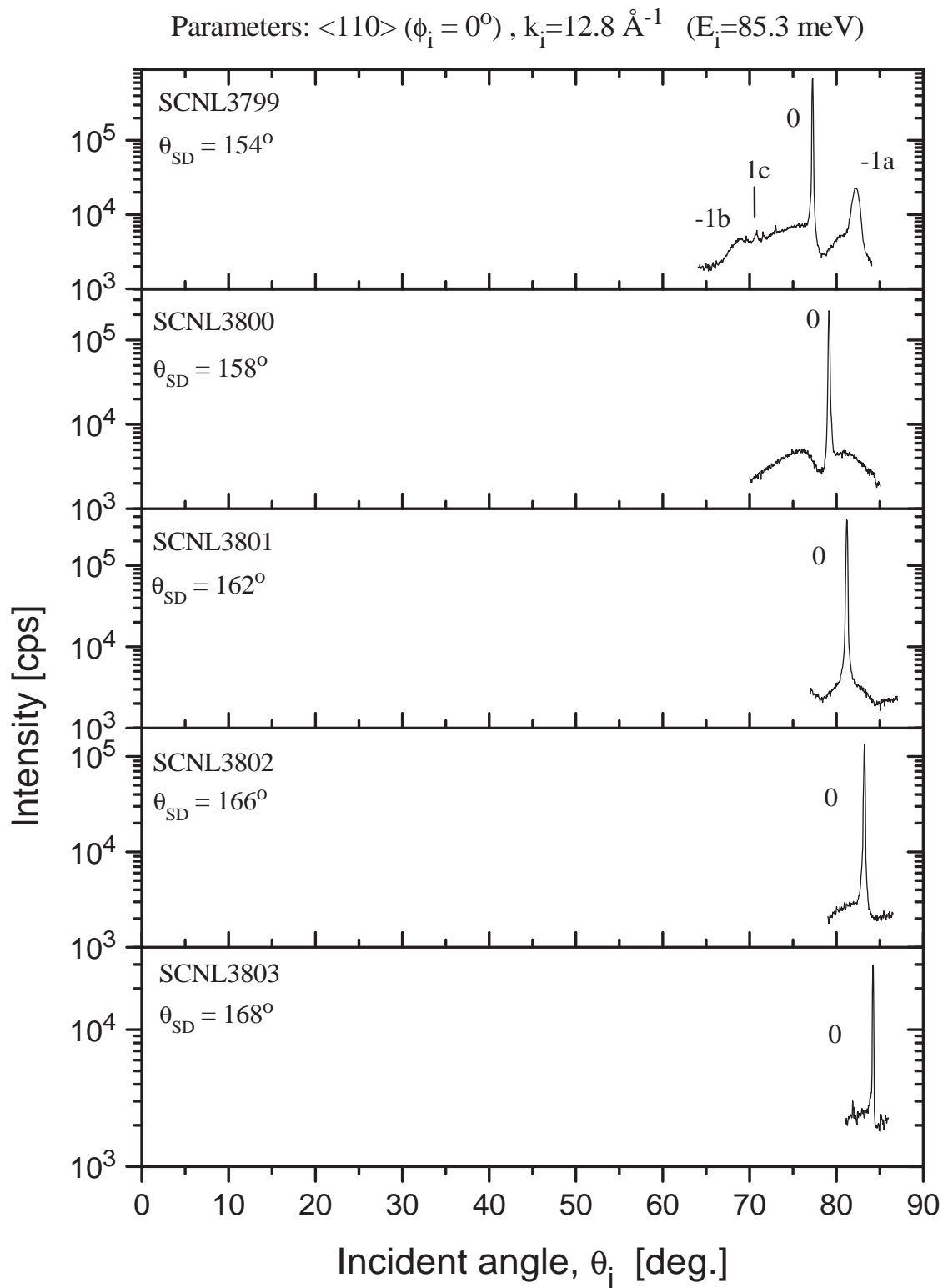
Parameters: $\langle 110 \rangle$ ($\phi_i = 0^\circ$), $k_i = 12.8 \text{ \AA}^{-1}$ ($E_i = 85.3 \text{ meV}$)





Parameters: $\langle 110 \rangle$ ($\phi_i = 0^\circ$), $k_i = 12.8 \text{ \AA}^{-1}$ ($E_i = 85.3 \text{ meV}$)





Bibliography

- [1] E. L. KNUTH, *J. Chem. Phys.* **66**, 3515 (1977).
- [2] A. V. DEURSEN and J. REUSS, *Int. J. Mass Spect. and Ion Phys.* **11**, 483 (1973).
- [3] R. J. GORDON, Y. T. LEE, and D. R. HERSCHBACH, *J. Chem. Phys.* **54**, 2393 (1971).
- [4] H. FRANK, H. HOINKES, H. WILSCH, and U. WONKA, *Surface Sci.* **64**, 362 (1974).
- [5] Y. WATANABE, A. SAKAI, and T. SAKURAI, *J. of the Phys. Soc. of Japan* **66**, 649 (1997).
- [6] R. J. LEROY, *Surface Sci.* **59**, 541 (1976).
- [7] G. KROES and R. C. MOWREY, *J. Chem. Phys.* **103**, 2186 (1995).
- [8] R. C. MOWREY and D. J. KOURI, *Chem. Phys. Lett.* **119**, 285 (1985).
- [9] L. DUNOYER, *Le Radium* **8**, 142 (1911).
- [10] N. F. RAMSEY, *Molecular Beams*, Clarendon Press, Oxford, 1956.
- [11] A. KANTROWITZ and J. GREY, *Rev. Sci. Inst.* **22**, 328 (1951).
- [12] W. BECKER and K. BIER, *Z. Naturforschung* **9A**, 975 (1954).
- [13] G. SCOLES, editor, *Atomic and Molecular Beam Methods*, volume 1, New York Oxford, 1988, Oxford University Press.
- [14] G. SCOLES, editor, *Atomic and Molecular Beam Methods*, volume 2, New York Oxford, 1992, Oxford University Press.

- [15] R. CAMPARGUE, editor, *Atomic and Molecular Beams-The State of the Art 2000*, Berlin Heidelberg New York, 2001, Springer-Verlag.
- [16] P. W. HAIT, *Surface Sci.* **106**, 101 (1981).
- [17] M. KAPPES and S. LEUTWYLER, in *Atomic and Molecular Beam Methods*, edited by G. SCOLES, volume 1, p. 380, New York Oxford, 1988, Oxford University Press.
- [18] *Physics Today* **August**, 1 (2003).
- [19] J. RIFKIN, *The Hydrogen Economy: The Creation of the World-Wide Energy Web and the Redistribution of Power on Earth*, Tarcher/Putnam, 2002.
- [20] W. KRESS and F. DE WETTE, editors, *Surface Phonons*, Berlin Heidelberg, 1991, Springer Verlag.
- [21] G. BENEDEK and J. P. TOENNIES, *Surface Sci.* **299/300**, 587 (1994).
- [22] J. P. TOENNIES, *J. Vac. Sci. Technol. A* **2**, 1055 (1984).
- [23] B. POELSEMA and G. COMSA, *Scattering of Thermal Energy Atoms from Disordered Surfaces*, Springer Verlag, Berlin Heidelberg, 1989.
- [24] F. HOFMANN and J. P. TOENNIES, *Chem. Rev.* **96**, 1307 (1996).
- [25] A. T. YINNON, D. A. LIDAR, I. FARBMAN, R. B. GERBER, P. ZEPPENFELD, M. A. KRZYZOWSKI, and G. COMSA, *J. Chem. Phys.* **106**, 4228 (1997).
- [26] L. J. GOMEZ, S. BOURGEAL, J. IBANEZ, and M. SALMERON, *Phys. Rev.* **B31**, 2551 (1985).
- [27] A. P. GRAHAM, W. SILVESTRI, and J. P. TOENNIES, in *Surface Diffusion: Atomistic and Collective Processes*, edited by H. C. TRINGIDES, volume 360 of *NATO ASI Series B*, Plenum Press, 1997.
- [28] F. O. GOODMAN, *Surface Sci.* **26**, 327 (1971).
- [29] J. P. TOENNIES, *Appl. Phys.* **3**, 91 (1974).
- [30] H. HOINKES, *Rev. of Modern Phys.* **52**, 933 (1980).
- [31] J. A. BARKER and D. J. AUERBACH, *Surface Sci. Rep.* **4**, 1 (1985).

-
- [32] K. H. RIEDER, *Contemp. Phys.* **26**, 559 (1985).
- [33] R. B. GERBER, *Chem. Rev.* **87**, 29 (1987).
- [34] G. VIDALI, G. IHM, H. KIM, and M. W. COLE, *Surface Sci. Rep.* **12**, 133 (1991).
- [35] G. COMSA, *Surface Sci.* **299/300**, 77 (1994).
- [36] D. FARIAS and K. H. RIEDER, *Rep. Prog. Phys.* **61**, 1575 (1998).
- [37] E. HULPKE, editor, *Helium Atom Scattering from Surfaces*, Berlin Heidelberg, 1992, Springer Verlag.
- [38] G. BENEDEK and U. VALBUSA, editors, *Dynamics of Gas-Surface Interaction*, Berlin Heidelberg, 1982, Springer Verlag.
- [39] W. A. STEELE, *The Interaction of Gases with Solid Surfaces*, Pergamon Press Ltd., 1974.
- [40] F. O. GOODMAN and H. Y. WACHMAN, *Dynamics of Gas-Surface Scattering*, Academic Press, Inc., 1976.
- [41] U. VALBUSA, in *Atomic and Molecular Beam Methods*, edited by G. SCOLES, volume 2, p. 327, New York Oxford, 1992, Oxford University Press.
- [42] J. P. TOENNIES, Experimental Determination of Surface Phonons by Helium Scattering and EELS, in *Surface Phonons*, edited by W. KRESS and F. W. DE WETTE, Springer Series in Surface Sciences: 21, p. 111, Berlin, Heidelberg, 1991, Springer-Verlag.
- [43] R. B. DOAK, PhD thesis, Mass. Institute of Technology, Boston, USA, 1981.
- [44] J. M. HORNE and D. R. MILLER, *J. Vac. Sci. Technol.* **13**, 351 (1976).
- [45] E. A. HINDS and I. G. HUGHES, *L. Phys. D: Appl. Phys.* **32**, R119 (1999).
- [46] A. P. JARDINE, P. FOUQUET, J. ELLIS, and W. ALLISON, *Rev. Sci. Inst.* **72**, 3834 (2001).
- [47] R. B. DOAK, R. E. GRISENTI, S. REHBEIN, G. SCHMAHL, J. P. TOENNIES, and C. WÖLL, *Phys. Rev. Lett.* **83**, 4229 (1999).

- [48] B. HOLST and W. ALLISON, *Nature (London)* **390**, 244 (1997).
- [49] F. KNAUER and O. STERN, *Z. Physik* **53**, 779 (1929).
- [50] I. ESTERMANN and O. STERN, *Z. Physik* **61**, 95 (1930).
- [51] R. FRISCH and O. STERN, *Z. Physik* **84**, 430 (1933).
- [52] T. H. JOHNSON, *Phys. Rev.* **35**, 1299 (1930).
- [53] T. H. JOHNSON, *Phys. Rev.* **37**, 847 (1931).
- [54] M. F. BERTINO, A. L. GLEBOV, J. P. TOENNIES, F. TRAEGER, E. PIJPER, G. J. KROES, and R.C.MOWREY, *Phys. Rev. Lett.* **81**, 5608 (1998).
- [55] H. LEGGE, J. R. MANSON, and J. P. TOENNIES, *J. Chem. Phys.* **110**, 8767 (1999).
- [56] G. KROES, *J. Phys. Chem. B* **103**, 9397 (1999).
- [57] H. U. FINZEL, H. FRANK, H. HOINKES, M. LUSCHKA, H. NAHR, H. WILSCH, and U. WONKA, *Surface Sci.* **49**, 577 (1975).
- [58] G. BENEDEK, J. P. TOENNIES, and R. B. DOAK, *Phys. Rev. B* **28**, 7277 (1983).
- [59] G. DERRY, D. WESNER, S. V. KRISHNASWAMY, and D. R. FRANKL, *Surface Sci.* **74**, 245 (1978).
- [60] J. VOGT and H. WEISS, *Surface Sci.* **501**, 203 (2002).
- [61] J. G. ROBERTS, M. A. VAN HOVE, and G. A. SOMORJAI, *Surface Sci.* **518**, 49 (2002).
- [62] G. WOLKEN(JR.), *J. Chem. Phys.* **59**, 1159 (1973).
- [63] G. WOLKEN(JR.), *J. Chem. Phys.* **62**, 2730 (1975).
- [64] U. GARIBALDI, A. C. LEVI, R. SPADACINI, and G. E. TOMMEI, *Surface Sci.* **55**, 40 (1976).
- [65] N. R. HILL, *Phys. Rev. B* **19**, 4269 (1979).
- [66] R. B. GERBER, L. H. BEARD, and D. J. KOURI, *J. Chem. Phys.* **74**, 4709 (1981).

-
- [67] R. SCHINKE, *J. Chem. Phys.* **76**, 2352 (1982).
- [68] G. DROLSHAGEN, A.KAUFHOLD, and J. P. TOENNIES, *J. Chem. Phys.* **83**, 827 (1985).
- [69] D. R. O'KEEFE, J. N. SMITH, R. L. PALMER, and H. SALTSBURG, *J. Chem. Phys.* **52**, 4447 (1970).
- [70] E. PIJPER and G. KROES, *Phys. Rev. Lett.* **80**, 488 (1998).
- [71] A. C. LUNTZ, J. K. BROWN, and M. D. WILLIAMS, *J. Chem. Phys.* **93**, 5240 (1990).
- [72] A. ZANGWILL, *Physics at Surfaces*, Cambridge University Press, 1988.
- [73] V. CELLI, D. EICHENAUER, A. KAUFHOLD, and J. P. TOENNIES, *J. Chem. Phys.* **83**, 2504 (1985).
- [74] E. ZAREMBA and W. KOHN, *Phys. Rev. B* **13**, 2270 (1976).
- [75] E. M. LIFSHITZ, *Sov. Phys.-JETP* **2**, 73 (1956).
- [76] H. HOINKES, H. NAHR, and H. WILSCH, *Surface Sci.* **33**, 516 (1972), (Erratum: *Surface Sci.* **40**, 457 (1973)).
- [77] W. STEELE, *Chem. Rev* **93**, 2355 (1993).
- [78] U. GARIBALDI, A. C. LEVI, R. SPADACINI, and G. E. TOMMEI, *Surface Sci.* **48**, 649 (1975).
- [79] N. GARCIA, *Surface Sci.* **63**, 113 (1977).
- [80] N. GARCIA, V. CELLI, and F. O. GOODMAN, *Phys. Rev. B* **19**, 634 (1979).
- [81] J. E. LENNARD-JONES and A. F. DEVONSHIRE, *Proc. R. Soc. London, Ser.-A* **158**, 253 (1937).
- [82] G. DROLSHAGEN, A.KAUFHOLD, and J. P. TOENNIES, *Israel J. Chem.* **22**, 283 (1982).
- [83] H. CHOW and E. D. THOMPSON, *Surface Sci.* **59**, 225 (1976).
- [84] A. TSUCHIDA, *Surface Sci.* **52**, 685 (1975).

- [85] H. CHOW, *Surface Sci.* **66**, 221 (1977).
- [86] C. SCHWARTZ, M. W. COLE, and J. PLIVA, *Surface Sci.* **75**, 1 (1978).
- [87] G. BOATO, P. CANTINI, and L. MATTERA, *Jpn. J. Appl. Phys. Suppl.2-Pt.2*, 553 (1974).
- [88] M. F. BERTINO and D. FARIAS, *J.Phys.:Cons.Matter* **14**, 6037 (2002).
- [89] L. M. HUBBARD and W. H. MILLER, *J. Chem. Phys.* **78**, 1801 (1983).
- [90] R. B. GERBER, A. T. YINNON, Y. SHIMONI, and D. J. KOURI, *J. Chem. Phys.* **73**, 4397 (1980).
- [91] R. HORNE and L. J. F. HERMANS, *J. Chem. Phys.* **91**, 1261 (1989).
- [92] R. HORNE and L. J. F. HERMANS, *Chem. Phys. Lett.* **179**, 58 (1991).
- [93] E. PIJPER, PhD thesis, University of Leiden, Leiden, Netherlands, 2002.
- [94] P. W. FOWLER and J. M. HUTSON, *Phys. Rev. B* **33**, 3724 (1986).
- [95] J. C. SLATER and J. G. KIRKWOOD, *Phys. Rev.* **37**, 682 (1931).
- [96] J. G. KIRKWOOD, *Phys. Z* **33**, 57 (1932).
- [97] K. T. TANG and J. P. TOENNIES, *J. Chem. Phys.* **80**, 3726 (1984).
- [98] A. D. BUCKINGHAM, *Adv. Chem. Phys.* **12**, 107 (1967).
- [99] J. HARRIS and P. J. FEIBELMAN, *Surface Sci.* **115**, L133 (1982).
- [100] D. J. KOURI and R. B. GERBER, *Israel J. Chem.* **22**, 321 (1982).
- [101] G. WOLKEN(JR.), *J. Chem. Phys.* **58**, 3047 (1973).
- [102] D. KOSLOFF and R. KOSLOFF, *J. Comput. Phys.* **52**, 35 (1983).
- [103] R. KOSLOFF and D. KOSLOFF, *J. Chem. Phys.* **79**, 1823 (1983).
- [104] C. J. RAY and J. M. BOWMAN, *J. Chem. Phys.* **66**, 1122 (1977).
- [105] J. M. BOWMAN and S. PARK, *J. Chem. Phys.* **76**, 1168 (1982).
- [106] J. C. POLANYI and R. J. WOLF, *Ber. Bunsenges. Phys. Chem.* **86**, 356 (1982).

-
- [107] S. SAINI, D. A. DOWS, and H. S. TAYLOR, *Chem. Phys.* **90**, 87 (1984).
- [108] D. E. FITZ, L. H. BEARD, and D. J. KOURI, *Chem. Phys.* **59**, 257 (1981).
- [109] R. SCHINKE, *Chem. Phys. Lett.* **87**, 438 (1982).
- [110] J. E. ADAMS, *Surface Sci.* **97**, 43 (1980).
- [111] R. B. BERNSTEIN, editor, *Atom-Molecule Collision Theory*, New York, 1979, Plenum.
- [112] R. C. MOWREY and D. J. KOURI, *J. Chem. Phys.* **84**, 6466 (1986).
- [113] R. C. MOWREY and D. J. KOURI, *J. Chem. Phys.* **86**, 6140 (1987).
- [114] J. R. MANSON, in *Helium Atom Scattering from Surfaces*, edited by E. HULPKE, p. 173, Berlin Heidelberg, 1992, Springer Verlag.
- [115] J. R. MANSON, *Phys. Rev. B* **43**, 6924 (1991).
- [116] J. L. BEEBY, *J. Phys. C: Solid State Phys.* **4**, L359 (1971).
- [117] G. ARMAND and J. R. MANSON, *Phys. Rev. B* **37**, 4363 (1988).
- [118] V. CELLI and A. A. MARADUDIN, *Phys. Rev. B* **31**, 825 (1985).
- [119] J. E. LENNARD-JONES and A. F. DEVONSHIRE, *Nature* **137**, 1069 (1936).
- [120] S. MIRET-ARTES, *Surface Sci.* **366**, L735 (1996).
- [121] U. HARTEN, J. P. TOENNIES, and C. WOELL, *J. Chem. Phys.* **85**, 2249 (1986).
- [122] G. BRUSDEYLINS, R. B. DOAK, and J. P. TOENNIES, *J. Chem. Phys.* **75**, 1784 (1981).
- [123] G. LILIENKAMP and J. P. TOENNIES, *J. Chem. Phys.* **78**, 5210 (1983).
- [124] R. VOLLMER, PhD thesis, Georg-August Universität, Göttingen, Germany, 1992.
- [125] R. DAVID, K. KERN, P. ZEPPEFELD, and G. COMSA, *Rev. Sci. Instrum.* **57**, 2771 (1986).
- [126] T. MIYAKE, E. S. GILLMAN, I. OODAKE, and H. PETEK, *Jpn. J. Appl. Phys.* **36**, 4531 (1997).

- [127] G. BOATO, P. CANTINI, and L. MATTERA, *Surface Sci.* **55**, 141 (1976).
- [128] T. ENGEL and K. H. RIEDER, *Surface Sci.* **109**, 140 (1981).
- [129] D. A. MACLAREN, W. ALLISON, and B. HOLST, *Rev. Sci. Inst.* **71**, 2625 (2000).
- [130] D. FARIAS, M. PATTING, K. H. RIEDER, and J. R. MANSON, *Phys. Rev. B* **65**, 165435 (2002).
- [131] R. B. DOAK and A. V. G. CHIZMESHYA, *Europhys. Lett* **51**, 381 (2000).
- [132] F. SHIMIZU, *Phys. Rev. Lett.* **86**, 987 (2001).
- [133] J. BRAUN, P. K. DAY, J. P. TOENNIES, G. WITTE, and E. NEHER, *Rev. Sci. Inst.* **68**, 3001 (1997).
- [134] K. KUHNKE, K. KERN, R. DAVID, B. LINDENAU, and G. COMSA, *Rev. Sci. Inst.* **65**, 653 (1994).
- [135] D. J. AUERBACH, in *Atomic and Molecular Beam Methods*, edited by G. SCOLES, volume 1, p. 362, New York Oxford, 1988, Oxford University Press.
- [136] D. J. AUERBACH, C. A. BECKER, J. P. COWIN, and L. WHARTON, *Rev. Sci. Inst.* **49**, 1518 (1978).
- [137] P. A. THIEL and J. W. ANDEREGG, *Rev. Sci. Inst.* **55**, 1669 (1984).
- [138] J. T. YATES(JR.), *Experimental Innovations in Surface Science A Guide to Practical Laboratory Methods and Instruments*, Springer-Verlag New York, Inc., 1988.
- [139] G. LILIENKAMP, Master thesis, Georg-August Universität, Göttingen, 1981.
- [140] R. B. DOAK, in *Atomic and Molecular Beam Methods*, edited by G. SCOLES, volume 2, p. 384, New York Oxford, 1992, Oxford University Press.
- [141] B. SAMELIN, Master thesis, Georg-August Universität, Göttingen, Germany, 1993.
- [142] G. L. WEISSLER and R. W. CARLSON, editors, *Methods of Experimental Physics Vacuum Physics and Technology*, volume 14, London, 1979, Academic Press, Inc.

-
- [143] D. R. MILLER, in *Atomic and Molecular Beam Methods*, edited by G. SCOLES, volume 1, p. 14, New York Oxford, 1988, Oxford University Press.
- [144] G. BRUSDEYLINS, R. B. DOAK, and J. P. TOENNIES, *Phys. Rev. B* **27**, 3662 (1983).
- [145] G. BENEDEK, G. BRUSDEYLINS, R. B. DOAK, and J. P. TOENNIES, *Phys. Rev. B* **27**, 2488 (1983).
- [146] G. BENEDEK, G. BRUSDEYLINS, R. B. DOAK, J. G. SCOFRONICK, and J. P. TOENNIES, *Phys. Rev. B* **28**, 2104 (1983).
- [147] G. COMSA and R. DAVID, *Surface Sci. Rep.* **5**, 145 (1985).
- [148] T. M. ELLIS, G. SCOLES, U. VALBUSA, H. JONSSON, and J. H. WEARE, *Surface Sci.* **155**, 499 (1985).
- [149] B. J. HINCH, D. R. FRANKL, and W. ALLISON, *Surface Sci.* **180**, 371 (1987).
- [150] D. M. SMILGIES and J. P. TOENNIES, *Rev. Sci. Inst.* **59**, 2185 (1988).
- [151] G. COMSA, *Surface Sci.* **81**, 57 (1979).
- [152] T. M. LU and M. G. LAGALLY, *Surface Sci.* **120**, 47 (1982).
- [153] L. K. VERHEIJ, B. POELSEMA, and G. COMSA, *Surface Sci.* **162**, 858 (1985).
- [154] B. CROSET and C. DE BEAUVAIS, *Surface Sci.* **409**, 403 (1998).
- [155] Rarefied Gas Dynamics Symposium Series.
- [156] J. B. ANDERSON, *Molecular Beams and Low Density Gas Dynamics*, pp. 1–91, Dekker, New York, 1974.
- [157] J. B. FENN, *Applied Atomic Collision Physics* **5**, 349 (1982).
- [158] R. CAMPARGUE, *J. Chem. Phys.* **88**, 4466 (1984).
- [159] M. D. MORSE, Atomic, Molecular, and Optical Physics: Atoms and Molecules, in *Experimental Methods in the Physical Sciences*, edited by F. B. DUNNIG and R. G. HULET, volume 29B, pp. 21–47, Academic Press, Inc., 1996.
- [160] K. BIER and O. HAGENA, in *Rarefied Gas Dynamics*, edited by J. H. DE LEEUW, volume 2 of *4th Symposium*, p. 260, New York, 1966, Academic Press.

- [161] H. ASHKENAS and F. S. SHERMAN, in *Rarefied Gas Dynamics*, edited by J. H. DE LEEUW, volume 2 of *4th Symposium*, p. 84, New York, 1966, Academic Press.
- [162] J. B. FENN and J. DECKERS, in *Rarefied Gas Dynamics*, edited by J. A. LAURMANN, volume 1 of *3rd Symposium*, p. 497, New York, 1963, Academic Press.
- [163] U. BOSSEL, F. C. HURLBUT, and F. S. SHERMAN, in *Rarefied Gas Dynamics*, edited by L. TRILLING and H. Y. WACHMAN, volume 2 of *5th Symposium*, p. 945, New York, 1969, Academic Press.
- [164] H. BEIJERINCK, R. VAN GERWEN, E. KERSTEL, J. MARTENS, E. VAN VLIEBERGEN, M. SMITS, and G. KAASHOEK, *Chem. Phys.* **96**, 153 (1985).
- [165] H. BEIJERINCK and N. VERSTER, *Physica* **111C**, 327 (1981).
- [166] L. PRANTL, K. OSWATITSCH, and K. WIEGHARDT, *Führer durch die Strömungslehre*, Vieweg Verlag, Braunschweig, 1969.
- [167] E. L. KNUTH, Lecture Notes on Supersonic Molecular Beams, Bericht 20/1988, Max-Planck-Institut für Strömungsforschung, Göttingen, 1988.
- [168] H. PAULY, *Atom, Molecule and Cluster Beams*, Springer Verlag, Berlin Heidelberg, 2000.
- [169] J. HIRSCHFELDER, C. CURTISS, and R. BIRD, *Molecular Theory of Gases and Liquids*, Wiley, 1954.
- [170] H. M. HABETS, PhD thesis, Technische Hogeschool Eindhoven, Eindhoven, The Netherlands, 1977.
- [171] J. P. TOENNIES and K. WINKELMANN, *J. Chem. Phys.* **66**, 3965 (1977).
- [172] K. WINKELMANN, PhD thesis, Georg-August Universität, Göttingen, Germany, 1977.
- [173] J. WANG, A. SHAMAMIAN, B. R. THOMAS, J. M. WILKINSON, J. RILEY, C. F. GIESE, and W. R. GENTRY, *Phys. Rev. Lett.* **60**, 696 (1988).
- [174] H. R. MURPHY and D. R. MILLER, *J. Chem. Phys.* **88**, 4474 (1984).
- [175] R. D. MCCARTY, *J. Phys. Chem. -Ref. Data* **2** (1973).

-
- [176] H. M. HABETS, H. C. W. BEIJERINCK, N. F. VERSTER, and J. P. L. M. N. DE WARRIMONT, in *Rarefied Gas Dynamics*, edited by J. L. POTTER, volume 2 of *10th Symposium*, p. 919, New York, 1976, AIAA.
- [177] H. BEIJERINCK, G. KAASHOEK, J. BEIJERS, and M. VERHEIJEN, *Physica* **121C**, 425 (1983).
- [178] G. BRUSDEYLINS, H. D. MEYER, J. P. TOENNIES, and K. WINKELMANN, in *Rarefied Gas Dynamics*, edited by J. L. POTTER, volume 2 of *10th Symposium*, p. 1047, New York, 1976, AIAA.
- [179] P. POULSEN and D. R. MILLER, in *Rarefied Gas Dynamics*, edited by J. L. POTTER, volume 2 of *10th Symposium*, p. 899, New York, 1976, AIAA.
- [180] U. BUCK, H. PAULY, D. PUST, and J. SCHLEUSENER, in *Rarefied Gas Dynamics*, edited by M. BECKER and M. FIEBIG, volume 2 of *9th Symposium*, p. 10, DFVLR-Press, 1974.
- [181] H. M. PARKER, A. R. KUHLETHAU, R. ZAPATA, and J. E. S. JR., in *Rarefied Gas Dynamics*, edited by F. M. DEVIENNE, 1st Symposium, p. 69, New York, 1960, Pergamon.
- [182] R. G. ALBRIGHT, J. PEETERS, M. BOURGUIGNON, R. L. L. ROY, and J. M. DECKERS, in *Rarefied Gas Dynamics*, edited by J. H. DE LEEUW, volume 2 of *4th Symposium*, p. 350, New York, 1966, Academic Press.
- [183] G. A. BIRD, *Phys. Fluids* **19**, 1486 (1976).
- [184] S. S. FISHER and E. L. KNUTH, *AIAA Journal* **7**, 1174 (1969).
- [185] D. R. MILLER, PhD thesis, Princeton University, Princeton, N.J. USA, 1966.
- [186] R. J. GALLAGHER and J. B. FENN, *J. Chem. Phys.* **60**, 3487 (1974).
- [187] R. J. GALLAGHER and J. B. FENN, *J. Chem. Phys.* **60**, 3492 (1974).
- [188] M. LABOWSKY, S. RYALI, J. B. FENN, and D. R. MILLER, in *Rarefied Gas Dynamics*, edited by S. S. FISHER, volume 2 of *12th Symposium*, p. 695, New York, 1980, AIAA.
- [189] K. P. HUBER and G. HERZBERG, *Molecular Spectra and Molecular Structure*, volume 4, Van Nostrand, New York, 1978.

- [190] K. KERN, R. DAVID, and G. COMSA, *J. Chem. Phys.* **82**, 5673 (1985).
- [191] S. YAMAZAKI, M. TAKI, and Y. FUJITANI, in *Rarefied Gas Dynamics*, edited by S. S. FISHER, volume 2 of *12th Symposium*, p. 802, New York, 1980, AIAA.
- [192] J. E. POLLARD, D. J. TREVOR, J. E. REUTT, Y. T. LEE, and D. A. SHIRLEY, *J. Chem. Phys.* **77**, 34 (1982).
- [193] J. E. POLLARD, D. J. TREVOR, Y. T. LEE, and D. A. SHIRLEY, *J. Chem. Phys.* **77**, 4818 (1982).
- [194] H. P. GODFRIED, I. F. SILVERA, and J. VAN STRAATEN, in *Rarefied Gas Dynamics*, edited by S. S. FISHER, volume 2 of *12th Symposium*, p. 772, New York, 1980, AIAA.
- [195] K. WINKELMANN, in *Rarefied Gas Dynamics*, edited by R. CAMPARGUE, volume 2 of *11th Symposium*, p. 899, Paris, 1979, CEA.
- [196] F. REIF, *Fundamentals of Statistical and Thermal Physics*, McGraw-Hill, Singapore, 1965.
- [197] M. FAUBEL, F. A. GIANTURCO, F. RAGNETTI, L. Y. RUSIN, F. SONDERMANN, and U. TAPPE, *J. Chem. Phys.* **101**, 8800 (1994).
- [198] R. PRYDZ, K. D. TIMMERHAUS, and R. B. STEWART, in *Advances in Cryogenic Engineering*, edited by K. D. TIMMERHAUS, volume 13, p. 384, New York, 1968, Plenum Press.
- [199] W. SCHOELLKOPF, Master thesis, Georg-August Universität, Göttingen, Germany, 1994.
- [200] W. BECKER, K. BIER, and W. HENKES, *Z. Phys.* **146**, 335 (1956).
- [201] E. W. BECKER, R. KLINGELHÖFER, and P. LOHSE, *Z. Naturforschg.* **17 a**, 432 (1962).
- [202] K. BUCHHEIT and W. HENKES, *Z. Angew. Phys.* **24**, 191 (1968).
- [203] R. KLINGELHÖFER and H. O. MOSER, *J. Appl. Phys.* **43**, 4575 (1972).
- [204] E. L. KNUTH, F. SCHÜNEMANN, and J. P. TOENNIES, *J. Chem. Phys.* **102**, 6258 (1995).

-
- [205] B. TROSTELL, *Nucl. Instr. and Meth. in Phys. Res. A* **362**, 41 (1995).
- [206] A. KHOUKAZ, T. LISTER, C. QUENTMEIER, R. SANTO, and C. THOMAS, *Eur. Phys. J. D* **5**, 275 (1999).
- [207] W. OBERT, in *Rarefied Gas Dynamics*, edited by J. L. POTTER, volume 2 of *10th Symposium*, p. 1153, New York, 1976, AIAA.
- [208] D. GOLOMB, R. E. GOOD, A. B. BAILEY, M. R. BUSBY, and R. DAWBARN, *J. Chem. Phys.* **57**, 3844 (1972).
- [209] R. M. YEALLAND, J. M. DECKER, I. D. SCOTT, and C. T. TUORI, *Can. J. Phys.* **50**, 2464 (1972).
- [210] D. GOLOMB, R. E. GOOD, and R. F. BROWN, *J. Chem. Phys.* **52**, 1545 (1970).
- [211] T. A. MILNE, A. E. VANDERGRIFT, and F. T. GREENE, *J. Chem. Phys.* **52**, 1552 (1970).
- [212] D. L. BUNKER, *J. Chem. Phys.* **32**, 1001 (1960).
- [213] E. L. KNUTH, *J. Chem. Phys.* **107**, 9125 (1997).
- [214] T. A. MILNE and F. T. GREENE, *J. Chem. Phys.* **47**, 4095 (1967).
- [215] H. J. DITTMERS, C. SCHUETZE, B. FISCHER, and K. SCHUEGERL, *Z. Phys. Chem.* **80**, 220 (1972).
- [216] G. DANBY, *J. Phys. B: Mol. Opt. Phys.* **22**, 1785 (1989).
- [217] D. E. STOGRYN and J. O. HIRSHFELDER, *J. Chem. Phys.* **31**, 1531 (1959).
- [218] W. SCHOELLKOPF and J. P. TOENNIES, *J. Chem. Phys.* **104**, 1155 (1996).
- [219] A. P. J. V. DEURSEN, PhD thesis, Katholieke Universiteit te Toernooiveld, Nijmegen, The Netherlands, 1976.
- [220] J. J. HUANG, M. E. SCHWARTZ, and G. V. PFEIFER, *J. Chem. Phys.* **56**, 775 (1972).
- [221] P. K. SHARMA, E. L. KNUTH, and W. S. YOUNG, *J. Chem. Phys.* **64**, 4345 (1976).

- [222] A. V. DEURSEN and J. REUSS, *Int. J. Mass Spect. and Ion Phys.* **23**, 109 (1977).
- [223] M. SCHWARTZ and R. P. ANDRES, in *Rarefied Gas Dynamics*, edited by J. L. POTTER, volume 1 of *10th Symposium*, p. 135, New York, 1976, AIAA.
- [224] O. CARNAL, M. SIGEL, T. SLEATOR, H. TAKUMA, and J. MLYNCK, *Phys. Rev. Lett.* **67**, 3231 (1991).
- [225] W. G. F. KAENDERS, A. RICHTER, R. WYNANDS, and D. MESCHEDE, *Nature (London)* **375**, 214 (1995).
- [226] T. M. ROACH, H. ABELE, M. G. BOSHER, H. L. GROSSMAN, K. P. ZETIE, and E. HINDS, *Phys. Rev. Lett.* **75**, 629 (1995).
- [227] W. G. F. KAENDERS, F. LISON, I. MÜLLER, A. RICHTER, R. WYNANDS, and D. MESCHEDE, *Phys. Rev. A* **54**, 5067 (1996).
- [228] R. E. GRISENTI, Private communication.
- [229] S. REHBEIN, R. B. DOAK, R. E. GRISENTI, G. SCHMAHL, J. P. TOENNIES, and C. WÖLL, in *Proceedings of the Micro- and Nano-Engineering '99 Conference*, edited by M. GENTILI, E. D. FABRIZIO, and M. MENEGHINI, Rome, Italy, 1999, (Elsevier, Amsterdam) 1999.
- [230] R. E. GRISENTI, PhD thesis, Georg-August Universität, Göttingen, Germany, 2000.
- [231] D. KORSCH, *Reflective Optics*, Academic Press, New York, 1991.
- [232] D. A. MACLAREN, PhD thesis, University of Cambridge, England, 2002.
- [233] J. R. BUCKLAND, PhD thesis, University of Cambridge, England, 1998.
- [234] J. R. BUCKLAND, B. HOLST, and W. ALLISON, *Chem. Phys. Lett.* **303**, 107 (1999).
- [235] R. J. WILSON, B. HOLST, and W. ALLISON, *Rev. Sci. Inst.* **70**, 2960 (1999).
- [236] B. HOLST, J. M. HUNTLEY, R. BALSOD, and W. ALLISON, *J. Phys. D: Appl. Phys.* **32**, 2666 (1999).
- [237] B. HOLST, PhD thesis, University of Cambridge, England, 1997.

-
- [238] G. SCHULZE and M. HENZLER, *Surface Sci.* **124**, 336 (1983).
- [239] U. HARTEN, J. P. TOENNIES, and C. WOELL, *Phys. Rev. B* **38**, 3305 (1988).
- [240] P. JACOB and Y. J. CHABAL, *J. Chem. Phys.* **95**, 2897 (1991).
- [241] G. J. PIETSCH, U. KÖHLER, and M. HENZLER, *J. Appl. Phys.* **73**, 4797 (1993).
- [242] J. J. LANDER, G. W. GOBELLI, and J. MORRISON, *J. Appl. Phys.* **34**, 2298 (1963).
- [243] R. E. SCHLIER and H. E. FARNSWORTH, *J. Chem. Phys.* **30**, 917 (1959).
- [244] T. TAKAHAGI, I. NAGAI, A. ISHITANI, and H. KURODA, *J. Appl. Phys.* **64**, 3516 (1988).
- [245] G. W. TRUCKS, K. RACHAVACHARI, G. S. HIGASHI, and Y. J. CHABAL, *Phys. Rev. Lett.* **65**, 504 (1990).
- [246] D. A. MACLAREN, N. J. CURSON, P. ATKINSON, and W. ALLISON, *Surface Sci.* **490**, 285 (2001).
- [247] D. A. MACLAREN, N. J. CURSON, P. ATKINSON, B. HOLST, D. J. JOHNSON, and W. ALLISON, *J. Vac. Sci. Technol. A* **20**, 285 (2002).
- [248] V. S. SMENTKOWSKI and J. J. T. YATES, *J. Vac. Sci. Technol. A* **14**, 260 (1996).
- [249] V. G. LIFSHITS, A. A. SARANIN, and A. V. ZOTOV, *Surface Phases on Silicon*, Wiley, Chichester, 1994.
- [250] R. S. BECKER, G. S. HIGASHI, Y. J. CHABAL, and A. J. BECKER, *Phys. Rev. Lett.* **65**, 1917 (1990).
- [251] M. B. NARDELLI, F. FINNOCCHI, M. PALUMMO, R. D. FELICA, C. M. BERTONI, F. BERNADINI, and S. OSSICINI, *Surface Sci.* **269/270**, 879 (1992).
- [252] J. R. BUCKLAND and W. ALLISON, *J. Chem. Phys.* **112**, 970 (2000).
- [253] Y. C. HUANG, J. FLIDR, T. A. NEWTON, and M. A. HINES, *Phys. Rev. Lett.* **80**, 4462 (1998).
- [254] C. P. WADE and C. E. D. CHIDSEY, *Appl. Phys. Lett.* **71**, 1679 (1997).

- [255] Balzers AG, Lichtenstein, *Partialdruckmessung in der Vakuumtechnik*, 1983, Technical manual:BG 800 169 PD (8711).
- [256] P. W. HAIT, *Vacuum* **17**, 547 (1967).
- [257] C. BAKER and J. J. MANURA, in *PITTCON Meeting*, Chicago, IL, USA, March 1994.
- [258] R. J. ELSEY, *Vacuum* **25**, 347 (1975).
- [259] T. SIGMOND, *Vacuum* **25**, 239 (1975).
- [260] B. POELSEMA, S. T. DE ZWART, and G. COMSA, *Phys. Rev. Lett.* **49**, 578 (1982).
- [261] B. SANDFORT, A. MAZUR, and J. POLLMANN, *Phys. Rev.* **51**, 7168 (1995).
- [262] R. HONKE, P. PAVONE, and U. SCHRÖDER, *Surface Sci.* **367**, 75 (1996).
- [263] X. ZENG and H. E. ELSAYED-ALI, *Surface Sci.* **442**, L977 (1999).
- [264] B. W. BUSCH and T. GUSTAFSSON, *Phys. Rev.* **B61**, 16097 (2000).
- [265] G. HELGESEN, D. GIBBS, A. P. BADDORF, D. M. ZEHNER, and S. G. J. MOCHRIE, *Phys. Rev. B* **48**, 15320 (1993).
- [266] J. H. CHO, ISMAIL, Z. ZHANG, and E. W. PLUMMER, *Phys. Rev. B* **59**, 1677 (1999).
- [267] A. MIKKELSEN, J. JIRUSE, and D. L. ADAMS, *Phys. Rev. B* **60**, 7796 (1999).
- [268] K. POHL, J. H. CHO, K. TERAOKURA, M. SCHEFFLER, and E. W. PLUMMER, *Phys. Rev. Lett.* **80**, 2853 (1998).
- [269] M. LAZZERI and S. DE GIRONCOLI, *Phys. Rev. Lett.* **81**, 2096 (1998).
- [270] A. KARA, P. STAIKOV, A. N. AL-RAWI, and T. RAHMAN, *Phys. Rev. B* **55**, R13 440 (1997).
- [271] J. M. WILSON and T. J. BASTOW, *Surface Sci.* **26**, 461 (1971).
- [272] ISMAIL, E. W. PLUMER, M. LAZZERI, and S. DE GIRONCOLI, *Phys. Rev. B* **63**, 233401 (2001).

-
- [273] O. KAMISHIMA, T. ISHII, H. MAEDA, and S. KASHINO, *Solid State. Comm.* **103**, 141 (1997).
- [274] T. S. CHEN, G. P. ALLDREGE, and F. W. D. WETTE, *Phys. Rev. B* **6**, 623 (1972).
- [275] T. S. CHEN, G. P. ALLDREGE, and F. W. D. WETTE, *Surface Sci.* **57**, 25 (1976).
- [276] T. S. CHEN, G. P. ALLDREGE, and F. W. D. WETTE, *Surface Sci.* **62**, 675 (1977).
- [277] E. ALLEN, *J. Vac. Sci. Technol.* **9**, 934 (1972).
- [278] V. E. KENNER and R. E. ALLEN, *Phys. Rev. B* **8**, 2916 (1973).
- [279] L. DOBRZYNSKI and A. A. MARADUDIN, *Phys. Rev. B* **7**, 1207 (1973).
- [280] Y. W. TSANG and L. M. FALICOV, *Phys. Rev. B* **12**, 2441 (1975).
- [281] T. YANAGIHARA and K. YOMOGITA, *Surface Sci.* **219**, 407 (1989).
- [282] A. SHI and M. WORTIS, *Phys. Rev. B* **47**, 9804 (1993).
- [283] A. GLEBOV, PhD thesis, Georg-August Universität, Göttingen, Germany, 1997.
- [284] F. TRAEGER, PhD thesis, Georg-August Universität, Göttingen, Germany, 2001.
- [285] B. A. NESTERENKO, A. D. BORODKIN, and O. V. SNITKO, *Sov. Phys. Solid State* **15**, 1731 (1974).
- [286] LANDOLT-BÖRNSTEIN, volume 24, Group-III, Subvolume A of *New Series*, Springer-Verlag, 1993, pp.23.
- [287] J. T. LEWIS, A. LEHOCZKY, and C. V. BRISCOE, *Phys. Rev.* **161**, 877 (1967).
- [288] G. VIDALI and C. HUTCHINGS, *Phys. Rev. B* **37**, 10374 (1988).
- [289] J. R. BLEDSOE and S. S. FISHER, *Surface Sci.* **46**, 129 (1974).
- [290] G. ARMAND, L. LAPUJOLADE, and Y. LEJAY, *Surface Sci.* **63**, 143 (1977).

- [291] G. G. BISHOP, E. S. GILLMAN, J. BAKER, J. J. HERNANDEZ, S. A. SAFRON, J. G. SKOFRONICK, S. M. WEERA, and J. R. MANSON, *Phys. Rev. B* **52**, 13229 (1995).
- [292] J. ESTEL, H. HOINKES, H. KAARMAN, H. NAHR, and H. WILSCH, *Surface Sci.* **54**, 393 (1976).
- [293] D. PASHLEY, *Adv. Phys.* **14**, 327 (1965).
- [294] W. BAYH and H. PFLUG, *Z. Angewandte Phys.* **25**, 358 (1968).
- [295] G. BOATO, P. CANTINI, and L. MATTERA, *J. Chem. Phys.* **65**, 544 (1976).
- [296] B. LUCKSCHEITER, Phd thesis, Tübingen Universität, Tübingen, Germany, 1973.
- [297] J. W. MATHEWS and E. GRUENBAUM, *Phil. Mag.* **11**, 1233 (1965).
- [298] P. BARRACLOUGH and P. G. HALL, *Surface Sci.* **46**, 393 (1974).
- [299] A. L. GLEBOV, J. P. TOENNIES, and F. TRAEGER, *Phys. Rev. Lett.* **82**, 4492 (1999).
- [300] G. C. BENSON, *J. Chem. Phys.* **35**, 2113 (1961).
- [301] G. C. BENSON, P. I. FREEMAN, and E. DEMPSEY, *J. Chem. Phys.* **39**, 302 (1963).
- [302] G. C. BENSON and K. S. YUN, in *The Solid-Gas Interface*, edited by M. DEKKER, p. Chap. 8, New York, 1967.
- [303] E. G. MCRAE and C. W. CALDWELL, *Surface Sci.* **2**, 509 (1964).
- [304] G. E. LARAMORE and A. C. SWITENDICK, *Phys. Rev. B* **7**, 3615 (1973).
- [305] J. VOGT and H. WEISS, *Surface Sci.* **491**, 155 (2001).
- [306] G. C. BENSON and T. A. CLAXTON, *J. Chem. Phys.* **48**, 1356 (1968).
- [307] F. W. DE WETTE, W. KRESS, and U. SCHRÖDER, *Phys. Rev. B* **32**, 4143 (1985).
- [308] M. CAUSA, R. DOVESI, and F. RICCA, *Surface Sci.* **280**, 1 (1993).

-
- [309] D. OCHS, M. BRAUSE, P. STRACKE, S. KRISCHOK, F. WIEGERHAUS, W. MAUS-FRIEDRICH, V. KEMPTER, V. E. PUCHIN, and A. L. SHULGER, *Surface Sci.* **383**, 162 (1997).
- [310] N.-P. WANG, M. ROHLFING, P. KRÜGER, and J. POLLMANN, *Phys. Rev. B* **67**, 115111 (2003).
- [311] A. P. M. JR and W. S. CRANE, *Phys. Rev. B* **31**, 3988 (1985).
- [312] S. J. BURNS and W. W. WEBB, *J. Appl. Phys.* **41**, 2078 (1970).
- [313] S. J. BURNS and W. W. WEBB, *J. Appl. Phys.* **41**, 2086 (1970).
- [314] M. J. YACAMAN and T. O. Z., *J. Appl. Phys.* **48**, 418 (1977).
- [315] H. BETHGE and H. HÖCHE, *Z. Naturforschung* **16**, 321 (1961).
- [316] H. HÖCHE and H. BETHGE, *J. of Crystal Growth* **33**, 246 (1976).
- [317] J. P. MATHISON, S. C. LANGFORD, and J. T. DICKINSON, *J. Appl. Phys.* **65**, 1923 (1989).
- [318] C. COUPEAU and J. GRILHE, *Mat. Sci. Eng.* **A271**, 242 (1999).
- [319] D. SCHMICKER, J. P. TOENNIES, R. VOLLMER, and H. WEISS, *J. Chem. Phys.* **95**, 9412 (1991).
- [320] G. LANGE, J. P. TOENNIES, R. VOLLMER, and H. WEISS, *J. Chem. Phys.* **98**, 10096 (1993).
- [321] T. E. GALLON, I. G. HIGGINBOTHAM, M. PRUTTON, and H. TOKUTAKA, *Surface Sci.* **21**, 224 (1970).
- [322] E. MEYER, H. HEINZELMANN, D. BRODBECK, G. OVERNY, R. OVERNY, L. HOWALD, H. HUG, T. JUNG, H. R. HIDBER, and H. J. GÜNTHERODT, *J. Vac. Sci. Technol. B* **9**, 1329 (1991).
- [323] W. A. SCHLUP and K. H. RIEDER, *Phys. Rev. Lett.* **56**, 73 (1985).
- [324] G. DROLSHAGEN and R. VOLLMER, *J. Chem. Phys.* **87**, 4948 (1987).
- [325] M. E. STRAUMANIS and J. S. SHAH, *Z. Anorg. All. Chem.* **391**, 79 (1972).
- [326] B. YATES and C. H. PANTER, *Proc. Phys. Soc.* **80**, 373 (1962).

- [327] J. E. RAPP and H. D. MERCHANT, *J. Appl. Phys.* **44**, 3919 (1973).
- [328] P. D. PATHAK and N. G. VASAVADA, *Acta Cryst. Sect:A* **28**, 30 (1972).
- [329] K. F. VON TROST, *Z. Naturforsch.* **18B**, 662 (1963).
- [330] K. K. SRIVASTAVA and H. D. MERCHANT, *J. Chem. Phys.* **34**, 2069 (1973).
- [331] Y. S. TOULOUKIAN, R. K. KIRBY, R. E. TAYLOR, and T. Y. R. LEE, *Thermodynamical Properties of Matter*, volume 13: Thermal Expansion (Nonmetallic Solids), Plenum, New York, Washington, 1977.
- [332] D. R. O'KEEFE, J. N. SMITH, R. L. PALMER, and H. SALTSBURG, *Surface Sci.* **20**, 27 (1970).
- [333] R. G. ROWE and G. EHRLICH, *J. Chem. Phys.* **63**, 4648 (1975).
- [334] R. G. ROWE, L. RATHBUN, and G. EHRLICH, *Phys. Rev. Lett.* **35**, 1104 (1975).
- [335] E. KOLODNEY and A. AMIRAV, *Surface Sci.* **155**, 715 (1985).
- [336] G. BRUSDEYLINS, G. DROLSHAGEN, A. KAUFHOLD, J. SKOFRONICK, and J. P. TOENNIES, *Surface Sci.* **189/190**, 972 (1987).
- [337] R. M. LOGAN, *Mol. Phys.* **17**, 147 (1969).
- [338] J. HALBRITTER, *Z. Naturforsch.* **29a**, 1723 (1974).
- [339] N. CABRERA, V. CELLI, F. O. GOODMAN, and R. MANSON, *Surface Sci.* **19**, 67 (1970).
- [340] F. O. GOODMAN and W. S. LIU, *Surface Sci.* **49**, 417 (1975).
- [341] A. CAPELLINI and A. P. J. JANSEN, *J. Chem. Phys.* **104**, 3366 (1996).
- [342] M. EHARA, H. D. MEYER, and L. S. CEDERBAUM, *J. Chem. Phys.* **105**, 8865 (1996).
- [343] G. BRUSDEYLINS and J. P. TOENNIES, *Surface Sci.* **126**, 647 (1983).
- [344] A. TSUCHIDA, *Surface Sci.* **14**, 375 (1969).
- [345] A. KAUFHOLD, PhD thesis, Georg-August Universität, Göttingen, Germany, 1985.

-
- [346] R. SCHINKE, *Surface Sci.* **127**, 283 (1983).
- [347] M. CHIESA, L. MATTERA, R. MUSENICH, and C. SALVO, *Surface Sci.* **151**, L145 (1985).
- [348] W. ALLISON and B. FEUERBACHER, *Phys. Rev. Lett.* **45**, 2040 (1980).
- [349] G. DARLING, *Gas-Surface News* **34**, 2 (2002).
- [350] H. F. BUSNENGO, W. DONG, P. SAUTET, and A. SALIN, *Phys. Rev. Lett.* **87**, 127601 (2001).
- [351] F. O. GOODMAN, *Surface Sci.* **46**, 118 (1974).
- [352] J. D. MCCLURE, *J. Chem. Phys.* **52**, 2712 (1970).
- [353] G. BOATO, P. CANTINI, U. GARIBALDI, A. C. LEVI, L. MATTERA, R. SPADACINI, and G. E. TOMMEI, *J. Phys. C* **6**, L394 (1973).
- [354] J. A. BARKER, A. W. KLEYN, and D. J. AUERBACH, *Chem. Phys. Lett.* **97**, 9 (1983).
- [355] G. TEPPER and D. MILLER, *Phys. Rev. Lett.* **69**, 2927 (1992).
- [356] G. TEPPER and D. MILLER, *J. Chem. Phys.* **98**, 9585 (1993).
- [357] A. R. W. MCKELLAR and J. SCHAEFER, *J. Chem. Phys.* **95**, 3081 (1991).
- [358] D. FARIAS, R. MIRANDA, and K. H. RIEDER, *J. Chem. Phys.* **117**, 2255 (2002).
- [359] R. ELBER and R. B. GERBER, *Chem. Phys. Lett.* **119**, 269 (1985).
- [360] B. FEUERBACHER, in *Vibrations at Surfaces*, edited by R. CAUDANO, J. M. GILLES, and A. A. LUCAS, p. 79, New York, 1980, Plenum Press.
- [361] R. BRÜHL, A. KALININ, O. KORNILOV, T. SAVAS, J. P. TOENNIES, R. GUARDIOLA, and J. NAVARRO, Diffraction of Neutral Helium Clusters: Evidence for Magic Numbers, to be published.
- [362] D. A. KING, *Physica Scripta* **T4**, 34 (1983).
- [363] C. Z. WANG, A. FASOLINO, and E. TOSATTI, *Phys. Rev. B* **37**, 2116 (1988).

- [364] B. SALANON and J. LAPUJOLADE, *Surface Sci. Lett.* **173**, 613 (1986).
- [365] J. KMETKO, C. YU, G. EVMENENKO, S. KEWALRAMANI, and P. DUTTA, *Phys. Rev. Lett.* **89**, 186102 (2002).
- [366] A. SZABO and N. S. OSTLAND, *Modern Quantum Chemistry*, Dover publications Inc., Mineola, New York, 1996.

Acknowledgements

I would like to thank to a number of people who helped and supported me during the realization of this work.

I am grateful to **Prof. J. Peter Toennies** for his constant support, friendly encouragement and guidance and for digging out papers whenever I asked something.

Special thanks to **Prof. F. Huisken** and **Prof. W. Lauterborn** for their kindness of taking the responsibility of being "Referent" and "Korreferent" for me and the final polishing of this manuscript.

Franziska Traeger is gratefully acknowledged, who was the most patient person to read and discuss experimental reports and to improve the most parts of this manuscript. Her assistance and fruitful discussions were invaluable.

Bodil Holst deserves my genuine thanks for giving me the freedom of experimenting with Magie-2 in the last year of my Ph.D. work and for discussions on Chapter 5.

I also thank **Jens Pick** and **Horst Wuttke**. They are wonderful people and highly skilled technicians and their support makes research like this possible¹. Also many thanks to all the staff in the workshops.

My heartfelt thanks go to **Geert-Jan Kroes** and **Rosendo Valero** for their delightful collaboration, providing me theoretical results and discussions on D_2 -LiF(001).

I am deeply thankful to **Bill Allison** and **Donald MacLaren** in Cavendish Lab, Cambridge who supplied Si(111):H(1×1) crystals.

I am indebted to **Eldon Knuth** for illuminating discussions with him on molecular beams; and also to **Jochen Vogt** and **Prof. G. Benedek** for fruitful suggestions for understanding the lattice expansion results.

I must also express my gratitude for the financial support provided by Max-Planck Gesellschaft.

I wish to thank **Andrew Graham**, **Rüdiger Brühl** and **Stephan Bartholmei** for their help with technical and computational problems, and once again **Rüdiger** and **Stephan** and also **Robert Grisenti** for card-games in *Holzofenbäcker* and even in secret corners of the Institute. I should also thank **Bahri Uzunoglu** of the DLR for keeping me in track with turkish daily news.

Last but not least, I would like to thank my wife **Dilek** for her love and patience throughout this work.

¹"Helium scattering is not a pursuit for the faint-hearted!" Bruce Doak.

Remark: Hopefully this is the last footnote.

Lebenslauf

Persönliche Daten

Name: Yasin Ekinçi
Geburtsdatum: 01.04.1976
Geburtsort: Denizli, Türkei
Familienstand: verheiratet und Vater eines Sohnes
Staatsangehörigkeit: türkisch

Wissenschaftlicher Werdegang

1991 - 1994 Yamanlar College, Izmir, Türkei
Schulabschluss mit Hochschulzulassung

1994 - 1997 Middle East Technical University, Ankara, Türkei
Bachelor of Science in Physik mit Status: High Honor

1997 - 1998 Middle East Technical University, Ankara, Türkei
Einjähriger Studiumgang in M.Sc. in Physik. Erfahrung als Tutor (Teaching assistant). Erfahrung in der Theorie der 'Elektronischen Eigenschaften niedrig-dimensionaler Halbleiter'.

1998 - 1999 De Montfort University, Leicester, England
Master of Philosophy (äquivalent zum Diplom). Titel der Arbeit: *Fabrication and Characterisation of PECVD Nanocrystalline Silicon Thin Films.*

1999 - 2003 Als Doktorand und wissenschaftlicher Mitarbeiter am Max-Planck-Institut für Strömungsforschung unter Leitung von Prof. J. P. Toennies. Erfahrung in Molekularstrahlstreuung an Oberflächen.

Veröffentlichungen

- G. Kartopu, S. C. Bayliss, Y. Ekinçi, E. H. C. Parker and T. Naylor *Observation of phonon confinement in SiGe nanocrystals and preferential etching of Si in porous Si_{1-x}Ge_x films* Phys. Stat. Solidi **197**, 263 (2003).
- U. Serincan, G. Kartopu, A. Guennes, T. G. Finstad, R. Turan, Y. Ekinçi and S. C. Bayliss *Characterization of Ge nanocrystals embedded in SiO₂ by Raman Spectroscopy*

A. Lebenslauf

Semicond. Sci. Technol. **19**, 247 (2004).

- R. B. Doak, Y. Ekinici, B. Holst, J. P. Toennies, T. Al-Kassab and A. Heinrich *Field ionization detection of supersonic molecular beams* submitted to Rev. Sci. Inst. **75**, 405 (2004).
- G. Kartopu, and Y. Ekinici *Further evidence on the observation of compositional fluctuation in $Si_{1-x}Ge_x$ alloy nanocrystals prepared in anodized porous SiGe films* submitted to Thin Solid Films.
- G. Kartopu, S.C. Bayliss, R.E. Hummel, Y. Ekinici and S.-S. Chang *Simultaneous micro-Raman and PL study of spark-processed Ge: Report on the origin of the orange PL emission band* submitted to J. Appl. Phys. (accepted)